University of Ljubljana
Faculty of Mathematics and Physics
Department of Physics

Tadej Novak

Search for type-III seesaw heavy leptons with the ATLAS detector at the LHC

Doctoral thesis

Adviser: prof. dr. Borut Paul Kerševan

Ljubljana, 2020

Univerza v Ljubljani
Fakulteta za matematiko in fiziko
Oddelek za fiziko

Tadej Novak

Iskanje težkih leptonov v gugalničnem mehanizmu tipa III z detektorjem ATLAS na trkalniku LHC

Doktorska disertacija

Mentor: prof. dr. Borut Paul Kerševan

Ljubljana, 2020

Acknowledgements

First of all I would like to thank my supervisor, prof. dr. Borut Kerševan, for all the patience and support throughout the whole duration of my PhD, giving me the possibility not only to work on the search for new physics at the ATLAS experiment, but also to participate in technical areas of the experiment that interest me. I am also grateful to be able to attend exciting conferences, schools and other international meetings during this time.

I would also like to thank all members of the Department for Experimental Particle Physics at Jožef Stefan Institute for all the support and ideas they offered, including interesting day-to-day discussions. I enjoyed working with my fellow PhD students, especially I would like to thank Miha Muškinja for the practical introduction to the ATLAS experiment and to data analysis. He is still a person that I can turn to with questions and problems about physics and work.

During my PhD I spent a lot of time at CERN, where I would like to express my gratitude to many friendly and helpful members of the ATLAS Collaboration with whom I worked data analysis and technical projects. I would thank John Chapman and other members of ATLAS simulation and software group for introducing me to large scale simulation software and giving me an opportunity to contribute significantly to such a big experiment.

Finally I am also grateful to my parents, family and friends for their endless support throughout my whole education.

Iskanje težkih leptonov v gugalničnem mehanizmu tipa III z detektorjem ATLAS na trkalniku LHC

Izvleček

V doktorskem delu bom predstavil iskanje težkih leptonov v gugalničnem mehanizmu tipa III z detektorjem ATLAS na Velikem hadronskem trkalniku. Za analizo so bili uporabljeni podatki, zajeti pri trkih protonov s težiščno energijo 13 TeV med drugim obdobjem trkov in meritev (Run 2). Skupna integrirana luminoznost znaša 139 fb^{-1}. Pri analizi sem se osredotočil na končna stanja z dvema lahkima leptonoma (elektroni ali mioni) v različnih možnih kombinacijah okusa in naboja, ob tem pa sta v dogodku še vsaj dva pljuska hadronov in visoka manjkajoča transverzalna gibalna količina. V sklopu dela sem razširil pristop pravokotnih rezov s strojnim učenjem. Statistična obdelava podatkov ne nakazuje nobene sledi novih delcev. Iz rezultatov sem izpeljal spodnje meje za mase težkih leptonov po gugalničnem mehanizmu tipa III, ki znašajo 790 GeV pri uporabi pravokotnih rezov in 950 GeV z uporabo strojnega učenja.

Ključne besede:

gugalnični mehanizem	gugalnični mehanizem tipa III	triplet fermionov
strojno učenje	odločitvena drevesa	nevronske mreže
ATLAS	CERN	LHC Run 2
dva leptona	dva pljuska hadronov	manjkajoča transverzalna gibalna količina

SEARCH FOR TYPE-III SEESAW HEAVY LEPTONS WITH THE ATLAS DETECTOR AT THE LHC

ABSTRACT

The thesis presents a search for the pair production of heavy leptons as predicted by the type-III seesaw mechanism. The search uses proton–proton collision data at a centre-of-mass energy of 13 TeV, corresponding to 139 fb^{-1} of integrated luminosity recorded by the ATLAS detector during Run 2 of the Large Hadron Collider. The analysis focuses on the final state with two light leptons (electrons or muons) of different flavour and charge combinations, with at least two jets and large missing transverse momentum. A cut-based approach is extended using a multivariate analysis. No significant excess over the Standard Model expectation is observed. The results are translated into exclusion limits on heavy lepton masses, and the observed lower limit on the mass of the type-III seesaw heavy leptons is 790 GeV using cut-based and 950 GeV using multivariate approach at 95% confidence level.

Keywords:

seesaw mechanism	type-III seesaw	fermion triplet
machine learning	boosted decision trees	neural networks
ATLAS	CERN	LHC Run 2
dilepton	two jets	missing transverse energy

Contents

LIST OF FIGURES

List of Tables

PART I

INTRODUCTION

CHAPTER 1

Type-III Seesaw Mechanism

The fundamental structure of the world around us has always been humanity's interest. The Standard Model (SM) is a fundamental theory combining the currently known elementary particles and the interactions among them. Since its conception in the 1960s and 1970s it has been thoroughly tested by numerous and diverse particle physics experiments. Discovery of the Higgs boson in 2012 represented the final experimental confirmation making the SM nowadays as a self-sufficient theory.

Although being very successful by providing correct predictions, several phenomena are left unexplained. It does not fully explain the asymmetry between matter and antimatter, the mystery of dark matter and dark energy, and also the origin of neutrino masses. The latter can be explained by the type-III seesaw mechanism which is the motivation for this thesis.

1.1 Standard Model of Particle Physics

The Standard Model of particle physics is a quantum field theory framework successfully describing fundamental particles and their interactions, where the particles are described as excited states of the respective fields. There are four fundamental forces in nature. Three of them are described by the SM, while gravitational force is orders of magnitude weaker and currently has no valid quantum description. Each of the forces is mediated by a fundamental carrier particle called a gauge boson. These spin 1 particles need to be exchanged to allow interaction between twelve fermions, half-integer spin particles.

Fermions can first be split into two primary types, quarks and leptons. Each type is further split into three generations. There are six quark flavours, three with positive fractional electric charge, also called "up-type" quarks (u, c and t), and three with negative charge, also called "down-type" quarks (d, s and b). Each lepton generation also corresponds to one flavour. Furthermore, they can be split into charged leptons

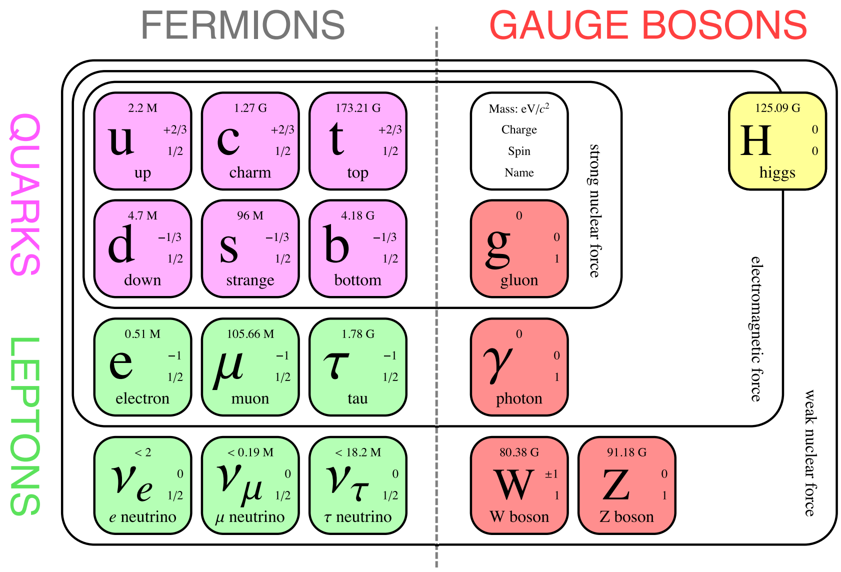

Figure 1.1: Diagram of the Standard Model of particle physics. Based on Ref. [1].

(e, μ and τ) with their corresponding neutral partners neutrinos (ν_e, ν_μ and ν_τ). All fermions also have their antiparticles with electric charge and other quantum numbers reversed.

The strong nuclear force is mediated by eight massless and electrically-neutral gluons. They carry a special type of charge called colour and interact only with quarks. Quarks are besides gluons the only other kind of particles carrying colour charge. The strong interaction was described in the quantum chromodynamics (QCD) theory with contributions from many physicists. Among them, Gell-Mann and Zweig [2, 3] proposed quarks as fundamental particles interacting with strong force. The QCD coupling constant is small for small distances, which is called asymptotic freedom and was postulated by Gross, Politzer and Wilczek [4, 5]. This results in the fact that in nature quarks exist only in bound states.

The second elementary force is the electromagnetic force, mediated by a massless and neutral photon. Any particle carrying electric charge can interact electromagnetically. This is true for all fermions except for neutrinos. They interact via the final fundamental force, the weak nuclear force. Three massive gauge bosons, the W^+, W^- and Z^0, act as mediators. The fact that photons have zero rest mass allows the range of the electromagnetic force to be infinite, but the range of the weak force reaches only across the atomic nucleus. Glashow, Salam and Weinberg provided a unified description of the electromagnetic and weak interactions with the so-called electroweak theory [6–8].

The final piece of the Standard Model is the Higgs boson, a scalar particle proposed by Brout, Englert and Higgs [9, 10], providing a mechanism through which particles acquire their mass. Higgs boson was discovered in 2012 by the ATLAS [11] and CMS [12] experiments representing the final experimental confirmation of the Standard Model. A diagram of all elementary particles and forces of the SM is illustrated in Figure 1.1.

Quantum field theories rely on the Lagrangian formalism of the classical field theory. The Lagrangian density $\mathcal{L}(\phi)$ allows for the derivation of the equations of motion of the field $\phi(x^\mu)$ using the Euler-Lagrange equation

$$\partial_\mu \left(\frac{\partial \mathcal{L}}{\partial(\partial_\mu \phi)} \right) - \frac{\partial \mathcal{L}}{\partial \phi} = 0\,. \tag{1.1}$$

The electroweak theory follows the $\mathrm{SU}(2)_L \times \mathrm{U}(1)_Y$ gauge symmetry group, where $\mathrm{SU}(2)_L$ is the symmetry group of the electroweak interaction that only couples to left-handed fermions. Right handed fermions are $\mathrm{SU}(2)_L$-singlets and do not interact weakly within the SM. $\mathrm{U}(1)_Y$ represents the symmetry group generated by the weak hypercharge Y, which is related to the electric charge Q and the third component of the weak isospin I_3 by the Gell-Mann–Nishijima formula [13, 14]

$$Q = I_3 + \frac{Y}{2}\,. \tag{1.2}$$

Three vector gauge fields W^a_μ $(a = 1, 2, 3)$ are associated to the $\mathrm{SU}(2)_L$ gauge group and one vector gauge field B_μ to the $\mathrm{U}(1)_Y$ group. Covariant derivatives can be defined as

$$D_\mu = \partial_\mu + i\frac{g}{2}\tau_a W^a_\mu + i\frac{g'}{2} Y B_\mu \tag{1.3}$$

and field strength tensors as $W^a_{\mu\nu} = \partial_\mu W^a_\nu - \partial_\nu W^a_\mu - g\epsilon^{abc} W^b_\mu W^c_\nu$ and $B_{\mu\nu} = \partial_\mu B_\nu - \partial_\nu B_\mu$, where g and g' are two coupling constants, ϵ^{abc} the structure constants of the SU(2) group, and τ_a Pauli matrices. The Lagrangian of the electroweak interaction can then be written as

$$\mathcal{L}_{\mathrm{EW}} = \overline{\psi} i \gamma^\mu D_\mu \psi - \frac{1}{4} W^{\mu\nu}_a W^a_{\mu\nu} - \frac{1}{4} B^{\mu\nu} B_{\mu\nu}\,, \tag{1.4}$$

where ψ are Dirac spinors and γ^μ are the four Dirac matrices. It is useful to define a product of gamma matrices $\gamma^5 = i\gamma^0\gamma^1\gamma^2\gamma^3$. Dirac spinors can be split into left-handed and right-handed components, $\psi_L = (1 - \gamma^5)\psi/2$ and $\psi_R = (1 + \gamma^5)\psi/2$. By definitions the two components are eigenstates of the γ^5 operator, also called *chirality* operator. *Helicity* can also be defined as the sign of projection of the spin vector onto the momentum vector. In the ultrarelativistic limit chirality and helicity coincide. The experimental evidence of many experiments [15–17] strongly supports the premise that only left-handed neutrinos are involved in weak interactions making it a chiral theory.

Electroweak interaction by itself treats all particles as massless. An additional complex scalar field needs to be introduced to introduce masses as

$$\phi = \begin{pmatrix} \phi^+ \\ \phi^0 \end{pmatrix} = \frac{1}{\sqrt{2}} \begin{pmatrix} \phi_1 + i\phi_2 \\ \phi^3 + i\phi_6 \end{pmatrix}\,, \tag{1.5}$$

also called the *Higgs field*. It can be introduced in the SM Lagrangian by adding

$$\mathcal{L}_{\text{Higgs}} = \left(D_\mu \phi\right)^\dagger (D^\mu \phi) - \left(\mu^2 \phi^\dagger \phi + \lambda (\phi^\dagger \phi)^2\right) \tag{1.6}$$

where the first therm is a kinetic term, with D_μ the electroweak covariant derivative (Eq. 1.3), and the second term is the *Higgs potential* $V(\phi)$. For values $\mu^2 < 0$ and $\lambda > 0$ the potential has a finite minimum value of

$$\phi^\dagger \phi = -\frac{1}{2}\frac{\mu^2}{\lambda} \equiv \frac{1}{2} v^2 \,. \tag{1.7}$$

A specific realisation of the minimum can be chosen with $\phi_1 = \phi_2 = \phi_4 = 0$ and $\phi_3 = v$ which breaks the symmetry of the electroweak interaction in a process called *spontaneous symmetry breaking* [18]. The final field after the breaking can be written as

$$\phi_0 = \frac{1}{\sqrt{2}} \begin{pmatrix} 0 \\ v + h(x) \end{pmatrix} , \tag{1.8}$$

where $h(x)$ is a small excitation above the minimum and represents the physical Higgs boson. Spontaneous symmetry breaking also causes the mixing of the electroweak fields. Gauge-boson fields observed in nature are not in the same basis as the electroweak interaction gauge fields. The two neutral fields, photon field A_μ and Z^0 boson field Z_μ connect with W^3_μ and B_μ with the Weinberg angle [7] or weak mixing angle θ_W as

$$\begin{pmatrix} Z_\mu \\ A_\mu \end{pmatrix} = \begin{pmatrix} \cos\theta_W & -\sin\theta_W \\ \sin\theta_W & \cos\theta_W \end{pmatrix} \begin{pmatrix} W^3_\mu \\ B_\mu \end{pmatrix} . \tag{1.9}$$

Weinberg angle can be expressed as a function of the weak coupling constants $\theta_W = g/\sqrt{g^2 + g'^2}$. The charged bosons $W^\pm$ are a superposition of fields W^1_μ and W^2_μ,

$$W^\pm_\mu = \frac{1}{\sqrt{2}} \left(W^1_\mu \mp i W^2_\mu\right) . \tag{1.10}$$

Entering this into the SM Lagrangian (kinetic term in Eq. 1.6) directly yields masses of the gauge bosons

$$m(W^\pm) = \frac{1}{2} v g \,, \quad m(Z^0) = \frac{vg}{2\cos\theta_W} = \frac{m(W^\pm)}{\cos\theta_W} \,, \quad m(H) = \sqrt{2\lambda} v \,, \tag{1.11}$$

where a mass term for a field X is of the form $\frac{1}{2} m^2 X_\mu X^\mu$.

Leptons have experimentally also been observed as massive. The Higgs term of the SM Lagrangian does not explain their mass so an additional *Yukawa interaction* [19] needs to be introduced. It couples a scalar field ϕ to a Dirac field ψ in a form of $V \sim g\overline{\psi}\phi\psi$. To derive the lepton masses due to the Higgs scalar field, the Yukawa term for leptons can be written as

$$\begin{aligned}\mathcal{L}_{\text{Yukawa}}^{\text{leptons}} &= -\frac{y_\ell}{\sqrt{2}}\left((\overline{\nu_\ell}, \overline{\ell})_L \begin{pmatrix} 0 \\ v+h \end{pmatrix} \ell_R + \overline{\ell}_R\,(0, v+h)\begin{pmatrix} \nu_\ell \\ \ell \end{pmatrix}_L\right) \\ &= -\frac{y_\ell v}{\sqrt{2}}\overline{\ell}\ell - \frac{y_\ell}{\sqrt{2}} h\overline{\ell}\ell\,.\end{aligned} \tag{1.12}$$

Charged lepton masses are directly proportional to Yukawa couplings y_ℓ as $m(\ell) = y_\ell v/\sqrt{2}$. Note that the right-handed lepton forms a singlet term ℓ_R because there are no right-handed neutrinos in the SM, while the left-handed charged leptons and neutrinos form a doublet. Consequently there is no neutrino mass term of the type $m_\nu \overline{\nu}\nu$. They are thus considered massless in the context of the Standard Model. Yukawa term can be generalised for all fermions as

$$\mathcal{L}_{\text{Yukawa}} = -m_f \overline{f} f \left(1 + \frac{h}{v}\right)\,. \tag{1.13}$$

The first term in Eq. 1.13 is also also called the Dirac mass term and the second one represents the lepton coupling to the Higgs field excitation (the Higgs boson).

At this point individual fermion generations are not interacting between each other. No direct decays of muons into electrons via $\mu \to e\gamma$ have been experimentally observed and both individual generation lepton number L_ℓ and total lepton number L are considered conserved. On the other hand electroweak decays of $K^+ \to \mu^+\nu_\mu$ have been experimentally confirmed. The K^+ meson is made of a u and a $\bar{s}$ quarks which means the interaction between different quark generations is possible. Mass eigenstates of quarks are thus not the same as the weak interaction eigenstates. The two bases are connected with the complex Cabibbo–Kobayashi–Maskawa (CKM) matrix [20, 21]

$$\begin{pmatrix} d' \\ s' \\ b' \end{pmatrix} = \begin{pmatrix} V_{ud} & V_{us} & V_{ub} \\ V_{cd} & V_{cs} & V_{cb} \\ V_{td} & V_{ts} & V_{tb} \end{pmatrix} \begin{pmatrix} d \\ s \\ b \end{pmatrix}, \tag{1.14}$$

where $|V_{ab}|^2$ is the probability to change quark flavour from a to b. Diagonal elements of the matrix have absolute values close to 1 indicating transitions mostly occur within a generation.

1.2 NEUTRINO MASSES AND THE SEESAW MECHANISM

Neutrinos are unique in that they can only interact by the weak interaction. They are colourless and electrically neutral. Experimentally available neutrinos are always polarised, where neutrinos are always left-handed and anti-neutrinos are always right-handed. As derived in the previous section, the Standard Model does not predict neutrino masses. If right-handed neutrinos would exist this implicates their interaction with matter is very different from left-handed neutrinos and is not covered by the SM.

Quark mixing in the weak interaction (Eq. 1.14) provoked ideas about the presence of mixing also in lepton sector [22]. Lepton number violating processes like $\mu \to e\gamma$ would require neutrino oscillations between left- and right-handed states and also between different neutrino flavours [23]. Neutrino mixing may take place only when the neutrino masses differ from zero. The flavour and mass bases are not necessarily the same which by definition makes flavour fields ν_{lL} for a flavour with index l a superposition of left-handed components of the neutrino fields with definite masses

$$\nu_{lL} = \sum_k U_{lk} \nu'_{kL} \,, \tag{1.15}$$

where ν'_k is the neutrino field with mass m_k and U is a unitary matrix called Pontecorvo–Maki–Nakagawa–Sakata (PMNS) matrix [24].

As neutrino charge is zero, neutrinos may be either Dirac particles or neutral Majorana particles. Ettore Majorana proposed a type of neutral fermions that can be described with a real wave equation [25]. They are their own antiparticles as particle and antiparticle fields are related by complex conjugation. A Majorana neutrino can be defined as $\nu = \nu_L + \nu_L^C$, where ν_L^C is the charge conjugated field $\nu_L^C = C\overline{\nu}_L^T$.

The neutrino Dirac mass term is of the form

$$\mathcal{L}^{\mathrm{D}} = -\sum_{l',l} \overline{\nu}_{l'L} M^{\mathrm{D}}_{l',l} \nu_{lR} + \mathrm{h.c.} \,, \tag{1.16}$$

where M^{D} is a complex, non-diagonal matrix, that can be diagonalised using the PMNS relation from Eq. 1.15. To be able to construct the Dirac mass term right-handed neutrinos are needed. As they are not experimentally observed such particles would only be sensitive to gravitational force and Higgs fields, and can be called *sterile neutrinos* [23]. The neutrino Majorana mass term can be defined as

$$\mathcal{L}^{\mathrm{M}} = -\frac{1}{2} \sum_{l',l} \overline{\nu}_{l'L} M^{\mathrm{M}}_{l',l} (\nu_{lL})^C + \mathrm{h.c.} \,, \tag{1.17}$$

where M^{M} is again a complex, non-diagonal matrix, diagonalisable with the PMNS matrix. The PMNS matrix can be extended with additional sterile neutrinos that allow SM neutrino masses to have both Dirac and Majorana terms. While the Dirac mass term can be generated by the standard Higgs mechanism, the Majorana term can be generated only by beyond the SM mechanisms as there is no such term in the SM Lagrangian.

Discovery of the neutrino oscillations by the Super-Kamiokande [26] observatory in Japan and Sudbury Neutrino Observatory (SNO) [27] in Canada confirmed that at least two neutrinos have non-zero mass and was recognised with the 2015 Nobel Prize for Physics. This requires modifications to the SM.

To account for tiny Majorana neutrino masses with only the Standard Model degrees of freedom a higher dimensional effective operator is needed, symbolically written as

$$\mathcal{L}_{\text{eff}} = y_{ij}\frac{L_i\phi\phi L_j}{M}\,, \tag{1.18}$$

where L_i are the SM left-handed leptonic doublets $L_i = (\nu_i, \ell_i)_L$, ϕ the SM Higgs doublet $\phi = (\phi^+, \phi^0)$, y_{ij} effective Yukawa couplings, and M a mass scale representing the scale of new physics introduced. Neutrinos get Majorana masses with the spontaneous electroweak symmetry breaking by the Higgs vacuum expectation value v as

$$m_\nu = y\frac{v^2}{M}\,. \tag{1.19}$$

To be able to achieve small neutrino masses either M is much larger than v or y has to be small. The main consequence of the operator is $\Delta L = 2$ lepton number violation. The operator itself is not renormalisable which can be fixed by adding new particles as part of the *seesaw mechanism*. It connects SM left-handed neutrino masses with the masses of new right-handed neutrino-like particles. The higher the mass of the right-handed neutrino, the lower the mass of the left-handed neutrinos. In the minimal scenario of adding just one new type of particles there are three possible extensions of the SM by introducing

1. at least two fermionic singlets, called right-handed neutrinos — type-I seesaw [28–32];
2. a scalar $SU(2)_L$ triplet — type-II seesaw [33–35];
3. at least two fermionic $SU(2)_L$ triplets — type-III seesaw [36].

Combinations of the seesaw models are also possible: Left-right symmetric models contain both type-I and type-II seesaw particles, while a hybrid scenario of both type-I and type-III is possible in the adjoint representation of SU(5) [37, 38].

1.3 TYPE-III SEESAW MODEL

The type-III seesaw model [36] introduces additional triplets of heavy fermionic fields with zero hypercharge in the adjoint representation of $SU(2)_L$ that couple to electroweak gauge bosons and generate neutrino masses through Yukawa couplings to the Higgs boson and neutrinos. Consequently, these new charged and neutral heavy leptons could be produced in EW processes in proton–proton collisions at the Large Hadron Collider at observable rates. The new fermionic triplet components are denoted $(\Sigma^+, \Sigma^-, \Sigma^0)$. The Yukawa interaction with one of the triplets can be defined as

$$\begin{aligned}\mathcal{L}^{\text{type-III seesaw}}_{\text{Yukawa}} = &- \left(\sum_{i,j=e,\mu,\tau} y_{1ij} \overline{L}_{iL} \phi \ell_{jR} + \sum_{i=e,\mu,\tau} y_{2i} (\phi^{CT} \overline{\Psi}_L L^C_{iL} + \phi^T \overline{\Psi}^C_L L_{iL}) + \text{h.c.} \right) \\ &- y_3 \mathrm{Tr}(\overline{\Psi}\Psi) \,,\end{aligned} \tag{1.20}$$

where y are Yukawa couplings, y_3 an explicit mass term for the triplet and Ψ

$$\Psi = \begin{pmatrix} \Sigma^+ & \Sigma^0/\sqrt{2} \\ \Sigma^0/\sqrt{2} & \Sigma^- \end{pmatrix} . \tag{1.21}$$

After the spontaneous symmetry breaking this simplifies into

$$\mathcal{L}^{\text{type-III seesaw}}_{\text{Yukawa}} = \frac{1}{2} \overline{\eta'} M_\nu \eta' + (\overline{\Psi'}_L M_\ell \Psi'_R + \text{h.c.}) \,. \tag{1.22}$$

Standard Model leptons here mix with the newly introduced heavy leptons in vectors $\eta' = (\nu_e, \nu_\mu, \nu_\tau, \Sigma^0)^T$, $\Psi'_L = (e_L, \mu_L, \tau_L, \Sigma^-_R)^T$ and $\Psi'_R = (e_R, \mu_R, \tau_R, \Sigma^-_L)^T$. M_ν and M_ℓ represent mass mixing matrices for neutrinos and charged leptons.

A simplified model introducing only one fermionic triplet is used for this thesis, which generates a single light neutrino mass. This model should really be viewed as the low energy limit of a more complete theory. In order to satisfy experimental requirements from the neutrino oscillation experiments and generate an additional neutrino mass, either another type-III seesaw fermionic triplet or a type-I seesaw singlet can be added. The simplifying assumption of a single fermionic triplet has little impact on LHC physics as in most theoretical models only the lighter states can be generated in TeV collider experiments. In addition all phases of the Yukawa couplings are ignored and the PMNS matrix will be considered real. The single triplet will be denoted (L^+, L^-, N^0) and also referred to as heavy leptons. L^+ is the antiparticle of L^- and N^0 is its own antiparticle (i.e. a Majorana particle).

The heavy leptons in a triplet are assumed to be degenerate in mass. This assumption does not limit the generality of results because the theoretical calculations predict only a small mass-splitting due to radiative corrections and the resulting transitions between heavy leptons are highly suppressed [39]. In addition all phases of the Yukawa couplings will be ignored and the PMNS matrix will be considered real, as this should have no consequence on the process signature at the LHC.

The triplets of the type-III seesaw model, N^0 and $L^\pm$, are produced in pairs in the pp collisions at the LHC through gauge coupling [40]. The production mechanism happens via $q\bar{q}$ interaction mediated by a virtual boson, either Z or W boson (Figures 1.3 and 1.4). Their allowed decay modes are listed in Eq. 1.23.

$$\begin{aligned} &N^0 \to l^\pm W^\mp \qquad && L^\pm \to \nu W^\pm \\ &N^0 \to \nu Z && L^\pm \to l^\pm Z \\ &N^0 \to \nu H && L^\pm \to l^\pm H \end{aligned} \tag{1.23}$$

The remaining degrees of freedom in the considered simplified model are the unknown mixing angles V_α ($\alpha = e, \mu, \tau$) between the SM leptons and the new heavy lepton states, which enter only in the expressions for the $L^\pm$ and N^0 decay widths. The production cross-section does not depend on the V_α parameters because the heavy leptons are produced through the coupling to the EW bosons. Only the branching fraction $\mathcal{B}_\alpha$ of the $L^\pm$ and N^0 decays to lepton flavour α depends on the values of the mixing angles and is proportional to

$$\mathcal{B}_e \propto \frac{|V_e|^2}{|V_e|^2 + |V_\mu|^2 + |V_\tau|^2} \,. \tag{1.24}$$

In this analysis the decay branching ratios are assumed to be equal for all three lepton flavours, with $\mathcal{B}_e = \mathcal{B}_\mu = \mathcal{B}_\tau = 1/3$. References [41–43] derive in detail the following bounds on the allowed combinations of couplings for the type-III seesaw model as listed in Eq. 1.25.

$$\begin{aligned} |V_e| &< 5.5 \times 10^{-2} \qquad & |V_e V_\mu| &< 1.7 \times 10^{-7} \\ |V_\mu| &< 6.3 \times 10^{-2} & |V_e V_\tau| &< 4.2 \times 10^{-4} \\ |V_\tau| &< 6.3 \times 10^{-2} & |V_\mu V_\tau| &< 4.9 \times 10^{-4} \end{aligned} \tag{1.25}$$

The decay branching fractions also depend on the mass of the heavy leptons and are shown in Figure 1.2 for the flavour democratic scenario. The process with the largest effective cross-section is the one with both N^0 and $L^\pm$ decaying into final states containing a W boson as shown in Figure 1.3:

$$\begin{aligned} q\bar{q} &\to N^0 + L^\pm \to W^\pm + \ell^\mp + W^\pm + \nu \\ q\bar{q} &\to N^0 + L^\pm \to W^\mp + \ell^\pm + W^\pm + \nu \end{aligned} \tag{1.26}$$

1.4 SEARCHES AT THE LARGE HADRON COLLIDER

Several type-III seesaw heavy lepton searches have been performed previously in different decay channels at the Large Hadron Collider. The search presented in this thesis is an extension of a similar search performed by ATLAS in the LHC Run 1 at $\sqrt{s} = 8\,\text{TeV}$ [44], which excluded heavy leptons with masses below 335 GeV for the

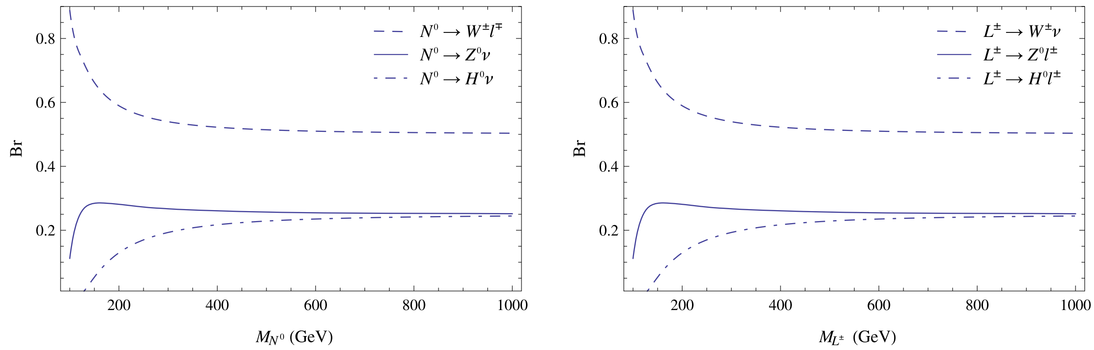

(a) (b)

Figure 1.2: Branching ratios of the minimal type-III seesaw heavy leptons into Z (continuous line), W (dashed line) and H bosons (dot-dashed line). Flavour democratic scenario is used with $V_\tau = V_e = V_\mu$. (a) shows decay branching ratios of N^0 and (b) shows decay branching ratios of $L^{\pm}$. Adapted from Ref. [40].

same decay channels and final state, consisting of two light leptons and two jets. In Run 1 this search was complemented by another ATLAS search for heavy leptons using the three-lepton final state [45], excluding heavy lepton masses below 470 GeV. A Run 2 search performed by the CMS experiment at $\sqrt{s} = 13$ TeV [46] focused on multi-lepton final states, requiring using at least three leptons, excluding the type-III seesaw heavy leptons with masses up to 880 GeV. Consequently, the search presented in this thesis, using the full ATLAS Run 2 dataset, is currently the only type-III seesaw search performed by the LHC experiments in Run 2 in this challenging final state, and, as it will be shown, providing competitive sensitivity to the recently published ones. Substantial refinements relative to the published Run 1 ATLAS analysis have been made in the background estimation and selection of signal candidate events, as well as the theoretical signal modelling and signal cross-section next-to-leading-order calculation, which all have a significant impact on the achieved measurement sensitivity of this analysis.

The search presented is optimized for the dominant processes with two leptons in the final state, where one W boson decays leptonically and the other decays hadronically. The two dominant Feynman diagrams are shown in Figure 1.3. There are other diagrams that contribute to the dilepton final states, for example pair production via Z boson with L^+ decaying into W and L^- into Z boson as displayed in Figure 1.4.

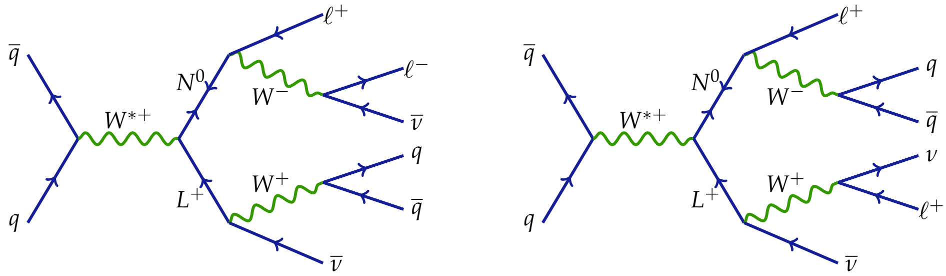

(a)

(b)

Figure 1.3: Feynman diagrams of the dominant production and decay process in the (a) opposite-charge and (b) same-charge final state cases.

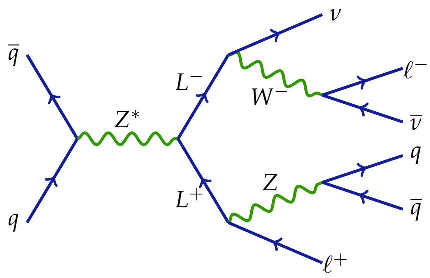

Figure 1.4: Example feynman diagram also contributing to the dilepton final state.

CHAPTER 2

INTRODUCTION TO MACHINE LEARNING

Machine Learning is the science of programming computers so they can learn from data. The term itself is fairly old and was defined by Arthur Samuel in 1959 as "the field of study that gives computers the ability to learn without being explicitly programmed". But why not use traditional programming to analyse and process data? Machine learning algorithms can replace long lists of rules and fine-tuning or even find a solution to a problem that could not be solved before. They help analyse large amount of complex data and also adapt while data are being collected.

Nowadays machine learning is a very broad field with many different applications from spam filtering to speech and image recognition. Many existing applications are also used in particle physics, from generating calorimeter responses of a particle to categorising types of hadronic jets based on the quark flavour. This thesis will only focus on a small subset needed to separate possible new physics from the large Standard Model background. As the ATLAS experiment dataset contains a large number of observables it is demanding to select the discriminant ones by hand. Definitions of machine learning concepts and classification techniques summarised in this chapter are based on Refs. [47–49].

2.1 MACHINE LEARNING FUNDAMENTALS

The main concept of machine learning is to show the computer examples of the problem to solve and let it figure out how to solve it itself instead of telling it the exact steps required to solve a problem. Results need to be derived using the input information called *features*. Classification problems assign *labels* to each of the inputs, e.g. separating signal from background. A problem is described by a *model*. The model is a sequence of mathematical operations that give you the solution of the problem based on the inputs and the model *parameters* or *weights*. The choice of model is arbitrary and mostly depends on the type of problem, for example a model can be a simple polynomial that we want to fit on the data and the polynomial coefficients are the weights. The goal of the computer is to estimate the model parameters as good as possible. The learning stage is usually called *training*, an iterative process trying to improve the result each step. Automatic means of testing the effectiveness of any current weight assignment are needed. Testing of all the possible parameter combinations would be too long so the weights at each step should be assigned in a way to improve the performance. The basic sketch of training of a machine learning model is shown in Figure 2.1.

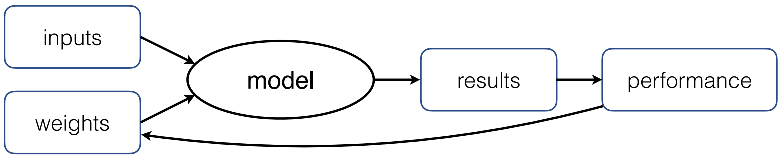

Figure 2.1: Training a machine learning model.

There are different types of machine learning algorithms based on how the model is trained. *Supervised learning* uses labelled data to solve regression or classification problems. The resulting model can be used to predict labels. On the other hand *unsupervised learning* does not know any specific label or category of the input data. It is trying to understand patterns and clusters of data. A special case of unsupervised learning is *reinforcement learning* where the algorithm interacts with the environment by performing actions and learns from errors or rewards. This thesis focuses on supervised learning on a binary classification problem trying to separate signal from background assigning two labels. It is important to train on representative dataset as a model can only learn to operate on patterns seen in the input data used to train it. The most general simulated background sample needs to be used to avoid signal events being misidentified as background. Only labels assigned on the training sample are then predicted by the model, no additional information is extracted while learning.

The performance of the model needs to be estimated reliably. When running over real data, our model trained on simulation should give comparable results. By design the accuracy of prediction on the training sample should increase with the duration of the training as the model is getting better. This does not tell us anything about the performance using data the model has not seen yet. To solve this we define independent *training* and *validation* sets, where the model learns from the properties of the training set but the performance is estimated using the validation set. If training for too long, especially if the size of the input data is small, the accuracy of the model will start to get worse. This is called *over-fitting* as model stops being general enough. A common practice is to stop the training once the performance estimate has worsened for several iterations in the row. While two separate sets will prevent over-fitting the input data might still be slightly biased. A third *test* set can be used after the training to get the final

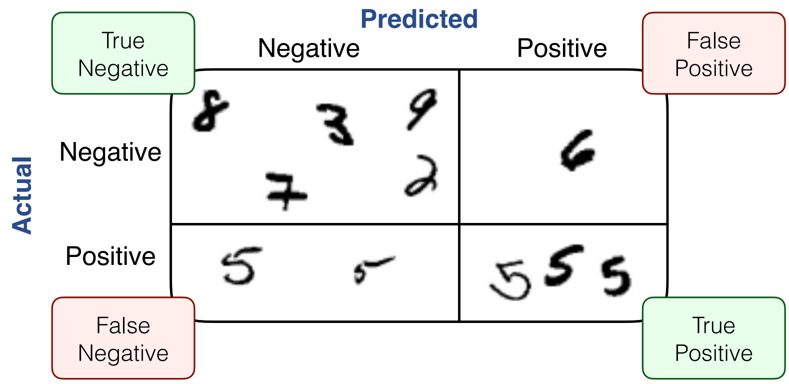

Figure 2.2: An illustrated binary classification confusion matrix shows examples of true negatives (top left), false positives (top right), false negatives (lower left), and true positives (lower right). The goal of the model is to analyse images of handwritten digits and separate digit 5 from others. Adapted from Ref. [47].

performance estimate. Using the data the model never used in the optimisation process gives a realistic performance estimate which should be similar to using the validation set.

There are many different performance metrics. Classification predictions can be described in a confusion matrix, an example of which is illustrated in Figure 2.2. Each row represents an actual class, while each column represents a predicted class. This gives four classes in a simple case of a binary classifier. Correctly predicted cases are called *true positives* (*TP*) and *true negatives* (*TN*), while wrongly predicted classes are called *false positives* (*FP*) and *false negatives* (*FN*). A perfect classifier would have only true positives and true negatives, so its confusion matrix would have non-zero values only on its main diagonal. Classifier *accuracy* can be defined as

$$\text{accuracy} = \frac{TP + TN}{TP + TN + FP + FN}\,. \tag{2.1}$$

Together with the confusion matrix this gives basic information about the classifier performance. Accuracy of the positive predictions, called the *precision* of the classifier is defined as

$$\text{precision} = \frac{TP}{TP + FP}\,, \tag{2.2}$$

corresponding to the purity of the selected signal events. The ratio of positive instances that are correctly detected by the classifier, named *recall*, *sensitivity* or *true positive rate*, is defined as

$$\text{recall} = \frac{TP}{TP + FN}\,, \tag{2.3}$$

representing signal selection efficiency. On the other hand *false positive rate* is defined as

$$\text{false positive rate} = \frac{FP}{FP + TN}\,, \tag{2.4}$$

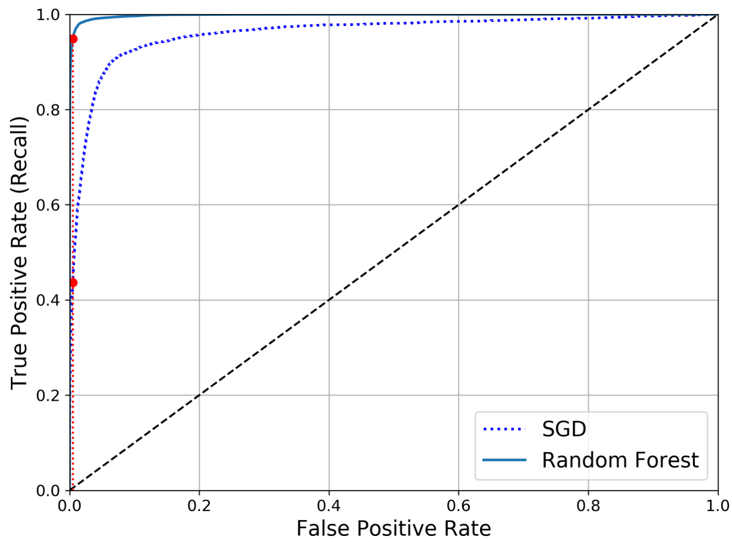

Figure 2.3: An illustrated ROC curves comparison of two different binary classifiers. The Random Forest classifier is superior to the SGD classifier because its ROC curve is much closer to the top-left corner, and it has a greater AUC. The dotted line represents the ROC curve of a purely random classifier. The red circles highlight the difference in recall for a chosen false positive rate. Taken from Ref. [47].

which is the fraction of background events incorrectly identified as signal. The combination of defined metrics can be used to optimise the structure of the model and also stop the training after the right number of iterations. In many applications of binary classifiers, including separating signal from background in a particle physics data analysis, the amount of positively labelled data should be as high as possible while keeping the number of mistakes low, meaning the precision should be as high as possible.

The *receiver operating characteristic* (ROC) curve plots the true positive rate against the false positive rate. The performance of different classifiers can also be compared with the measurement of the area under the ROC curve (AUC). A perfect classifier will have a ROC AUC equal to 1, whereas a purely random classifier will have a ROC AUC equal to 0.5. Moving along the ROC curve can adapt the performance of the classifier according to the application requirements. The higher the recall, the more false positives the classifier produces. This is illustrated in Figure 2.3. In the context of the thesis we can interpret the ROC curve as signal efficiency as a function of background contamination. If a background events number close to zero is required to be classified as signal signal efficiency will also be low. The ROC curve is only defined for binary classifiers but the confusion matrix can be generalised for multi-class classification where each extra class adds one additional column and row.

2.2 BOOSTED DECISION TREES

A decision tree builds upon iteratively asking questions to partition data. Decision trees are usually binary with each question splitting the number of options by approximately half. An illustration of a binary decision tree is shown in Figure 2.4. In machine learning decision trees split the data into two groups using a cut on one of the features.

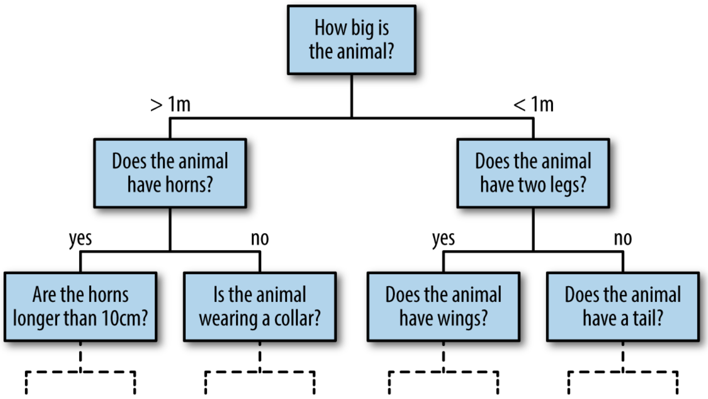

Figure 2.4: An example of a binary decision tree to classify animals. Taken from Ref. [50].

The depth of a decision tree defines the complexity of the model. Unfortunately even a few levels deep decision trees can quickly adapt on the training sample and are prone to over-fitting. Machine learning algorithms which are only slightly better than random guessing are called *weak learners*, one example being a decision tree. On the other hand a *strong learner* can provide a good classification prediction that is well-correlated with the true classification. A simple improvement over basic decision trees is called *bagging* (short for bootstrap aggregation). The training set is randomly sampled into N subsets with each used as an input to an independent decision tree. The ensemble of trained weak learners can then be averaged to yield a better prediction. An extension of this method is the *random forest* algorithm. Bagging is first performed on a random number of features of data, which finds the best feature in the subset. The resulting decision trees are then averaged over random data samples and combined in a final classifier.

An alternative to bagging is *boosting*, combining a learning algorithm in series to achieve a strong learner from many sequentially connected weak learners. Each tree attempts to minimise the errors of previous tree. Adding many trees in series and each focusing on the errors from previous one make boosting a highly efficient and accurate model. Unlike bagging, boosting does not involve bootstrap sampling. Every time a new tree is added, it fits on a modified version of initial dataset. The algorithm used in this thesis is called *gradient boosting*. Each predictor in the ensemble learns from residual errors made by the previous predictor, where a gradient of a loss function is used. A commonly used loss function for gradient boosting is cross-entropy or "log-loss", which measures the performance of a classification model whose output is a probability value between 0 and 1, defined as

$$H(p,q) = -\sum_i p_i \log q_i \,, \tag{2.5}$$

where p is the set of true labels and q set of predictions. In case of binary classification where p and q are sets $p \in \{0,1\}$ and $q \in (0,1)$ this simplifies to

$$H(p,q) = -p \log q - (1-p) \log(1-q) \,. \tag{2.6}$$

2.3 Neural Networks

Another type of machine learning algorithm are *artificial neural networks* (ANNs), commonly shortened as *neural networks* (NNs). They are inspired by human brain by connecting artificial *neurons* in multiple layers to connect the input data with the output prediction. Each neural network has one input layer and one output layer connected with one or more hidden layers. When multiple hidden layers are used these networks are called *deep neural networks*. While the number of neurons in hidden layers is arbitrary, input and output layers have the same number of neurons as the dimension of the input and output, respectively. Binary classifiers usually yield one probability value. A schematic of a typical neural network with two hidden layers is presented in Figure 2.5(a).

The output of a neuron $h_{\mathbf{w}}$ is defined as a weighted sum of an input vector $\mathbf{x}$ and an activation f function applied

$$h_{\mathbf{w}}(\mathbf{x}) = f(\mathbf{x} \cdot \mathbf{w}) \,, \tag{2.7}$$

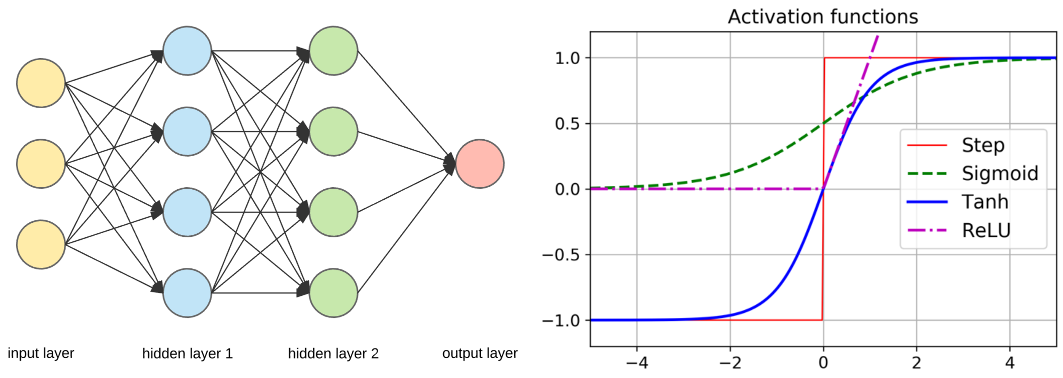

(a) (b)

Figure 2.5: (a) A schematic of a typical neural network with an input layer, two hidden layer and an output layer with one neuron in case of a binary classification. Taken from Ref. [51]. (b) Activation functions used in neural networks. Taken from Ref. [47].

where **w** is a vector of weights. To avoid bias due to the phase space of the input data, features are commonly normalised in an interval between 0 and 1 or -1 and 1.

A neutral network is trained using the *backpropagation* algorithm. Input data are split into batches with one batch being analysed at the time. Each pass through the whole training set is called an *epoch*. For each layer the algorithm computes the output of all the neurons in the layer and passes the result to the next layer. This is called the forward pass. Compared with making predictions all intermediate results are preserved since they are needed for the backpropagation. Next, the loss function is used to estimate the performance of the network. The errors are then backpropagated in reverse direction through all layers and assigns contributions to each connection. This step efficiently measures the error gradient across all the connection weights in the network by propagating the error gradient backward through the network. Finally, a gradient descent optimisation step is used to adapt all the weights in the network, using the error gradients it just computed.

Several activation functions can be used, illustrated in Figure 2.5(b):

- the step function,
- the logistic (sigmoid) function $\sigma(z) = 1/(1 + \exp(-z))$,
- the hyperbolic tangent function $\tanh(z) = 2\sigma(2z) - 1$,
- the Rectified Linear Unit function $\mathrm{ReLU}(z) = \max(0, z)$.

The step function is not commonly used as its gradient is zero. ReLU on the other hand is often the first choice as it is fast to compute.

PART II

The ATLAS Experiment at the Large Hadron Collider

CHAPTER 3

The ATLAS Detector

The ATLAS detector (A Toroidal LHC ApparatuS) [52] is a general purpose detector designed to perform both SM measurements and searches for new physics phenomena at TeV scale. It is situated at the interaction point 1 of the Large Hadron Collider [53] (overview in Section 3.1) about 100 m underground. ATLAS has cylindrical shape being about 44 m long and 25 m high, and is forward-backward symmetric with respect to the interaction point. The overall weight of the full detector is about 7000 t.

The overview of main ATLAS components and subdetectors is illustrated in Figure 3.1. The experiment got its name from the three large superconducting toroid magnets (one barrel and two endcaps). The main toroid consists of 8 coils evenly distributed around the barrel. The second part of the magnetic configuration is a thin superconducting solenoid surrounding the inner-detector cavity.

Charged particle tracks and their origin vertices are reconstructed in the inner detector. It consists of semiconductor pixel and strip detectors in the inner part and of transition radiation detectors in the outer part of the subdetector as detailed in Section 3.2. Energy of the particles is measured by slowing them down the liquid-argon electromagnetic sampling calorimeters and the scintillator-tile hadronic calorimeters. Both technologies are explained in Section 3.3. Finally the muon spectrometer surrounds the calorimeters and is designed to measure the position and momentum of charged muon tracks as described in Section 3.4.

Before looking at each subdetector system in detail the coordinate system and nomenclature used to describe the ATLAS detector need to be defined. The origin of the coordinate system coincides with the nominal interaction point, where the z-axis is defined in the direction of the beam. As all interactions happen in the center of the detector spherical coordinates are usually preferred. The polar angle θ is measured from the beam axis and the azimuthal angle ϕ is measured around the beam axis. Instead of θ the pseudorapidity is used, defined as $\eta = -\ln\tan(\theta/2)$. All the transverse quantities such as the transverse momentum p_{T}, the transverse energy E_{T} and the

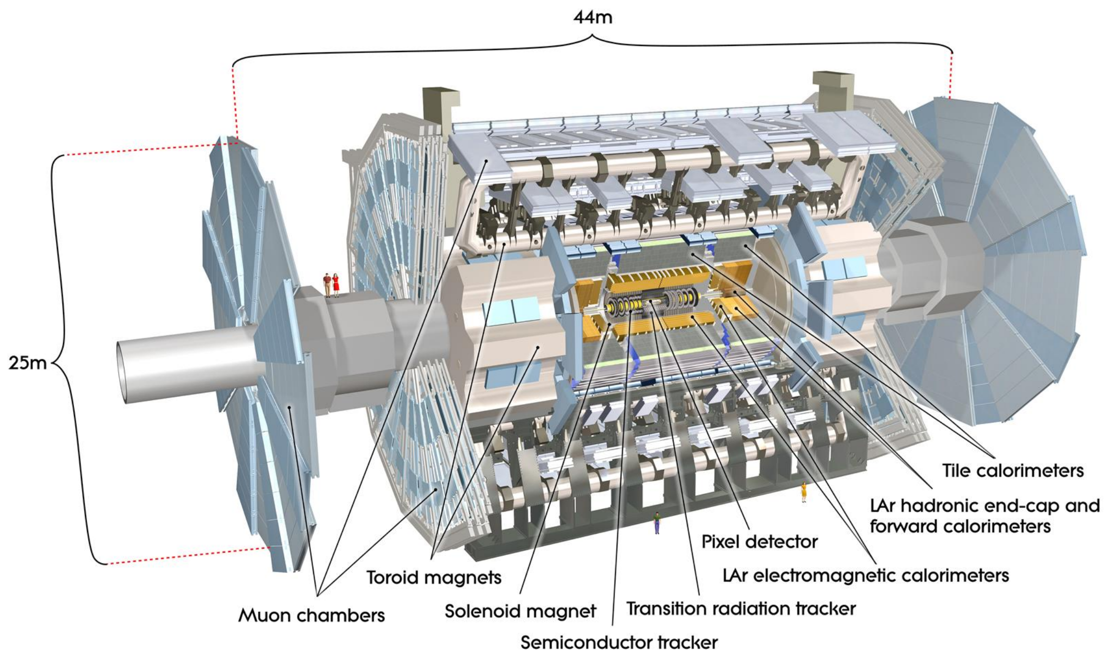

Figure 3.1: Cut-away view of the ATLAS detector showing the magnet configuration and four main components, the Inner Detector (Pixel, SCT and TRT), the Liquid Argon Calorimeter, the Tile Calorimeter and the Muon Spectrometer. Taken from Ref. [52].

missing transverse energy $E_{\mathrm{T}}^{\mathrm{miss}}$ are defined in the x-y plane. The distance ΔR in the pseudorapidity-azimuthal angle space is defined as $\Delta R = \sqrt{\Delta\eta^2 + \Delta\phi^2}$.

3.1 LARGE HADRON COLLIDER

The Large Hadron Collider (LHC) is a two-ring-superconducting-hadron accelerator and collider. It is installed in the existing 26.7 km tunnel previously occupied by the LEP machine. The tunnel has eight straight sections and eight arcs and lies between 45 m and 170 m below the surface.

The LHC is designed to accelerate not only proton beams, but also heavy ions, for example lead (Pb) or xenon (Xe) nuclei. It is the final stage of the CERN accelerator complex, illustrated in Figure 3.2. The proton source is a simple bottle of hydrogen gas. An electric field is used to strip hydrogen atoms of their electrons to yield protons. Linear accelerator Linac 2, the first in the chain, accelerates the protons to the energy of 50 MeV. The beam is then injected into the Proton Synchrotron Booster (PSB), which accelerates the protons to 1.4 GeV, followed by the Proton Synchrotron (PS), which

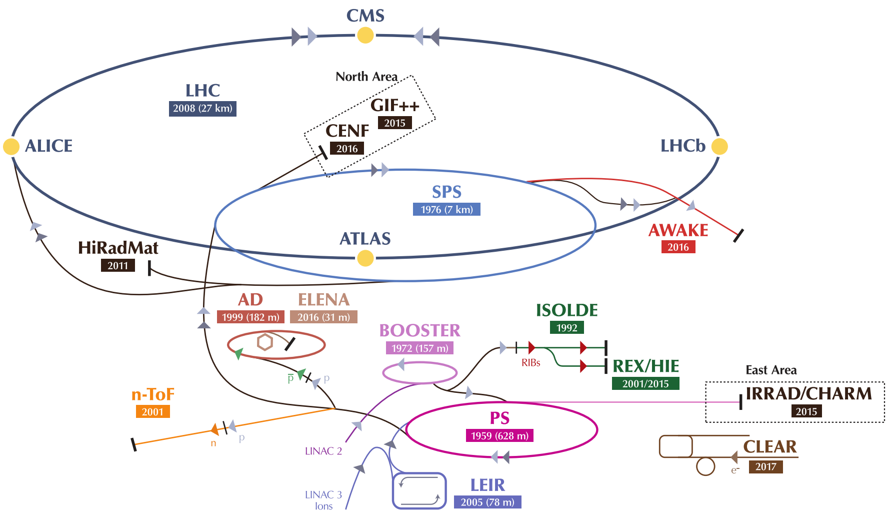

Figure 3.2: The CERN accelerator complex in August 2018. The path of proton and ion beams is marked with grey arrows and the main LHC experiments are marked with yellow circles. Adapted from Ref. [54].

pushes the beam to 25 GeV. Protons are then sent to the Super Proton Synchrotron (SPS) where they are accelerated to 450 GeV. Lead ions for the LHC start from a source of vaporised lead and enter a different starting accelerator, Linac 3, before being collected and accelerated in the Low Energy Ion Ring (LEIR). They then follow the same route to maximum energy as the protons.

To bend the protons at the full energy of 6.5 TeV superconducting dipole magnets made of niobium-titanium (Nb-Ti) alloy are used. They are cooled down to the operating temperature of 1.9 K by superfluid helium and can reach magnetic fields up to 8.3 T. The beams are focused using quadrupole magnets and also higher order magnets closer to the interaction point.

Proton beams are bunched together into up to 2808 bunches as they are accelerated by an oscillating electric field. This also allows timing control of when collisions happen. Collisions take place every 25 ns at four interaction points at the ATLAS, ALICE, CMS and LHCb experiments.

3.2 INNER DETECTOR

The goal of the ATLAS Inner Detector (ID) is to provide robust pattern recognition and tracking including primary and secondary vertex measurements for tracks above $p_T = 0.5$ GeV within $|\eta| = 2.5$. Additionally the transition radiation tracker complements calorimeters in electron identification up to $|\eta| < 2.0$. The ID is immersed in a 2 T

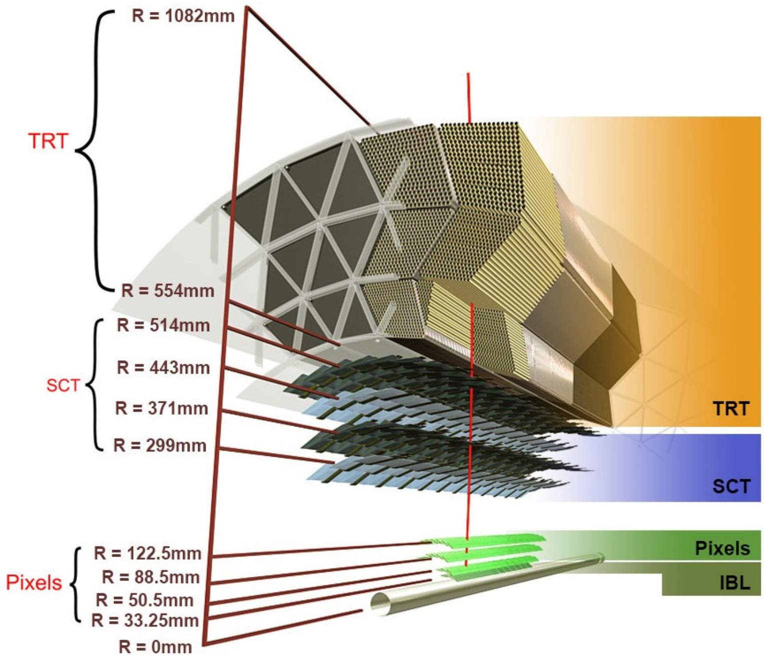

Figure 3.3: Drawing of detector components and structural elements of the barrel inner detector, traversed by a charged track shown in red ($p_{\mathrm{T}} = 10\,\mathrm{GeV}$, $\eta = 0.3$). Taken from Ref. [55].

magnetic field provided by the central solenoid. A schematic of the components is shown in Figure 3.3.

Originally the Pixel Detector consisted of 1744 modules [52] distributed in three barrel layers and two endcaps, each with three disk layers. The position accuracy in the R–ϕ direction is down to 10 µm and in the perpendicular direction down to 115 µm.

During the first long shutdown (LS1) of the LHC between Run 1 and Run 2 an additional layer of pixel detectors has been installed between the new narrower beam pipe and the old innermost pixel layer (B-layer), called The Insertable B-Layer (IBL) [56]. The motivation for such change was the increase of tracking precision by improving the quality of the impact parameter reconstruction of tracks being closer to the interaction point. Additionally the IBL can help keep high vertexing efficiency even in case of high radiation damage of the original B-layer.

The Semiconductor Tracker (SCT) consists of 4088 modules of silicon microstrip detectors arranged in four barrel layers and two endcaps each containing nine disk layers [52]. Each module consists of four sensors, two the top and two at the bottom side which are rotated by 20 mrad to improve the resolution. Every track crosses eight strip layers resulting in four space points. The position accuracy of SCT in the R–ϕ direction is down to 17 µm and in the perpendicular direction down to 580 µm.

The Transition Radiation Tracker (TRT) [52] is the final part of the inner tracker. The barrel part consists of 73 straw layers interleaved with fibres and the endcap part consists of 160 straw layers interleaved with foils. Each straw is 4 mm in diameter and is filled with xenon-based gas mixture. To avoid pollution due to leaks and consequent absorption of photons outside the straw the space between them is filled with CO_2.

The number of hits from the TRT is much larger compared with other inner detector components and is typically 36 per track. Only information about the track in the R–ϕ direction is provided with the accuracy down to 130 µm per straw.

Low-energy transition radiation photons are absorbed in the Xe-based gas mixture in the straws, producing much larger signal amplitudes than minimum-ionising charged particles. These signals can be distinguished from tracking signals using separate low and high thresholds in the front-end electronics. This information is used for electron identification between 0.5 GeV and 150 GeV. About 10 high-threshold hits from transition radiation are expected for electrons with energies above 2 GeV.

3.3 LIQUID ARGON AND TILE CALORIMETERS

ATLAS calorimeter system consists of the electromagnetic (EM) calorimeter, measuring the energy of electrons and photons, and the hadronic calorimeter, measuring the energy of protons, neutrons, pions and kaons. The EM calorimeter [57] is composed of liquid argon (LAr) active layers and lead absorbers in an accordion geometry, which provides complete ϕ coverage without azimuthal cracks between individual cells. The barrel part of the calorimeter is covering a pseudorapidity range of $|\eta| < 1.475$ and the two endcap components are covering $1.375 < |\eta| < 3.2$. In the precision measurement region $|\eta| < 2.5$ three layers of the detectors are used. Additionally a thin presampler layer is placed in front of the calorimeter to correct for the energy lost by electrons and photons before arriving to the detector subsystem. A sketch of the accordion structure of the EM calorimeter in this region is shown in Figure 3.4 where also the grouping of cells into trigger towers is shown in the third calorimeter layer. Details about the trigger usage of the calorimeter are presented in Section 3.7. In the forward region of the calorimeter only two layers of detector modules are used and the granularity is coarser than the central region. In total the EM calorimeter consists of more than 170000 readout channels.

There are three types of hadronic calorimeters used, the tile barrel calorimeter, the LAr hadronic endcap calorimeter (HEC) and the LAr froward calorimeter (FCal) [52]. The three layers of tile calorimeter cover the range $|\eta| < 1.7$. It is a sampling calorimeter using steel as the absorber and scintillating tiles as the active material. Two sides of the scintillating tiles are read out by wavelength shifting fibres into two separate photomultiplier tubes. The hadronic endcap calorimeter extends out to $|\eta| = 3.2$ and

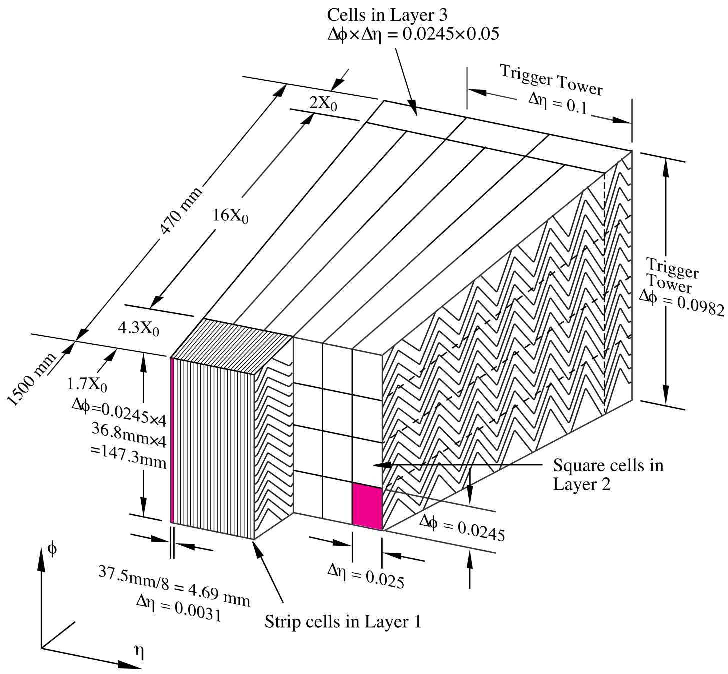

Figure 3.4: Sketch of the accordion structure of the EM calorimeter in the precision measurement region $\eta < 2.5$. Adapted from Ref. [57].

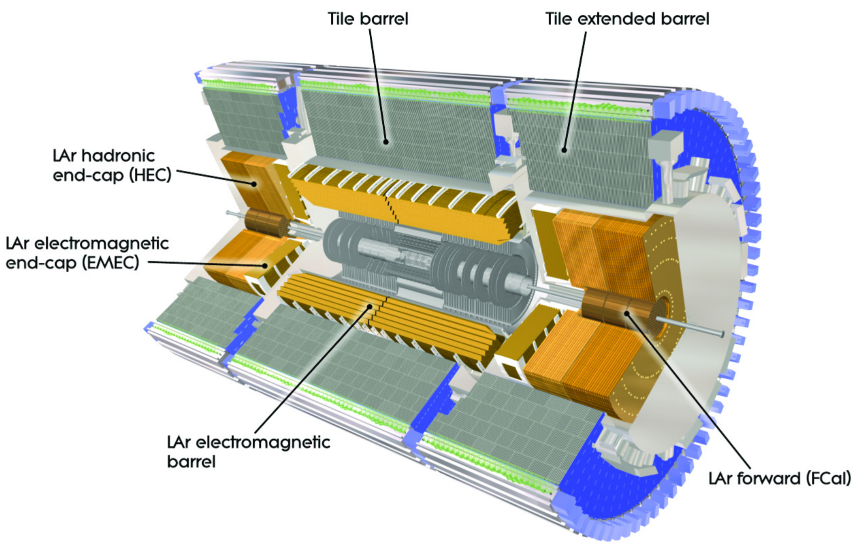

Figure 3.5: Cut-away view of the ATLAS calorimeter system. Taken from Ref. [52].

works similarly as the LAr EM calorimeter but uses copper absorber plates. The FCal calorimeter covers the remainder of the ATLAS measurement range up to $|\eta| = 4.9$. It consists of three modules in each endcap, the first, made of copper, optimised for electromagnetic measurements, and two made of tungsten, predominately measuring the hadronic interactions.

The goal of the calorimeters is to provide good containment for electromagnetic and hadronic showers and must also limit punch-through into the muon system. Thus, the calorimeter depth is optimised to about 11 interaction lengths and allows good resolution for high-energy jets and with large η coverage also ensuring a good missing transverse energy ($E_{\mathrm{T}}^{\mathrm{miss}}$) measurement. A cut-away view of the ATLAS calorimeter system is drawn in Figure 3.5.

3.4 Muon Spectrometer

The goal of the muon spectrometer [58] is to measure muon tracks and momenta and to provide muon triggering. Muons are bent in the R–z plane by the large superconducting toroid magnets up to $|\eta| = 2.7$. There are four main components of the muon spectrometer. Monitored Drift Tubes (MDTs) and Cathode Strip Chambers (CSCs) provide precision tracking measurements while Resistive Plate Chambers (RPCs) and Thin Gap Chambers (TGCs) primarily provide triggering information. A three-dimensional view of the muon spectrometer is sketched in Figure 3.6.

The muon spectrometer is designed for a momentum resolution $\Delta p_{\mathrm{T}}/p_{\mathrm{T}} < 10^{-4} \times p/\mathrm{GeV}$ for $p_{\mathrm{T}} > 300\,\mathrm{GeV}$. At smaller momenta the resolution is limited by multiple scattering in the magnet and detector structures. Monitored drift chambers cover most of the solid angle covered by the spectrometer. They are 30 mm aluminium tubes with a central W-Re wire, filled with a mixture of argon, methane and nitrogen at 3 bar. The single-wire resolution is typically 80 µm. Cathode strip chambers complement MDTs with providing finer granularity in the first station in the endcap region and for pseudorapidities $|\eta| > 2$. CSCs are multiwire proportional chambers with cathode strip readout and with a symmetric cell in which the anode-cathode spacing is equal to the anode wire pitch of 2.54 µm. The readout cathode is also segmented with the pitch twice as large. With the addition of charge interpolation between the neighbouring strips resolution of the detector is up to 60 µm.

The trigger chambers of the muon spectrometer are required to trigger with well-defined p_{T} cut-offs with a granularity of the order of 1 cm. Additionally they measure the second coordinate in a direction orthogonal to the one measured in the precision chambers with a resolution of about 10 mm. The trigger system consists of resistive plate chambers in the barrel and thin gap chambers in the endcap region. The basic RPC unit is a narrow gas gap formed by two parallel resistive bakelite plates, separated by insulating spacers.

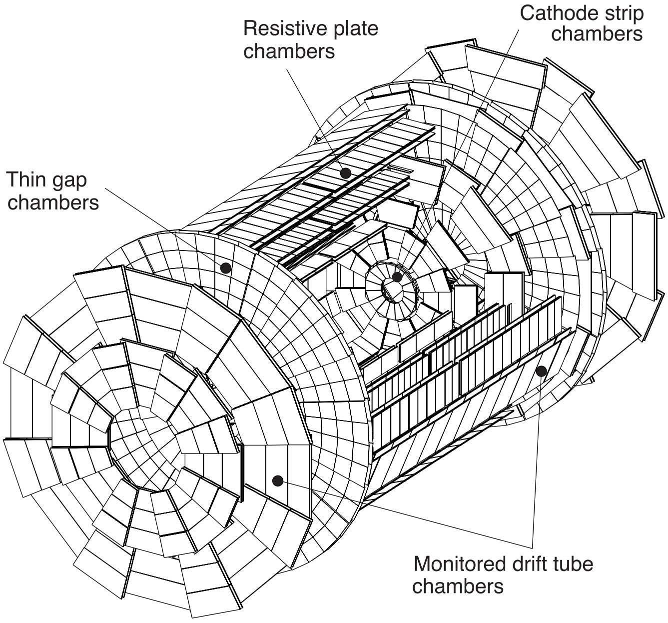

Figure 3.6: Three-dimensional view of the muon spectrometer instrumentation indicating the areas covered by the four different chamber technologies. Taken from Ref. [58].

The primary ionisation electrons are multiplied into avalanches by a high, uniform electric field of 4.5 kV/mm. A trigger chamber is made from two orthogonal rectangular layers aligned to the MDT wires. A typical space-time resolution of the detector is 1 cm $\times$ 1 ns. Thing gap chambers are very similar to multiwire proportional chambers with the anode wire pitch larger than the distance between electrodes. To form a trigger signal, the readout of several anode wires is done together, between 4 and 20 chambers in a group, depending on the desired granularity. More details of the ATLAS trigger system are provided in Section 3.5.

3.5 TRIGGER AND DATA ACQUISITION

During the nominal operation collisions take place every 25 ns. As the average physics event size is about 1.2 MB [59] this would yield a transfer rate of about 50 TB per second which is too much to handle. Processing that much data would also take a very long time. To filter the collected events for the ones potentially containing new physics the ATLAS Trigger and Data Acquisition (TDAQ) system [60] is used. It consists of a hardware-based first-level (L1) trigger and a software-based high-level trigger (HLT). The L1 trigger reduces the event rate from 40 MHz to 100 kHz and utilises information from dedicated calorimeters and muon detectors. After the acceptance the events are buffered in the Read-Out System (ROS) and processed by the HLT, which reduces the event rate further down to an average rate of 1 kHz. The L1 trigger passes on Region-of-Interest (ROI) information which allows regional reconstruction in the trigger algorithms. Events passing the HLT requirements are transferred to the local storage at the experimental site and reconstructed at the CERN computing centre. The ATLAS TDAQ diagram is illustrated in Figure 3.7.

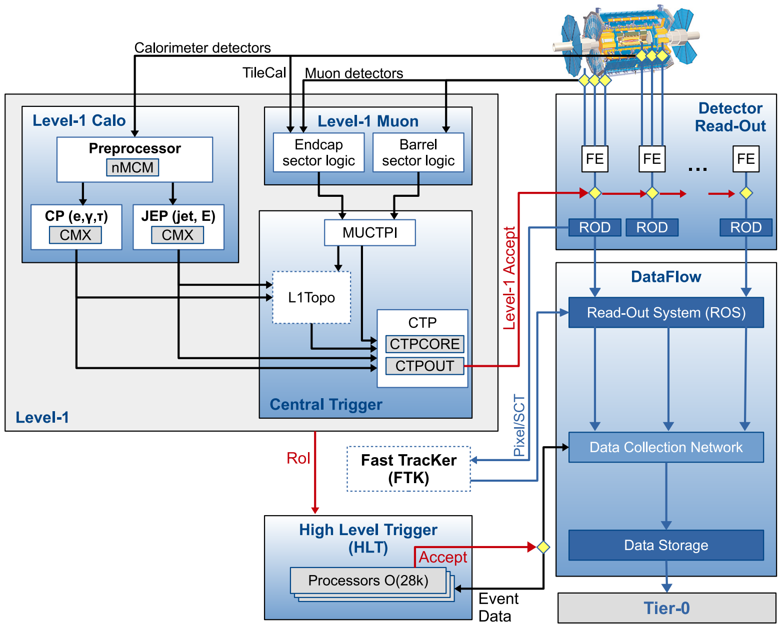

Figure 3.7: The ATLAS TDAQ system in Run 2 with emphasis on the components relevant for triggering. L1Topo and FTK were being commissioned during the Run 2 data taking and have not been used in triggers used in this thesis. Taken from Ref. [60].

The L1 calorimeter trigger algorithm search separately for electron/photon and jet candidates. In the first case it identifies a 2×2 trigger tower cluster in the EM calorimeter exceeding the predefined energy threshold. Additionally isolation requirements can be applied looking at the 12 surrounding EM trigger towers, as well as for hadronic tower sums in a central 2×2 core behind the EM cluster and the ring around it. As both types of trigger towers are calibrated together at the EM scale this causes slight energy underestimation. Jet RoIs are such defined as 4×4 or 8×8 trigger tower clusters where both electromagnetic and hadronic transverse energy exceeds the predefined thresholds. The L1 muon trigger algorithms uses multiplicities of tracks in RPCs in the barrel region and TGCs in the endcap and forward regions of ATLAS. The 16 highest-p_T candidates are used to define regions of interest. The information from both L1 systems is processed by the Central Trigger Processor which forms the trigger decision.

After the L1 acceptance, the events are processed by the HLT using finer-granularity calorimeter information and more precise tracking information from the ID and MS subsystems. To reduce the processing time RoIs passed from the L1 stage are reconstructed first with the region extended to the full detector later if needed. A selection of L1 and HLT trigger combinations called the trigger menu is defined each year of data taking based on the requirements of the ATLAS physics programme. To ensure the final average trigger rate of 1 kHz prescale factors can be applied to L1 and HLT triggers in a way that only a certain fraction of events may be accepted by them. This allows triggering on events used for efficiency and performance measurements which might occur too often for the computing infrastructure to handle.

3.6 BEAM CONDITIONS AND LUMINOSITY MEASUREMENTS

The ATLAS detector is a delicate and expensive machine. Collimators at the far ends of the detector act as a protection from protons deviating from the beam. Still, several proton bunches hitting the collimators would cause enormous instantaneous radiation rate that can cause detector damage. The ATLAS Beam Conditions Monitor (BCM) [61] is designed to detect such incidents and trigger an abort before they happen. Two detector stations are placed close to the beam pipe symmetrically to the interaction point. Showers from ordinary collisions reach the detectors at the same time, while showers from collimators reach them with a delay. As bunch crossings occur every 25 ns the time difference should be out of phase at 12.5 ns requiring the BCM stations located at $z \pm 1.9$ m. Interactions from minimum bias proton Interactions in each bunch crossing might yield less than a particle/cm^2. This requires BCM to be sensitive to single minimum ionising particles and also survive in a high radiation environment. Thus the detector modules use synthetic diamonds, photographed in Figure 3.8, instead of silicon.

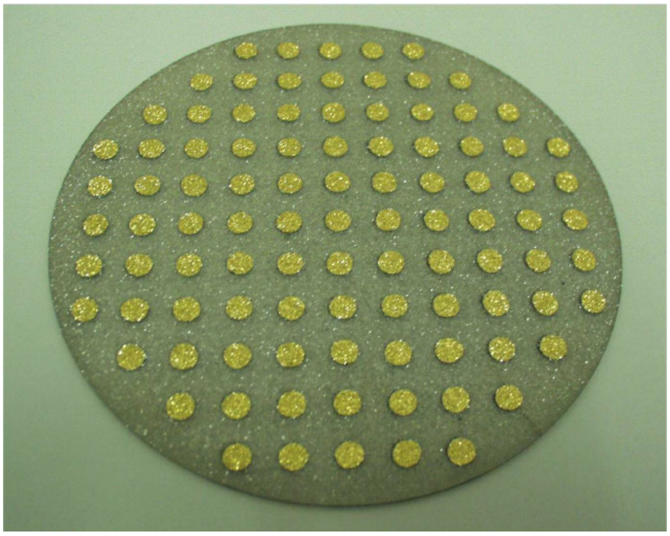

Figure 3.8: A 13cm diameter wafer of polycrystalline CVD diamond. Taken from Ref. [61].

Luminosity is measured by the LUCID-2 detector [62]. It consists of several small Cherenkov detectors surrounding the beam pipe on both sides of the interaction point. Thin quartz windows of photomultipliers (PMTs) act as Cherenkov medium producing enough photons for a signal. As PMTs are under constant stress of high anode current their gain is reduced with time. Small deposits of radioactive ^{207}Bi sources are used to monitor the stability of photomultipliers. Its 33 years half-life and low activity allows long-term calibration support without effecting luminosity measurements.

The hits in LUCID PMTs are used to provide luminosity measurements [63]. The per-bunch instantaneous luminosity is defined as

$$\mathcal{L}_b = \frac{\mu_{\text{vis}} f_r}{\sigma_{\text{vis}}}, \tag{3.1}$$

where f_r is the LHC revolution frequency (11 246 Hz for protons), μ_{vis} a visible interaction rate per bunch crossing measured with the photomultipliers and σ_{vis} visible cross-section. The visible cross-section is measured using dedicated low-luminosity van der Meer [64] scan fills during each year of Run 2 and depends on number of protons in each of the beams and the separation between the beams in the horizontal plane x-y. The total instantaneous luminosity is the sum of $\mathcal{L}_b$ over all colliding bunch pairs. The final luminosity is integrated over well-defined time periods called luminosity blocks with a typical length of 60 seconds. The total uncertainties in the integrated luminosities for each individual year of data-taking range from 2.0 to 2.4%, and are partially correlated between years. After typical data-quality selections, the full Run 2 pp data sample corresponds to an integrated luminosity of 139 fb^{-1}, with an uncertainty of 1.7%.

CHAPTER 4

Simulation of Particle Interactions

The ATLAS simulation infrastructure [65] is used to produce Monte Carlo (MC) samples to be used in physics and performance studies. The simulation software chain is divided into three steps: generation of the event and immediate decays, simulation of the detector and physics interactions, and digitisation of the energy deposited in the sensitive regions of the detector into voltages and currents for comparison with the readout of the ATLAS detector. The simulation program is integrated into the ATLAS software framework, Athena [66]. While each stage can run individually, the digitisation step is usually run together with the reconstruction step, where real physics objects such as jets, muons and electrons are reconstructed.

4.1 ATLAS Simulation Framework

All physics processes have to be *generated* first; special purpose MC generators software is used to sample interacting proton constituents of proton–proton collisions from specific probability density functions (PDFs). Events are sampled from differential cross-sections, which required large statistics to sufficiently describe the whole phase space. These events can be filtered at generation time so that only events with a certain property are kept, e.g. filtering on number of leptons in the event. The details of specific signal and background processes considered in this thesis are outlined in Section 4.3. Furthermore, the corresponding cross-section of the generated events can be computed by integrating the contributions of each sampled event. Only prompt decays are the responsibility of the generator. All the other particles are propagated through the detector in the next step, together with the decay products of prompt decays. More details on non-prompt decays are provided in Chapter 7.

Each generated particle is propagated through the full ATLAS detector by the Geant 4 toolkit [67]. All particle interactions with the material of the detector are accurately simulated. A representative state of the detector configuration is provided to the framework, including misalignments and distortions. This allows simulation output to be as close to the real data collected. The energies deposited in the sensitive parts of the detector are recorded as "hits," containing the total energy deposition, position, and time. As Geant 4 simulation is based on particle propagation using very small steps it can be very slow, especially for calorimeters where particles are slowing down and depositing energy. For this reason the Integrated Simulation Framework (ISF) [68] is used to steer the simulation task. This allows using different engines for different subdetectors. To be able to simulate as many different BSM processes as possible, a special Fast Calorimeter Simulation is used [65], achieving approximately a factor of 10 speed-up, which will be referred to as "fast simulation" compared with "full simulation" when using only Geant 4.

In both event generation and detector simulation, additional information called "truth" is recorded for each event. In the generation jobs, the truth is a history of the interactions from the generator, including incoming and outgoing particles. At the simulation level energy deposits are matched to the actual detector hits for each of the interacting particles.

4.2 Digitisation and pile-up

The ATLAS digitisation software converts the hits produced by the core simulation into detector response objects — "digits." A digit is produced when the voltage or current on a particular readout channel rises above a pre-configured threshold within a particular time window. While most of the subdetectors record only that the threshold has been exceeded, some also contain information on the signal shape.

In addition to the hard-scatter pp interaction which causes the event to be triggered, the ATLAS detector is also sensitive to proton–proton collisions in the same or surrounding bunch crossings. This is collectively known as "pile-up". The average number of these interactions per bunch crossing, denoted by $\langle\mu\rangle$ has been increasing almost each year of Run 2 data taking, from 13.4 in 2015 to 37.8 in 2017 [69] as seen in Figure 4.1. This is foreseen to rise further to more than 200 during high-luminosity LHC running, scheduled to start in 2026 [70].

ATLAS subdetector signals of the triggered bunch crossing are sensitive to not only the current bunch crossing, but also to bunch crossings in a finite time window around the triggered time. If detector relaxation time is longer than the 25 ns bunch spacing past collisions affect the measurement, while if detector readout takes a longer time future collisions might affect it. This makes pile-up difficult to model accurately and

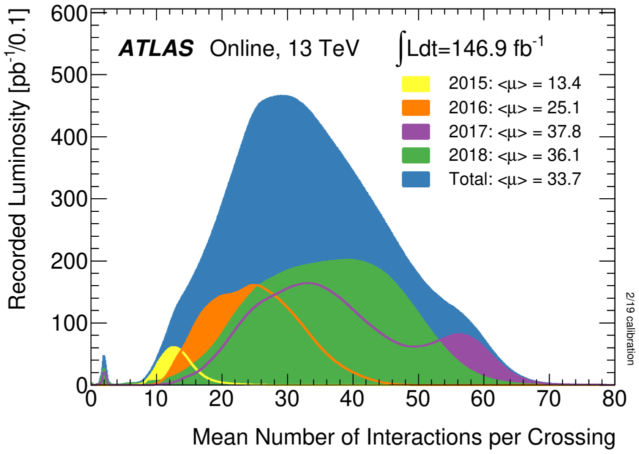

Figure 4.1: The luminosity-weighted distribution of the mean number of interactions per crossing for Run 2 pp collision data at 13 TeV centre-of-mass energy. All data recorded by ATLAS during stable beams is shown, and the integrated luminosity and the mean μ values are given in the figure. Taken from Ref. [69].

represents a significant computational time in the simulation chain. Digitisation CPU requirements are directly proportional to the number of soft collisions, which motivates an improvement to the method.

For any given hard scattering interaction the additional pile-up interactions must be included in a realistic model of detector response. They are simulated separately at the event generation and simulation stages. At the digitisation step, hits from the hard scattering are combined with those from pile-up before the detector response is calculated. Most subdetector responses are affected also by interactions from neighbouring bunch crossings, up to 32 before and 6 after the triggering one. Taking the average value of pile-up $\langle\mu\rangle = 34$ for Run 2 data taking, more than 1000 so-called "minimum bias" events need to be selected at random and processed. The workflow overview is presented in Figure 4.2. The current method suffers from two main shortcomings: random event selection causes large random I/O, which can additionally also damage hard drives, and the whole digitisation stage takes a lot of time for large μ values, since the digitisation of pile-up events is repeated for each hard-scatter process.

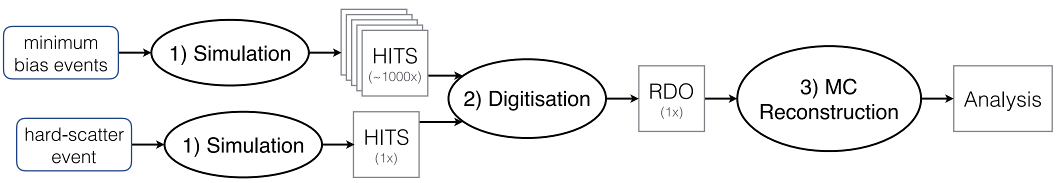

Figure 4.2: Current digitisation stage workflow diagram. Taken from Ref. [71].

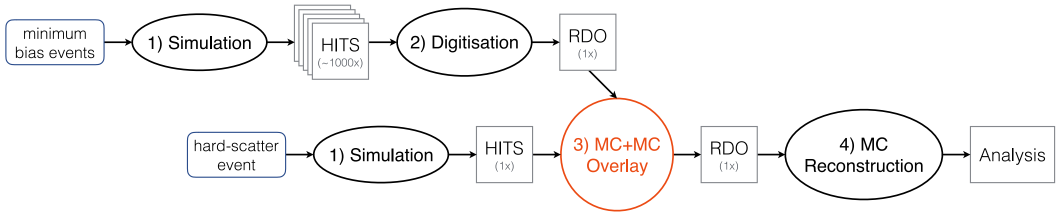

Figure 4.3: MC+MC overlay workflow diagram. Taken from Ref. [71].

A new MC+MC overlay method [72] is proposed to replace the current digitisation, outlined in Figure 4.3. An additional step is introduced where pile-up events are pre-mixed. A standard pile-up digitisation is run using zero-hard-scatter events (i.e. "empty" events) where additional digits below threshold are stored to account for possibility going above threshold once the main event will be added. Each simulated hard-scatter event is then digitised and overlaid on pre-mixed pile-up digits at the overlay stage.

The new method has two main benefits: the background dataset only needs to be digitised once per production campaign; and CPU and I/O requirements are also much lower and have almost no dependence on μ as seen in Figure 4.4. There are also a few

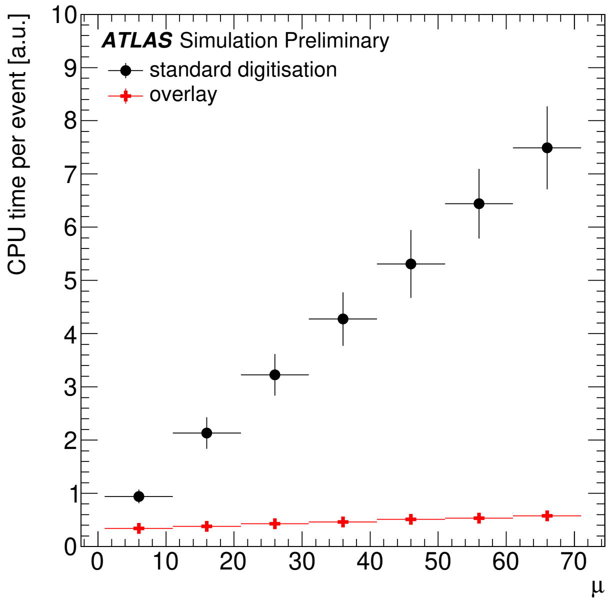

Figure 4.4: Average CPU time per event comparison between the standard digitisation (black circles) and the MC+MC overlay (red crosses) as a function of the number of proton-proton collisions per bunch crossing (μ). Horizontal error bars represent the width of the bin where a flat distribution of μ has been used. Vertical error bars represent the standard deviation of multiple measurements of the CPU time. Taken from Ref. [71].

drawbacks. Two sub-threshold signals from different events causing a signal above threshold are now lost, which mostly affects the Inner Detector. Additionally, different datasets can have an identical set of merged pile-up events, the effects of which still need to be investigated.

4.3 SIMULATED MONTE CARLO SAMPLES USED IN THE ANALYSIS

4.3.1 SIMULATED SIGNAL SAMPLES

The signal considered in the simplified type-III seesaw model [40] is implemented in the MADGRAPH5_aMC@NLO [73] generator at leading order (LO) using FEYNRULES [74]. For the simulated signal production MADGRAPH5_aMC@NLO was interfaced to PYTHIA 8.230 [75] for parton showering. The `A14` set of tuned parameters [76] was used for the parton shower. The `NNPDF3.0lo` [77] parton distribution function (PDF) set was used in the matrix element calculation and the `NNPDF2.3lo` [78] was used in the parton shower.

The signal cross-section is calculated at next-to-leading order (NLO) plus next-to-leading logarithmic (NLL) accuracy, assuming that the heavy leptons, $L^{\pm}$ and N^0, are $\mathrm{SU}(2)$ triplet fermions [79, 80].

For each considered mass point samples are sliced by lepton multiplicities, requiring either 2, 3 or 4 light leptons with or without hadronic τ decays. The generated samples with their cross-sections and filter efficiencies are listed in Table 4.1. The fast simulation of the ATLAS detector response using the GEANT 4 toolkit and Fast Calorimeter Simulation is performed for all slices.

4.3.2 SIMULATED BACKGROUND SAMPLES

Simulated background samples include Drell–Yan ($q\bar{q} \to Z/\gamma^* \to \ell^+\ell^-$ $(\ell = e, \mu, \tau)$), diboson (WW, ZZ, WZ), top quark pair ($t\bar{t}$) and single top quark production processes. The generators used for the MC samples and the cross-section calculation used for their normalisation are provided in Table 4.2. However, the normalisation of some MC samples is considered as a free parameter in the final likelihood fit, as described in Chapter 8, to ensure that any possible normalisation mis-modelling of the simulated samples is corrected in the specific phase space considered in this search.

The production of $t\bar{t}$ events was modelled using the POWHEG-BOX v2 [83–86] generator, which provides matrix elements at next-to-leading-order (NLO) in the strong coupling constant α_S with the `NNPDF3.0nlo` [77] parton distribution function. The h_{damp} parameter in Powheg controls the matching between the matrix element and the parton

Table 4.1: Cross-sections of signal Monte Carlo samples for mass points considered in this analysis. Leading order cross-sections (σ_{LO}) are computed by the generator and next-to-leading cross-sections ($\sigma_{\text{NLO+NLL}}$) with their corresponding uncertainties are taken from Refs. [81] and [82]. Branching ratios into at least two leptons are presented with the corresponding effective cross-section.

$m(N^0, L^\pm)$ [GeV]	$\sigma_{\text{NLO+NLL}}$ [fb]	$\mathcal{B}(2\ell$ or more)	$\sigma(2\ell$ or more) [fb]
400	180 ± 14	0.45	82.2 ± 6.6
500	68.5 ± 6.1	0.46	31.7 ± 2.8
600	29.6 ± 3.0	0.46	13.8 ± 1.4
700	13.9 ± 1.5	0.47	6.53 ± 0.70
800	6.97 ± 0.81	0.47	3.27 ± 0.38
900	3.65 ± 0.45	0.47	1.72 ± 0.21
1000	1.97 ± 0.25	0.47	0.93 ± 0.12
1100	1.08 ± 0.15	0.47	0.511 ± 0.071
1200	0.612 ± 0.084	0.47	0.290 ± 0.040

shower, and effectively regulates the high-p_{T} radiation against which the $t\bar{t}$ system recoils. It is set to $1.5\,m_{\text{top}}$ [87], using a top-quark mass of $m_{\text{top}} = 172.5$ GeV. The functional form of the renormalisation and factorisation scale is set to the default scale $\sqrt{m_{\text{top}}^2 + p_{\text{T}}^2}$. The events were interfaced with Pythia 8.230 [88] for the parton shower and hadronisation, using the A14 set of tuned parameters [76] and the NNPDF2.3lo set of PDFs [78]. The decays of bottom and charm hadrons were simulated using the EvtGen v1.6.0 program [89].

The $t\bar{t}$ sample cross-section is computed at next-to-next-to-leading-order (NNLO) in QCD including the resummation of next-to-next-to-leading-logarithmic (NNLL) soft-gluon terms calculated using Top++2.0 [90–96]. For proton–proton collisions at a centre-of-mass energy of $\sqrt{s} = 13$ TeV, this cross-section corresponds to $\sigma(t\bar{t})_{\text{NNLO+NNLL}} = 832 \pm 51$ pb using a top quark mass of $m_{\text{top}} = 172.5$ GeV. The uncertainties in the cross-section due to the PDF set and α_{S} were calculated using the PDF4LHC prescription [97] with the MSTW2008 68% CL NNLO [98, 99], CT10 NNLO [100, 101] and NNPDF2.3lo 5f FFN [78] PDF sets, and were added in quadrature to the scale uncertainty.

The uncertainty due to initial-state-radiation (ISR) is estimated by comparing the nominal $t\bar{t}$ sample with two additional samples [102]. To simulate higher parton radiation, the factorisation and renormalisation scales are varied by a factor of 0.5 while simultaneously increasing the h_{damp} value to $3.0\,m_{\text{top}}$ and using the Var3c up variation from the A14 tune. For lower parton radiation, μ_r and μ_f are varied by a factor of 2.0 while keeping the h_{damp} value to $1.5\,m_{\text{top}}$ and using the Var3c down variation in the parton shower. The Var3c A14 tune variation [76] largely corresponds to the variation of α_{S} for

Table 4.2: The event generator, parton shower generator, cross-section normalisation, and PDF set used for the Matrix Element (ME) calculation are shown for each simulated signal and background event sample. The generator cross-section is used where not specifically stated otherwise.

Physics process	Event generator	ME PDF set	Cross-section normalisation	Parton shower generator
$N^0/L^\pm$	MadGraph5_aMC@NLO	NNPDF3.0lo	LO	Pythia 8.230 & EvtGen1.6.0
Top physics				
$t\bar{t}$	Powheg-Box v2	NNPDF3.0nlo	NNLO+NNLL	Pythia 8.230 & EvtGen1.6.0
Single t	Powheg-Box v2	NNPDF3.0nlo	NLO	
$t\bar{t}+V$	Powheg-Box v2	NNPDF3.0nlo	NLO	
Multiboson				
ZZ, WZ, WW	Sherpa 2.2.1 & 2.2.2	NNPDF3.0nnlo	NLO	Sherpa
VVV	Sherpa 2.2.2	NNPDF3.0nnlo	NLO	Sherpa
Drell–Yan				
$Z/\gamma^* \to \ell^+\ell^-$	Sherpa 2.2.1	NNPDF3.0nnlo	NNLO	Sherpa

initial state radiation (ISR) in the A14 tune. The impact of final-state-radiation (FSR) is evaluated using PS weights which vary the renormalisation scale for QCD emission in the FSR by a factor of 0.5 and 2.0, respectively.

To evaluate the PDF uncertainties for the nominal PDF, the 100 NNPDF3.0nlo replicas are taken into account. The central value of this PDF is further compared to the central values of the CT14nnlo [103] and MMHT2014 NNLO [104] PDF sets.

The impact of the parton shower and hadronisation model is evaluated by comparing the nominal generator set-up with a sample generated also with PowhegBox v2 but interfaced with the Herwig 7.13 [105, 106], using the Herwig 7.1 default set of tuned parameters [106] and the MMHT2014 LO PDF set. To assess the uncertainty in the matching of NLO matrix elements and parton shower, the Powheg sample is compared with a sample of events generated with MadGraph5_aMC@NLO v2.6.0 interfaced with Pythia8.230.

The SM Drell–Yan processes with decays $Z \to ee$, $Z \to \mu\mu$, and $Z \to \tau\tau$ were simulated with the Sherpa v2.2.1 [107] generator. In this set-up, NLO-accurate matrix elements for up to 2 jets, and LO-accurate matrix elements for up to 4 jets were calculated with the Comix [108] and OpenLoops [109, 110] libraries. The default Sherpa parton shower [111] based on Catani–Seymour dipoles and the cluster hadronisation model [112] are used. They employ the dedicated set of tuned parameters developed by the Sherpa authors and the NNPDF3.0nnlo set.

The NLO matrix elements of a given jet-multiplicity were matched to the parton shower using a colour-exact variant of the MC@NLO algorithm [113]. Different jet multiplicities were then merged into an inclusive sample using an improved CKKW matching procedure [114, 115] which was extended to NLO accuracy using the MEPS@NLO prescription [116]. The merging threshold was set to 20 GeV.

The Z + jets samples are normalised to a next-to-next-to-leading-order (NNLO) prediction [117].

Samples of diboson final states (VV) were simulated with the Sherpa v2.2.1 or v2.2.2 generator depending on the process, including off-shell effects and Higgs boson contributions, where appropriate. Fully leptonic final states and semileptonic final states, where one boson decays leptonically and the other hadronically, were generated using matrix elements at NLO accuracy in QCD for up to one additional parton and at LO accuracy for up to three additional parton emissions. Samples for the loop-induced processes $gg \rightarrow VV$ were generated using LO-accurate matrix elements for emission of up to one additional parton for both the fully leptonic and semileptonic final states. Electroweak production of a diboson in association with two jets ($VVjj$) is also accurate up to leading order. The matrix element calculations were matched and merged with the Sherpa parton shower based on Catani–Seymour dipole using the MEPS@NLO prescription. The virtual QCD corrections were provided by the OpenLoops library. The `NNPDF3.0nnlo` set of PDFs was used, along with the dedicated set of tuned parton-shower parameters developed by the Sherpa authors.

Uncertainties from missing higher orders in all Sherpa samples are evaluated [118] using seven variations of the QCD factorisation and renormalisation scales in the matrix elements by factors of 0.5 and 2 avoiding variations in opposite directions.

Uncertainties in the nominal PDF set are evaluated from 100 replica variations. Additionally, the results are cross-checked using the central values of the `CT14nnlo` and `MMHT2014 NNLO` PDF sets. The effect of the uncertainty in the strong coupling constant $\alpha_S = 0.118$ is assessed by variations of ± 0.001.

For all samples, a full simulation of the ATLAS detector response using the Geant 4 toolkit was performed. The effect of multiple interactions in the same and neighbouring bunch crossings (pile-up) was modelled by overlaying the original hard-scattering event with simulated inelastic pp events generated with Pythia 8.186 using the `NNPDF2.3lo` set of PDFs and the `A3` set of tuned parameters [119].

The MC events are weighted to reproduce the distribution of the average number of interactions per bunch crossing ($\langle\mu\rangle$) observed in the data. The $\langle\mu\rangle$ value in MC samples is rescaled by a factor of 1.03 ± 0.07 to improve the level of agreement between data and simulation in the visible inelastic pp cross-section [120].

Other background processes, not described in this section, do not contribute significantly to the regions defined in this analysis and are outlined only in Table 4.2.

CHAPTER 5

Reconstruction of Simulated and Data Events

5.1 Tracks and Vertices

Track reconstruction [121] is the basis for reconstruction of leptons and jets. Primarily it is based on the information from the pixel and SCT detectors but can also be extended with the TRT [122]. The first part of the charged particle track reconstruction is assembling clusters from raw measurements. Pixels and strips sharing a common edge or corner with collected charge above threshold are grouped into clusters. These are a base of three-dimensional measurements called "space-points", the point where the particle traversed the inner detector. In the case of SCT clusters from both sides of a strip layer are combined. In dense environments with high pile-up multiple tracks might share one cluster. Two types of clusters can be defined, single-particle clusters created by charge deposits from only one particle and merged clusters created by multiple particles. The difference between the two types is illustrated in Figure 5.1.

Sets of three space-points are then used to form track seeds as the minimum required number of points to estimate the momentum is three. Perfect helical trajectories in a uniform magnetic field are assumed. To ensure good quality tracks different seed types are considered, starting with SCT-only, pixel-only, and finally mixed-detector seeds. After seeds are formed, an additional space-point compatible with the estimated seed trajectory is required. Track candidates are then built using a combinatorial Kalman filter [123] by incorporating additional space-points from the remaining layers of pixel and SCT detectors. As multiple track extensions compatible with the preliminary trajectory can exist the filter creates a track candidate for each case. This yields multiple track candidates where space-points overlap or have been incorrectly assigned.

The correct tracks are selected using the ambiguity solver algorithm. Each candidate is assigned the track score based on the number of clusters and holes assigned. Holes are

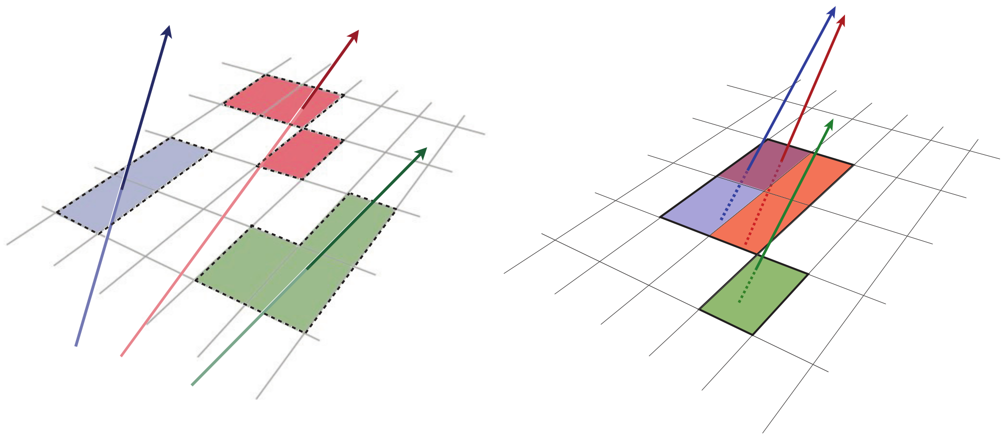

(a) (b)

Figure 5.1: Illustration of (a) single-particle pixel clusters on a pixel sensor and (b) a merged pixel cluster due to very collimated charged particles. Different colours represent energy deposits from different charged particles traversing the sensor and the particles trajectories are shown as arrows. Taken from Ref. [121].

defined as intersections of the reconstructed track trajectory with a sensitive detector element that does not contain a matching cluster. Additionally to reduce the significance of poorly fitted tracks the χ^2 is also considered. The logarithm of the track momentum helps to reduce the large number of tracks with incorrectly assigned clusters, which typically have low p_T. To properly take into account shared clusters a track candidate is only compared with previously accepted tracks. Clusters can be shared only between two tracks and a track can have at most two shared clusters. An artificial neural network is helping the ambiguity solver with the identification of merged pixel clusters. After the scoring tracks are also rejected if the track p_T is lower than 400 MeV, has less than seven clusters or more than two holes, or is not in the longitudinal acceptance range of the inner detector.

At this point track impact parameters can be defined. The transverse impact parameter d_0 is calculated with respect to the measured beam line position. The longitudinal impact parameter z_0 represents the difference along the beam line between the point where d_0 is measured and the primary vertex or the beam spot, while the primary vertex is not yet known. All tracks should fulfil the requirements on the impact parameters $|d_0| < 2.0\,\text{mm}$ and $|z_0 \sin\theta| < 3.0\,\text{mm}$, where θ is the polar angle of the track. Later in the analysis d_0 significance will also be used defined as $|d_0|/\sigma(d_0)$.

Final track candidates that have not been removed at any stage of the reconstruction are re-fitted using a high-resolution fit using all available information. This is a very CPU-intensive process and is the last step of the reconstruction to minimise the number of times the fitter is called.

Once tracks are selected they can be grouped into vertices. The procedure can be divided into two stages, vertex finding and vertex fitting [124]. The seed track is the one closest to the beam spot position. The actual position is fitted using an iterative χ^2 minimisation. At each iteration tracks are weighted based on their compatibility with the vertex. After the final iteration tracks found incompatible with the vertex by more than seven standard deviations are removed from the vertex candidate and returned to the pool of unused tracks. The full procedure is repeated until all tracks have a vertex assigned. The primary vertex of the event is the one with the highest sum of squares of transverse momenta of contributing tracks, denoted as $\sum p_{\mathrm{T}}^2$. Commonly primary vertex is required to contain at least two tracks.

Tracking and vertexing depend on an accurate beam spot estimation [124]. It is based on an unbinned maximum-likelihood fit to the spatial distribution of primary vertices collected from many events. A representative subset of the data called the "express stream" is used for this purpose and is collected during the detector calibration performed approximately every ten minutes.

5.2 Electrons

While traversing through the detector an electron can lose a significant amount of its energy due to bremsstrahlung. The radiated photon may convert into an electron-position pair also interacting with the detector material. The main result of these processes are electromagnetic showers observed in the calorimeter. The produced secondary particles are usually very collimated with the original particle trajectory and are reconstructed as part of the same electromagnetic cluster. However these interactions can also occur in the beam pipe or in the inner detector resulting in multiple tracks all originating from the same electron. A schematic illustration of the path of an electron through the detector is shown in Figure 5.2.

The electron reconstruction [125, 126] begins by using the "topo-cluster" reconstruction algorithm [127] which attempts to group calorimeter cells in topologically connected clusters in attempt to extract the significant signal from a background of electronic noise and other sources of fluctuations such as pile-up. Although the algorithm can be used for both the EM and hadronic calorimeters, electron reconstruction only uses EM calorimeter cells. The cluster formation begins with selecting an initialising cell with signal-to-noise significance $|\zeta_{\mathrm{cell}}^{\mathrm{EM}}| \geq 4$, where

$$\zeta_{\mathrm{cell}}^{\mathrm{EM}} = \frac{E_{\mathrm{cell}}^{\mathrm{EM}}}{\sigma_{\mathrm{noise,cell}}^{\mathrm{EM}}}, \tag{5.1}$$

$E_{\mathrm{cell}}^{\mathrm{EM}}$ is the cell energy only accounting electromagnetic showers and $\sigma_{\mathrm{noise,cell}}^{\mathrm{EM}}$ is the expected cell noise. The expected cell noise includes the known electronic noise and an

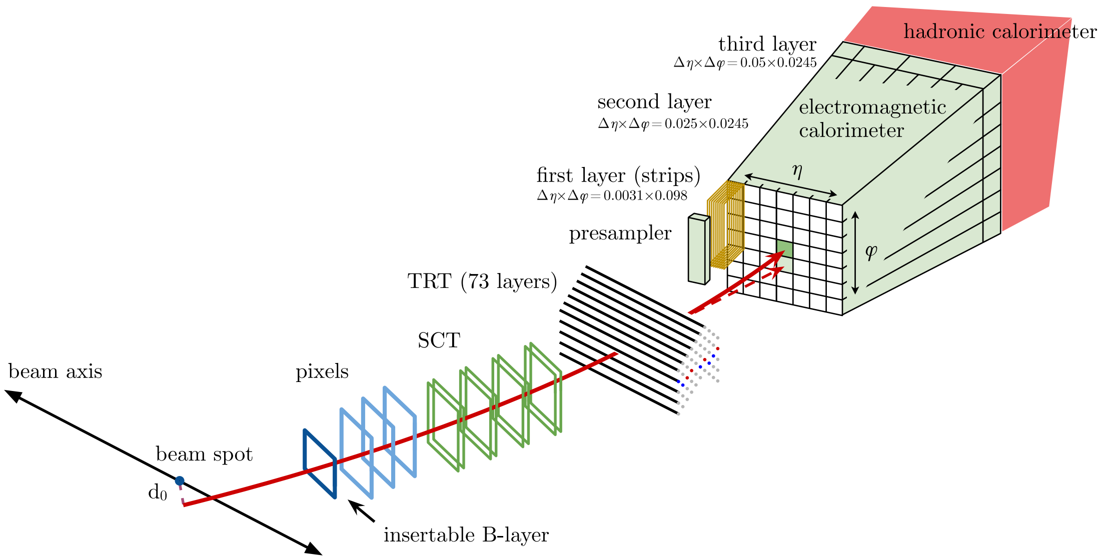

Figure 5.2: A schematic illustration of the path of an electron through the detector. The red trajectory shows the hypothetical path of an electron, which first traverses the tracking system (pixel detectors, then silicon-strip detectors and lastly the TRT) and then enters the electromagnetic calorimeter. The dashed red trajectory indicates the path of a photon produced by the interaction of the electron with the material in the tracking system. Adapted from Ref. [125].

estimate of the pile-up noise corresponding to the average instantaneous luminosity expected for Run 2. The neighbouring cells with $|\zeta^{\mathrm{EM}}_{\mathrm{cell}}| \geq 2$ are then added to the cluster and become a seed in the next iteration.

Tracks from the Inner Detector are then matched to the produced clusters accounting the possible energy loss of up to 30% of the electron due to interaction with the detector material. They are then refitted using an optimised Gaussian-sum filter (GSF) [128] designed to better account for energy loss of charged particles in material, taking into account measured energy in matched clusters. Resulting tracks are extrapolated to the second layer of the calorimeter and are required to have low separation from the cluster $|\eta_{\mathrm{cluster}} - \eta_{\mathrm{track}}| < 0.05$ and one of two alternative requirements on the azimuthal separation between the cluster position and the track: $-0.10 < \Delta\phi < 0.05$ or $-0.10 < \Delta\phi_{\mathrm{res}} < 0.05$, where $\Delta\phi$ and $\Delta\phi_{\mathrm{res}}$ are calculated as $-q \cdot (\phi_{\mathrm{cluster}} - \phi_{\mathrm{track}})$ with q the sign of the electric charge of the particle, and the momentum of the track rescaled to the energy of the cluster for $\Delta\phi_{\mathrm{res}}$.

The final step is to build "super-clusters". The initial list of topo-clusters is sorted according to descending transverse energy E_{T}. Super-clusters are seeded with topo-clusters with $E_{\mathrm{T}} \geq 1\,\mathrm{GeV}$ that are matched to a track with at least four hits in the silicon tracking detectors. All clusters inside a window of $\Delta\eta \times \Delta\phi = 0.075 \times 0.125$ are then added. Additionally if a cluster inside $\Delta\eta \times \Delta\phi = 0.125 \times 0.300$ shares the "best-matched" track with the seed it is also added. Finally tracks are re-matched to the created super-clusters creating analysis-level electron candidates.

The energy of an electron candidate needs to be calibrated to better match the original electron energy. First the estimation of the energy of the electron from the energy deposits in the calorimeter is estimated based on a multivariate regression algorithm trained on simulated events and applied both on data and simulation. Then the relative energy scales of the different layers of the EM calorimeter are adjusted, based on studies of muon energy deposits and electron showers. This adjustment is applied as a correction to the data before the estimation of the energy of the electron. The ratio of the measured calorimeter energy to the track momentum for electrons and positrons from Z boson decays is then used to correct residual local non-uniformities in the calorimeter response. These include geometric effects at the boundaries between calorimeter modules and non-nominal high-voltage settings in some regions of the calorimeter. The final step of the calibration is the adjustment of the overall energy scale in the data, done using a large sample of Z boson decays to electron–positron pairs. At the same time, a correction to account for the difference in energy resolution between data and simulation is derived, and applied to the simulation.

Further quality criteria, called "identification selections", are used to improve the purity of selected electron objects [126]. The identification of prompt electrons relies on a likelihood discriminant constructed from quantities that are able to discriminate prompt isolated electrons from energy deposits from hadronic jets, from converted photons and from genuine electrons produced in the decays of heavy-flavour hadrons. These variables describe properties of the primary electron track, the lateral and longitudinal development of the electromagnetic shower in the EM calorimeter, and the spatial compatibility of the primary electron track with the reconstructed cluster. Three operating points *loose*, *medium* and *tight* are defined based on average identification efficiencies of 93%, 88% and 80%, respectively. Data efficiencies in dependence of E_{T} are shown in Figure 5.3(a).

Identification criteria alone might not be enough to achieve pure electrons. Additional isolation criteria can be applied to better select prompt leptons in dense environment with high pile-up. As the choice of isolation depends a lot on a specific analysis several different working points are defined based on different upper bounds on the calorimeter-based ($E_{\mathrm{T}}^{\mathrm{cone20}}$) and track-based ($p_{\mathrm{T}}^{\mathrm{varcone20}}$) isolation requirements. The variable $E_{\mathrm{T}}^{\mathrm{cone20}}$ is defined as the sum of energies of all topo-clusters inside the cone with radius $\Delta R = 0.2$ with the electron energy subtracted. Similarly the variable $p_{\mathrm{T}}^{\mathrm{varcone20}}$ is defined as the scalar sum of the transverse momenta of the tracks with $p_{\mathrm{T}} > 1\,\mathrm{GeV}$ in a cone of size $\Delta R = \min\left(10\,\mathrm{GeV}/p_{\mathrm{T}}(e), 0.2\right)$ around the electron, excluding the electron track itself. Figure 5.3(b) shows data efficiencies for different isolation working points as a function of pile-up. For all working points efficiencies are higher than 85% even for high $\langle\mu\rangle$ values.

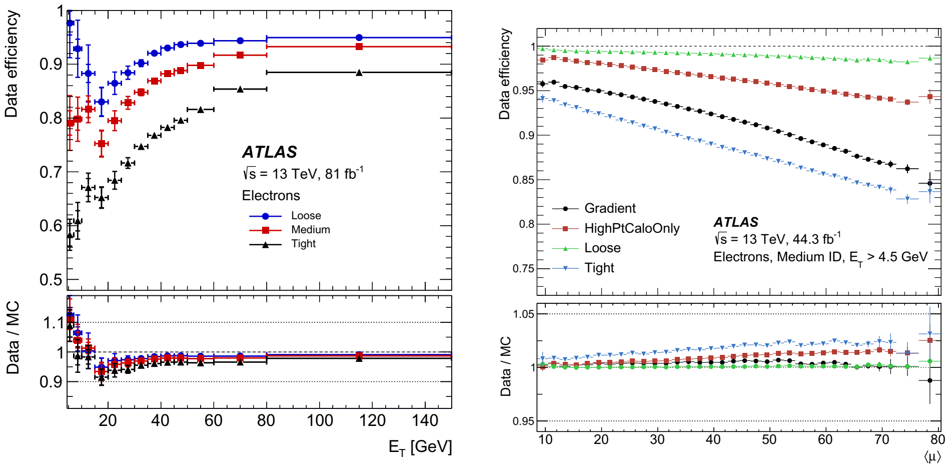

(a) (b)

Figure 5.3: Electron (a) identification efficiency as a function of E_T and (b) isolation efficiency as a function of pile-up in inclusive $Z \to ee$ events. The lower panels show the ratio of the efficiencies measured in data and in MC simulations. Taken from Ref. [126].

5.3 Muons

Muon reconstruction is first performed independently in the inner detector and the muon spectrometer [129]. The ID track reconstruction is done in the same way as for any other charged particle and is described in Section 5.1.

Hit patterns in each of the muon chambers are first grouped into segments. The MDT segments are reconstructed by performing a straight-line fit to the hits that are found in each layer and aligned on a trajectory in the bending plane of the detector. On the other hand the RPC or TGC hits measure the coordinate orthogonal to the bending plane. Lastly the CSC segments are built using a separate combinatorial search in the η and ϕ detector planes. Muon track candidates are then built by fitting together hits from segments in different layers. The seeds are chosen from the middle layers, where more trigger hits are available, and then moving inwards and outwards. Finally tracks are re-fitted using a global χ^2 fit. Hits largely reducing the quality are removed and the fit is repeated. If additional hits compatible with the trajectory are found they are added to the candidate and the fit is also repeated.

Once particle candidates are reconstructed in the ID, MS, and calorimeters the combined muon reconstruction can be performed. Four muon types are defined depending on which subdetectors are used in reconstruction:

- *Combined (CB) muons:* Muon candidates are reconstructed with a global refit of the ID and MS tracks. In most cases muons are first reconstructed in the MS and then extrapolated inward and matched to an ID track. Complementary some muons might also be reconstructed in the ID first. During the global fit procedure, MS hits may be added to or removed from the track similarly to the standalone MS reconstruction.

- *Segment-tagged (ST) muons:* ID tracks are extrapolated to the MS and need to be associated with at least one local track segment in the MDT or CSC chambers.
- *Calorimeter-tagged (CT) muons:* Used to recover the muon acceptance in regions where cabling and other services are provided to other parts of the detector i.e. $|\eta| < 0.1$ and $15 < p_{\mathrm{T}} < 100\,\mathrm{GeV}$. Tracks from the ID are matched to an energy deposit in the calorimeter compatible with a minimum-ionizing particle.
- *Extrapolated (ME) muons:* The reconstruction is based only on the MS track and a loose compatibility with originating from the interaction point, based on the estimated energy loss of the muon in the calorimeters. The muon is required to traverse at least two layers of MS chambers in the barrel and at least three layers in the forward region. ME muons are mainly used to extend the acceptance for muon reconstruction into the region not covered by the ID.

When two muon types share the same ID track, preference is given to CB muons, then to ST, and finally to CT muons. The overlap with ME muons in the muon system is resolved by analysing the track hit content and selecting the track with better fit quality and larger number of hits.

To suppress the background mainly originating from pion and kaon decays additional muon identification requirements are imposed. One of the main identification requirements is the q/p significance, defined as the absolute difference between the ratio of the muon charge and momentum measured in the ID and MS divided by the corresponding uncertainties. Additionally $\rho' = |p_{\mathrm{T}}^{\mathrm{ID}} - p_{\mathrm{T}}^{\mathrm{MS}}|/p_{\mathrm{T}}$ and the combined fit χ^2 are used.

Four muon identification working points are provided:

- *Medium muons:* Only CB and ME tracks are used. The former are required to have at least three hits in at least two MDT layers, except for tracks in the $|\eta| < 0.1$ region, where tracks with at least one MDT hit but no more than one MDT holes are allowed. The latter are required to have at least three MDT or CSC layers and are used only in the $2.5 < |\eta| < 2.7$ region to extend the acceptance outside the ID geometrical coverage. For both cases the q/p significance is required to be less than seven. This selection minimises the systematic uncertainties associated with muon reconstruction and calibration.
- *Loose muons:* All muon types are used. CT and ST muons are added to the *medium* selection but restricted to the $|\eta| < 0.1$ region. This selection is designed to maximise the reconstruction efficiency while providing good-quality muon tracks.

- *Tight muons:* Only *medium* CB muons with hits in at least two stations of the MS are considered. The normalised χ^2 of the combined track fit is required to be < 8 to remove pathological tracks. A two-dimensional cut in the ρ' and q/p significance variables is performed as a function of the muon p_T to ensure stronger background rejection for momenta below 20 GeV where the misidentification probability is higher. This selection maximises the purity of muons at the cost of some efficiency.

- *High-p_T muons:* The selection is optimised for searches for high-mass resonances and aims to maximise the momentum resolution for tracks with $p_T > 100$ GeV. CB muons passing the *medium* selection and having at least three hits in three MS stations are selected. While the muon reconstruction efficiency is reduced by about 20%, the p_T resolution of muons above 1.5 TeV is improved by approximately 30%.

The muon reconstruction efficiency for *medium* muons estimated from the $J/\psi \to \mu^+\mu^-$ and $Z \to \mu\mu$ events are higher than 98% for all muons with p_T above 4 GeV as shown in Figure 5.4. For *high-p_T* muons the efficiency can drop down to 80%.

Similar to electrons further isolation requirements can be imposed on muon candidates. The goal is to reduce the background contribution from muons from semileptonic decays, which are embedded in jets. Track-based requirements on $p_T^{\text{varcone30}}/p_T^{\mu}$ and calorimeter-based requirements on $E_T^{\text{cone20}}/p_T^{\mu}$ are used.

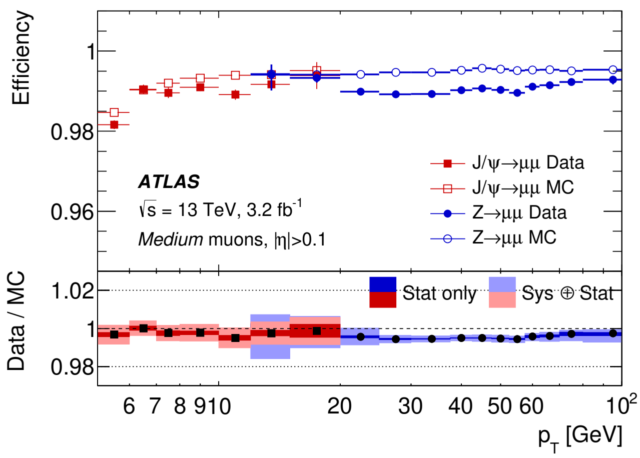

Figure 5.4: Reconstruction efficiency for the *medium* muon identification selection as a function muon p_T with $0.1 < |\eta| < 2.5$ obtained with $J/\psi \to \mu^+\mu^-$ and $Z \to \mu\mu$ events. The error bars on the efficiencies indicate the statistical uncertainty only. The panel at the bottom shows the ratio of the measured and predicted efficiencies, with both statistical and systematic uncertainties. Taken from Ref. [129].

5.4 JETS

Hadronic jets reconstruction is based on the "particle flow" algorithm [130]. The task of the algorithm is to properly combine momentum and energy measurements made in the inner detector and calorimeters, respectively.

Well-reconstructed tracks are selected first, as described in Section 5.1. Calorimeter topo-clusters are formed in the same way as for electrons, outlined in Section 5.2. Each track is then matched to a single topo-cluster if possible. The deposited energy in the calorimeter is computed based on the cluster position and the track momentum. As a single particle can deposit energy in multiple topo-clusters, each track-cluster pair gets assigned a probability that the particle energy estimate is not complete. In about 10% of cases a particle is matched to multiple clusters with similar probabilities. Topo-clusters within a cone of $\Delta R = 0.2$ around the track position are then merged. The expected energy deposited in the calorimeter by the particle that produced the track is then subtracted cell by cell from the set of matched topo-clusters. The clusters that remain should be compatible with the expected shower fluctuations of a single particle's signal, as estimated from a calibration sample of single pions, and are removed.

Particle flow jets are reconstructed using the anti-k_t algorithm [131] with radius parameter $R = 0.4$ using the FASTJET software package [132]. Only topo-clusters with positive energy surviving the energy subtraction step and the selected tracks that are matched to the primary vertex are used as the input. To reduce the pile-up contribution tracks are selected by requiring $|z_0 \sin\theta| < 2.0\,\text{mm}$. Reconstructed jets are then calibrated using the procedure described in Ref. [133]. First pile-up contamination of jets is reduced using the area-based pile-up correction of jet momenta which reduces the impact of charged underlying-event hadrons, charged particles from out-of-time interactions, and neutral particles from pile-up interactions. Residual pile-up correction is then applied on jet p_T as a function of μ and number of primary vertices. The jet energy scale (JES) calibration corrects the jet four-momentum to the simulated particle-level energy scale. The reconstructed energy is additionally corrected using the calorimeter, muon spectrometer, and track-based variables in the global sequential calibration. A residual "in situ" calibration is applied to correct jets in data using well-measured reference objects, such as photons, Z bosons, and calibrated jets. This yields particle flow jets with good energy scale and resolution performance compared with the MC simulation as presented in Figure 5.5.

Not all reconstructed jets originate from the hard-scatter vertex so it is important that those pile-up jets are suppressed. They arise from two sources, hard hadronic jets originating from a pile-up vertex, and local fluctuations of pile-up activity. Pile-up jets originating from local fluctuations are jets reconstructed from a random combination of multiple pile-up vertices and are also called "stochastic jets". They usually have low p_T. The pile-up hadronic jets are genuine jets that are associated with a valid vertex

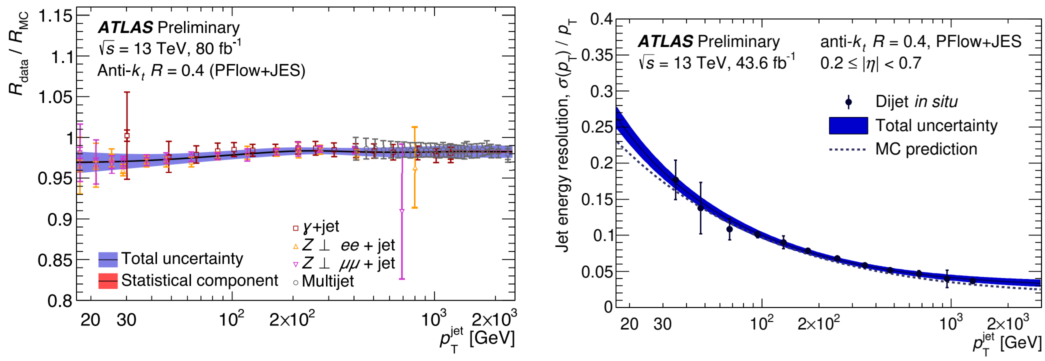

(a) (b)

Figure 5.5: (a) Data-to-simulation ratio of the average jet p_{T} response as a function of jet p_{T} where errors represent the statistical (inner error bars and small inner band) and the total uncertainty (outer error bars and outer band). Taken from Ref. [134]. (b) The relative jet energy resolution $\sigma(p_{\mathrm{T}})/p_{\mathrm{T}}$ as a function of jet p_{T}. The result of the in situ calibration is shown as the dark line with the corresponding uncertainty band. Taken from Ref. [135].

and usually have higher p_{T} than stochastic jets. A special "jet-vertex-tagger" (JVT) discriminant [136] has been developed to reject pile-up jets in the barrel region of the detector ($|\eta| < 2.4$) in the momentum range $20\,\mathrm{GeV} < p_{\mathrm{T}} < 60\,\mathrm{GeV}$. It looks at the scalar sum of the p_{T} of the tracks that are associated with the jet and originate from the hard-scatter vertex and compares this with the sum of the p_{T} of all associated track originating from any vertex and also with the p_{T} of the jet itself. As the pile-up rejection efficiency is not the same for data and MC correction factors need to be applied.

Reconstructed particle jets can be split by flavour into jets containing hadrons with b-quarks (b-jets), jets containing hadrons with c-quarks (c-jets) but no b-quarks, or containing neither b- or c-quarks (light-flavour jets). The procedure is collectively called b-tagging [137]. Long lifetime, high mass and high decay multiplicity of b-hadrons can be used to identify b-jets. Several b-tagging algorithms have been developed by ATLAS [138]. The MV2c10 algorithm, based on a BDT discriminant is used for this analysis. It is trained on a hybrid sample of simulated $t\bar{t}$ and Z' events. The latter is included to optimise the b-tagging performance at high jet p_{T}. The training sample is split into signal sample containing b-jets and background sample containing 7% of c-jets and 93% of light-flavour jets to ensure good charm rejection. Distribution of the output discriminant of the tagger is shown in Figure 5.6(a). Several different working points define a cut the discriminant based on an average efficiency of the b-tagging of either 60%, 70%, 77% or 85%. To account for differences between data and MC efficiencies, correction factors are defined as a ratio of both to correct the simulation. Efficiencies for the 77% working point as a function of jet p_{T} for both data and MC samples are displayed in Figure 5.6(b).

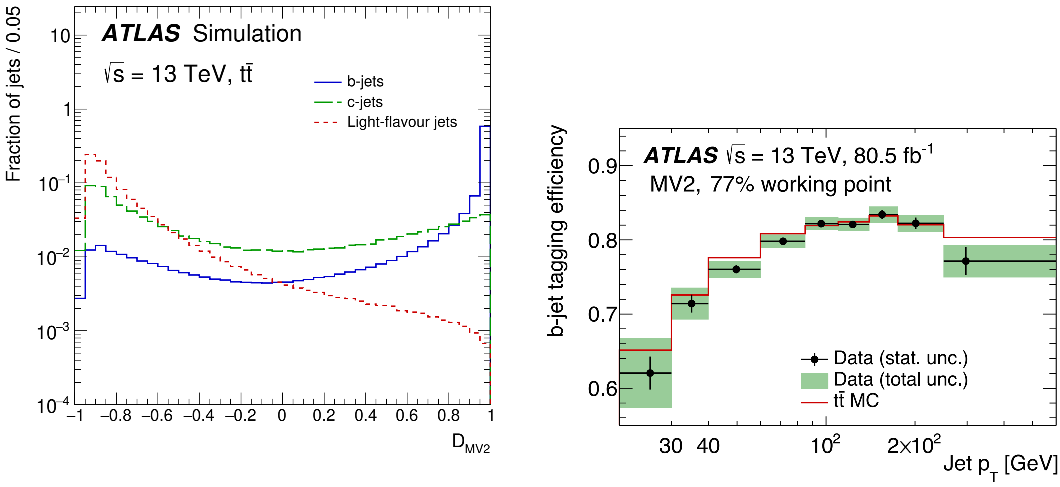

(a) (b)

Figure 5.6: (a) Distribution of the output discriminant of the MV2 b-tagging algorithm for b-jets, c-jets and light-flavour jets in the baseline $t\bar{t}$ simulated events. (b) b-jet tagging efficiency for the 77% working point as a function of jet p_{T}. The efficiency measurement is shown together with the efficiency derived from $t\bar{t}$ simulated events. Taken from Ref. [137].

5.5 Missing Transverse Momentum

Momentum conservation in the plane transverse to the beam axis implies that the transverse momenta of all particles in the final state should sum to effectively zero. Unfortunately not all particles can be detected by the ATLAS. Besides the Standard Model neutrinos also new particles proposed by the models beyond the SM can escape the detector. Such momentum imbalance is called the missing transverse momentum ($E_{\mathrm{T}}^{\mathrm{miss}}$) [139, 140].

The $E_{\mathrm{T}}^{\mathrm{miss}}$ reconstructions is the most challenging as it needs to combine all individual particle information into one quantity. $E_{\mathrm{T}}^{\mathrm{miss}}$ can be split into two main contributions. The *hard term* is a result of momenta of fully reconstructed and calibrated particles and jets. While jets are always part of the computation, other particles are up to the specific analysis to include. The *soft term* consists of reconstructed charged-particle tracks associate with the hard-scatter vertex but not with any of the reconstructed objects.

The missing transverse momentum is a vector quantity $\mathbf{E}_{\mathrm{T}}^{\mathrm{miss}}$ defined with Eq. 5.2 as a vector sum of individual contributions with only x and y components different from zero. Throughout the document the missing transverse momentum refers to its magnitude $E_{\mathrm{T}}^{\mathrm{miss}} = |\mathbf{E}_{\mathrm{T}}^{\mathrm{miss}}|$.

$$\mathbf{E}_{\mathrm{T}}^{\mathrm{miss}} = \underbrace{\underbrace{-\sum_{\substack{\text{selected}\\\text{electrons}}} \mathbf{p}_{\mathrm{T}}^{e}}_{\mathbf{E}_{\mathrm{T}}^{\mathrm{miss},\, e}} \underbrace{-\sum_{\substack{\text{selected}\\\text{photons}}} \mathbf{p}_{\mathrm{T}}^{\gamma}}_{\mathbf{E}_{\mathrm{T}}^{\mathrm{miss},\, \gamma}} \underbrace{-\sum_{\substack{\text{selected}\\\tau\text{-leptons}}} \mathbf{p}_{\mathrm{T}}^{\tau_{\mathrm{had}}}}_{\mathbf{E}_{\mathrm{T}}^{\mathrm{miss},\, \tau_{\mathrm{had}}}} \underbrace{-\sum_{\substack{\text{selected}\\\text{muons}}} \mathbf{p}_{\mathrm{T}}^{\mu}}_{\mathbf{E}_{\mathrm{T}}^{\mathrm{miss},\, \mu}} \underbrace{-\sum_{\substack{\text{accepted}\\\text{jets}}} \mathbf{p}_{\mathrm{T}}^{\mathrm{jet}}}_{\mathbf{E}_{\mathrm{T}}^{\mathrm{miss},\, \mathrm{jet}}}}_{\text{hard term}} \underbrace{\underbrace{-\sum_{\substack{\text{unused}\\\text{tracks}}} \mathbf{p}_{\mathrm{T}}^{\mathrm{track}}}_{\mathbf{E}_{\mathrm{T}}^{\mathrm{miss},\, \mathrm{soft}}}}_{\text{soft term}} \tag{5.2}$$

As detector response can be reconstructed in different particle candidates the order of $E_{\mathrm{T}}^{\mathrm{miss}}$ computation is important. The hard term is always calculated first. The output of electron reconstruction is considered to be the purest and all electrons passing the selection are included. When adding the additional particle terms each particle should not overlap with other types of particles already used in the computation. Electrons are usually followed by photons, hadronic τ-lepton decays, and muons. Hadronic jets are added last and are additionally required to have high enough JVT score to reduce the pile-up contamination. The track-based soft term is always computed at the end as it includes all contributions from tracks not associated to selected hard objects.

The consistency of the reconstructed $E_{\mathrm{T}}^{\mathrm{miss}}$ with momentum resolution and particle identification efficiencies can be estimated with the $E_{\mathrm{T}}^{\mathrm{miss}}$ significance, $\mathcal{S}(E_{\mathrm{T}}^{\mathrm{miss}})$. ATLAS in the past used an event-based $E_{\mathrm{T}}^{\mathrm{miss}}$ significance defined as $\mathcal{S}(E_{\mathrm{T}}^{\mathrm{miss}}) = E_{\mathrm{T}}^{\mathrm{miss}}/\sqrt{H_{\mathrm{T}}}$ or $\mathcal{S}(E_{\mathrm{T}}^{\mathrm{miss}}) = E_{\mathrm{T}}^{\mathrm{miss}}/\sqrt{E_{\mathrm{T}}}$, where H_{T} is the scalar sum of event transverse momenta and E_{T} is the magnitude of vector sum of event transverse momenta. This is extended with the object-based $E_{\mathrm{T}}^{\mathrm{miss}}$ significance [141], defined to test the hypothesis that the total transverse momentum carried by invisible particles is equal to zero against the hypothesis that it is different than zero. The square of $\mathcal{S}(E_{\mathrm{T}}^{\mathrm{miss}})$ can be defined as

$$\mathcal{S}(E_{\mathrm{T}}^{\mathrm{miss}})^2 = \left(\mathbf{E}_{\mathrm{T}}^{\mathrm{miss}}\right)^{\mathsf{T}} \left(\sum_i \mathbf{V}^i\right)^{-1} \left(\mathbf{E}_{\mathrm{T}}^{\mathrm{miss}}\right), \tag{5.3}$$

where the index i indicates each reconstructed object considered in the $\mathbf{E}_{\mathrm{T}}^{\mathrm{miss}}$ calculation and $\mathbf{V}^i$ is the corresponding covariance matrix. In the coordinate system aligned with the momenta of each contributing particle they are diagonal 2D matrices. For hard particles diagonal elements correspond to the momentum resolution $\sigma^2_{p_{\mathrm{T}}^i}$ and angular resolution multiplied with the momentum ${p_{\mathrm{T}}^i}^2\sigma^2_{\phi^i}$, where the measurements of p_{T}^i and ϕ^i are considered uncorrelated. The soft term covariance matrix has both diagonal elements equal to the resolution σ^2_{soft}. The use of object-based $E_{\mathrm{T}}^{\mathrm{miss}}$ significance improves background rejection and signal selection efficiency for selecting events with expected high $E_{\mathrm{T}}^{\mathrm{miss}}$ as presented in Figure 5.7.

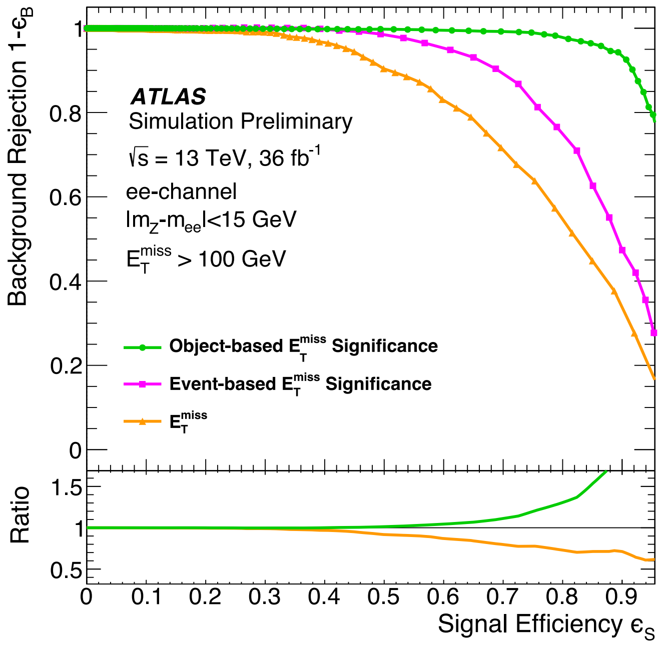

Figure 5.7: Background rejection versus signal efficiency in simulated $Z \to ee$ and $Z \to ee\nu\nu$ samples selecting $Z \to ee$ events with $E_{\mathrm{T}}^{\mathrm{miss}} > 100\,\mathrm{GeV}$. The performance is shown for $E_{\mathrm{T}}^{\mathrm{miss}}$, event-based $\mathcal{S}(E_{\mathrm{T}}^{\mathrm{miss}})$, and object-based $\mathcal{S}(E_{\mathrm{T}}^{\mathrm{miss}})$ as discriminants. The lower panel of the figures shows the ratio of other definitions with the event-based $\mathcal{S}(E_{\mathrm{T}}^{\mathrm{miss}})$. Adapted from Ref. [141].

PART III

SEARCH FOR TYPE-III SEESAW HEAVY LEPTONS

CHAPTER 6

ANALYSIS STRATEGY

The goal of the analysis is to explore the possibility of the type-III seesaw signal being present in the data measured by the ATLAS experiment. As any possible new physics has much lower cross-section that the Standard Model processes with similar final states, event-level and object-level selection needs to be applied to filter the signal candidate events from the inclusive dataset.

Selected events are then categorised into exclusive categories (*analysis regions*) based on different sets of requirements on reconstructed objects. These regions are grouped according to their purpose into signal regions, control regions, and validation regions. Signal regions (SRs) are defined with the aim to achieve the best sensitivity to the targeted models with an enhanced signal-to-background ratio and are used to compare data with each signal hypothesis plus the expected background using the statistical methodology detailed in Chapter 8. The purpose of control regions (CRs) and validation regions (VRs) is to evaluate and validate the background contamination in the SRs. The CRs and VRs are thus constructed with the purpose of minimizing the signal presence while maximising the contributions of distinct types of background. Consequently, the CRs and VRs are constructed to be kinematically close to the SRs, which is done by modifying one or more kinematics requirements, while also ensuring orthogonality with SRs and among themselves. In CRs the background prediction is fitted to data by assigning floating parameters to the normalisation of the dominant background processes. In VRs the background estimation methods are validated by comparing the background model with data.

While optimising the SR definition to maximise the signal significance, the measured data are omitted (blinded), until the background modelling has been validated. Likewise, as a part of the same strategy, while validating the background predictions, the data are compared with the background estimates only in the CR and VR, which are designed to have negligible signal contamination. A signal-to-background significance [142] can be defined as

$$\sqrt{2[(S+B)\ln(1+S/B)-S]}\,, \tag{6.1}$$

where S and B are the total numbers of the expected signal and background events, respectively, based on the MC simulation for a given set of selection requirements.

This thesis covers two different analysis strategies. Events can be selected either with a *cut-based* approach, where cuts are orthogonal in parameter space, or with a *multivariate analysis* using machine learning techniques, where a functional dependence on multiple observables is used. Analysis regions derived for each of the strategies are optimised individually as presented in Sections 6.2 and 6.3 using the same analysis object definitions. The presented cut-based analysis strategy and results were also published in Ref. [143].

Before the optimisation studies a reasonable pre-selection needs to be defined. After the application of beam, detector and data-quality requirements, events containing jets failing to satisfy the quality criteria described in Ref. [144] are rejected to suppress events with large calorimeter noise or non-collision backgrounds. To further reject non-collision backgrounds originating from cosmic rays and beam-halo events, at least one reconstructed primary vertex is required with at least two associated tracks.

All selected events as defined are required to contain exactly one pair of light leptons (electrons or muons) in one of the possible flavour combinations (ee, $e\mu$ or $\mu\mu$) where the pairs can have either same-sign charge (SS) or opposite-sign charge (OS). The six OS and SS analysis channels are defined according to the flavour combination ee, $e\mu$, $\mu\mu$. Events must pass dilepton triggers, where the applied p_{T} thresholds are optimised depending on the lepton flavour combination and the data-taking year and p_{T} range from 12 GeV to 22 GeV for the leading and from 8 GeV to 17 GeV for the sub-leading lepton. A summary of the trigger requirements is presented in Table 6.1. None of the triggers used are prescaled. Additionally for a trigger to be accepted both trigger objects need to be matched with a reconstructed particle of the same type.

6.1 Definitions of Physics Objects

The main motivation of the analysis object selection is to select candidates of largest possible quality and reconstruction efficiency but not remove too much of expected signal. The data driven method used by the analysis for the prediction of fake leptons in the signal region requires two distinct definitions of leptons, called *tight* and *loose*. The method relies on measuring the transition probability of leptons between both regions and is described in Chapter 7. Tight lepton candidates are used as signal

Table 6.1: Summary of the triggers used to select events for the three analysis channels during 2015, 2016, 2017 and 2018 data taking, presenting the trigger flavour type and p_{T} thresholds. For the electron+muon trigger the first number corresponds to the electron threshold, the second to the muon threshold. The dimuon trigger has different thresholds for the first and second muon.

Analysis channel	**Trigger flavour type**	**p_{T} thresholds [GeV]** 2015	2016	2017	2018
ee	dielectron	12	17	17	17
$e\mu$	electron+muon	17 & 14	17 & 14	17 & 14	17 & 14
$\mu\mu$	dimuon	18 & 8	22 & 8	22 & 8	22 & 8

candidates throughout the analysis while loose lepton candidates are considered to be *fake*, originating from a misidentified particle or a non-prompt lepton. The overview of the lepton selection is presented in Tables 6.2 and 6.3.

The electron candidates in this analysis required to pass the *tight* likelihood-based identification selection, to have transverse momentum $p_{\mathrm{T}} > 40\,\mathrm{GeV}$ and to be in the fiducial volume of the inner detector, $|\eta| < 2.47$. The transition region between the barrel and endcap calorimeters ($1.37 < |\eta| < 1.52$) is excluded because it has very poor detecting capability with service conduits being located there. The track associated with the electron candidate must have an d_0 impact parameter significance satisfying the requirement $|d_0|/\sigma(d_0) < 5$. A longitudinal impact parameter value of $|z_0 \sin(\theta)| < 0.5\,\mathrm{mm}$ is also required. Electrons built using bad quality calorimeter clusters or fake clusters originating from calorimeter problems are not used in the analysis. In addition, electron candidates must also satisfy the *loose* isolation criterion requiring calorimeter-based $E_{\mathrm{T}}^{\mathrm{cone20}}/p_{\mathrm{T}} < 0.2$ and track-based $p_{\mathrm{T}}^{\mathrm{varcone30}}/pT < 0.15$ selection. Electron candidates are discarded if their angular distance to a jet is within a cone with radius $0.2 < \Delta R = 0.4$. Background electrons are required to pass looser *loose* identification selection. As tight electrons are a subset of loose ones background electrons are explicitly required not to contain signal electrons. Additionally no isolation requirement is imposed.

The muon candidates are required to have $p_{\mathrm{T}} > 40\,\mathrm{GeV}$, $|\eta| < 2.5$ and the d_0 significance of $|d_0|/\sigma(d_0) < 3$. Analogously to electrons, a longitudinal impact parameter value of $|z_0 \sin(\theta)| < 0.5\,\mathrm{mm}$ is required for muons. In rare cases reconstructed muon candidates might have momentum very poorly reconstructed. As such muons affect other measured quantities such as $E_{\mathrm{T}}^{\mathrm{miss}}$ events with such muons are vetoed. Muon candidates are required to pass the *medium* muon identification requirements below 300 GeV, while at higher values of p_{T} the special *high-p_T* muon identification procedure is used. The muon candidates must also fulfil the *tight* track-based only isolation definition requiring $p_{\mathrm{T}}^{\mathrm{varcone20}}/pT < 0.06$. Muons failing the isolation requirement are classified as background ones. Muons within $\Delta R = 0.4$ of a jet having more than three tracks and with $p_{\mathrm{T}}(\mu)/p_{\mathrm{T}}(\mathrm{jet}) < 0.5$ are discarded. If a muon candidate overlapping with an electron leaves a sufficiently high energy deposit in the calorimeter and shares a track reconstructed in the inner detector with the electron, this muon candidate is also discarded.

Jets are reconstructed using the particle flow algorithm as described in Section 5.4. The *medium* jet-vertex-tagger working point is used which has an average efficiency of 92%. Jets within $\Delta R = 0.2$ of an electron are discarded. Additionally jets within $\Delta R = 0.2$ of a muon and featuring less than three tracks or having $p_{\mathrm{T}}(\mu)/p_{\mathrm{T}}(\mathrm{jet}) > 0.5$ are also removed. Jets considered in this analysis are required to have $p_{\mathrm{T}} > 20\,\mathrm{GeV}$ with $|\eta| < 2.5$. Jets fulfilling these kinematic criteria are probed for containing b-hadrons and categorised as b-tagged jets. The algorithm is used at the working point providing a b-tagging efficiency of 77%. This corresponds to rejection factors of approximately 134, 6 and 22 for light-quark and gluon jets, c-jets, and τ-leptons decaying hadronically, respectively. Furthermore, jets in the forward direction are used in the $E_{\mathrm{T}}^{\mathrm{miss}}$ calculation if they satisfy $p_{\mathrm{T}} > 30\,\mathrm{GeV}$.

Table 6.2: A summary of the baseline electron definitions used in the analysis.

Requirement	Signal electrons (tight)	Background electrons (loose)
Identification	*tight*	*loose* OR
Isolation	*loose*	fail *loose*
p_{T} cut	$p_{\mathrm{T}} > 40\,\mathrm{GeV}$	
η cut	$|\eta| < 2.47$ and veto $1.37 < |\eta| < 1.52$	
$|d_0|/\sigma_{d_0}$ cut	$|d_0|/\sigma_{d_0} < 5.0$	
$|z_0 \sin(\theta)|$ cut	$|z_0 \sin(\theta)| < 0.5\,\mathrm{mm}$	
Bad cluster veto	yes	

Table 6.3: A summary of the baseline muon definitions used in the analysis.

Requirement	Signal muons (tight)	Background muons (loose)
Quality	*high-p_{T}* if $p_{\mathrm{T}} > 300\,\mathrm{GeV}$ else *medium*	
Isolation	*track-only*	fail *track-only*
p_{T} cut	$p_{\mathrm{T}} > 40\,\mathrm{GeV}$	
η cut	$|\eta| < 2.5$	
$|d_0|/\sigma_{d_0}$ cut	$|d_0|/\sigma_{d_0} < 3.0$	
$|z_0 \sin(\theta)|$ cut	$|z_0 \sin(\theta)| < 0.5\,\mathrm{mm}$	
Bad resolution event veto	yes	

6.2 CUT-BASED ANALYSIS STRATEGY AND SELECTION

All regions used in the cut-based approach, with the corresponding selection criteria, are summarised in Table 6.4 and described below.

As the signal process contains neutrinos in the final state, one of the most important selection criteria is based on the $E_{\mathrm{T}}^{\mathrm{miss}}$ significance $\mathcal{S}(E_{\mathrm{T}}^{\mathrm{miss}})$. The SR selection criteria are optimised to maximise the analysis sensitivity. This results in different selection values for the OS and SS channels due to different background compositions and associated event topologies. Consequently, the $E_{\mathrm{T}}^{\mathrm{miss}}$ significance selection value is $\mathcal{S}(E_{\mathrm{T}}^{\mathrm{miss}}) > 10$ for the OS channels and $\mathcal{S}(E_{\mathrm{T}}^{\mathrm{miss}}) > 7.5$ for the SS channels.

At least two jets with $p_{\mathrm{T}} > 20\,\mathrm{GeV}$ and $|\eta| < 2.5$ are required for each region. A b-jet veto is applied to all the jets in SR events to suppress background from SM processes involving top quarks. For each signal event, the dijet invariant mass (m_{jj}) of the two

Table 6.4: Summary of all cut-based analysis regions defined in the analysis. The region definitions are the same for all analysis channel flavour combinations.

	OS ($\ell^+\ell^- = e^+e^-, e^\pm\mu^\mp, \mu^+\mu^-$)		
	Top CR	m_{jj} **VR**	**SR**
N(jet)	≥ 2	≥ 2	≥ 2
N(b-jet)	≥ 2	0	0
m_{jj} [GeV]	$(60, 100)$	$(35, 60) \cup (100, 125)$	$(60, 100)$
$m_{\ell\ell}$ [GeV]	≥ 110	≥ 110	≥ 110
$\mathcal{S}(E_{\mathrm{T}}^{\mathrm{miss}})$	≥ 5	≥ 10	≥ 10
$\Delta\phi(E_{\mathrm{T}}^{\mathrm{miss}}, \ell)_{\mathrm{min}}$	—	—	≥ 1
$p_{\mathrm{T}}(jj)$ [GeV]	—	—	≥ 100
$p_{\mathrm{T}}(\ell\ell)$ [GeV]	—	—	≥ 100
$H_{\mathrm{T}} + E_{\mathrm{T}}^{\mathrm{miss}}$ [GeV]	≥ 300	≥ 300	≥ 300
	SS ($\ell^\pm\ell^\pm = e^\pm e^\pm, e^\pm\mu^\pm, \mu^\pm\mu^\pm$)		
	Diboson CR	m_{jj} **VR**	**SR**
N(jet)	≥ 2	≥ 2	≥ 2
N(b-jet)	0	0	0
m_{jj} [GeV]	$(0, 60) \cup (100, 300)$	$(0, 60) \cup (100, 300)$	$(60, 100)$
$m_{\ell\ell}$ [GeV]	≥ 100	≥ 100	≥ 100
$\mathcal{S}(E_{\mathrm{T}}^{\mathrm{miss}})$	≥ 5	≥ 5	≥ 7.5
$\Delta\phi(E_{\mathrm{T}}^{\mathrm{miss}}, \ell)_{\mathrm{min}}$	—	—	—
$p_{\mathrm{T}}(jj)$ [GeV]	—	—	≥ 60
$p_{\mathrm{T}}(\ell\ell)$ [GeV]	—	—	≥ 100
$H_{\mathrm{T}} + E_{\mathrm{T}}^{\mathrm{miss}}$ [GeV]	$(300, 500)$	≥ 500	≥ 300

highest-p_{T} jets is expected to be close to the W mass. The dijet invariant mass is thus required to be in the window $60\,\mathrm{GeV} < m_{jj} < 100\,\mathrm{GeV}$.

In the SR definition, a lower bound on the invariant mass of the lepton pair ($m_{\ell\ell}$) is introduced and is found to give optimal results at 110 GeV (100 GeV) in the OS (SS) regions. This choice aims to remove the Drell–Yan events around the $Z \to ee$ peak, where the electron charge might also have been misidentified.

Furthermore, in the SR definition for the OS analysis channels, the azimuthal angle $\Delta\phi(E_{\mathrm{T}}^{\mathrm{miss}}, \ell)_{\mathrm{min}}$ between the directions of $E_{\mathrm{T}}^{\mathrm{miss}}$ and and the closest lepton has been shown to have good separation power between signal and background events, especially reducing the SR background contamination from $t\bar{t}$ and diboson events. This is explained by differences between the sources of measured $E_{\mathrm{T}}^{\mathrm{miss}}$ for signal and background, because the latter tends to have a spurious component due to misreconstructed jets. After optimisation, a requirement of $\Delta\phi(E_{\mathrm{T}}^{\mathrm{miss}}, \ell)_{\mathrm{min}} > 1$ is used. In the SR definition for the SS analysis channels, this selection criterion is not applied, because other criteria already reduce the $t\bar{t}$ and diboson background contamination, and this criterion is not very effective in reducing the fake background contribution, whose contribution is significantly larger for the SS analysis channels.

To further increase the expected signal significance, additional selection criteria are introduced: the dijet transverse momentum must fulfil the condition $p_{\mathrm{T}}(jj) > 100\,\mathrm{GeV}$ (60 GeV) for the OS (SS) regions, while the dilepton transverse momentum must satisfy $p_{\mathrm{T}}(\ell\ell) > 100\,\mathrm{GeV}$ for both OS and SS events. These selection requirements exploit the boosted decay topology of object pairs, which would be expected in the presence of heavy leptons.

Due to the probed high masses of the heavy leptons in the decay chain, the signal process is expected to contain high-p_{T} leptons, jets and neutrinos. Since the optimal measure for the high-p_{T} activity of the neutrinos escaping the detector is the $E_{\mathrm{T}}^{\mathrm{miss}}$, and a commonly-used estimator of the event activity for the measured objects is the scalar sum of the transverse momenta of selected leptons and jets H_{T}, a combined $H_{\mathrm{T}} + E_{\mathrm{T}}^{\mathrm{miss}} > 300\,\mathrm{GeV}$ selection criterion is applied in all analysis regions. The $H_{\mathrm{T}} + E_{\mathrm{T}}^{\mathrm{miss}}$ is also the observable used in the final likelihood fit, described in Chapter 8.

To evaluate the significance of each applied cut special $N - 1$ distributions are used. Each of the observables used in the selection is plotted with the cut on it omitted. The distributions for signal regions are shown in Figures 6.1–6.4.

The dominant background contribution (almost 50% of the total) in the OS channels is $t\bar{t}$ production in which the two W bosons in the final state decay leptonically. In the SS channels the $t\bar{t}$ contribution is at the level of 25%. To estimate the contribution from the $t\bar{t}$ decays, an OS control region enriched in top quark events is defined (Top CR). In this region, the SR selection is modified by requiring the number of b-tagged jets to be $N(b\text{-jet}) \geq 2$. Furthermore, all requirements on the transverse momenta, $p_{\mathrm{T}}(jj)$ and

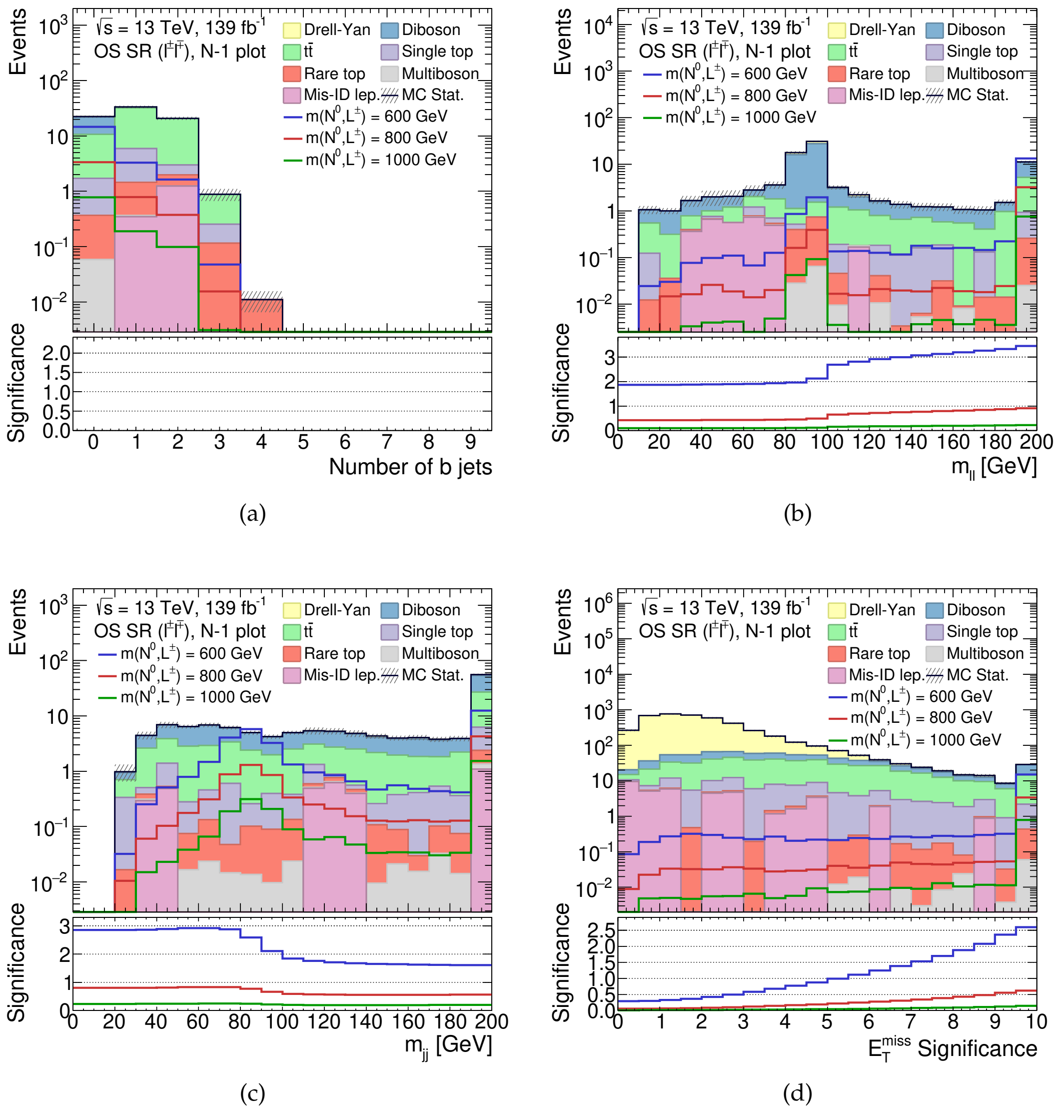

Figure 6.1: Expected signal and background $N-1$ distributions in the opposite-sign signal region inclusive in lepton flavour. Each of the observables is plotted with the cut on it omitted. Some distributions are zoomed in into the interesting range. Uncertainties are statistical only. (a) number of b-jets, (b) invariant mass of the two leptons, (c) invariant mass of the two leading jets, and (d) $E_{\mathrm{T}}^{\mathrm{miss}}$ significance of the event.

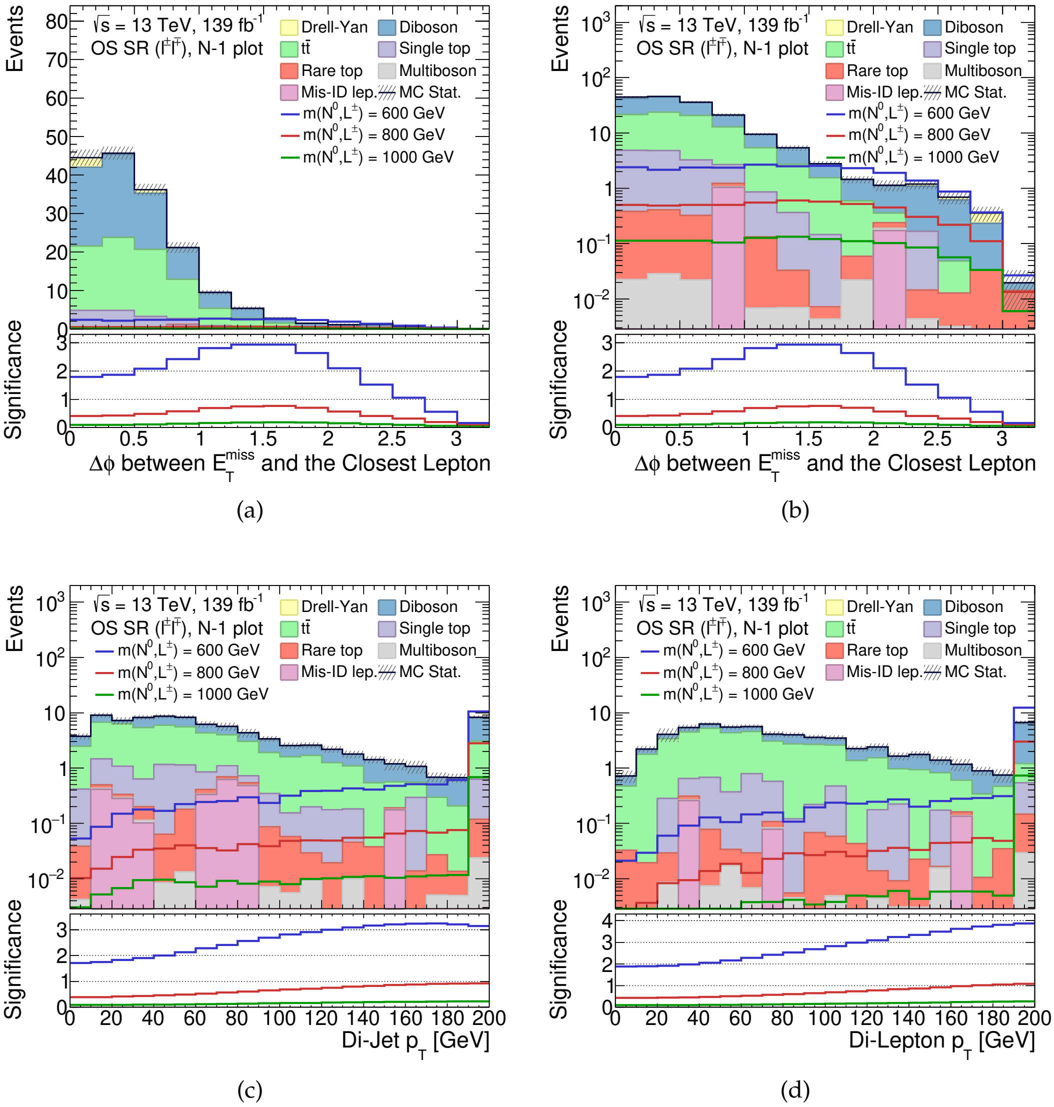

Figure 6.2: Expected signal and background $N-1$ distributions in the opposite-sign signal region inclusive in lepton flavour. Each of the observables is plotted with the cut on it omitted. Some distributions are zoomed in into the interesting range. Uncertainties are statistical only. (a) $\Delta\phi(E_{\mathrm{T}}^{\mathrm{miss}}, \ell)_{\mathrm{min}}$ in linear and (b) in logarithmic scale, (c) di-jet p_{T}, and (d) di-lepton p_{T}.

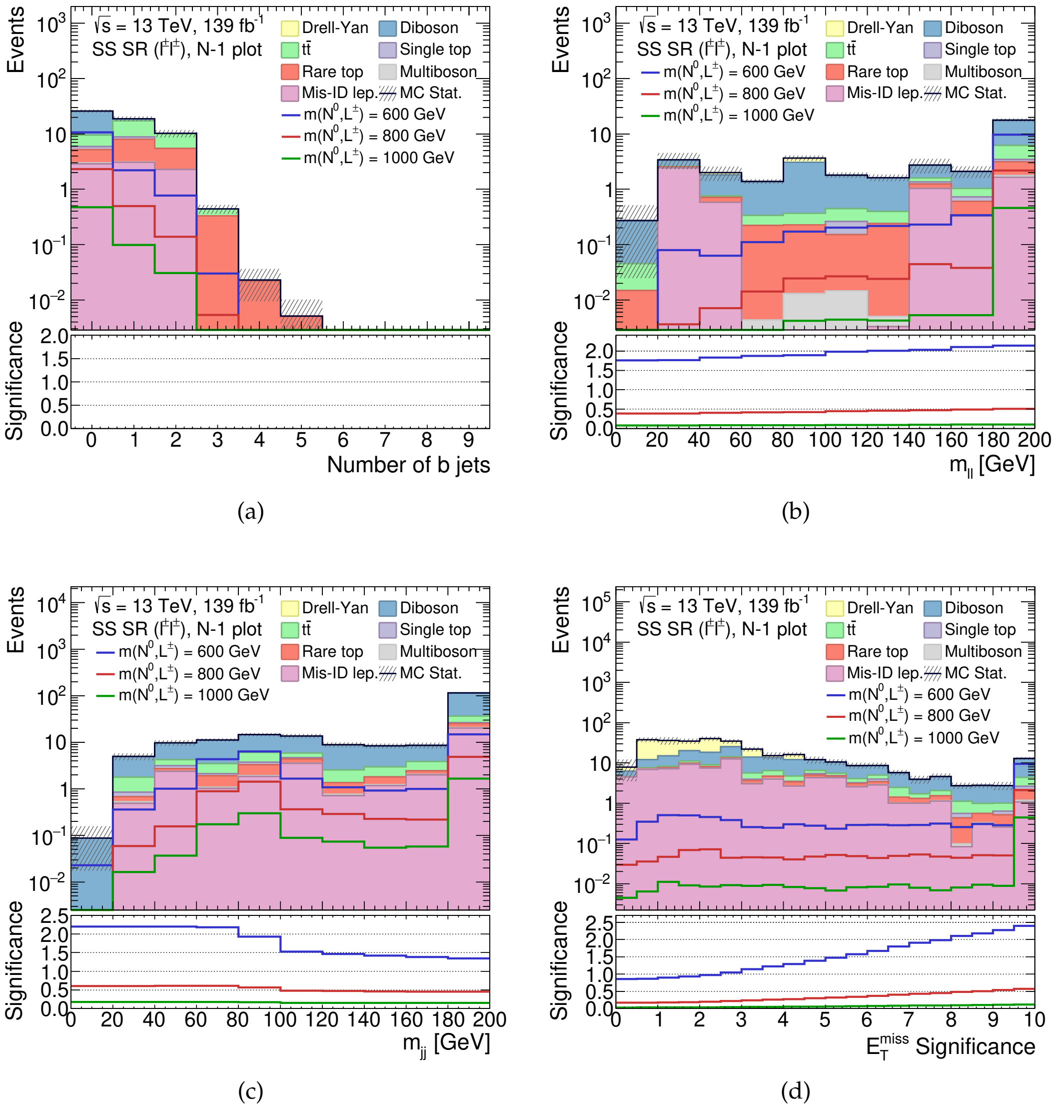

Figure 6.3: Expected signal and background $N-1$ distributions in the same-sign signal region inclusive in lepton flavour. Each of the observables is plotted with the cut on it omitted. Some distributions are zoomed in into the interesting range. Uncertainties are statistical only. (a) number of b-jets, (b) invariant mass of the two leptons, (c) invariant mass of the two leading jets, and (d) $E_{\mathrm{T}}^{\mathrm{miss}}$ significance of the event.

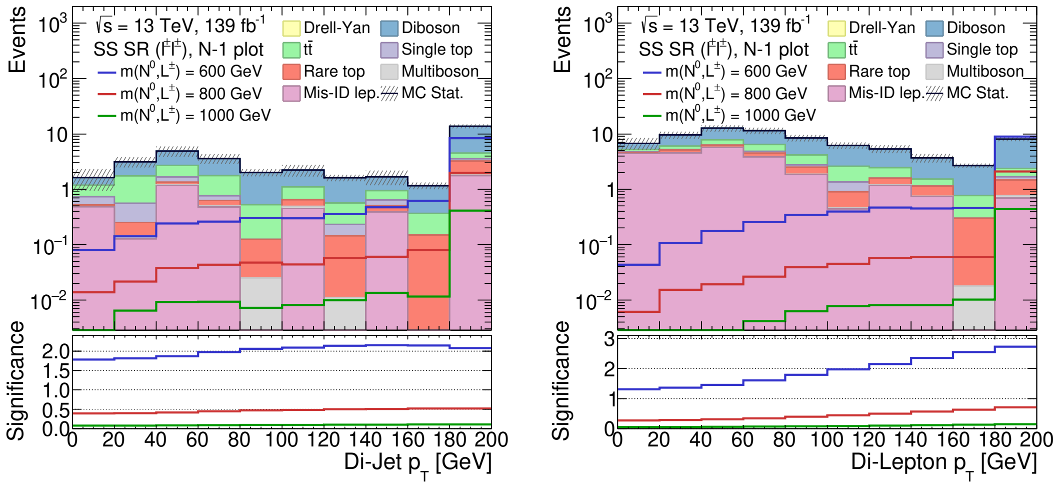

(a) (b)

Figure 6.4: Expected signal and background $N-1$ distributions in the same-sign signal region inclusive in lepton flavour. Each of the observables is plotted with the cut on it omitted. Some distributions are zoomed in into the interesting range. Uncertainties are statistical only. (a) di-jet p_{T} and (b) di-lepton p_{T}.

$p_{\mathrm{T}}(\ell\ell)$, as well as the azimuthal angle, $\Delta\phi(E_{\mathrm{T}}^{\mathrm{miss}},\ell)_{\mathrm{min}}$, are omitted, and the $\mathcal{S}(E_{\mathrm{T}}^{\mathrm{miss}})$ selection is relaxed to $\mathcal{S}(E_{\mathrm{T}}^{\mathrm{miss}}) > 5$, which is crucial to ensure that there are enough events in the CRs. The normalisation of the $t\bar{t}$ MC sample is a free parameter in the simultaneous likelihood fit across all CRs, as described in Chapter 8.

To obtain validation and control regions with a high content of diboson events, the dijet mass m_{jj} selection is inverted relative to the SR definition. Since the m_{jj} selection in the SR requires a pair of jets to match the W mass window, the inverted selection defines a kinematic sideband, with low signal contamination but still selecting events kinematically similar to those in the SR. In addition, all requirements on the transverse momenta, $p_{\mathrm{T}}(jj)$ and $p_{\mathrm{T}}(\ell\ell)$, as well as the azimuthal angle, $\Delta\phi(E_{\mathrm{T}}^{\mathrm{miss}},\ell)_{\mathrm{min}}$, are omitted. This selection defines the m_{jj} VR for the OS analysis channels, while for the SS analysis channels the $\mathcal{S}(E_{\mathrm{T}}^{\mathrm{miss}})$ selection is also relaxed to $\mathcal{S}(E_{\mathrm{T}}^{\mathrm{miss}}) > 5$. The Diboson CR is then defined by introducing an additional requirement $300\,\mathrm{GeV} < H_{\mathrm{T}} + E_{\mathrm{T}}^{\mathrm{miss}} < 500\,\mathrm{GeV}$, while the remaining kinematic region with $H_{\mathrm{T}} + E_{\mathrm{T}}^{\mathrm{miss}} > 500\,\mathrm{GeV}$ is used as the m_{jj} VR. The diboson background contributes only slightly less (45%) than the $t\bar{t}$ background to the contamination in the OS SR and more than half (55%) of the total background in the SS SR. The normalisation of the diboson MC sample used in the analysis is then estimated in the SS Diboson CR. This is achieved by using the normalisation value of the diboson MC sample as a free parameter in the simultaneous likelihood fit across all CRs, as described in Chapter 8.

For the likelihood fit, all CRs and SRs are binned in the $H_{\mathrm{T}} + E_{\mathrm{T}}^{\mathrm{miss}}$ variable in bins uniformly defined in $\log(H_{\mathrm{T}} + E_{\mathrm{T}}^{\mathrm{miss}})$ in the range $300\,\mathrm{GeV} < H_{\mathrm{T}} + E_{\mathrm{T}}^{\mathrm{miss}} < 2\,\mathrm{TeV}$, where the last bin also includes any overflow values. The SRs have six, the Top CRs two and Diboson CRs two bins. The VRs have four and three bins for OS and SS events, respectively.

6.3 Multivariate Analysis Strategy and Selection

Building upon the cut-based analysis approach, the multivariate analysis is designed to improve the sensitivity to the type-III seesaw signal. A loose pre-selection is first defined as an input to the machine learning training and evaluation steps. At this stage events are not yet categorised by lepton charge or flavour. All events with exactly two leptons are selected. Additionally, to keep the same overall pre-selection, at least two jets with $p_{\mathrm{T}} > 20\,\mathrm{GeV}$ and $|\eta| < 2.5$ are required. A b-jet veto is applied on all the jets to suppress backgrounds coming from SM processes involving top quarks.

To remove the Drell–Yan events around the $Z \to ee$ peak, where the electron charge might also have been misreconstructed, a lower bound on the invariant mass of the lepton pair ($m_{\ell\ell}$) is introduced at 100 GeV. While a decay chain involving Z decays is possible, the sensitivity to such events is highly reduced by using the Z peak for electron and muon calibration; any BSM physics with a low cross-section is thus calibrated away in this region.

The signal topology is expected to contain high-p_{T} leptons, jets and neutrinos. To train the machine learning algorithm on events similar to the signal, a combined $H_{\mathrm{T}} + E_{\mathrm{T}}^{\mathrm{miss}} > 500\,\mathrm{GeV}$ selection criterion is also applied. The $N-1$ plots of the $m_{\ell\ell}$ and $H_{\mathrm{T}} + E_{\mathrm{T}}^{\mathrm{miss}}$ variables are shown in Figure 6.5.

The pre-selected data and MC events are then used as an input of two specific machine learning algorithms: CatBoost [145], a gradient boosting library, and TensorFlow [146], a machine learning library with neural networks support. The goal is to compare the performance of boosted decision trees and neural networks so exactly the same input structure is used in both cases.

Binary classification into signal and background events is performed. Simulated events are labelled according to their type (signal or background) and physics process. All signal mass points are considered at the same time to train a universal model. Events are sampled randomly into training, validation and test samples in the $2:1:1$ ratio. All three samples retain the same fraction of different background processes and signal events from different mass points. The models are trained inclusively with both OS and SS lepton pairs and all lepton flavour combinations. 24 features are considered as listed in Table 6.5, where $N_{W,H}$ is the number of W and H boson candidates in the event. Any

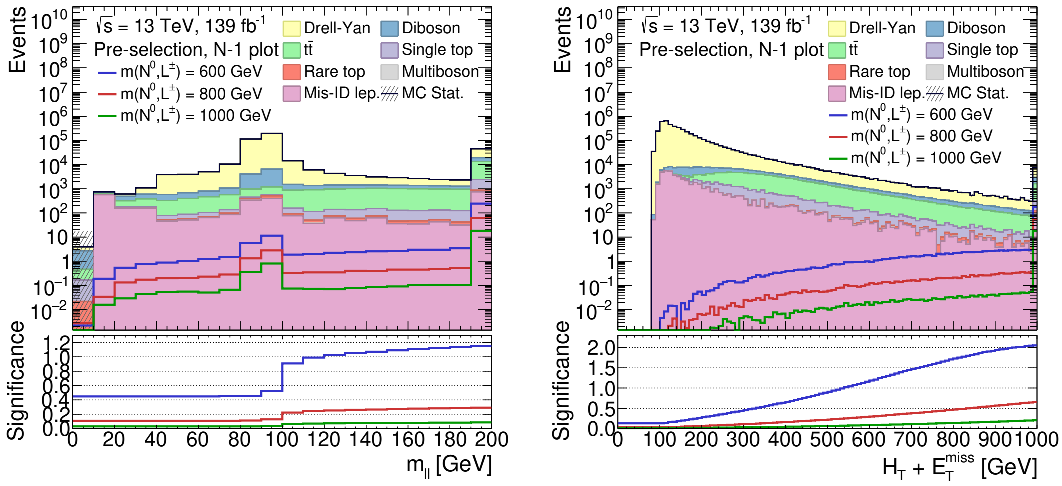

(a)

(b)

Figure 6.5: Expected signal and background $N - 1$ distributions of the MVA pre-selection inclusive in lepton flavour. Each of the observables is plotted with the cut on it omitted. Some distributions are zoomed in into the interesting range. Uncertainties are statistical only. (a) invariant mass of the two leptons, and (b) $H_{\mathrm{T}} + E_{\mathrm{T}}^{\mathrm{miss}}$ of the two leptons and two leading jets.

dijet pair with an invariant mass m_{jj} in the interval 20 GeV (25 GeV) below and above the W (H) mass of 80 GeV (125 GeV) is considered a candidate. The transverse mass of the dilepton system $m_{\mathrm{T}}(\ell\ell)$ is defined as $m_{\mathrm{T}}^2(\ell\ell) = (E_{\mathrm{T},1} + E_{\mathrm{T},2})^2 - (\mathbf{p}_{\mathrm{T},1} + \mathbf{p}_{\mathrm{T},2})^2$ and the "minimax" mass as

$$m_{\mathrm{minimax}}(\ell_1\ell_2 j_1 j_2) = \min\left(\max\left(m(\ell_1 j_1), m(\ell_2 l_2)\right), \max\left(m(\ell_1 j_2) m(\ell_2 l_1)\right)\right). \tag{6.2}$$

Additionally $\Delta\phi(E_{\mathrm{T}}^{\mathrm{miss}}, jj)$ and $\Delta\phi(E_{\mathrm{T}}^{\mathrm{miss}}, \ell\ell)$ represent a difference in angle between $E_{\mathrm{T}}^{\mathrm{miss}}$ and a dijet or a dilepton system.

The features are selected by the physics impact on the selection and by looking at the

Table 6.5: List of features used in the machine learning model.

$p_{\mathrm{T}}(\ell_{\mathrm{lead.}})$	$p_{\mathrm{T}}(\ell_{\mathrm{sub\text{-}lead.}})$	$p_{\mathrm{T}}(\ell\ell)$	$N_{W,H}$
$p_{\mathrm{T}}(j_{\mathrm{lead.}})$	$p_{\mathrm{T}}(j_{\mathrm{sub\text{-}lead.}})$	$p_{\mathrm{T}}(jj)$	N_{jets}
$m(\ell\ell)$	$m(jj)$	$m(jj\ell_{\mathrm{lead.}})$	$m(jj\ell_{\mathrm{sub\text{-}lead.}})$
$m_{\mathrm{T}}(\ell\ell)$	$m_{\ell\ell} + E_{\mathrm{T}}^{\mathrm{miss}}$	$E_{\mathrm{T}}^{\mathrm{miss}}$	$\mathcal{S}(E_{\mathrm{T}}^{\mathrm{miss}})$
m_{minimax}	$H_{\mathrm{T}} + E_{\mathrm{T}}^{\mathrm{miss}}$	$p_{\mathrm{T}}(\ell_{\mathrm{lead.}}) + p_{\mathrm{T}}(\ell_{\mathrm{sub\text{-}lead.}}) + E_{\mathrm{T}}^{\mathrm{miss}}$	$\Delta\eta(j_{\mathrm{lead.}}, j_{\mathrm{sub\text{-}lead.}})$
$\Delta\phi(E_{\mathrm{T}}^{\mathrm{miss}}, \ell)_{\mathrm{min}}$	$\Delta\phi(E_{\mathrm{T}}^{\mathrm{miss}}, jj)$	$\Delta\phi(E_{\mathrm{T}}^{\mathrm{miss}}, \ell\ell)$	$\Delta\phi(\ell_{\mathrm{lead.}}, \ell_{\mathrm{sub\text{-}lead.}})$

effect of the observable on the performance of the BDT. The three most discriminating variables are $m_{\ell\ell}$, $m_{\ell\ell} + E_{\mathrm{T}}^{\mathrm{miss}}$ and $\mathcal{S}(E_{\mathrm{T}}^{\mathrm{miss}})$.

Boosted decision trees have been trained using 10000 iterations with no additional requirements imposed. The neural network consisted of three hidden layers with 256 neurons each, activated by the ReLU activation function. The output layer used the sigmoid function to translate the prediction into values between 0 and 1, which can be interpreted as the signal probability ('score'). The training has been split in batches of size 128 and has run over 19 epochs. Additionally, to test the interpolation potential of neural networks, true signal is added as a parameter to the network, effectively being an additional feature [147]. Other samples, including data, use randomly sampled values from the interval between the lowest and the highest mass point studied.

The performance of both trained models is compared in Figure 6.6. While both types of algorithms give very good performance, the neutral network performs better. The AUC values for the BDT and the NN are 0.963 and 0.977, respectively. The difference in performance is also visible from the event classification score distribution (Figure 6.6(b)) with the NN showing better separation power. For this reason the neural network result is used to define further multivariate analysis regions selection criteria.

The main criterion for defining analysis regions is the multivariate analysis score, representing probability of an event to be a signal event. The score is also the observable used in the final likelihood fit, described in Chapter 8. For this reason the cut on the score is not optimised using the ROC curve but by maximising the significance using the neural network result. The inclusive score spectrum is displayed in Figure 6.7. This time signal and background contributions are compared according to their cross-sections

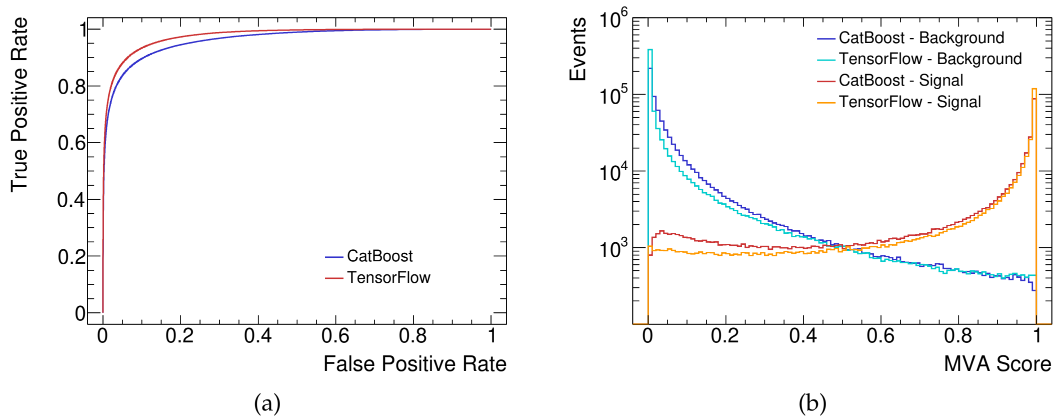

Figure 6.6: Comparison of the performance of trained multivariate models, showing (a) ROC curve and (b) event classification score distribution. The event distribution is not weighted by cross-section or other efficiency corrections. Each entry represents one simulated event.

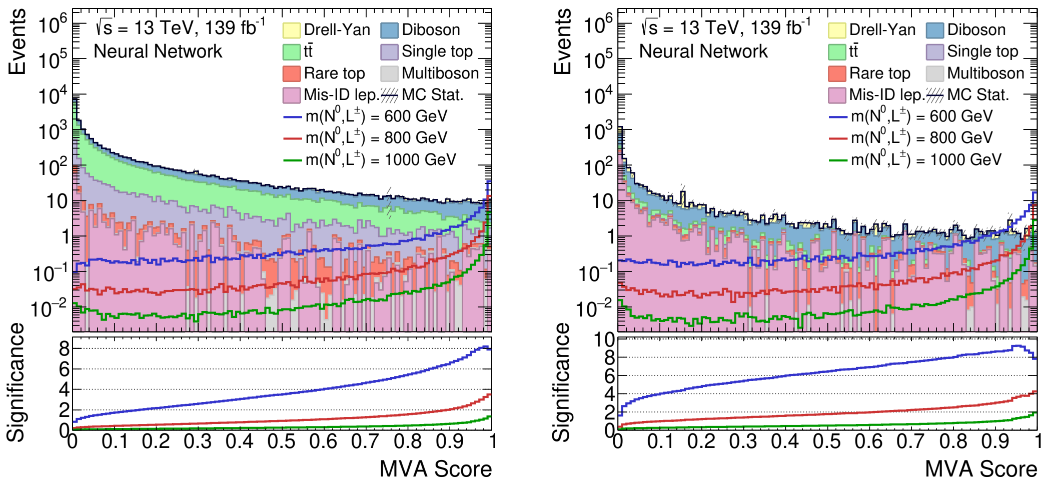

(a)

(b)

Figure 6.7: Expected signal and background distributions of the MVA score inclusive in lepton flavour, displaying (a) OS and (b) SS events. Uncertainties are statistical only.

and with all efficiency corrections applied.

Multivariate score of at least 0.8 is required in the signal regions to achieve good separation significance. The rest of the range is then used as control and validation regions. Validation regions are defined in the range $0.4 < \text{score} < 0.8$ and control regions below 0.4. As the model performance is similar for the OS and SS channels, the selection is kept the same for both channels. The only exception is the SS CR with the upper score cut reduced to 0.2 to avoid bins with very low statistics.

While in the SS channel the neural network separates events well in the whole $E_{\mathrm{T}}^{\mathrm{miss}}$ range, in the OS channel a $\mathcal{S}(E_{\mathrm{T}}^{\mathrm{miss}}) > 5$ still needs to be applied. This is to remove the large Drell–Yan background contamination. Only the SS ee channel suffers with a significant number of events with incorrectly reconstructed charge, so a $\mathcal{S}(E_{\mathrm{T}}^{\mathrm{miss}}) > 4$ is only applied for that flavour combination. This slightly reduces signal significance but also uncertainties in the background.

The dominant background contribution in the signal regions are diboson events with slight contributions from $t\bar{t}$ in the OS channel. Two separate control regions are defined to estimate the diboson background for each possible lepton pair charge combination, called the OS and SS control regions. As the OS CR is not pure enough and also contains a significant fraction of $t\bar{t}$ events, an additional the Top control region is defined to evaluate the normalisation of that background. It is inspired by the cut-based equivalent with the number of b-tagged jets required to be $N(b\text{-jet}) \geq 2$ but all other pre-selection cuts identical as the signal region. As the phase space is not used for the training no cut on the MVA score is applied.

To improve the purity of the backgrounds estimated in the control regions, mainly avoiding Drell–Yan events, the $\mathcal{S}(E_{\mathrm{T}}^{\mathrm{miss}})$ selection is tightened to $\mathcal{S}(E_{\mathrm{T}}^{\mathrm{miss}}) > 7.5$ in all OS control regions. Validation regions do not have any additional selection applied to be kept as close to signal regions as possible.

All regions used in the multivariate approach, with the corresponding selection criteria, are summarised in Table 6.6. Additional N-1 plots motivating the $\mathcal{S}(E_{\mathrm{T}}^{\mathrm{miss}})$ selection in signal regions are shown in Figure 6.8.

For the likelihood fit all SRs are binned in the MVA score variable with smaller bins where high number of signal events is expected. OS control regions are binned in the $H_{\mathrm{T}} + E_{\mathrm{T}}^{\mathrm{miss}}$ variable, where the last bin also includes any overflow values, while the SS control regions and validation regions also use the MVA score. The SRs and VRs have four, the Top CRs one and the rest of CRs two bins.

Table 6.6: Summary of all multivariate-based analysis regions defined in the analysis. The region definitions are the same for all analysis channel flavour combinations with the exception of the SS CR in the *ee* channel.

	OS ($\ell^+\ell^- = e^+e^-, e^\pm\mu^\mp, \mu^+\mu^-$)				**SS** ($\ell^\pm\ell^\pm = e^\pm e^\pm, e^\pm\mu^\pm, \mu^\pm\mu^\pm$)		
	Top CR	**CR**	**VR**	**SR**	**CR**	**VR**	**SR**
$N(\text{jet})$	≥ 2	≥ 2	≥ 2	≥ 2	≥ 2	≥ 2	≥ 2
$N(b\text{-jet})$	≥ 2	0	0	0	0	0	0
$m_{\ell\ell}$ [GeV]	≥ 100	≥ 100	≥ 100	≥ 100	≥ 100	≥ 100	≥ 100
$H_{\mathrm{T}} + E_{\mathrm{T}}^{\mathrm{miss}}$ [GeV]	≥ 500	≥ 500	≥ 500	≥ 500	≥ 500	≥ 500	≥ 500
$\mathcal{S}(E_{\mathrm{T}}^{\mathrm{miss}})$	≥ 7.5	≥ 7.5	≥ 5	≥ 5	≥ 4 (*ee*)	≥ 4 (*ee*)	≥ 4 (*ee*)
MVA score	—	$(0, 0.4)$	$(0.4, 0.8)$	$(0.8, 1)$	$(0, 0.2)$	$(0.4, 0.8)$	$(0.8, 1)$

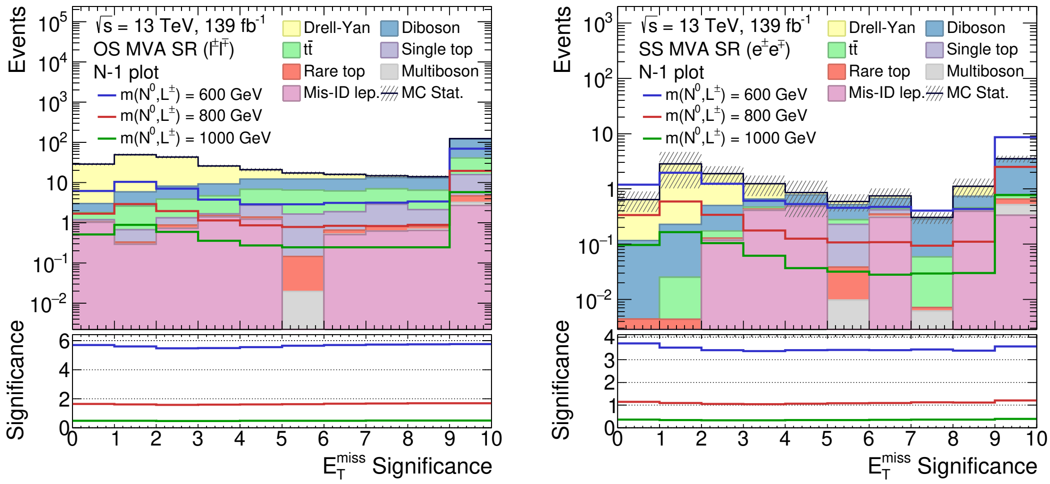

(a) (b)

Figure 6.8: Expected signal and background $N-1$ distributions of the MVA signal regions. Each of the observables is plotted with the cut on it omitted. Uncertainties are statistical only. (a) $\mathcal{S}(E_{\mathrm{T}}^{\mathrm{miss}})$ in the inclusive OS channel, and (b) $\mathcal{S}(E_{\mathrm{T}}^{\mathrm{miss}})$ in the SS ee channel.

6.4 Systematic Uncertainties

Experimental and theoretical systematic uncertainty sources affecting both background and signal predictions are accounted for in the analysis. The impact of systematic uncertainties on both the total event yields as well as the changes in the shape of kinematic distributions is taken into account for all background samples not floating in the fit when performing the statistical analysis as described in Chapter 8. Only shape systematics are considered for the $t\bar{t}$ and diboson backgrounds, and also signal samples, as their normalisation is determined from the fit.

6.4.1 Theoretical Uncertainties

Monte Carlo generation allows variations of theoretical models used to produce the samples. An inclusive cross-section $\sigma^{(n)}$ for $pp \to X$ calculated at n-th order in perturbation theory can be schematically given by

$$\sigma^{(n)} = \mathrm{PDF}(x_1, \mu_{\mathrm{F}}) \otimes \mathrm{PDF}(x_2, \mu_{\mathrm{F}}) \otimes \hat{\sigma}^{(n)}(x_1, x_2, \mu_{\mathrm{R}}) \tag{6.3}$$

with

$$\hat{\sigma}^{(n)} = \alpha_s \hat{\sigma}^{(0)} + \alpha_s^2 \hat{\sigma}^{(1)} + \ldots \alpha_s^n \hat{\sigma}^{(n)} + \mathcal{O}(\alpha_s^{n+1}), \tag{6.4}$$

where x_1 and x_2 are the fractions of momentum coming from each of the two partons, and μ_F and μ_R are factorisation and renormalisation scales, respectively. Scale variation uncertainties, PDF uncertainties and α_s uncertainties are estimated for the main two backgrounds, $t\bar{t}$ and diboson, and for the signal samples. Additionally for $t\bar{t}$ initial and final state variations are taken into account. Also the effect of the choice of generator software used for the hard process and for showering is estimated. Sample-specific theoretical uncertainties are described in detail in Section 4.3.2.

Missing higher orders in the perturbative expansion of the partonic cross-section are estimated by varying the renormalisation μ_R and factorisation μ_F scales. The uncertainty is evaluated by taking an asymmetric envelope of seven variations obtained by varying scales up and down by a factor of two, but excluding the variations where one is varied up and the other varied down, with options presented in Table 6.7.

Table 6.7: Applied renormalisation and factorisation scale variations.

μ_R \ μ_F	0.5	1	2
0.5	✓	✓	
1	✓	✓	✓
2		✓	✓

Besides the missing higher order uncertainties there are several sources of uncertainty that affect the determination of PDFs, mainly experimental uncertainties entering the datasets used in the PDF fits and the uncertainty in functional form used in the PDF fits. Other theory uncertainties such as the flavour scheme or nuclear effects are not explicitly taken into account, but some of these effects are indirectly probed when comparing different PDF sets. PDF uncertainties are calculated using the `LHAPDF6` toolkit [148].

The strong coupling constant α_s is determined experimentally from the combination of a different datasets and its value is quoted at the scale of the Z boson mass. There are two main sources of uncertainty, the experimental errors in the determination of α_s and the fact that the cross-section calculation is truncated at a fixed order in perturbation theory. The nominal value of $\alpha_s = 0.118$ is compared with $\alpha_s = 0.117$ and $\alpha_s = 0.119$ using

$$\delta^{\alpha_s}\sigma = \frac{\sigma(\alpha_s^{\mathrm{down}}) - \sigma(\alpha_s^{\mathrm{up}})}{2}\,. \tag{6.5}$$

Since the value of α_s affects the cross-sections of the processes used in the PDF fits, there is an interplay between the α_s and PDF uncertainties, however the correlation is small. To reduce the impact the two uncertainties are combined in squares as

$$\delta^{\alpha_s+\mathrm{PDF}}\sigma = \sqrt{(\delta^{\mathrm{PDF}}\sigma)^2 + (\delta^{\alpha_s}\sigma)^2}\,. \tag{6.6}$$

6.4.2 Experimental Uncertainties

The majority of experimental uncertainties arise due to differences between reconstruction results of data and simulated events. There are two main types of systematic uncertainties. Calibration uncertainties change particle momenta to account for uncertainties in momentum scale and track reconstruction. Efficiency uncertainties are the result of different reconstruction, object identification, charge identification, isolation, and trigger efficiencies of leptons in data compared with MC simulation and are estimated by varying the corresponding scale-factors. Each systematic uncertainty might have one or more nuisance parameters assigned. A summary of the sources of systematic uncertainty considered is presented in Table 6.8. Both types of experimental uncertainties are applied to both background and signal MC predictions but not to data.

The data-driven fake-factor estimate of the fake-lepton background has an additional uncertainty assigned. Fake-factors are varied to improve the modelling of the fake background as discussed in Sections 7.2.1 and 7.2.2.

Table 6.8: Summary of the sources of systematic uncertainty considered in the analysis.

Systematic uncertainty	Nuisance parameters
Luminosity	**1**
Pile-up modelling	**1**
Experimental uncertainties	**67**
Electron scale and resolution	3
Electron reconstruction efficiencies	1
Electron identification efficiencies	1
Electron charge identification efficiencies	2
Electron isolation efficiencies	1
Electron trigger efficiencies	2
Muon scale and resolution	5
Muon reconstruction efficiencies	3
Muon isolation efficiencies	2
Muon track-to-vertex association efficiencies	2
Muon trigger efficiencies	2
Jet energy scale — calibration	14
Jet energy scale — flavour dependence	3
Jet energy scale — pile-up dependence	4
Jet energy scale — calorimeter punch-through	2
Jet energy scale — MC non-closure	1
Jet energy resolution	9
Jet JVT efficiencies	1
Jet flavour tagging efficiencies	6
$E_{\mathrm{T}}^{\mathrm{miss}}$ uncertainties	3
Data-driven background uncertainties	**2**
Electron fake-factors	1
Muon fake-factors	1
$t\bar{t}$ modelling uncertainties	**7**
PDF choice and variation	2
QCD scale variation	1
ISR and FSR scale variation	2
Generator software choice	2
Diboson modelling uncertainties	**3**
PDF choice and variation	2
QCD scale variation	1
Signal modelling uncertainties	**2**
PDF variation	1
QCD scale variation	1
Total	**83**

CHAPTER 7

BACKGROUND ESTIMATION

Irreducible backgrounds containing real prompt leptons originate from Standard Model processes producing opposite-sign and same-sign lepton pairs, such as decays of Z, W and H bosons, or from prompt leptonic τ lepton and t quark decays. The predictions are obtained from Monte Carlo simulated samples which are summarised in Section 4.3.2. The final normalisations of $t\bar{t}$ and diboson MC samples are not taken from MC calculations but are derived in the simultaneous likelihood fit to the data in dedicated Top and Diboson CRs for the cut-based approach, and in Top, OS and SS CRs for the multivariate analysis approach, as introduced in Sections 6.2 and 6.3 and detailed in Chapter 8.

The same MC samples also provide a source of reducible background due to charge misidentification (charge-flip) in channels that contain electrons. The modelling of charge misidentification in MC simulation deviates from data which is corrected by data-driven scale factors as described in Section 7.1.

Another source of reducible background is given by events with at least one fake/non-prompt electron or muon, collectively called *fakes*. For both, electrons and muons, this contribution is caused by secondary decays into light leptons of light-flavour or heavy-flavour mesons, embedded within jets. For electrons, a significant component of fakes also arises from jets which satisfy the electron reconstruction criteria and from photon conversions. MC samples are not used to estimate this background because the simulation of jets and hadronisation have large uncertainties. Instead, a data-driven approach, outlined in Section 7.2, is used to assess this contribution from production of W+ jets, $t\bar{t}$ and multi-jet events.

7.1 CHARGE MISIDENTIFICATION OF ELECTRONS

Electron charge misidentification is caused predominantly by bremsstrahlung. The emitted photon can either convert to an electron-positron pair, which happens in most

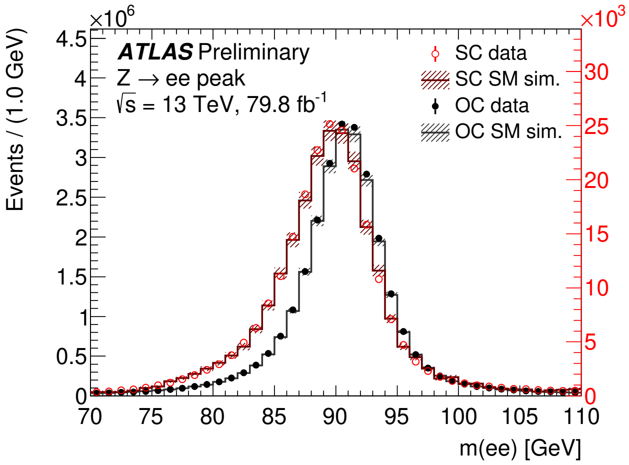

Figure 7.1: Dielectron invariant mass distributions for opposite-charge (OC, black) and same-charge (SC, red) pairs for data (circles) and MC simulation (continuous line). The latter includes a correction for charge misidentification. The hatched band indicates the statistical error applied to MC simulated events. Note that the scales for OC and SC are different and given at the left side (OC) and right side (SC), respectively. Taken from Ref. [149].

of the cases, or traverse the inner detector without creating any tracks. In the first case, the cluster corresponding to the initial electron can be matched to the wrong-charge track, or most of the energy is transferred from one track to the other because of the photon. In case of photon emission without subsequent pair production, the electron track has usually very few hits only in the silicon pixel layers, and thus a short lever arm on its curvature. Because the electron charge is derived from the track curvature, it could be incorrectly determined while the electron energy is likely appropriate as the emitted photon deposits all of its energy in the EM calorimeter as well. For a similar reason high-energy electrons are more often affected by charge misidentification, as their tracks are approximately straight and therefore challenging for the curvature measurement. The modelling of charge misidentification in simulation deviates from data due to the complex processes involved, which particularly rely on a very precise description of the detector material.

The effect of muon charge misidentification is negligible because muons undergo bremsstrahlung in the inner detector very rarely. Furthermore, their tracks are measured also in the muon spectrometer, complementary to the inner detector, which provides a much larger lever arm for the curvature measurement.

Charge reconstruction scale factors are derived in a data-driven way by comparing the charge misidentification probability measured in data with the one in simulation. These scale factors are then applied to the simulated background events to compensate for the differences. The charge misidentification probability is extracted by performing a likelihood fit on a dedicated $Z \to ee$ data and MC samples [126]. It is parametrised as a function of electron p_{T} and η, and is measured with the same method in a simulated $Z/\gamma^* \to ee$ sample and in data. All prompt electrons in simulated events are corrected with charge reconstruction scale factors. The scale factors are defined as $P(p_{\mathrm{T}}, \eta; \mathrm{data})/P(p_{\mathrm{T}}, \eta; \mathrm{MC})$ if the charge is wrongly reconstructed and $(1 - P(p_{\mathrm{T}}, \eta; \mathrm{data}))$ / $(1 - P(p_{\mathrm{T}}, \eta; \mathrm{MC}))$ if the charge is properly reconstructed, where P is the misidentification probability.

The opposite-charge (OC) and same-charge (SC) Z peaks are presented in Figure 7.1. The Z peak in the SC region is shifted by approximately 1.5 GeV to lower energies and the width is slightly broader compared with the Z peak in the OC region. This is due to electron charge-flip events arising from an electron radiating a photon which is then converted into an electron-positron pair. The particle with the wrong charge is reconstructed, which has lower energy than the parent electron.

7.2 FAKE-FACTOR METHOD

A hadronic jet can sometimes be reconstructed as an electron or muon. This allows events with a single real light lepton and even events without leptons to pass our signal event selection. As described in Chapter 4, background processes are usually predicted using Monte Carlo simulations. In this specific case however, data-driven approach is used to estimate the contribution of fake leptons to the analysis selection as the interactions causing incorrect identification of objects are very difficult to simulate. Additionally as these occurrences are rare a lot of simulated events would be needed to make accurate enough predictions. Leptons from non-prompt decays are commonly a result of jet constituent decays not assigned to a jet but kept as an individual reconstructed particle, which is also hard to model. Electron and muon fake background estimation method used in this analysis is called the *fake-factor method* [150].

The fake-factor method extrapolates the number of fake leptons passing the signal selection based on their number in a control region dominated by this kind of background. Each of the fake leptons is weighted by a *fake-factor* which is proportional to its probability to satisfy the prompt selection requirement. Events containing fake leptons are then multiplied with these weights.

Fake lepton control region is constructed by loosening certain identification criteria applied in the nominal selection. It can be then used to probe the probability of looser fake leptons entering the nominal selection. Two different selection criteria are defined in the fake-factor method:

- the *tight* (T) selection (same as the nominal selection),
- the *loose* (L) selection (orthogonal to the nominal selection).

Loose and tight lepton definitions used in the analysis are reported in Tables 6.2 and 6.3. By loosening the identification criteria the tight selection would by definition be a subset of those passing the loose selection. Thus loose leptons are additionally required to fail the tight selection to ensure orthogonality, as schematically portrayed in Figure 7.2.

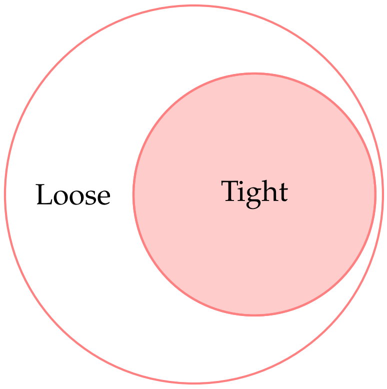

Figure 7.2: The loose and the tight regions of the fake-factor method. Loose leptons should fail the tight selection so the regions are orthogonal.

Fake estimation control regions should be orthogonal to the main analysis signal, control and validation region. They are defined for electrons in Section 7.2.1 and for muons in Section 7.2.2. To help with the definition of the estimation regions fake lepton composition is investigated in Appendix A.

The misidentification probability, usually called the *fake rate*, can now be defined as

$$f = \frac{N_{\text{tight}}}{N_{\text{tight}} + N_{\text{loose}}} \tag{7.1}$$

where N_{tight} and N_{loose} are the numbers of fake leptons satisfying and failing the identification requirement. The *fake-factor* can then be derived as

$$F = \frac{f}{1-f} = \frac{N_{\text{tight}}}{N_{\text{loose}}} \tag{7.2}$$

The fake-factor is measured as a function of one or more kinematic variables and can be used to weight loose leptons. The final amount of extrapolated fake background can is defined as

$$N_{\text{fakes}} = \left[\sum_{\text{events}}^{n\,\text{loose}} (-1)^{n-1} \prod_{i}^{n} F_i \right]_{\text{data}} - \left[\sum_{\text{events}}^{n\,\text{loose}} (-1)^{n-1} \prod_{i}^{n} F_i \right]_{\text{prompt simulation}} \tag{7.3}$$

where the inner product runs over the number of loose leptons in the event and the outer sum over all events with at least one loose lepton present. Tight leptons do not contribute to the final number of fake leptons. Fake-factors F_i depend on individual loose lepton kinematic properties. To avoid double counting the prompt contribution estimated with MC events needs to be subtracted from data, as indicated with square brackets in the formula. In the case of dilepton events the formula can be expanded as

$$N_{\text{fakes}}^{\text{dilepton}} = \left[\sum_{TL} F_2 + \sum_{LT} F_1 - \sum_{LL} F_1 F_2\right]_{\text{data}} - \left[\sum_{TL} F_2 + \sum_{LT} F_1 - \sum_{LL} F_1 F_2\right]_{\text{prompt simulation}} \tag{7.4}$$

7.2.1 ELECTRON FAKE-FACTOR MEASUREMENT

Electron fake-factors are estimated in a single electron + jets control region. The probabilities for reconstructing fake leptons are assumed to be independent on the number of leptons in a event. Although the analysis signal regions contain more than one lepton the chosen region is suitable because it is fakes-enriched. The following requirements characterise the selection:

- Exactly one electron and zero muons are required to ensure orthogonality with the signal region.
- Events are selected separately with $25\,\text{GeV} < E_{\text{T}}^{\text{miss}}$ and $25\,\text{GeV} \geq E_{\text{T}}^{\text{miss}}$ to get a good description of fakes for the whole phase space.
- At least two jets are required in the event with the b-jet veto applied.

As physics analyses are usually not interested in very loose electrons such events are not triggered-on by default. The nominal single-electron triggers have much tighter requirements on electron identification compared with our needs so prescaled single-electron triggers have to be used. The average prescale is lower with the increase of the trigger p_{T} threshold. Depending on the electron p_{T} the matching trigger with the lowest prescale is chosen. The list of triggers used is summarised in Table 7.1.

The dijet fakes-enriched region is shown in Figure 7.3. Prompt electrons from W+jets, Drell–Yan, $t\bar{t}$ and single top, diboson, rare top and triboson decays are subtracted from data before the calculation of fake-factors. The MC subtraction is much larger in the tight region compared with the loose region and amounts for up to 50% of all electrons. The fake-factor is measured in four η slices (2 slices for the forward region and 2 slices for the barrel region) and two $E_{\text{T}}^{\text{miss}}$ bins. The p_{T} binning is driven by the uncertainty of the fake-factor measurement for a specific bin. Bins are dynamically merged until the statistical uncertainty does not drop below a specific threshold. The last p_{T} bin includes the overflow and is extended to infinity and no extrapolation of the fake-factor is performed.

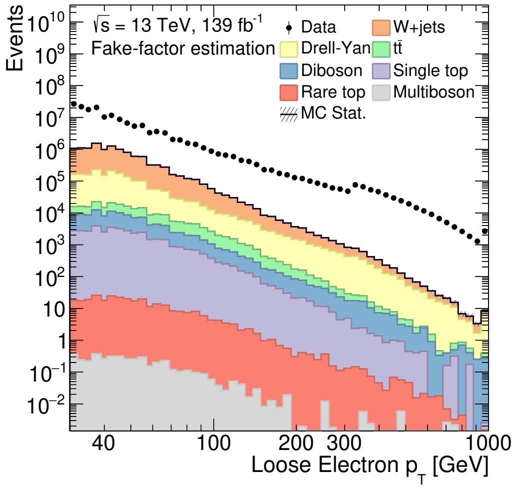

(a)

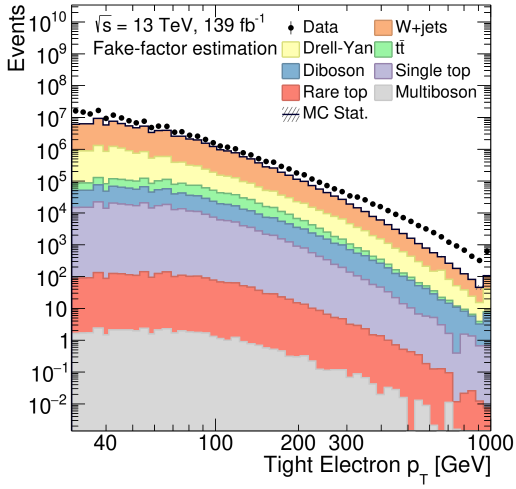

(b)

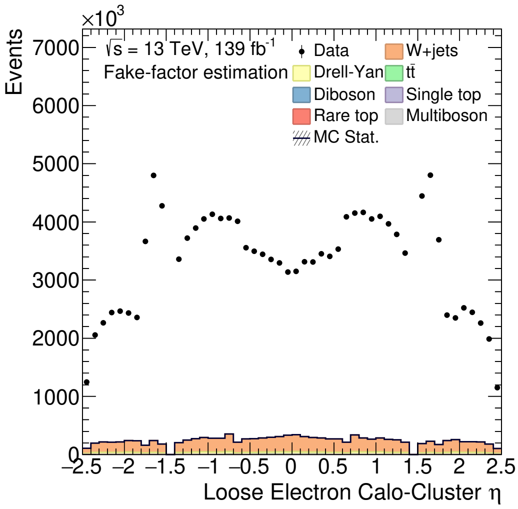

(c)

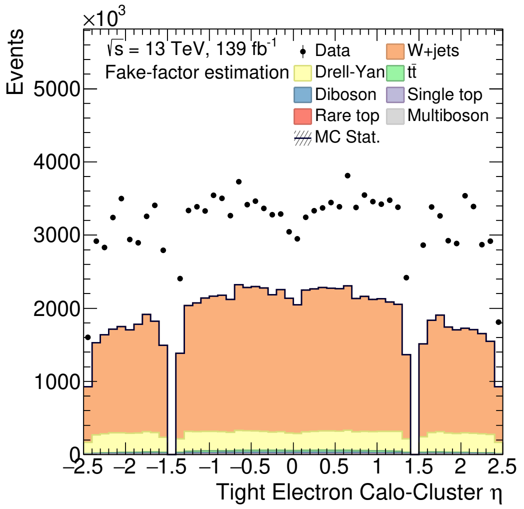

(d)

Figure 7.3: Electron fakes-enriched regions in the nominal selection. (a) p_{T} distribution of loose electrons, (b) p_{T} distribution of tight electrons, (c) η distribution of loose electrons, (d) η distribution of tight electrons. All the distributions show data events and the prompt MC component subtracted from data, to ensure a fake dominated region.

Table 7.1: Triggers used for the electron fake-factor estimation. The average prescale is calculated over all periods where the specific trigger was used.

Trigger	Average prescale	Periods
HLT_e26_lhvloose_nod0_L1EM20VH	111.2	2015–2016
HLT_e28_lhvloose_nod0_L1EM20VH	367.6	2017
HLT_e28_lhvloose_nod0_L1EM22VH	384.5	2018
HLT_e60_lhvloose_nod0	32.93	2015–2018
HLT_e70_lhvloose_nod0	64.13	2018
HLT_e80_lhvloose_nod0	40.43	2018
HLT_e100_lhvloose_nod0	19.45	2018
HLT_e120_lhvloose_nod0	12.15	2016, 2018
HLT_e140_lhvloose_nod0	2.637	2017–2018
HLT_e160_lhvloose_nod0	1.601	2017–2018
HLT_e200_etcut	/	2015
HLT_e300_etcut	/	2016–2018

The main sources of the systematic uncertainties of the fake-factor arise from Monte Carlo modelling of the subtracted leptons, from different composition of fake electrons in the fake enriched region compared with the signal region, and from the normalisation of Monte Carlo samples in the fakes-enriched region. The fake-factor is measured independently for each of those variations and all of them are presented in Table 7.2.

The resulting fake-factors for each variation are shown in Figures 7.4(a)–7.4(d). Combined systematics of the fake-factors is calculated by adding all variations and the statistical uncertainty in quadrature. The largest contribution to the uncertainty is the MC scaling. The measurement is relatively stable overall up to very high electron p_{T} but the maximum uncertainty can get very high, up to 100%.

The measured fake-factors are validated by performing the direct closure test in the fakes-

Table 7.2: Summary of the variations used for the determination of the systematic uncertainty of the electron fake-factors.

Variation	Purpose
Looser requirement on number of jets	fakes composition
Removed $E_{\mathrm{T}}^{\mathrm{miss}}$ requirement	fakes composition
MC samples scaled up by 10%	MC modelling and cross-section
MC samples scaled down by 10%	MC modelling and cross-section

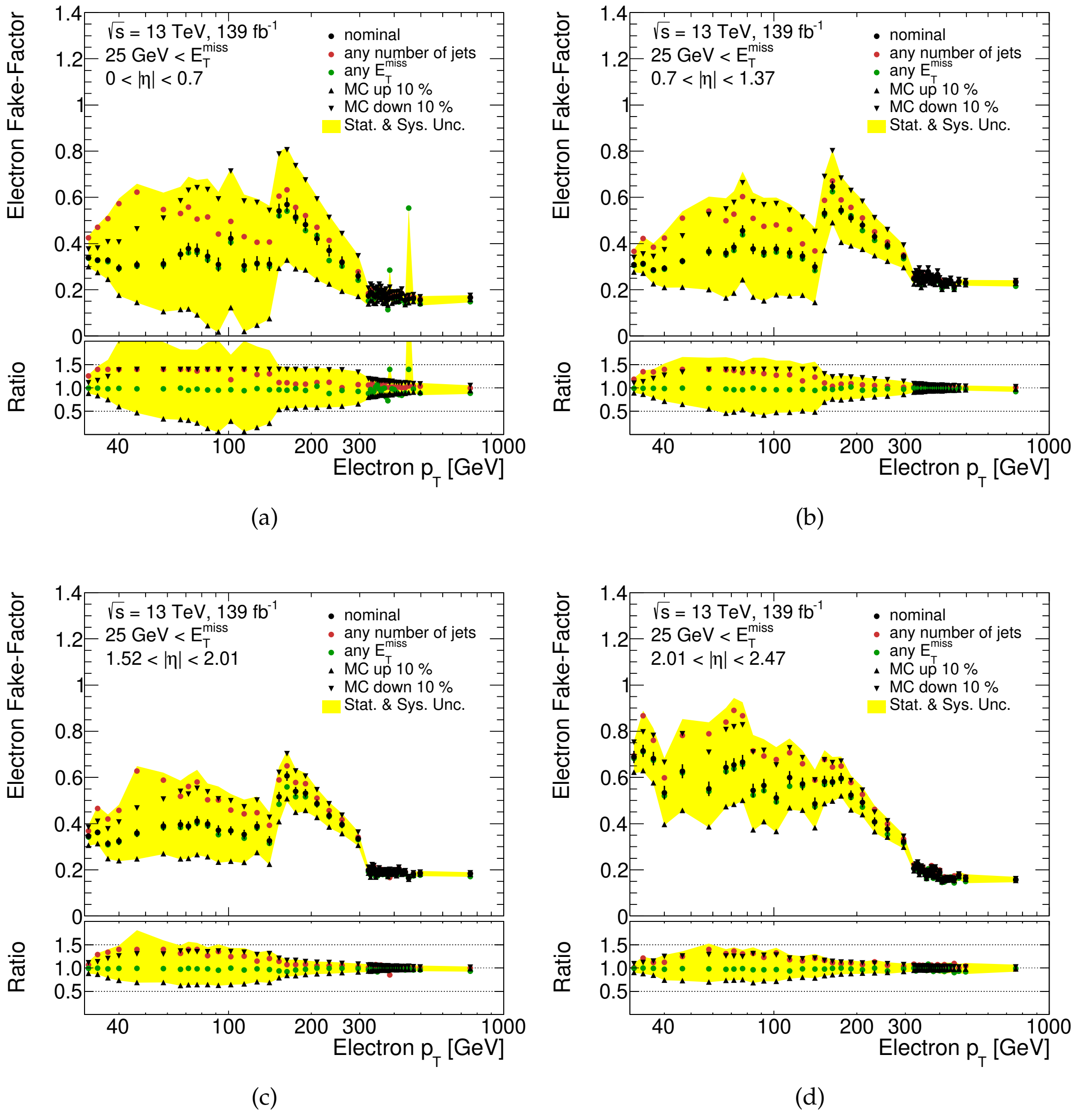

Figure 7.4: Measured electron fake-factors with systematic variations applied, summarised in Table 7.2. $E_{\mathrm{T}}^{\mathrm{miss}} > 25\,\mathrm{GeV}$ is required, (a) for the first η bin, (b) for the second η bin, (c) for the third η bin, and (d) for the last η bin.

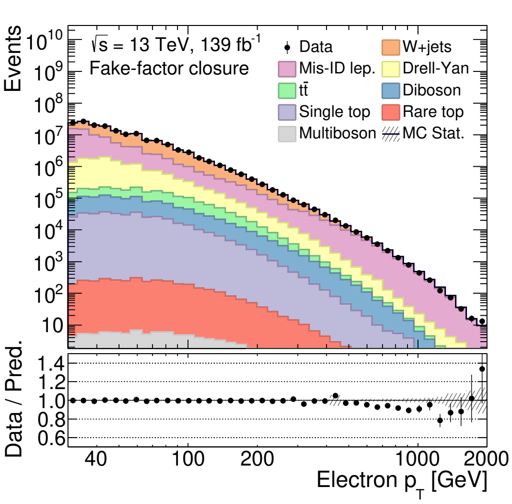

(a)

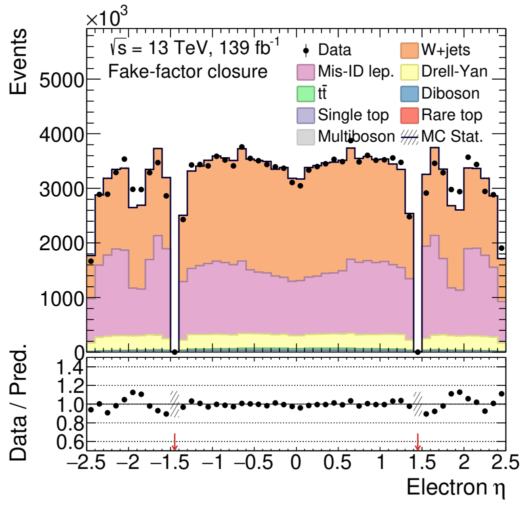

(b)

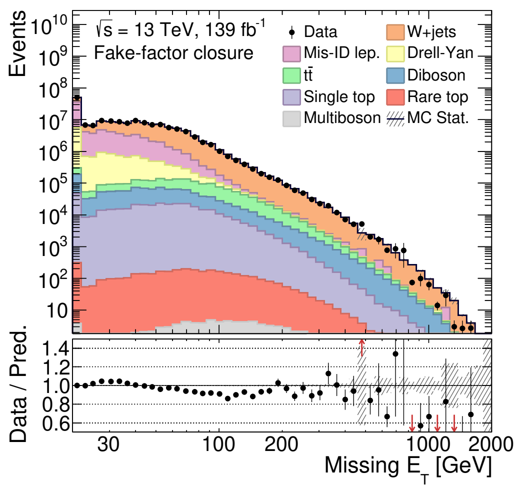

(c)

Figure 7.5: The electron fake-factors closure. (a) electron p_{T} distribution, (b) electron η distribution, and (c) $E_{\mathrm{T}}^{\mathrm{miss}}$ distribution. The orange band shows the systematic uncertainty associated to the fake-factor measurement.

enriched region using the exact same event selection as for the fake-factor derivation for data events and comparing them with the combined prediction of Monte Carlo and the fake-factor method. The reconstructed object selection is the same as the nominal event selection (Section 6.1).

Prompt Monte Carlo processes used are W+ jets, Drell–Yan, $t\bar{t}$ and single top, diboson, rare top and multiboson decays. The remaining events are described well by the fake-factor method as seen in Figure 7.5. The only considered systematic uncertainty in this region is the systematic uncertainty of the fake-factor. Overall the level of agreement is good even up to very high electron energies.

7.2.2 MUON FAKE FACTOR MEASUREMENT

Fake muons might arise from in-flight decays of mesons inside jets with the semi-leptonic decay of B meson as one of the largest contributions. Muon fake-factors are measured in a dedicated analysis region targeting dijet events. At least one hadronic jet and a reconstructed muon are required. The selected objects are assumed to fly in the opposite directions which is imposed by the angular requirement $\Delta\phi > 2.7$. Similar to electrons prescaled non-isolated single-muon triggers have to be used and are listed in Table 7.3.

The amount of muon fakes is not expected to be very high. To enrich the control region with fakes additional requirements are applied. The momentum of the leading jet should not be too low, $p_{\mathrm{T}}(\text{jet}) > 35\,\text{GeV}$. In addition $W \to \mu\nu$ events are rejected by requiring $E_{\mathrm{T}}^{\text{miss}} < 40\,\text{GeV}$. Finally, events featuring a b-jet are rejected to avoid fakes from heavy flavour decays. The distributions of muon p_{T} and η after all selection requirements are applied, are reported in Figure 7.6.

Systematic uncertainties in the measurement on muon fake-factors are estimated by altering the selection of dijet events. The nominal requirement on the missing transverse energy $E_{\mathrm{T}}^{\text{miss}}$ is varied by 10 GeV upward and downward in turn, for tight and loose muons simultaneously. This effect varies the fraction of W+ jets events contaminating

Table 7.3: Triggers used for the muon fake-factor estimation. The average prescale is calculated over all periods where the specific trigger was used.

Trigger	Average prescale	Periods
`HLT_mu24`	49.36	2015–2018
`HLT_mu50`	/	2015–2018

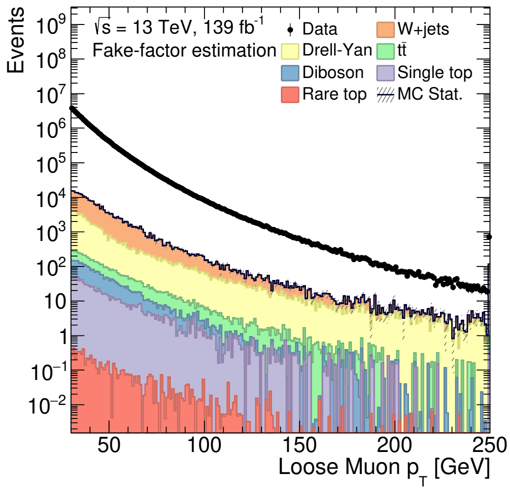

(a)

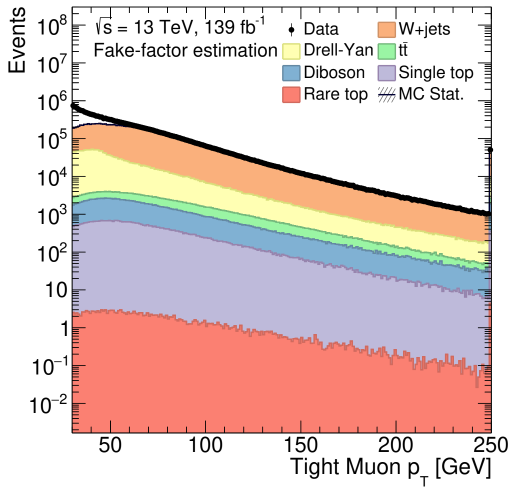

(b)

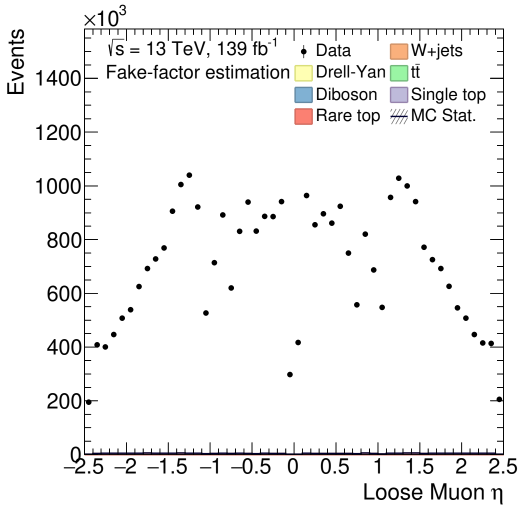

(c)

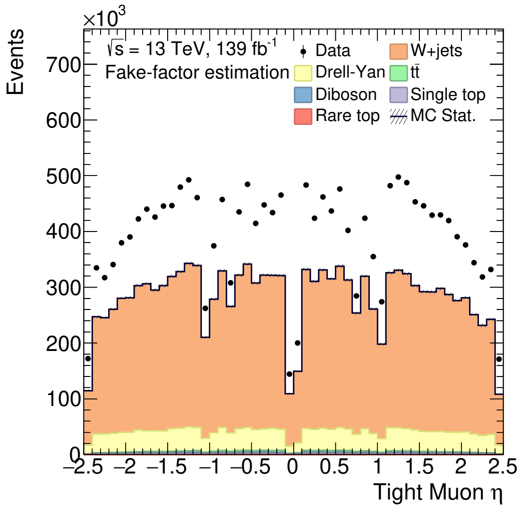

(d)

Figure 7.6: Muon fakes-enriched regions in the nominal selection. (a) p_T distribution of loose muons, (b) p_T distribution of tight muons, (c) η distribution of loose muons, (d) η distribution of tight muons. All the distributions show data events and the prompt MC component subtracted from data, to ensure a fake dominated region.

the selection, hence the largest fraction of prompt muons which have to be subtracted from data using simulation.

For the same reason, the isolation distribution of the fake muon might differ between the dijet selection and the sidebands. This effect can be addressed by varying the transverse momentum of the recoiling jet in the event up to $p_T(\text{jet}) > 40\,\text{GeV}$ hence altering the collimation of the fake jet.

The kinematic balance of the muon and the recoiling jet, which affects the isolation, might also be altered varying the back-to-back requirement $\Delta\phi(\mu, \text{jet})$. An upward and downward variation of 0.1 is chosen.

The effect of each systematic alteration on the nominal measurement can be seen in Figures 7.7(a)–7.8(c). Combined systematics of the fake-factors is calculated by adding all variations and the statistical uncertainty in quadrature. An uncertainty ranging between ≈ 10% and ≈ 50% is achieved across p_T intervals.

The measured fake-factors are validated by performing a closure test in the fakes-enriched region using similar event selection to the fake-factor derivation but dropping the jet angular requirements.

Prompt Monte Carlo processes used are W+jets, Drell–Yan, $t\bar{t}$ and single top, diboson, rare top and multiboson decays. The remaining events are described well by the fake-factor method as seen in Figure 7.9. The only considered systematic uncertainty in this region is the systematic uncertainty of the fake-factor.

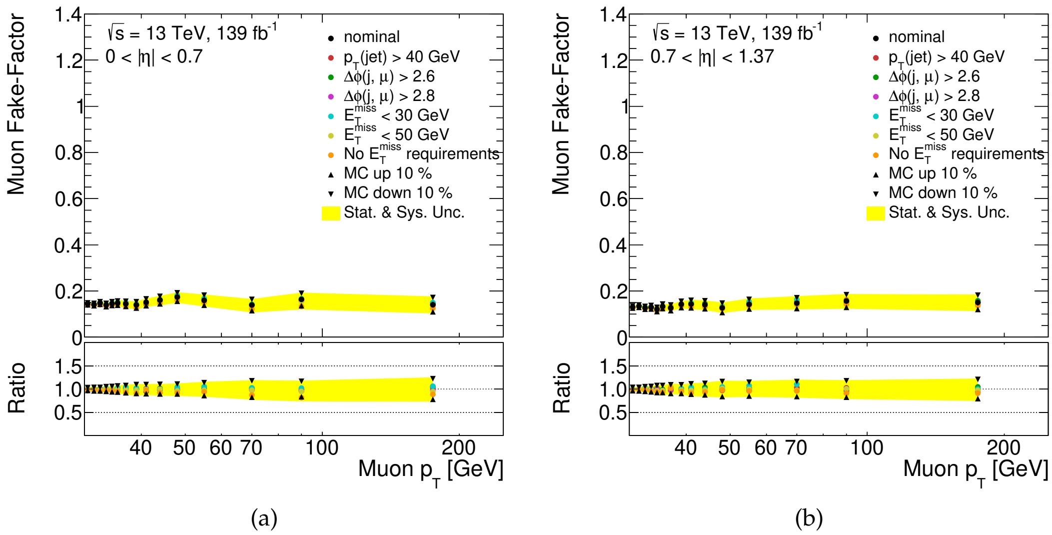

Figure 7.7: Measured muon fake-factors with systematic variations applied, (a) for the first η bin, (b) for the second η bin.

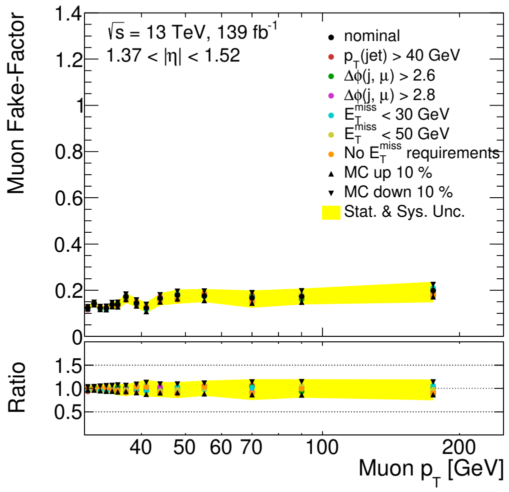

(a)

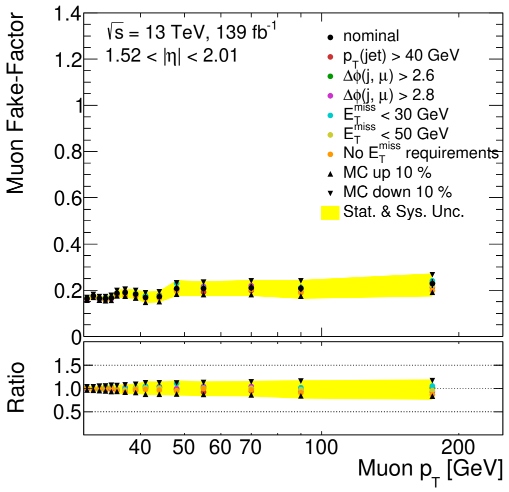

(b)

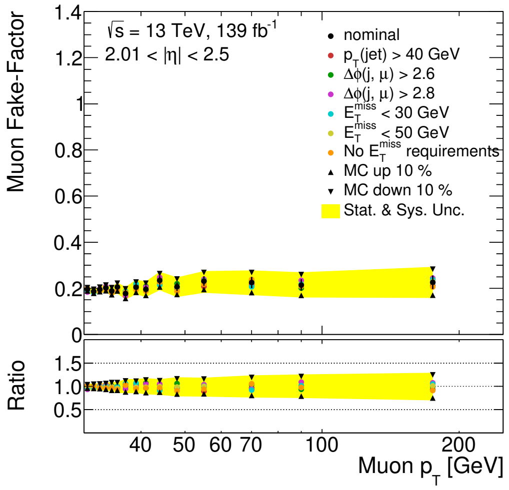

(c)

Figure 7.8: Measured muon fake-factors with systematic variations applied, (a) for the third η bin, (b) for the fourth η bin, and (c) for the last η bin.

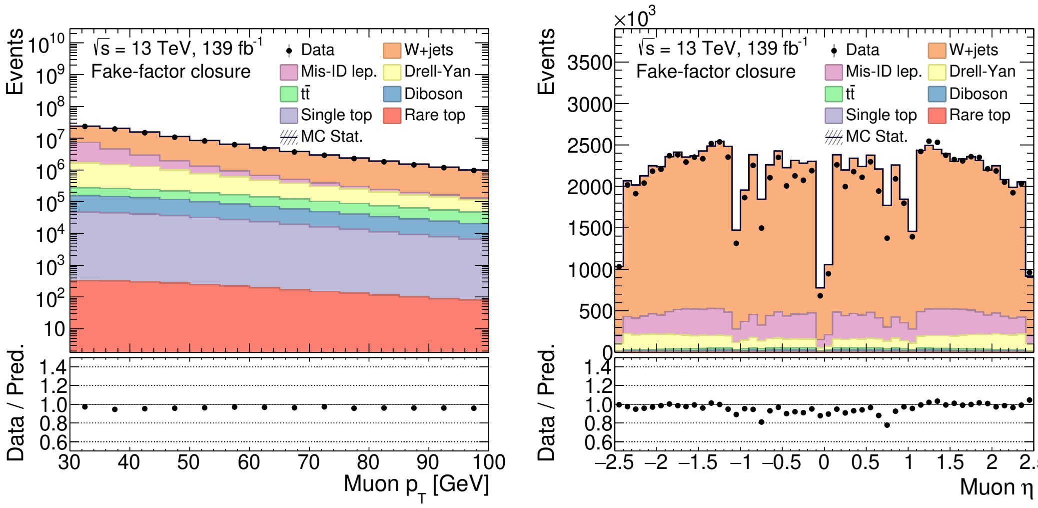

(a) (b)

Figure 7.9: The muon fake-factors closure. (a) muon p_{T} distribution, and (b) muon η distribution. The orange band shows the systematic uncertainty associated to the fake-factor measurement.

CHAPTER 8

STATISTICAL ANALYSIS AND RESULTS

The goal of the analysis is to evaluate the presence of signal in collected data and, if not present, set an upper bound on the production cross-section of the new physics process. The HISTFITTER [151] statistical framework is used, based on ROOT [152] and ROOFIT [153] frameworks. The expected signal yield is fitted in the signal regions while the the yield of the background predictions from Monte Carlo simulation is simultaneously fitted in the control regions. The validity and performance of the fit is estimated in validation regions where fitted parameters are applied.

8.1 STATISTICAL ANALYSIS

8.1.1 THE LIKELIHOOD FUNCTION

The starting point of every statistical analysis of the data is to construct a probability model $F(\mathbf{x})$ that describes the expected distribution of the studied observables, denoted as $\mathbf{x}$. The model depends on one or more physics parameters of interest (POIs), commonly denoted as $\boldsymbol{\mu}$. In the case of searches for BSM physics the process cross-section or the new particle mass are a common POIs, both also used for this analysis. The probability to observe data $\mathbf{x}_{\text{obs}}$ under the probability model is called the *likelihood* $L(\mathbf{x}\,|\,\boldsymbol{\mu})$.

Various uncertainties can be introduced in the likelihood as new model parameters $\boldsymbol{\theta}$. These uncertain degrees of freedom are generally referred to as *nuisance parameters* (NPs) to distinguish them from the parameters of interest. The response model of the physics measurement taking nuisance parameters into account can then be formulated. As a specific uncertainty can not be measured for all values of θ, for example experimental systematic uncertainties are estimated from dedicated calibration measurements. This information can be fully encoded in a separate *subsidiary* likelihood function $L_{\text{subs}}(\tilde{\theta}_{\text{obs}} \,|\, \theta)$, where $\tilde{\theta}_{\text{obs}}$ represents the data of the calibration measurement and θ is the nuisance parameter constrained by the measurement. The full likelihood function can be written as

$$L(\mathbf{x}, \tilde{\boldsymbol{\theta}} \,|\, \boldsymbol{\mu}, \boldsymbol{\theta}) = L_{\text{phys}}(\mathbf{x} \,|\, \boldsymbol{\mu}, \boldsymbol{\theta}) L_{\text{subs}}(\tilde{\boldsymbol{\theta}} \,|\, \boldsymbol{\theta}) \,. \tag{8.1}$$

The subsidiary likelihood function for a NP θ is commonly approximated by a Gaussian approximation

$$L_{\text{subs, Gauss}}(\tilde{\theta} \,|\, \theta) = \text{Gauss}(\tilde{\theta}|\theta, \sigma_\theta) \,, \tag{8.2}$$

where σ_θ is an uncertainty in θ. A Maximum Likelihood fit gives the estimates $\hat{\theta}$ and $\hat{\sigma}_\theta$. Additionally the likelihood is reduced to a unit Gaussian($\tilde{\alpha} = 0, \alpha, 1$), with $\alpha \equiv (\theta - \hat{\theta})/\hat{\sigma}_\theta$. The likelihood function from Eq. 8.1 reduces to

$$L_{\text{pll}}(\mathbf{x} \,|\, \boldsymbol{\mu}, \boldsymbol{\alpha}) = L_{\text{phys}}(\mathbf{x} \,|\, \boldsymbol{\mu}, \boldsymbol{\alpha}) \prod_{\alpha} L_{\text{Gauss}}(0, \alpha, 1) \tag{8.3}$$

and is usually called a *profile likelihood*. The physics response is modelled using a Poisson probability density function describing the observed number of events. In case of a binned likelihood with one POI μ affecting the expected signal yield, this term can be written as

$$L_{\text{phys}} = \prod_{i}^{\text{bins}} L_{\text{Poisson}}(N^i_{\text{data}} \,|\, \mu S^i(\boldsymbol{\alpha}) + B^i(\boldsymbol{\alpha})) \,, \tag{8.4}$$

where N^i_{data} is the observed number of data events in the i-th bin, S_i the expected signal yield, and B_i the expected background yield in the same bin.

Usually only a few values of nuisance parameters are available, most commonly only the central value and one sigma variations ($\alpha = -1, 0, 1$). The likelihood function is defined over the whole range of α so the functional dependence needs to be interpolated and extrapolated. For this analysis exponential extrapolation is used to avoid negative yields and interpolation using a fifth order polynomial to avoid discontinuities at the transition [154].

8.1.2 HYPOTHESIS TESTING

To test a hypothesised value of μ a discriminating test-statistic q_μ is defined as

$$q_\mu = -2 \ln \left(\frac{L(\mu, \hat{\hat{\boldsymbol{\theta}}}_\mu)}{L(\hat{\mu}, \hat{\boldsymbol{\theta}})} \right) , \tag{8.5}$$

where the denominator $L(\hat{\mu}, \hat{\boldsymbol{\theta}})$ is the maximised unconditional likelihood function with μ and $\boldsymbol{\theta}$ the values at the maximum. The nominator $L(\mu, \hat{\hat{\boldsymbol{\theta}}}_\mu)$ represents is the maximised conditional likelihood for a value of μ. The closer the values of the test-statistic are to zero, the better the proposed hypothesis agrees with the data. To quantify the level of agreement the p-value is computed, defined as

$$p_\mu = \int_{q_\mu^{\mathrm{obs}}}^{\infty} f(q_\mu \,|\, \mu)\, \mathrm{d}q_\mu \,, \tag{8.6}$$

where q_μ^{obs} is the value of the test-statistic observed in data and $f(q_\mu \,|\, \mu)$ the probability density (PDF) function of q_μ under the assumption of the signal strength μ. The value of the PDF is determined using a Monte Carlo generation of pseudo-experiments which is computationally very intensive. Asymptotic formulae [142] can be used instead when data statistics are sufficient.

The first step is to check for the presence of the signal by rejecting the $\mu = 0$ hypothesis, also called the background hypothesis (B). The disagreement is quantified with the p_0-value, representing the probability for the background to fluctuate and give the observed measurement. A lower p_0-value thus represents more significant deviations from the background prediction. In case of a good agreement the p_0-value is 0.5. In such case, upper limits on the signal production cross-section are derived at the 95% confidence level using the $\mathrm{CL_s}$ method [155]. The signal plus background hypothesis (S+B) is tested for multiple values of μ for a given set of physics model parameters. By the definition of the test-statistic q_μ, the probability of a background only hypothesis p_{B} is defined for values lower than the observed value, and the probability of a S+B hypothesis $p_{\mathrm{S+B}}$ for values higher than the observed value q_μ^{obs}.

$$p_{\mathrm{B}} = P(q_\mu < q_\mu^{\mathrm{obs}} \,|\, \mathrm{B}) = \int_{-\infty}^{q_\mu^{\mathrm{obs}}} f(q_\mu \,|\, \mathrm{B})\, \mathrm{d}q_\mu \tag{8.7}$$

$$p_{\mathrm{S+B}} = P(q_\mu > q_\mu^{\mathrm{obs}} \,|\, \mathrm{S+B}) = \int_{q_\mu^{\mathrm{obs}}}^{\infty} f(q_\mu \,|\, \mathrm{S+B})\, \mathrm{d}q_\mu \tag{8.8}$$

To exclude the signal strength μ at 95% C.L. the following needs to hold:

$$\mathrm{CL_s} \equiv \frac{p_{\mathrm{S+B}}}{1 - p_{\mathrm{B}}} < 5\% \tag{8.9}$$

The equation Eq. 8.9 can be interpreted as the probability that the signal+background hypothesis gives a background-like fluctuation given that the background only hypothesis gave a background-like test-statistic. Example distributions of the test statistic with probabilities entering the $\mathrm{CL_s}$ calculation is shown in Figure 8.1. For expected limits the probability is computed using the median of the background hypothesis test-statistic distribution as the observed value, while for the observed limits, the observed value is determined from measured data.

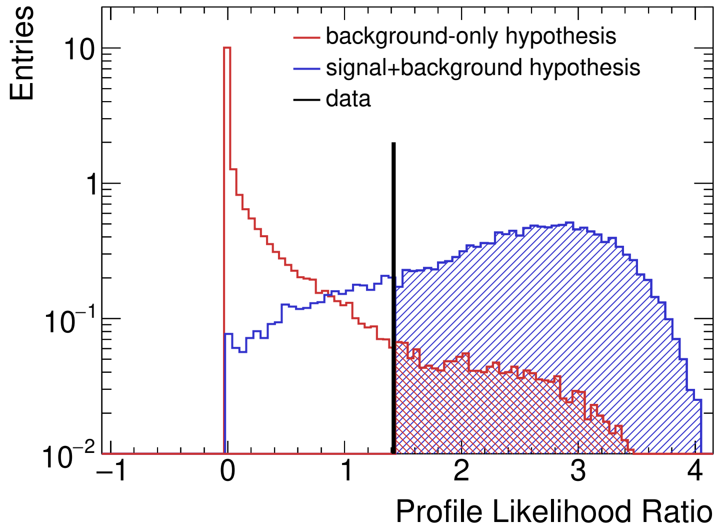

Figure 8.1: Example of distributions of the profile likelihood ratio, where the red histogram represents a background-only hypothesis and the blue histogram a signal+background hypothesis. The observed value in data is shown with a black line. Hatched areas illustrate probabilities entering the $\mathrm{CL_s}$ calculation, $p_{\mathrm{S+B}}$ in blue and $1 - p_B$ in red.

8.2 Results of the Cut-based Analysis Strategy

The final normalisations of $t\bar{t}$ and diboson MC samples are not taken from MC calculations but are derived in the simultaneous likelihood fit to the data in dedicated Top and Diboson CRs, as introduced in Section 6.2. Consequently, additional free parameters in the likelihood are introduced for the $t\bar{t}$ and the diboson background contributions, to fit their yields in the analysis Top and Diboson control regions, respectively. Fitting the yields of the largest backgrounds reduces the systematic uncertainty in the predicted yield from SM sources. The fitted normalisation scales are compatible with their SM predictions within the uncertainties and are listed in Table 8.1. Post-fit binned distributions of $H_{\mathrm{T}} + E_{\mathrm{T}}^{\mathrm{miss}}$ in the control regions are shown in Figures 8.2 and 8.3. The obtained normalisation is evaluated in the m_{jj} VRs. Good agreement between data and prediction is observed as seen in Figures 8.4 and 8.5. Additional selected distributions are shown in Appendix B.

The final assessment of systematic uncertainties $\boldsymbol{\theta}$ as determined by the fit is performed by looking at the post-fit values of α, in units of standard deviations. Both the nominal value and the uncertainties should not move significantly from their predicted values. That would indicate a suboptimal uncertainty estimate that has been shifted to a better value by the fit. Figure 8.6 outlines the uncertainties in the full likelihood fit. To validate the fit performance in case of potential signal, the MC prediction with injected signal

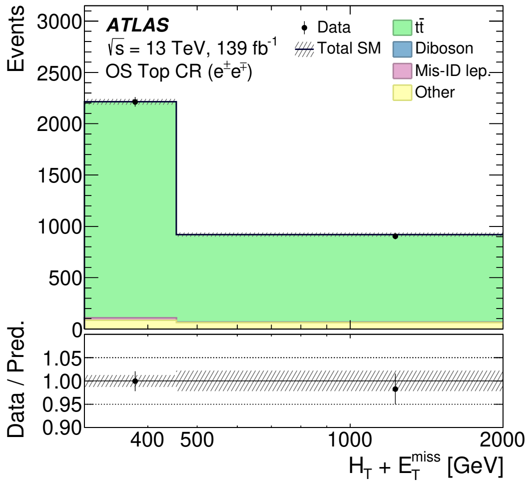

(a)

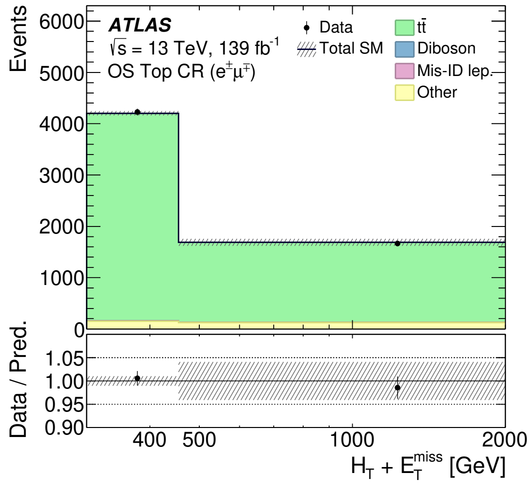

(b)

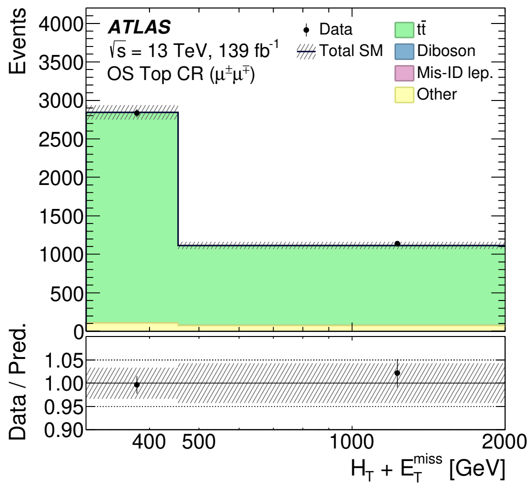

(c)

Figure 8.2: Post-fit distributions of $H_T + E_T^{miss}$ in cut-based Top control regions, namely (a) the electron–electron control region, (b) the electron–muon control region, and (c) the muon–muon control region. The hatched bands include all systematic uncertainties after the background-only fit with the correlations between various sources taken into account. Taken from Ref. [143].

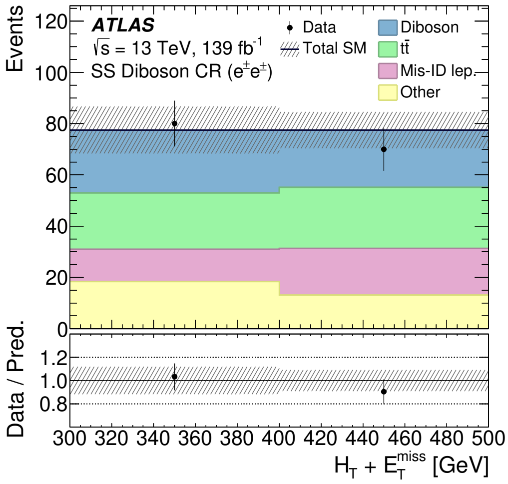

(a)

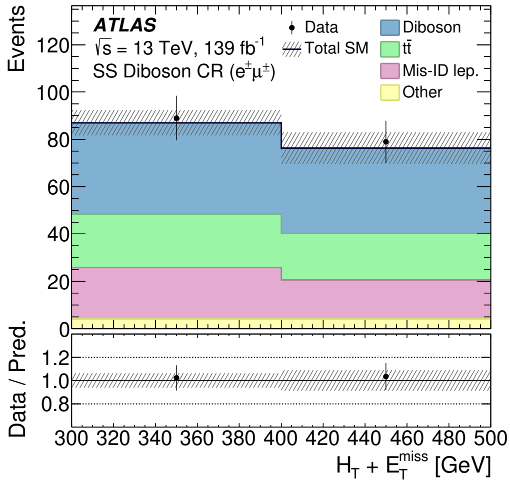

(b)

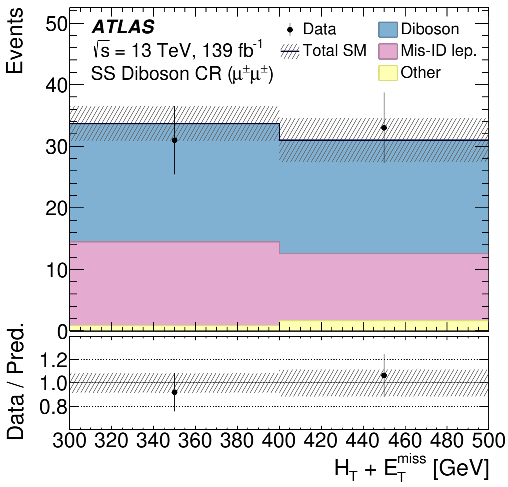

(c)

Figure 8.3: Post-fit distributions of $H_\mathrm{T} + E_\mathrm{T}^\mathrm{miss}$ in Diboson control regions, namely (a) the electron–electron control region, (b) the electron–muon control region, and (c) the muon–muon control region. The hatched bands include all systematic uncertainties after the background-only fit with the correlations between various sources taken into account. Taken from Ref. [143].

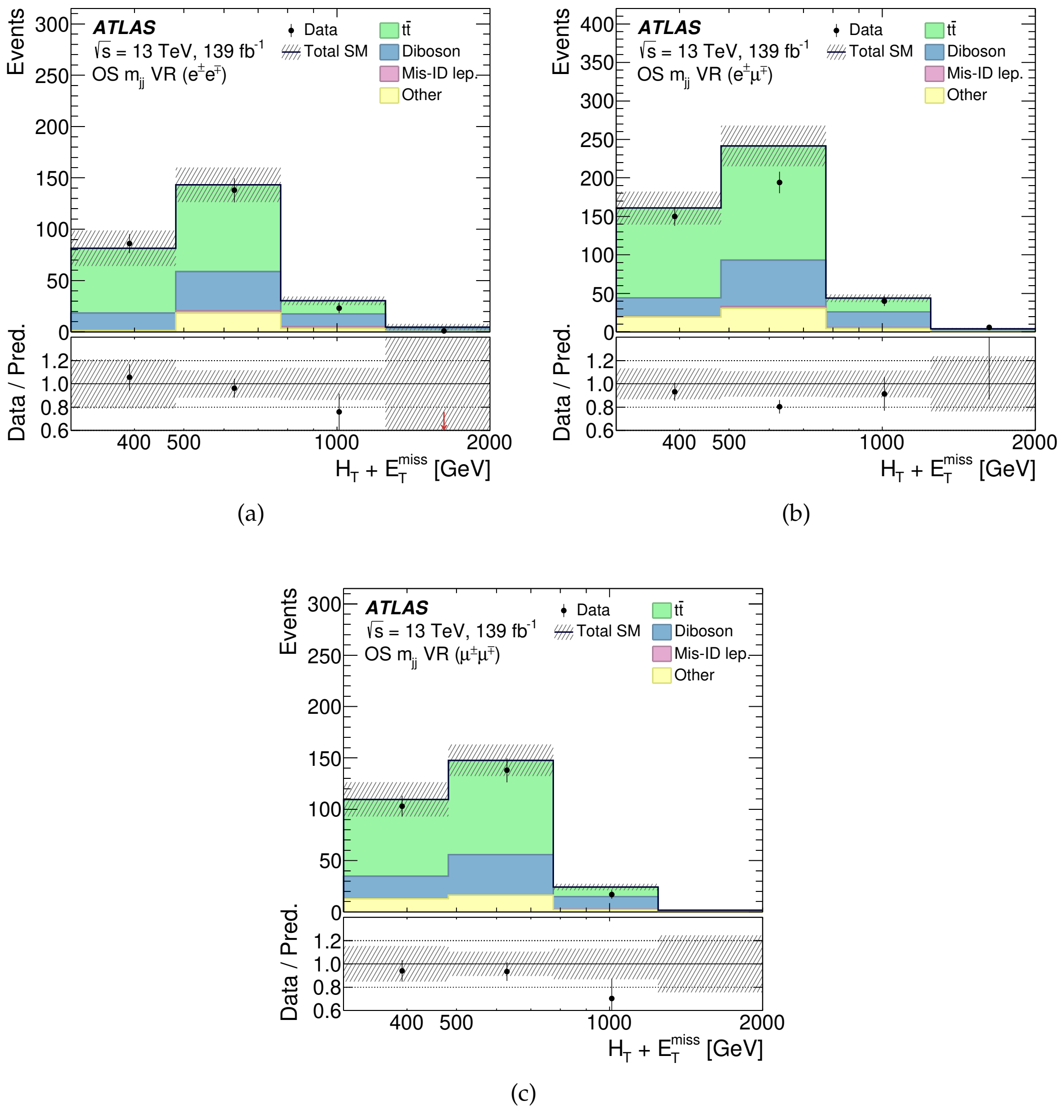

Figure 8.4: Post-fit distributions of $H_{\mathrm{T}} + E_{\mathrm{T}}^{\mathrm{miss}}$ in opposite-sign m_{jj} validation regions, namely (a) the electron–electron validation region and (b) the electron–muon validation region, and (c) the muon–muon validation region. The hatched bands include all systematic uncertainties after the background-only fit with the correlations between various sources taken into account. Taken from Ref. [143].

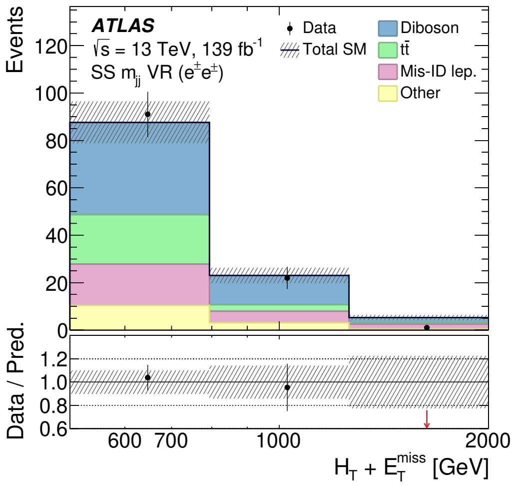

(a)

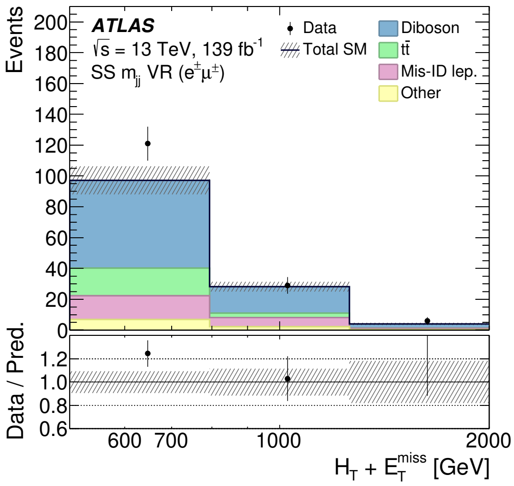

(b)

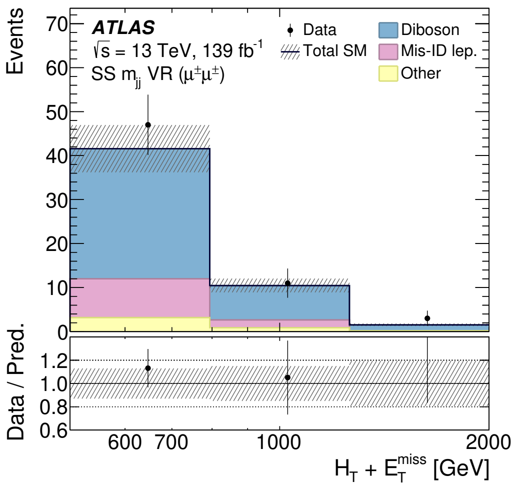

(c)

Figure 8.5: Post-fit distributions of $H_{\mathrm{T}} + E_{\mathrm{T}}^{\mathrm{miss}}$ in same-sign m_{jj} validation regions, namely (a) the electron–electron validation region, (b) the electron–muon validation region, and (c) the muon–muon validation region. The hatched bands include all systematic uncertainties after the background-only fit with the correlations between various sources taken into account. Taken from Ref. [143].

Table 8.1: Diboson and $t\bar{t}$ background normalisation scales using the cut-based analysis strategy with their uncertainties.

Background	**Normalisation scale**
Diboson	1.03 ± 0.19
$t\bar{t}$	0.96 ± 0.02

events is used in signal regions instead of the measured data. No significant deviations from the prediction are observed.

The effect of statistical and systematic uncertainties on the signal yield parameter of interest μ_{sig} is evaluated by fixing one nuisance parameter at the time to its $\pm 1\,\sigma$ variations and minimizing the likelihood function. After the fit, the impact on μ_{sig} is inspected with regard to the nominal fit where all parameters are free. Again, the corresponding fits have real data in all but signal regions, where the MC prediction with injected signal events is used. The dominant uncertainties are presented in Figure 8.7, where statistics-only uncertainty affects the signal yield for more than 40%. The dominant systematics uncertainties are the electron identification efficiency uncertainty and fake-factor uncertainties reaching 5%.

The total relative systematic uncertainty in the background after the fit, and its break-down into components, is presented in Figure 8.8. One can see that the contributions of

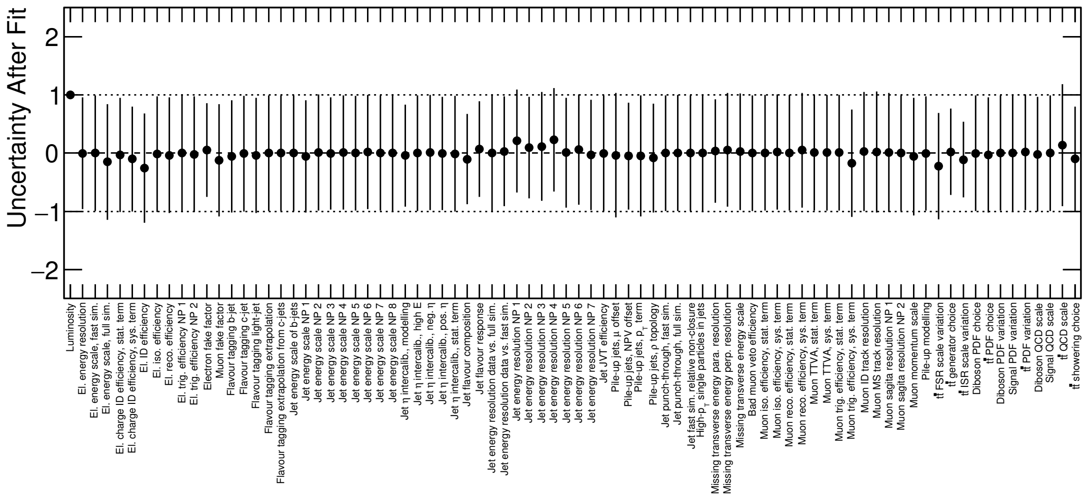

Figure 8.6: Post-fit nuisance parameters of the full likelihood fit in the cut-based scenario with real data in all but signal regions, expressed in units of standard deviation.

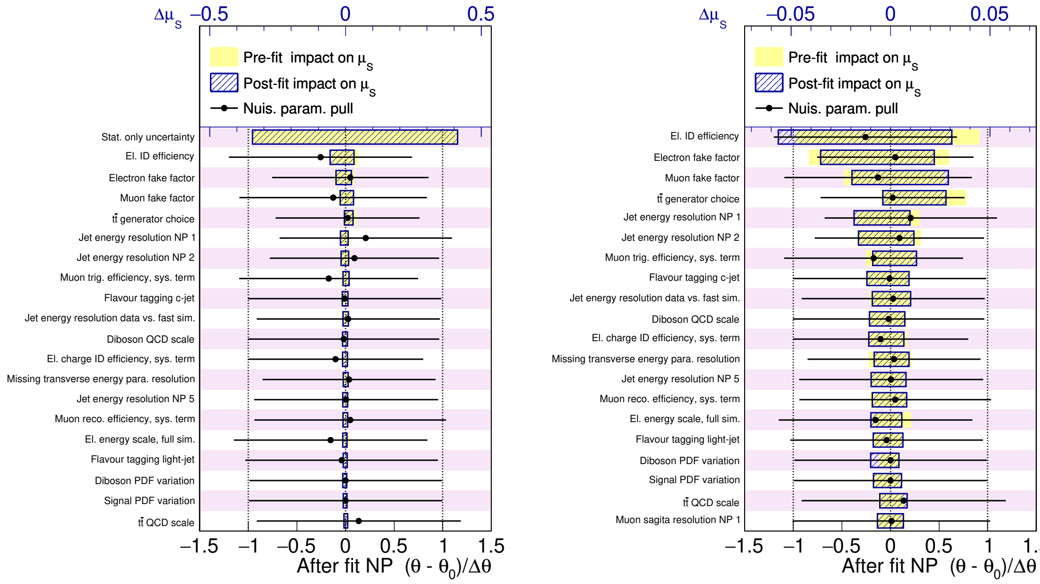

(a) (b)

Figure 8.7: Impact of systematic uncertainties on μ_{sig} in the cut-based scenario, (a) showing the impact of the dominant systematic sources and MC statistical uncertainty and (b) showing only the impact of the dominant systematic sources. Post-fit values of α are displayed with black points.

theoretical and experimental uncertainties in the SR are both of the order of 10%. One of the dominant uncertainties is due to the limited MC statistics of the simulated samples, which nevertheless gets reduced in the final fit combination, yielding a total uncertainty of less than 20%.

Once the stability of the fit is ensured and uncertainties modelling is validated, measured data are fitted on the expected background in signal regions allowing expected new physics with the parameter of interest μ_{sig}. After the fit, the compatibility between the data and the expected background in signal regions is assessed and good agreement is observed, with a p_0-value of 0.5 for the background-only hypothesis. Figure 8.9 shows a good agreement within the uncertainties between expected background and observed events in all the regions and channels considered in the analysis. The level of agreement between the data and background predictions in the CR and VR, well within the statistical and systematic uncertainties, demonstrates the validity of the used background estimation procedures.

Post-fit binned distributions of $H_{\text{T}} + E_{\text{T}}^{\text{miss}}$ are shown in Figures 8.10 and 8.11 for the signal regions with representative expected signal distributions overlaid. Predicted numbers of background events in signal regions are listed together with the observed

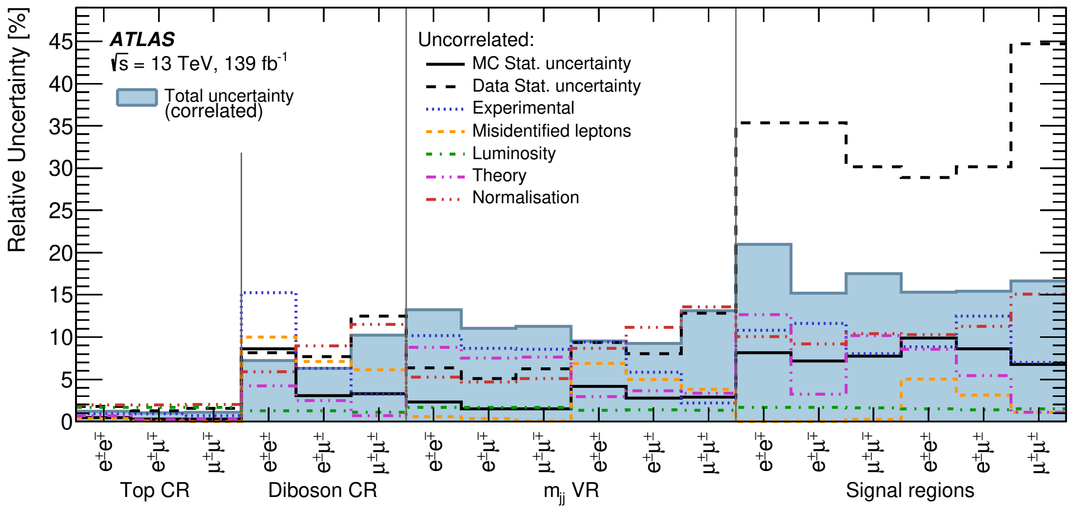

Figure 8.8: Relative contributions of different sources of statistical and systematic uncertainty in the total background yield estimation after the fit in the cut-based scenario. Systematic uncertainties are calculated in an uncorrelated way by shifting in turn only one nuisance parameter from the post-fit value by one standard deviation, keeping all the other parameters at their post-fit values, and comparing the resulting event yield with the nominal yield. Individual uncertainties can be correlated, and do not necessarily add in quadrature to the total background uncertainty, which is indicated by "Total uncertainty". Taken from Ref. [143].

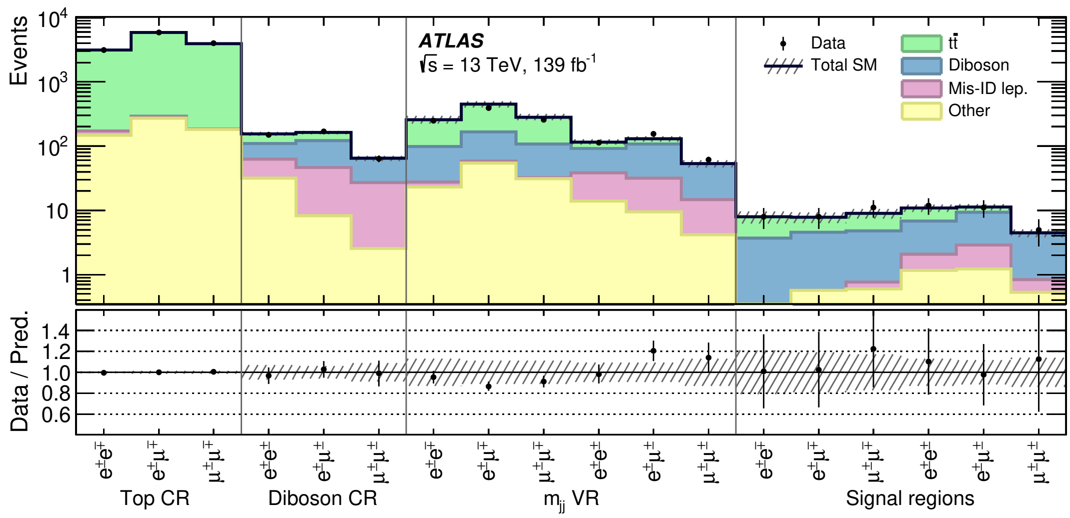

Figure 8.9: The numbers of observed and expected events in the control, validation, and signal regions for all considered channels in the cut-based scenario, split by flavour and electric charge combination. The background expectation is the result of the background-only fit described in the text. The hatched bands include all post-fit systematic uncertainties with the correlations between various sources taken into account. Taken from Ref. [143].

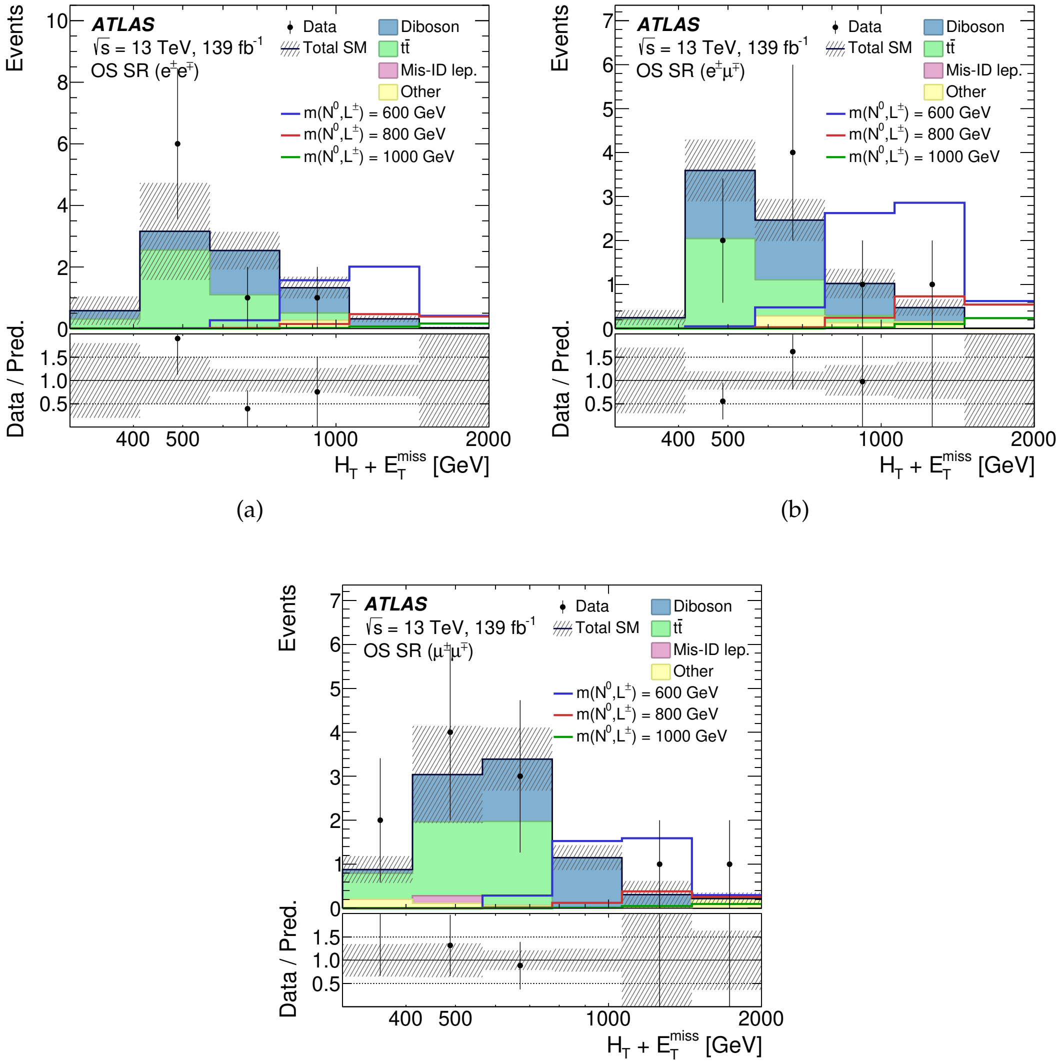

(a) (b) (c)

Figure 8.10: Post-fit distributions of $H_{\mathrm{T}} + E_{\mathrm{T}}^{\mathrm{miss}}$ in opposite-sign cut-based signal regions, namely (a) the electron–electron signal region, (b) the electron–muon signal region, and (c) the muon–muon signal region after the background-only fit described in the text. The hatched bands include all systematic uncertainties post-fit with the correlations between various sources taken into account. The coloured lines correspond to signal samples with the N^0 and $L^{\pm}$ mass stated in the legend. Taken from Ref. [143].

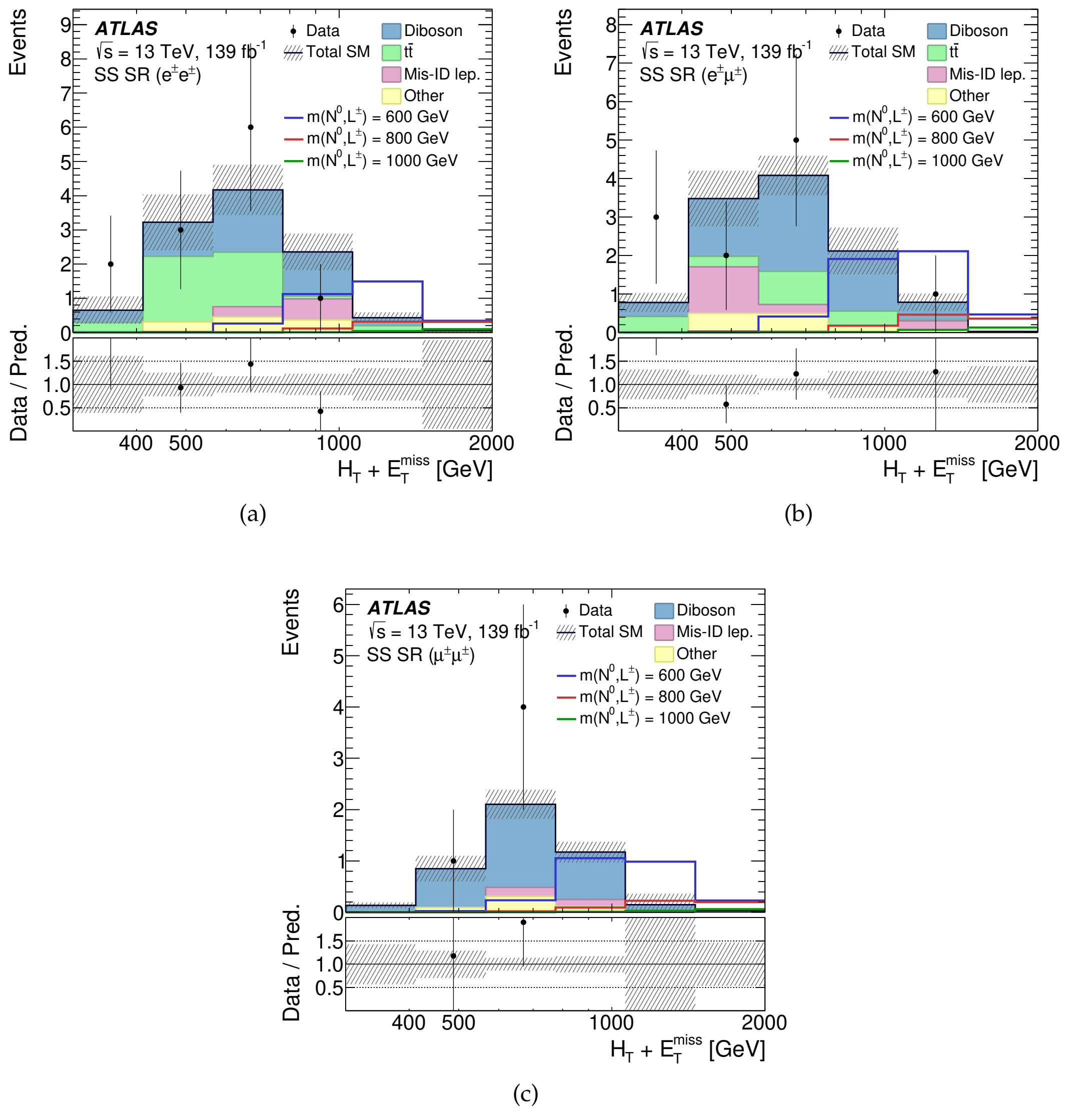

Figure 8.11: Post-fit distributions of $H_{\mathrm{T}} + E_{\mathrm{T}}^{\mathrm{miss}}$ in same-sign cut-based signal regions, namely (a) the electron–electron signal region, (b) the electron–muon signal region, and (c) the muon–muon signal region after the background-only fit described in the text. The hatched bands include all systematic uncertainties post-fit with the correlations between various sources taken into account. The coloured lines correspond to signal samples with the N^0 and $L^\pm$ mass stated in the legend. Taken from Ref. [143].

Table 8.2: The number of expected background events in cut-based signal regions after the likelihood fit, compared with the data. Uncertainties correspond to the total uncertainties in the predicted event yields, and are smaller for the total than for the individual contributions summed in quadrature because the latter are anti-correlated. Due to rounding the totals can differ from the sums of components. $t\bar{t}$ and diboson normalisations are allowed to float in the fit. For the reference purpose, representative signal yields and their errors for signal masses $m(N^0, L^\pm)$, denoted by m in the table, are shown in the bottom part of the table.

Signal regions	**OS $e^\pm e^\mp$**	**OS $e^\pm \mu^\mp$**	**OS $\mu^\pm \mu^\mp$**
Observed events	8	8	11
Total background	7.9 ± 1.7	7.8 ± 1.5	9.0 ± 1.5
$t\bar{t}$	4.2 ± 2.5	3.3 ± 1.2	4.2 ± 1.2
Diboson	3.4 ± 1.5	3.99 ± 0.60	4.03 ± 0.60
Other	0.31 ± 0.27	0.56 ± 0.29	0.60 ± 0.45
Fakes	0.0049 ± 0.0005	0.0051 ± 0.0005	0.17 ± 0.03
Signal expectation			
$m = 600\,\text{GeV}$	4.26 ± 0.31	6.64 ± 0.44	3.71 ± 0.23
$m = 800\,\text{GeV}$	1.02 ± 0.10	1.56 ± 0.15	0.78 ± 0.06
$m = 1000\,\text{GeV}$	0.24 ± 0.03	0.37 ± 0.04	0.17 ± 0.02
Signal regions	**SS $e^\pm e^\pm$**	**SS $e^\pm \mu^\pm$**	**SS $\mu^\pm \mu^\pm$**
Observed events	12	11	5
Total background	10.9 ± 1.4	11.3 ± 1.3	4.44 ± 0.63
$t\bar{t}$	4.0 ± 1.2	1.98 ± 0.57	—
Diboson	4.8 ± 1.0	6.4 ± 1.3	3.60 ± 0.52
Other	1.17 ± 0.12	1.24 ± 0.16	0.53 ± 0.20
Fakes	0.92 ± 0.35	1.65 ± 0.34	0.31 ± 0.04
Signal expectation			
$m = 600\,\text{GeV}$	3.24 ± 0.27	4.94 ± 0.34	2.53 ± 0.14
$m = 800\,\text{GeV}$	0.76 ± 0.08	1.03 ± 0.11	0.53 ± 0.04
$m = 1000\,\text{GeV}$	0.15 ± 0.02	0.22 ± 0.03	0.10 ± 0.01

Table 8.3: The number of expected background events in the cut-based Top control regions after the likelihood fit, compared with the data. Uncertainties correspond to the total uncertainties in the predicted event yields, and are smaller for the total than for the individual contributions summed in quadrature because the latter are anti-correlated. Due to rounding the totals can differ from the sums of components. $t\bar{t}$ and diboson normalisations are allowed to float in the fit.

Top CR	**OS $e^{\pm}e^{\mp}$**	**OS $e^{\pm}\mu^{\mp}$**	**OS $\mu^{\pm}\mu^{\mp}$**
Observed events	3116	5893	3973
Total background	3133 ± 32	5893 ± 80	3959 ± 58
$t\bar{t}$	2960 ± 31	5603 ± 76	3774 ± 50
Diboson	1.8 ± 1.1	2.02 ± 0.48	1.48 ± 0.30
Other	149 ± 14	273 ± 14	182 ± 15
Fakes	23.1 ± 7.1	15.0 ± 3.1	1.91 ± 0.21

Table 8.4: The number of expected background events in the Diboson control regions after the likelihood fit, compared with the data. Uncertainties correspond to the total uncertainties in the predicted event yields, and are smaller for the total than for the individual contributions summed in quadrature because the latter are anti-correlated. Due to rounding the totals can differ from the sums of components. $t\bar{t}$ and diboson normalisations are allowed to float in the fit.

Diboson CR	**SS $e^{\pm}e^{\pm}$**	**SS $e^{\pm}\mu^{\pm}$**	**SS $\mu^{\pm}\mu^{\pm}$**
Observed events	150	168	64
Total background	155 ± 11	163.3 ± 9.8	64.7 ± 5.8
$t\bar{t}$	45.8 ± 7.1	42.3 ± 7.1	—
Diboson	46.9 ± 6.0	75 ± 10	37.6 ± 6.0
Other	31 ± 11	8.2 ± 1.3	2.58 ± 0.42
Fakes	31 ± 11	38.2 ± 7.5	24.5 ± 3.3

Table 8.5: The number of expected background events in the m_{jj} validation regions after the likelihood fit, compared with the data. Uncertainties correspond to the total uncertainties in the predicted event yields, and are smaller for the total than for the individual contributions summed in quadrature because the latter are anti-correlated. Due to rounding the totals can differ from the sums of components. $t\bar{t}$ and diboson normalisations are allowed to float in the fit.

m_{jj} **VR**	**OS** $e^{\pm}e^{\mp}$	**OS** $e^{\pm}\mu^{\mp}$	**OS** $\mu^{\pm}\mu^{\mp}$
Observed events	248	390	258
Total background	260 $\pm$ 34	450 $\pm$ 50	283 $\pm$ 32
$t\bar{t}$	161 $\pm$ 30	284 $\pm$ 47	176 $\pm$ 29
Diboson	71 $\pm$ 14	108 $\pm$ 21	75 $\pm$ 14
Other	23 $\pm$ 15	54.6 $\pm$ 9.9	31.2 $\pm$ 4.5
Fakes	4.6 $\pm$ 1.6	4.2 $\pm$ 1.6	0.95 $\pm$ 0.18
m_{jj} **VR**	**SS** $e^{\pm}e^{\pm}$	**SS** $e^{\pm}\mu^{\pm}$	**SS** $\mu^{\pm}\mu^{\pm}$
Observed events	114	156	61
Total background	116 $\pm$ 11	129 $\pm$ 12	53.6 $\pm$ 7.0
$t\bar{t}$	24.5 $\pm$ 6.4	21.1 $\pm$ 6.0	—
Diboson	53 $\pm$ 10	77 $\pm$ 15	38.8 $\pm$ 7.5
Other	14.0 $\pm$ 3.3	9.4 $\pm$ 1.0	4.18 $\pm$ 0.33
Fakes	24.2 $\pm$ 8.0	22.0 $\pm$ 6.6	10.6 $\pm$ 2.1

number of events in data in Table 8.2, where also expected signal yields for several mass points are given for comparison. Furthermore, the number of events in control and validation regions are listed in Tables 8.3–8.5.

In absence of a significant deviation from expectations within uncertainties, 95% confidence level upper limits on the signal production cross-section are derived using the $\mathrm{CL_s}$ method. Pseudo-experiments are used to set the limit due to low statistics in signal regions, evaluated as a function of the heavy lepton mass. The resulting exclusion limits on the signal cross-section are shown in Figure 8.12. Consequently, comparing the upper limits on the cross-section with the theoretical model dependence of the cross-section on the heavy lepton mass, the lower mass limit on the mass of of the type-III seesaw heavy leptons N^0 and $L^{\pm}$ can be derived. The expected lower mass limit is 820^{+40}_{-60} GeV, where the uncertainties on the limit are extracted from the $\pm 1\,\sigma$ band, while the observed lower mass limit is placed at 790 GeV, excluding the mass values below this point. Sensitivity of individual channels is estimated using the asymptotic formulae and presented in Figure 8.13. The OS ee and $e\mu$ channels are the most sensitive ones as SS channels do not have enough statistics. On the other hand OS $\mu\mu$ is the least sensitive channel.

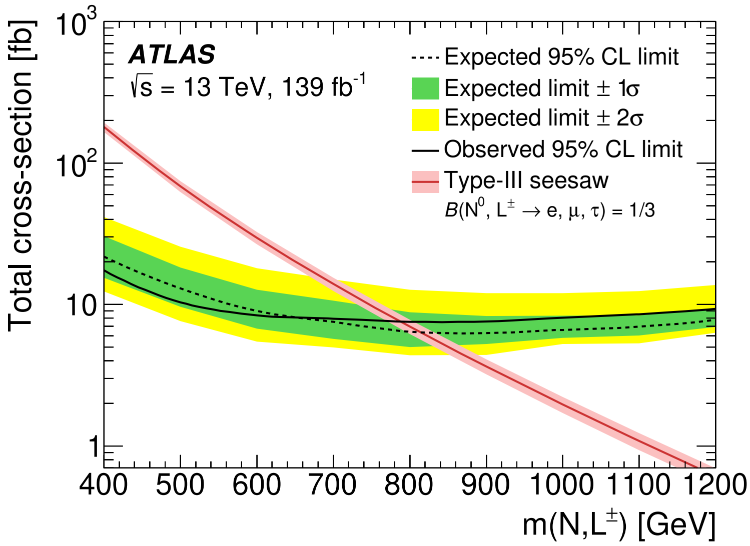

Figure 8.12: Expected and observed 95% CL_s exclusion limits in the cut-based scenario for the type-III seesaw process with the corresponding one- and two-standard-deviation bands, showing the 95% CL upper limit on the cross-section. The theoretical signal cross-section prediction, given by the NLO calculation, is shown as a red line with the corresponding uncertainty band. Taken from Ref. [143].

Given the low statistics as a result of very tight cuts applied in the signal regions asymptotic formulae might do worse job as they have problems approximating the likelihood function as distributions are less smooth. A comparison with pseudo-experiments is presented in Figure 8.14. Both expected and observed limits are slightly worse but well inside $1\,\sigma$ uncertainties. What is more notable is that uncertainty bands on the expected limit are reduced significantly, especially the lower band. Lower bands estimate how much the limit can still be improved over the central value which is limited by the minimum number of events that are needed to still set the limit. If no events are expected a limit can not be set at 95% confidence level if the number of observed events is below 3. The statistics-limited analysis can thus can not give arbitrarily good limits which is not taken into account by the asymptotic formulae.

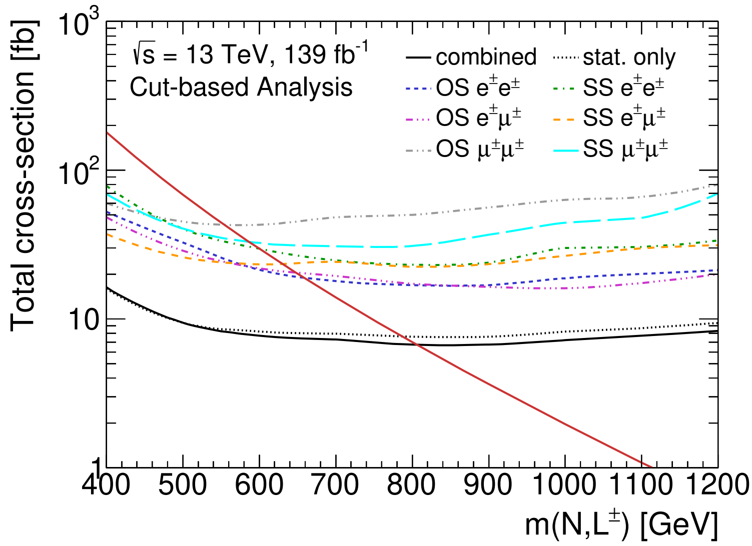

Figure 8.13: Expected and observed 95% CL$_s$ exclusion limits in the cut-based scenario for each individual channel. The theoretical signal cross-section prediction, given by the NLO calculation, is shown as a red line.

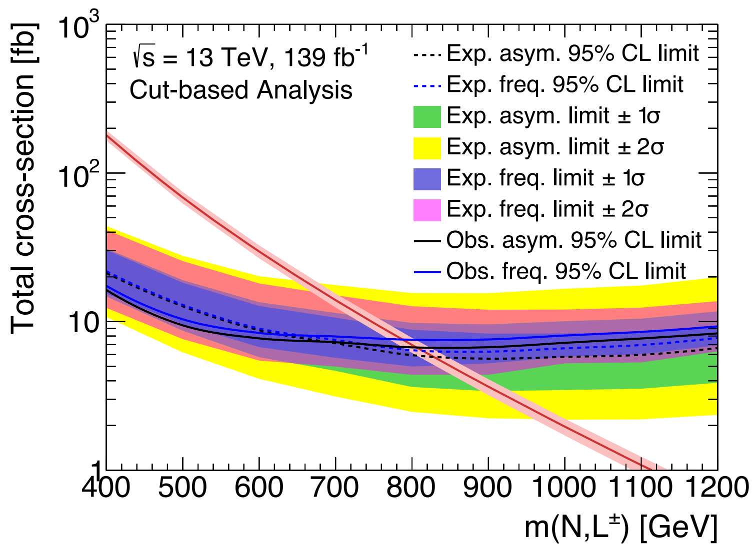

Figure 8.14: Comparison of expected and observed 95% CL$_s$ exclusion limits in the cut-based scenario using pseudo-experiments and asymptotic formulae. Pseudo-experiments are overlaid with central values shown in blue, and uncertainty bands in shades of blue and pink.

8.3 Results of the Multivariate Analysis Strategy

As in the cut-based analysis, the final normalisations of $t\bar{t}$ and diboson MC samples in the multivariate analysis are additional floating parameters in the likelihood fit. They are obtained from dedicated control regions as described in Section 6.3. A separate diboson background scaling factors are calculated for OS and SS regions as different processes contribute to each final state. Additionally each lepton flavour combination has a separate scale factor assigned. The fitted normalisation scales are close to their SM predictions, with OS diboson background differing for about 25%, and are listed in Table 8.6. Post-fit binned distributions of $H_{\mathrm{T}} + E_{\mathrm{T}}^{\mathrm{miss}}$ in the control regions are shown in Figures 8.15 and 8.17. The obtained normalisation is evaluated in the MVA VRs. Good agreement between data and prediction is observed as seen in Figures 8.18 and 8.19. Additional selected distributions are shown in Appendix C.

Table 8.6: Diboson and $t\bar{t}$ background normalisation scales using the multivariate analysis strategy with their uncertainties.

Background	**Normalisation scale**
Diboson (OS ee)	0.81 ± 0.07
Diboson (OS $e\mu$)	0.90 ± 0.06
Diboson (OS $\mu\mu$)	0.69 ± 0.06
Diboson (SS ee)	1.21 ± 0.12
Diboson (SS $e\mu$)	1.27 ± 0.06
Diboson (SS $\mu\mu$)	1.10 ± 0.08
$t\bar{t}$ (ee)	0.89 ± 0.01
$t\bar{t}$ ($e\mu$)	0.90 ± 0.01
$t\bar{t}$ ($\mu\mu$)	0.91 ± 0.01

The fit performance in case of potential signal is validated with the MC prediction with injected signal events is used in signal regions instead of the measured data. The results are presented in Figure 8.20, where several constraints are observed but with nominal values generally close to the expected ones.

The effect of statistical and systematic uncertainties on the signal yield parameter of interest μ_{sig} is presented in Figure 8.21. The statistics-only uncertainty is still dominant, but reduced for more than a half compared with the cut-based analysis to about 20%. The dominant systematics uncertainties are the choice of the $t\bar{t}$ showering procedure at 7%, followed by uncertainties in electron identification efficiencies, jet energy resolution and flavour tagging efficiencies at around 3%.

The total relative systematic uncertainty in the background after the fit, and its breakdown into components, is presented in Figure 8.22. One can see that the contributions

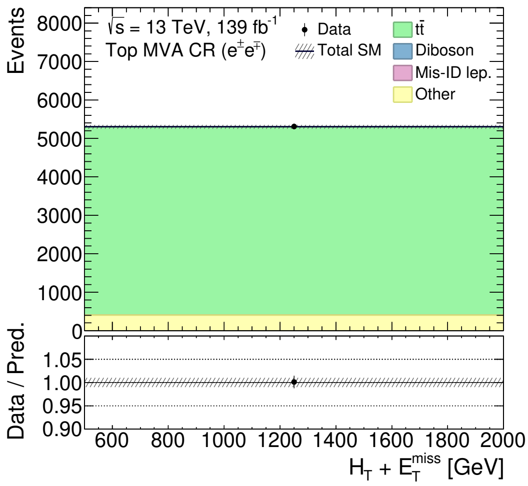

(a)

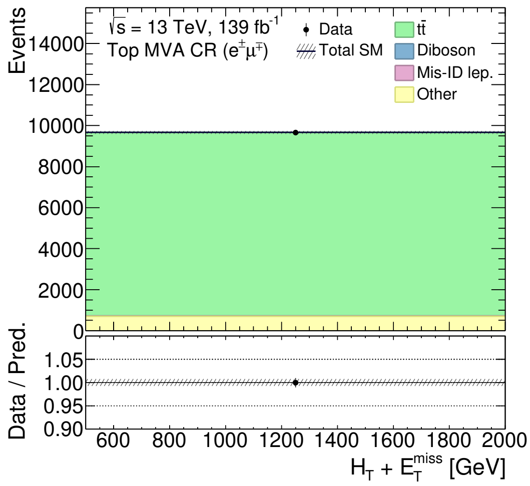

(b)

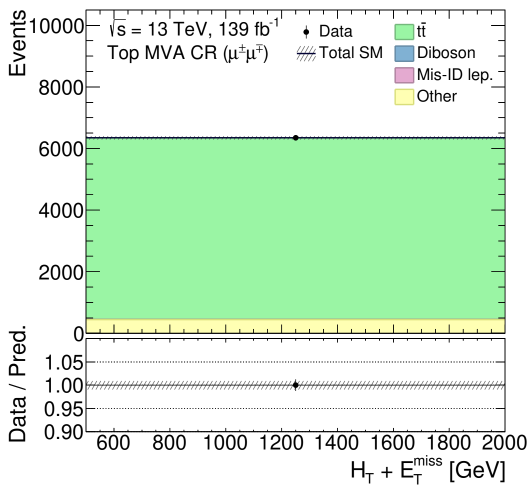

(c)

Figure 8.15: Post-fit distributions of $H_{\mathrm{T}} + E_{\mathrm{T}}^{\mathrm{miss}}$ in MVA Top control regions, namely (a) the electron–electron control region, (b) the electron–muon control region, and (c) the muon–muon control region. The hatched bands include all systematic uncertainties after the background-only fit with the correlations between various sources taken into account.

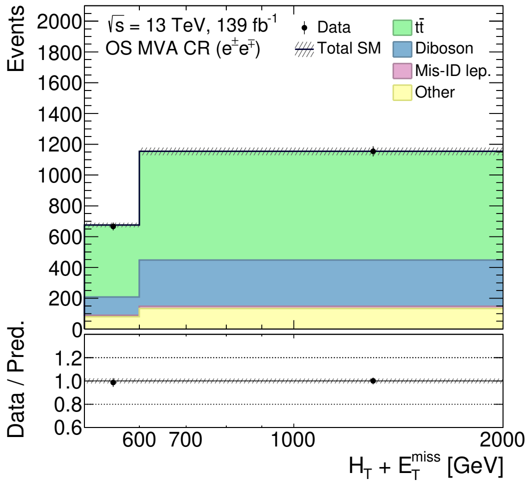

(a)

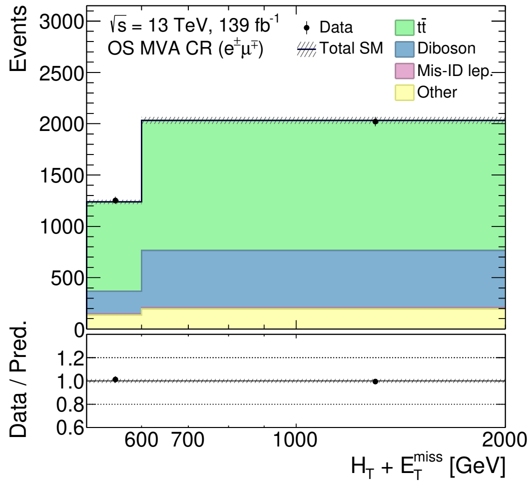

(b)

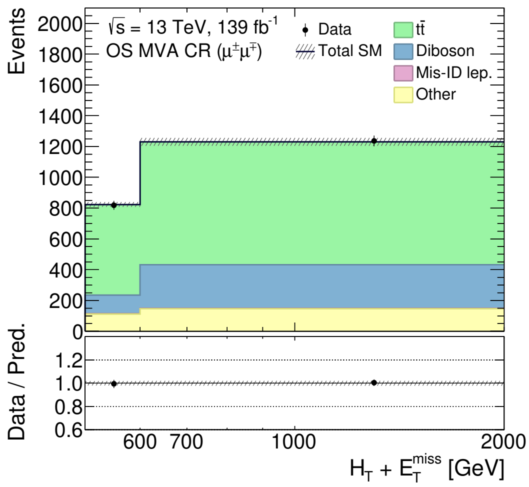

(c)

Figure 8.16: Post-fit distributions of $H_{\mathrm{T}} + E_{\mathrm{T}}^{\mathrm{miss}}$ in opposite-sign MVA control regions, namely (a) the electron–electron control region, (b) the electron–muon control region, and (c) the muon–muon control region. The hatched bands include all systematic uncertainties after the background-only fit with the correlations between various sources taken into account.

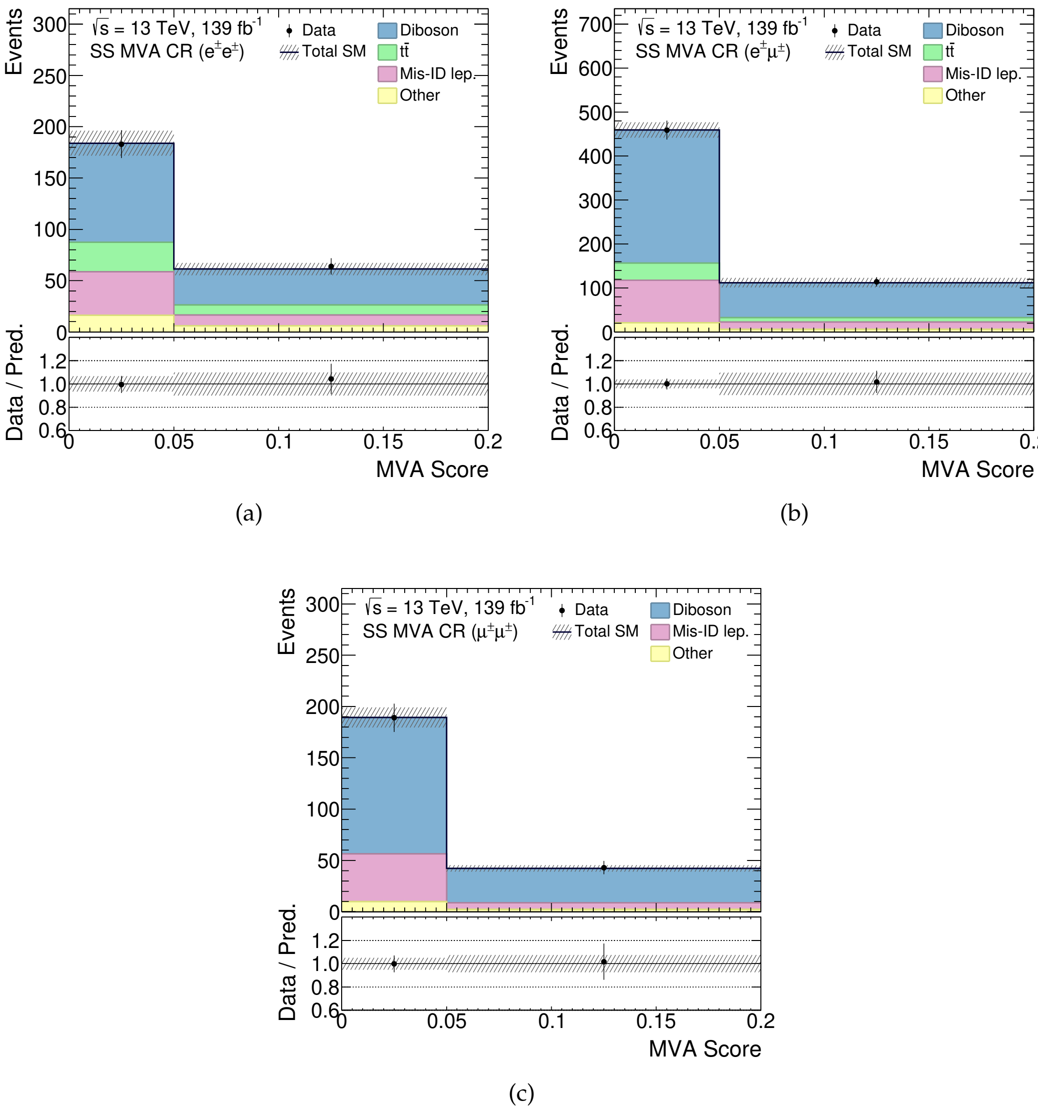

Figure 8.17: Post-fit distributions of $H_{\mathrm{T}} + E_{\mathrm{T}}^{\mathrm{miss}}$ in same-sign MVA control regions, namely (a) the electron–electron control region, (b) the electron–muon control region, and (c) the muon–muon control region. The hatched bands include all systematic uncertainties after the background-only fit with the correlations between various sources taken into account.

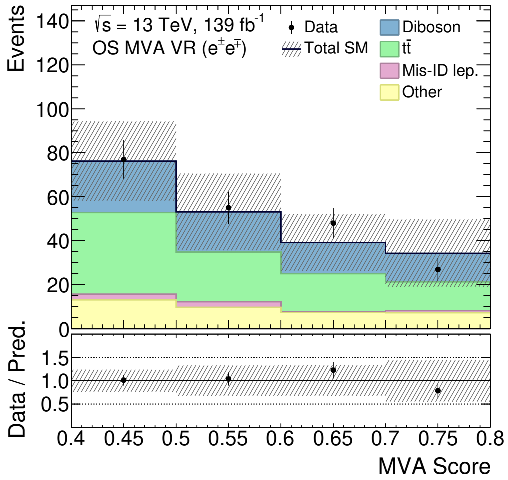

(a)

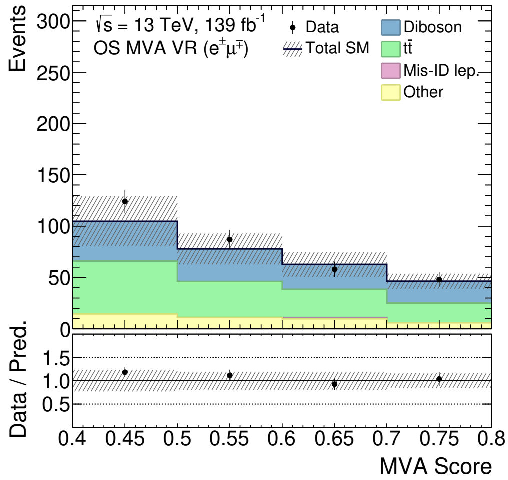

(b)

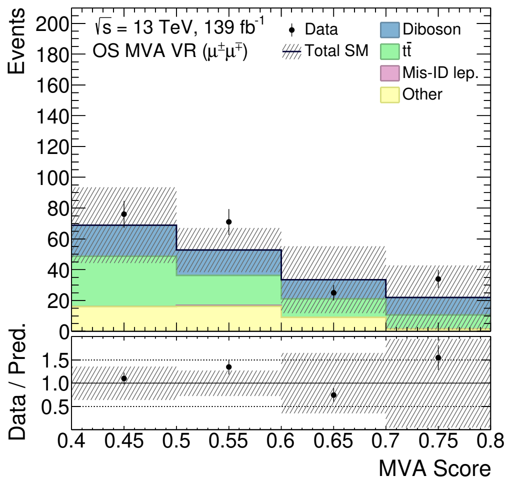

(c)

Figure 8.18: Post-fit distributions of $H_{\mathrm{T}} + E_{\mathrm{T}}^{\mathrm{miss}}$ in opposite-sign MVA validation regions, namely (a) the electron–electron validation region and (b) the electron–muon validation region, and (c) the muon–muon validation region. The hatched bands include all systematic uncertainties after the background-only fit with the correlations between various sources taken into account.

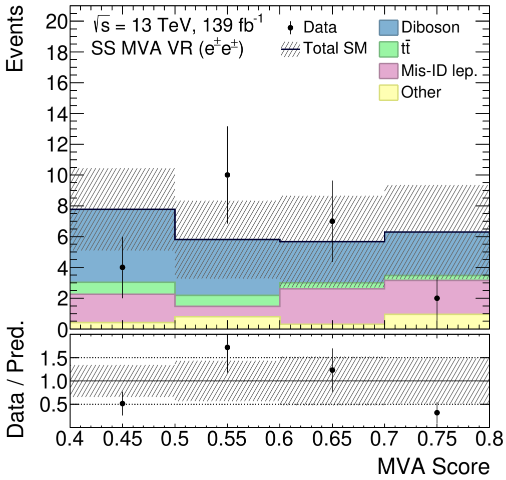

(a)

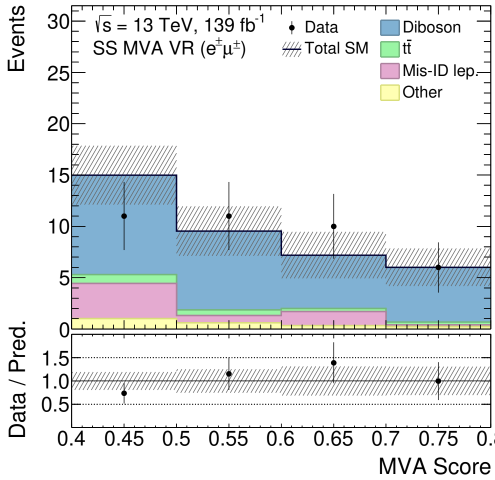

(b)

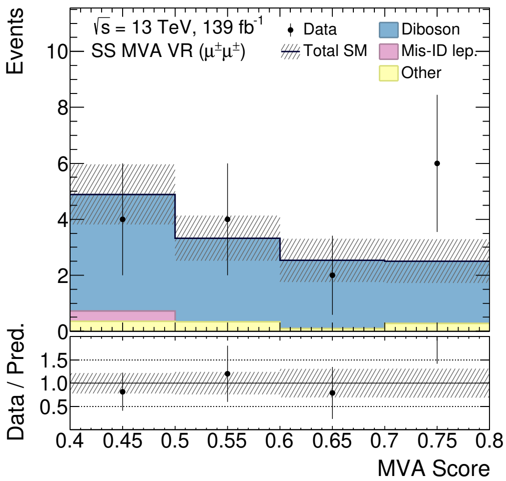

(c)

Figure 8.19: Post-fit distributions of $H_{\mathrm{T}} + E_{\mathrm{T}}^{\mathrm{miss}}$ in same-sign MVA validation regions, namely (a) the electron–electron validation region, (b) the electron–muon validation region, and (c) the muon–muon validation region. The hatched bands include all systematic uncertainties after the background-only fit with the correlations between various sources taken into account.

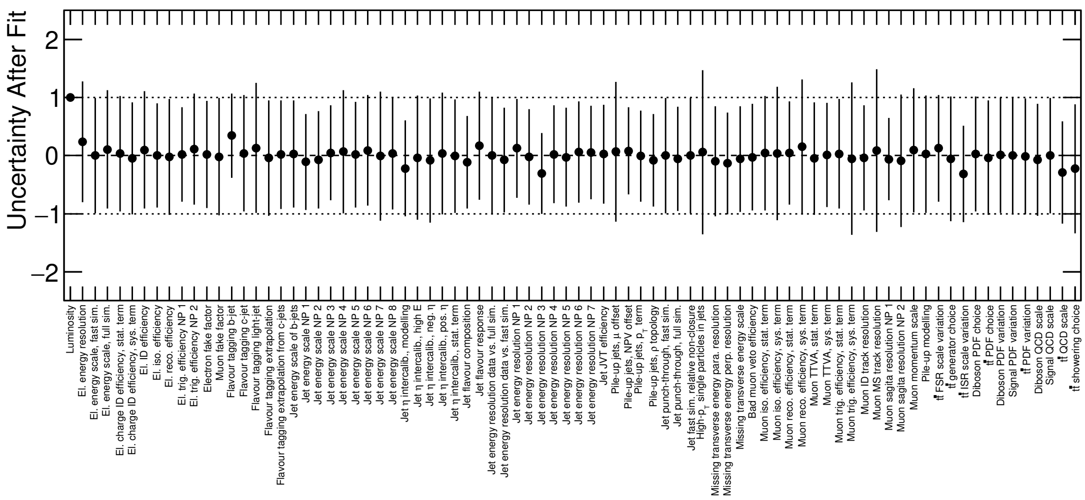

Figure 8.20: Post-fit nuisance parameters of the full likelihood fit in the multivariate scenario with real data in all but signal regions, expressed in units of standard deviation.

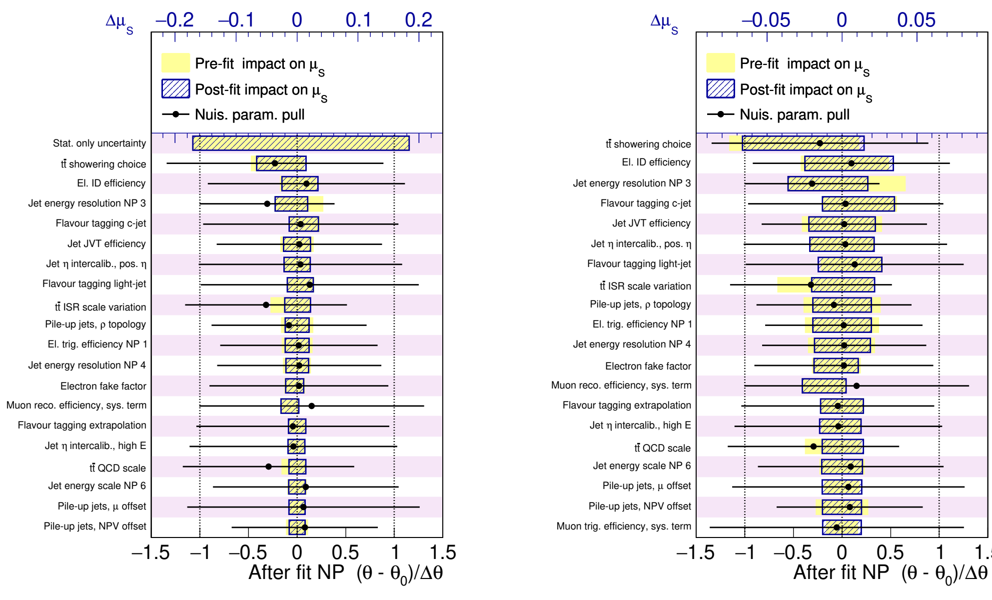

(a) (b)

Figure 8.21: Impact of systematic uncertainties on μ_{sig} in the multivariate scenario, (a) showing the impact of the dominant systematic sources and MC statistical uncertainty and (b) showing only the impact of the dominant systematic sources. Post-fit values of α are displayed with black points.

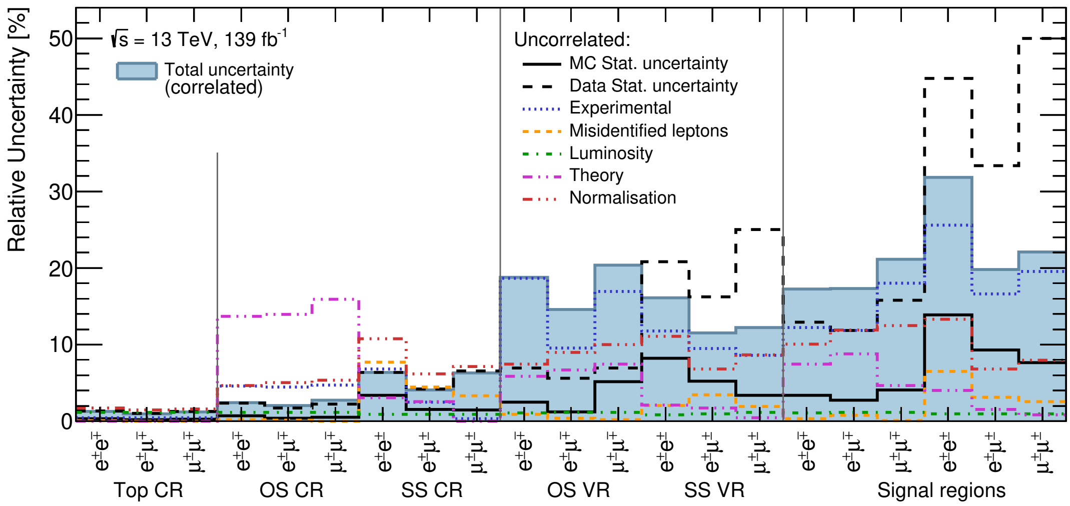

Figure 8.22: Relative contributions of different sources of statistical and systematic uncertainty in the total background yield estimation after the fit in the multivariate scenario. Systematic uncertainties are calculated in an uncorrelated way by shifting in turn only one nuisance parameter from the post-fit value by one standard deviation, keeping all the other parameters at their post-fit values, and comparing the resulting event yield with the nominal yield. Individual uncertainties can be correlated, and do not necessarily add in quadrature to the total background uncertainty, which is indicated by "Total uncertainty".

of theoretical and experimental uncertainties in the SR are between 15 and 25%. The uncertainty due to limited number of simulated events is less prominent here compared with the cut-based analysis. The total uncertainties are at the order of 20%, while in the SS *ee* channel they are about 30% as the uncertainty due to charge misidentification can not be reduced more.

Once the stability of the fit is ensured and uncertainties modelling is validated, measured data are fitted on the expected background in signal regions allowing expected new physics with the parameter of interest μ_{sig}. After the fit, the compatibility between the data and the expected background is assessed and good agreement is observed, with a p_0-value of 0.5 for the background-only hypothesis. Post-fit binned distributions of $H_{\text{T}} + E_{\text{T}}^{\text{miss}}$ are shown in Figures 8.23 and 8.24 for the signal regions with representative expected signal distributions overlaid.

Figure 8.25 shows a good agreement within the uncertainties between expected background and observed events in all the regions and channels considered in the analysis. The level of agreement between the data and background predictions in the CR and VR, well within the statistical and systematic uncertainties, demonstrates the validity of the used background estimation procedures.

Predicted numbers of background events in signal regions are listed together with the

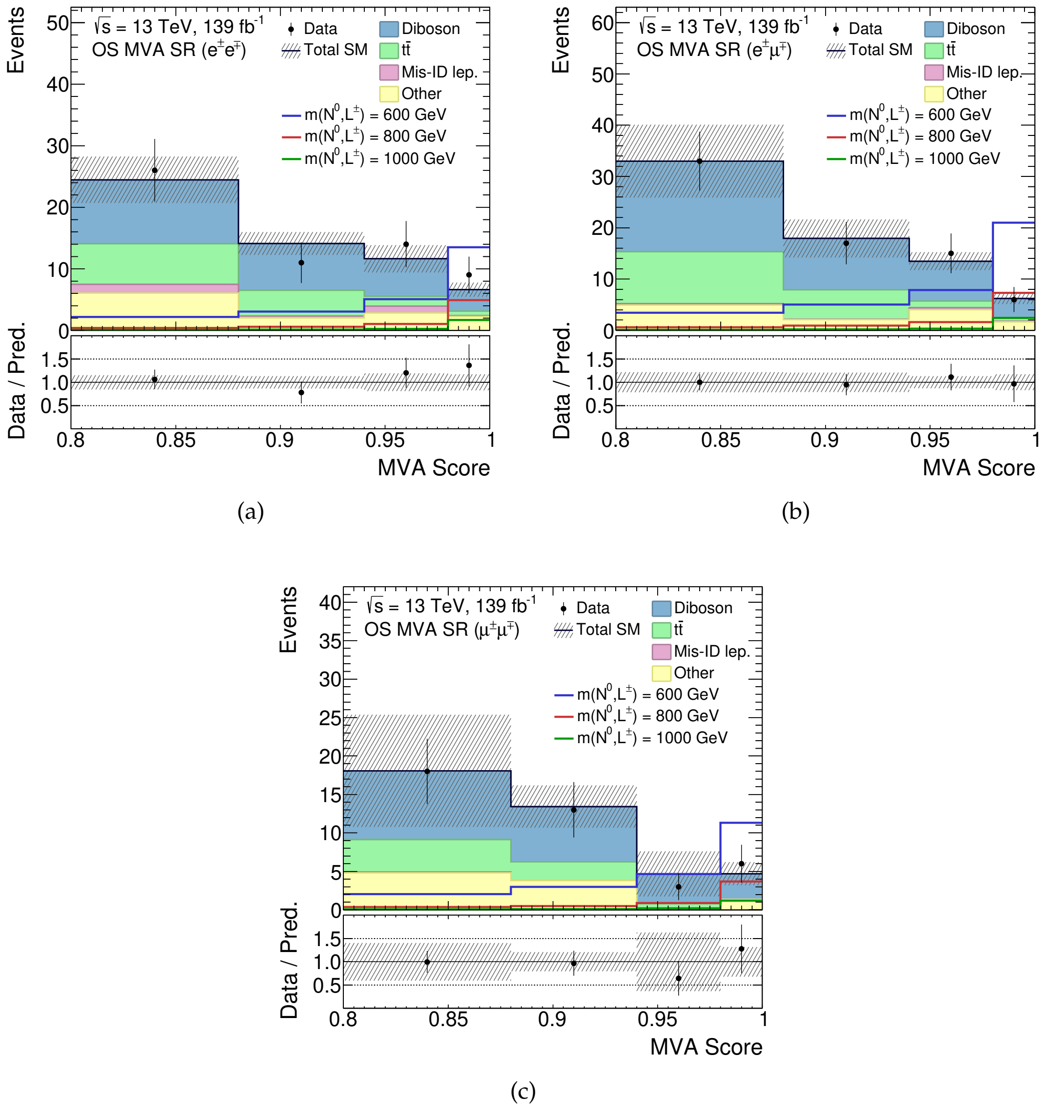

Figure 8.23: Post-fit distributions of $H_\mathrm{T} + E_\mathrm{T}^\mathrm{miss}$ in opposite-sign MVA signal regions, namely (a) the electron–electron signal region, (b) the electron–muon signal region, and (c) the muon–muon signal region after the background-only fit described in the text. The hatched bands include all systematic uncertainties post-fit with the correlations between various sources taken into account. The coloured lines correspond to signal samples with the N^0 and $L^\pm$ mass stated in the legend.

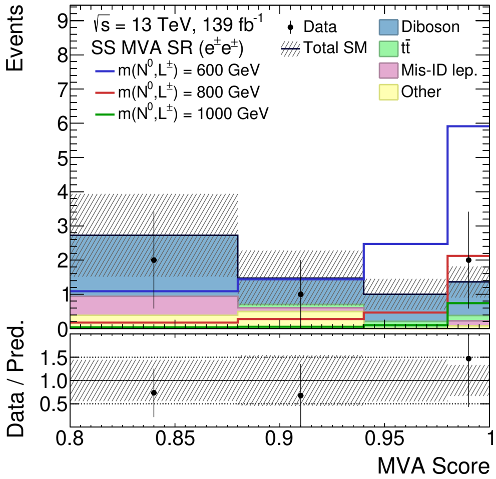

(a)

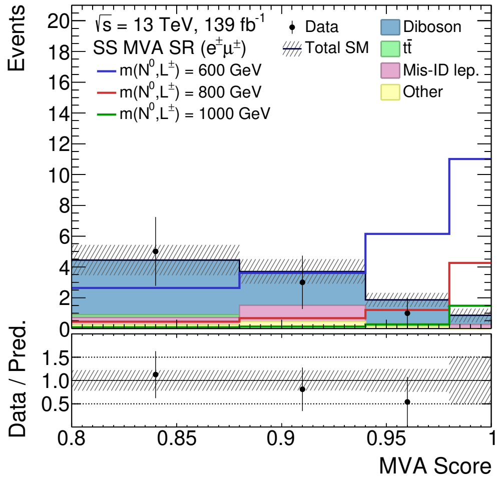

(b)

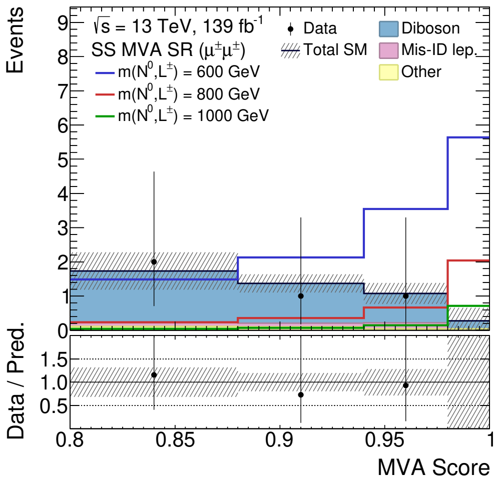

(c)

Figure 8.24: Post-fit distributions of $H_{\mathrm{T}} + E_{\mathrm{T}}^{\mathrm{miss}}$ in same-sign MVA signal regions, namely (a) the electron–electron signal region, (b) the electron–muon signal region, and (c) the muon–muon signal region after the background-only fit described in the text. The hatched bands include all systematic uncertainties post-fit with the correlations between various sources taken into account. The coloured lines correspond to signal samples with the N^0 and $L^{\pm}$ mass stated in the legend.

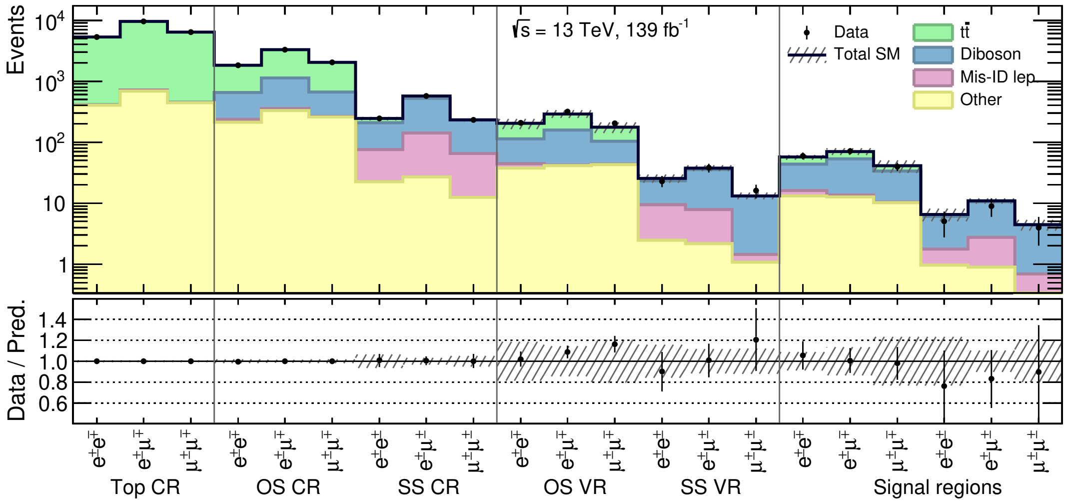

Figure 8.25: The numbers of observed and expected events in the control, validation, and signal regions for all considered channels in the multivariate scenario, split by flavour and electric charge combination. The background expectation is the result of the background-only fit described in the text. The hatched bands include all post-fit systematic uncertainties with the correlations between various sources taken into account.

observed number of events in data in Table 8.7, where also expected signal yields for several mass points are given for comparison. Furthermore, the number of events in control and validation regions are listed in Tables 8.8–8.10.

In absence of a significant deviation from expectations within uncertainties, 95% confidence level upper limits on the signal production cross-section are derived using the CL_s method. Although the statistics in the multivariate case is larger than in the cut-based analysis, pseudo-experiments are also used to ensure stability of the limit and comparable results between the two methods. The resulting exclusion limits on the signal cross-section are shown in Figure 8.26. Limits on the cross-section are derived, with the expected lower mass limit at 950^{+60}_{-70} GeV and the observed lower mass limit placed at 950 GeV, excluding the mass values below this point. Sensitivity of individual channels is estimated using the asymptotic formulae and presented in Figure 8.27. The SS $e\mu$ channel is the most sensitive one with SS $\mu\mu$ and OS $e\mu$ the next ones. Same-flavour OS channels are the least sensitive due to large background contamination.

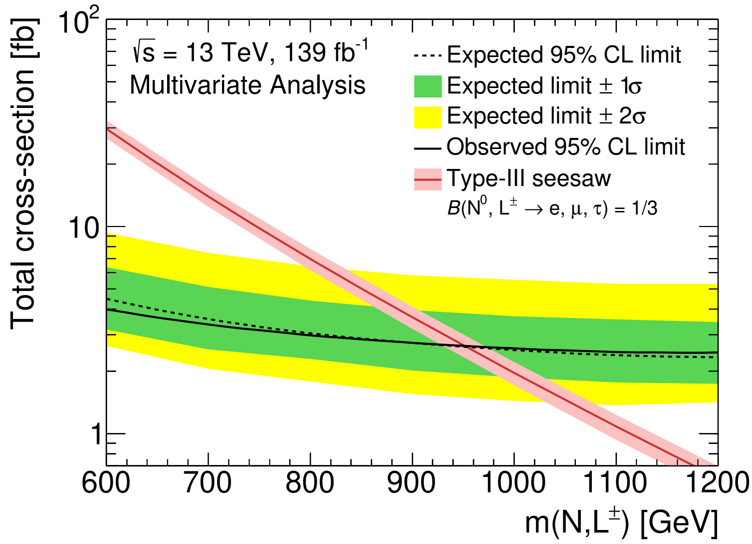

Figure 8.26: Expected and observed 95% CL_s exclusion limits in the multivariate scenario for the type-III seesaw process with the corresponding one- and two-standard-deviation bands, showing the 95% CL upper limit on the cross-section. The theoretical signal cross-section prediction, given by the NLO calculation, is shown as a red line with the corresponding uncertainty band.

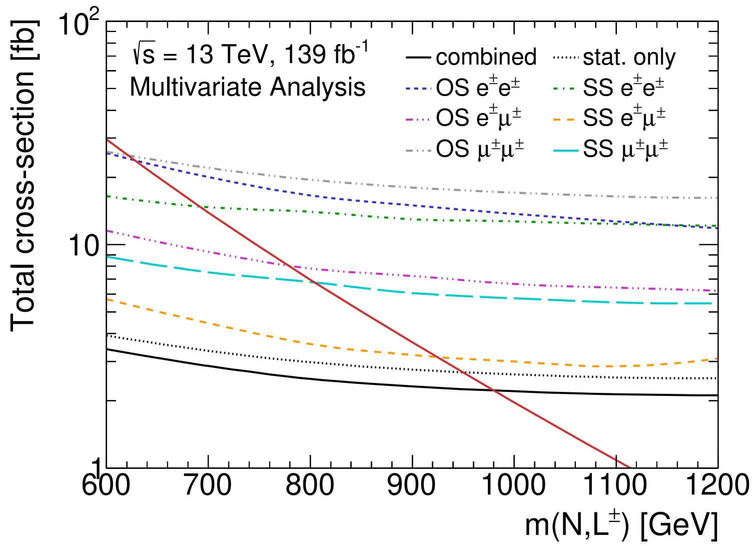

Figure 8.27: Expected and observed 95% CL_s exclusion limits in the multivariate scenario for each individual channel. The theoretical signal cross-section prediction, given by the NLO calculation, is shown as a red line.

Table 8.7: The number of expected background events in MVA signal regions after the likelihood fit, compared with the data. Uncertainties correspond to the total uncertainties in the predicted event yields, and are smaller for the total than for the individual contributions summed in quadrature because the latter are anti-correlated. Due to rounding the totals can differ from the sums of components. $t\bar{t}$ and diboson normalisations are allowed to float in the fit. For the reference purpose, representative signal yields and their errors for signal masses $m(N^0, L^\pm)$, denoted by m in the table, are shown in the bottom part of the table.

MVA signal regions	**OS $e^\pm e^\mp$**	**OS $e^\pm \mu^\mp$**	**OS $\mu^\pm \mu^\mp$**
Observed events	60	71	40
Total background	56.8 ± 5.1	70.6 ± 9.4	40.8 ± 9.6
$t\bar{t}$	13.2 ± 2.3	17.8 ± 1.9	7.2 ± 1.5
Diboson	27.5 ± 2.5	39.2 ± 4.4	23.3 ± 2.9
Other	13.2 ± 3.6	12.7 ± 5.9	10.1 ± 9.3
Fakes	2.95 ± 0.10	0.87 ± 0.24	0.17 ± 0.07
Signal expectation			
$m = 600\,\mathrm{GeV}$	24.2 ± 3.2	37.9 ± 4.8	21.3 ± 2.8
$m = 800\,\mathrm{GeV}$	7.1 ± 2.0	10.6 ± 2.9	5.6 ± 1.6
$m = 1000\,\mathrm{GeV}$	2.2 ± 1.4	3.2 ± 2.1	1.6 ± 1.1
Signal regions	**SS $e^\pm e^\pm$**	**SS $e^\pm \mu^\pm$**	**SS $\mu^\pm \mu^\pm$**
Observed events	5	9	4
Total background	6.6 ± 1.5	10.9 ± 1.1	4.45 ± 0.89
$t\bar{t}$	0.45 ± 0.50	0.23 ± 0.51	—
Diboson	4.34 ± 0.89	7.9 ± 1.0	3.76 ± 0.86
Other	0.95 ± 0.84	0.89 ± 0.48	0.30 ± 0.10
Fakes	0.82 ± 0.18	1.84 ± 0.30	0.39 ± 0.09
Signal expectation			
$m = 600\,\mathrm{GeV}$	11.1 ± 1.5	23.7 ± 3.0	12.9 ± 1.7
$m = 800\,\mathrm{GeV}$	3.09 ± 0.87	6.7 ± 1.9	3.36 ± 0.94
$m = 1000\,\mathrm{GeV}$	0.96 ± 0.63	2.0 ± 1.3	1.00 ± 0.65

Table 8.8: The number of expected background events in the MVA Top control regions after the likelihood fit, compared with the data. Uncertainties correspond to the total uncertainties in the predicted event yields, and are smaller for the total than for the individual contributions summed in quadrature because the latter are anti-correlated. Due to rounding the totals can differ from the sums of components. $t\bar{t}$ and diboson normalisations are allowed to float in the fit.

Top MVA CR	**OS $e^{\pm}e^{\mp}$**	**OS $e^{\pm}\mu^{\mp}$**	**OS $\mu^{\pm}\mu^{\mp}$**
Observed events	5308	9664	6345
Total background	5302 $\pm$ 53	9668 $\pm$ 74	6345 $\pm$ 58
$t\bar{t}$	4892 $\pm$ 52	8950 $\pm$ 72	5895 $\pm$ 59
Diboson	4.56 $\pm$ 0.50	8.38 $\pm$ 0.77	4.10 $\pm$ 0.53
Other	405 $\pm$ 11	693 $\pm$ 23	446 $\pm$ 13
Fakes	0.4 $\pm$ 1.3	16.65 $\pm$ 0.87	< 0.001

Table 8.9: The number of expected background events in the MVA control regions after the likelihood fit, compared with the data. Uncertainties correspond to the total uncertainties in the predicted event yields, and are smaller for the total than for the individual contributions summed in quadrature because the latter are anti-correlated. Due to rounding the totals can differ from the sums of components. $t\bar{t}$ and diboson normalisations are allowed to float in the fit.

MVA CR	**OS $e^{\pm}e^{\mp}$**	**OS $e^{\pm}\mu^{\mp}$**	**OS $\mu^{\pm}\mu^{\mp}$**
Observed events	1821	3274	2054
Total background	1830 $\pm$ 34	3270 $\pm$ 47	2053 $\pm$ 36
$t\bar{t}$	1176 $\pm$ 29	2137 $\pm$ 51	1386 $\pm$ 32
Diboson	417 $\pm$ 34	778 $\pm$ 48	404 $\pm$ 37
Other	211.7 $\pm$ 9.2	329 $\pm$ 17	258 $\pm$ 20
Fakes	25.2 $\pm$ 1.6	26.1 $\pm$ 2.7	4.76 $\pm$ 0.09
MVA CR	**SS $e^{\pm}e^{\pm}$**	**SS $e^{\pm}\mu^{\pm}$**	**SS $\mu^{\pm}\mu^{\pm}$**
Observed events	247	573	232
Total background	245 $\pm$ 16	571 $\pm$ 18	232 $\pm$ 12
$t\bar{t}$	38.6 $\pm$ 4.1	48.6 $\pm$ 5.2	—
Diboson	131 $\pm$ 12	382 $\pm$ 19	167 $\pm$ 11
Other	22 $\pm$ 11	27.1 $\pm$ 2.8	12.40 $\pm$ 0.39
Fakes	52.9 $\pm$ 8.0	113 $\pm$ 11	52.6 $\pm$ 5.5

Table 8.10: The number of expected background events in the MVA validation regions after the likelihood fit, compared with the data. Uncertainties correspond to the total uncertainties in the predicted event yields, and are smaller for the total than for the individual contributions summed in quadrature because the latter are anti-correlated. Due to rounding the totals can differ from the sums of components. $t\bar{t}$ and diboson normalisations are allowed to float in the fit.

MVA VR	**OS $e^{\pm}e^{\mp}$**	**OS $e^{\pm}\mu^{\mp}$**	**OS $\mu^{\pm}\mu^{\mp}$**
Observed events	207	317	206
Total background	203 ± 38	292 ± 42	177 ± 36
$t\bar{t}$	90 ± 13	133 ± 20	73 ± 13
Diboson	69 ± 15	116 ± 28	61 ± 19
Other	38 ± 31	41 ± 14	43 ± 24
Fakes	6.4 ± 1.8	1.4 ± 1.2	0.65 ± 0.35
MVA VR	**SS $e^{\pm}e^{\pm}$**	**SS $e^{\pm}\mu^{\pm}$**	**SS $\mu^{\pm}\mu^{\pm}$**
Observed events	23	38	16
Total background	25.6 ± 4.1	37.7 ± 4.4	13.3 ± 1.6
$t\bar{t}$	2.2 ± 1.3	2.0 ± 1.4	—
Diboson	13.9 ± 3.3	27.9 ± 4.0	11.8 ± 1.6
Other	2.5 ± 2.5	2.2 ± 1.4	1.07 ± 0.41
Fakes	7.00 ± 0.84	5.7 ± 1.3	0.37 ± 0.25

CHAPTER 9

Conclusions and Outlook

Neutrino masses are one of the unsolved questions of the Standard Model. Besides new particles, new mechanisms can be introduced to explain them. Type-III seesaw is one of those theories, introducing a triplet of heavy leptons. The search for them using the pp collision data from the ATLAS experiment has been the topic of this thesis.

Production cross-sections of the type-III seesaw model have a large dependence on the heavy lepton mass. The full Run 2 luminosity of 139 fb^{-1} a provided sufficiently large dataset to be sensitive to masses of the order of 1 TeV. The dominant decay branching ratio is into W bosons so this search focused into final states containing a lepton pair, at least two hadronic jets and high missing transverse energy.

Cut-based analysis strategy is a common approach in particle physics enriching signal regions with signal candidates and improving sensitivity (expected signal significance) to the new physics. A common issue with the method is that final selected statistics are very low. Although a constant increase of data collected at the collider experiments helps with the issue, this is not sustainable in the long run. Multivariate analysis using machine learning techniques are gaining traction in the field, utilising functional dependence of the measured quantities enabling better background rejection at increased sensitivity. A direct comparison between the two strategies has been performed to be able to estimate the level of improvement that can be achieved.

No significant excess over the Standard Model prediction has been observed. Lower limits on the masses of the type-III seesaw heavy leptons have been set at 790 GeV using cut-based and 950 GeV using multivariate approach at 95% confidence level. There is a 20% improvement observed when using machine learning algorithms over the simple cut-based approach. At the time of the writing this results in the highest lower limit on the masses of the type-III seesaw leptons.

Many lessons have been learned when making this analysis. Same-charge pairs are good for looking for new physics given the low Standard Model background. On the other hand, charge misidentification introduces large uncertainties and needs to be properly handled. Accurate background estimation is one of the pillars of a successful physics analysis to avoid potential signal events being classified as a background fluctuation.

To think about potential future improvements, to increase the sensitivity in the same final state topology hadronic tau decays could be introduced. This poses an additional challenge as such processes need to be separated from regular hadronic jets. Moving towards higher lepton multiplicities SM background cross-section decreases faster than the type-III seesaw one. A combined analysis covering also three, four and even five leptons in the event would increase the sensitivity to new physics.

On the other hand the use of machine learning algorithms leaves a lot of possibilities in dilepton events. Loosening requirements on number of b-jets (decays into Higgs bosons) and $E_{\mathrm{T}}^{\mathrm{miss}}$ (decays into Z bosons) would select more signal events. This is not possible by hand but using multivariate techniques would improve the selection. Additionally multiple neural networks could be used, each focusing on a subset of possible final states.

Particle physics is embracing machine learning techniques more and more. Using them not only for selection but also for simulation, reconstruction and other background estimation techniques will allow us to cope better with the increasing number of collected data.

Large Hadron Collider will operate at least until late 2030s and will in total collect an order of magnitude more collisions than it has until now. Just increasing the luminosity is not enough. ATLAS has many detector hardware and reconstruction software updates in progress to improve the performance of the experiment and be able to cope with the increased number of simultaneous proton–proton collision at the High-luminosity LHC [156]. A bright future of searches of new physics in multilepton final states is ahead of us which will allow better understanding of the unanswered questions about the world around us.

APPENDIX

APPENDIX A

Fake Lepton Composition

Detailed fake lepton composition can be studied to properly define fake-factor estimation regions and ensure compatibility between them. The origin of the fake leptons in Monte-Carlo simulation is analysed in this appendix.

The fake lepton background can be classified into several categories:

- prompt photon conversions,
- non-prompt muon decays in jets,
- non-prompt tau decays in jets,
- b-hadron decays in jets,
- c-hadron decays in jets,
- light hadron decays in jets,
- known unclassified fake leptons.

Additionally fake background events in signal regions separately classify events with both leptons misidentified or non-prompt.

The fake composition of the electron and muon fake estimation region is displayed in Figures A.1 and A.2, respectively. Cut-based signal regions composition is shown in Figures A.3–A.5 and multivariate signal regions composition in Figures A.6–A.8.

Most of the electron fakes are estimated to come from light hadron and b-hadron decays in jets. Muon fakes come from heavier-flavour jets, mainly c-jets and b-jets. Dijet events are the dominant contributor to the number of fake leptons in the estimation regions, followed by $W+$jets and $t\bar{t}$ events.

Cut-based signal regions composition match well with the fake-factor estimation composition. Opposite-sign signal regions expect a very low number of fake events which makes fake composition hard to estimate and discuss. Furthermore, multiboson events are hard to categorise so they mostly fall in the unclassified category. The electron channel matches the estimation region with light hadron decays from $W+$jets events the dominant ones. Similarly of the mixed-flavour channel, the composition is very similar to the electron estimation region as electron fakes are expected to be much more common. The same-sign muon channel has composition compatible with the muon estimation region with $t\bar{t}$ events contributing the most. Additionally multiboson events are expected to contribute a significant fraction of events with two fake leptons but given the low cross-section this contribution can be discarded.

Multivariate analysis signal regions show similar level of agreement with the estimation regions. $W+$jets events are the dominant contributor to the fake background with light-hadron decays in jets only significant source of fake electrons. Number of fake muons is again low with contributions from light and c-hadrons.

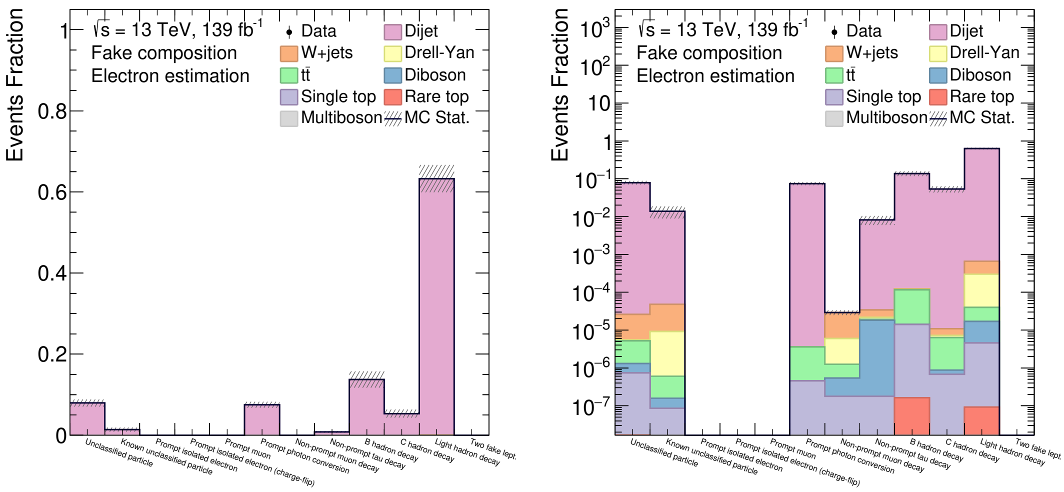

(a) (b)

Figure A.1: Fake composition of the electron fake-factor estimation region in (a) linear and (b) logarithmic scale.

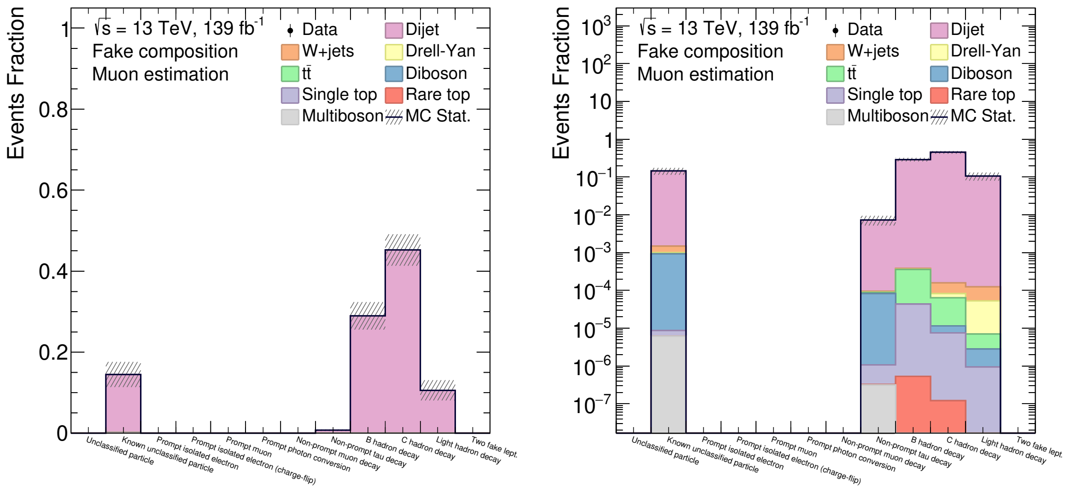

(a) (b)

Figure A.2: Fake lepton composition of the muon fake-factor estimation region in (a) linear and (b) logarithmic scale.

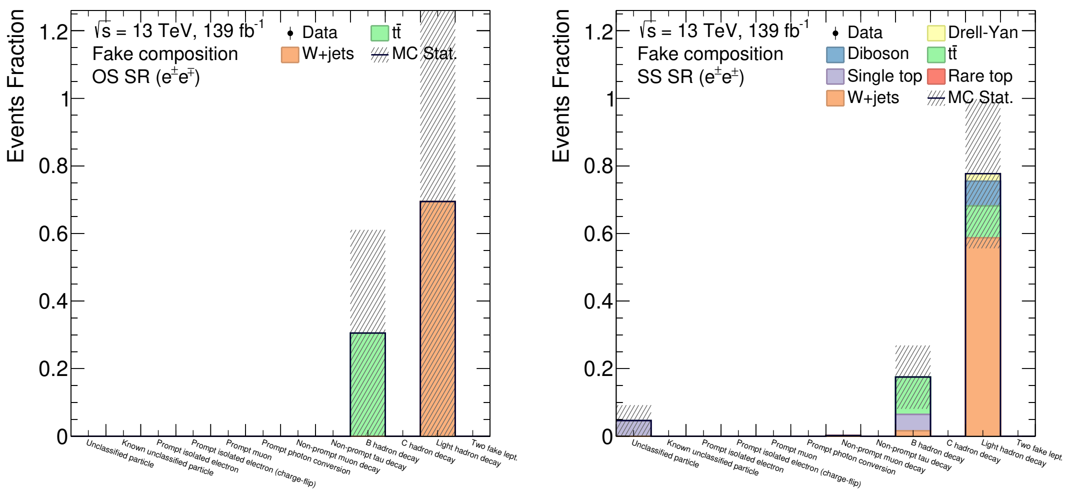

(a) (b)

Figure A.3: Fake lepton composition of the *ee* channel of the cut-based signal region for (a) opposite-sign and (b) same-sign lepton pairs.

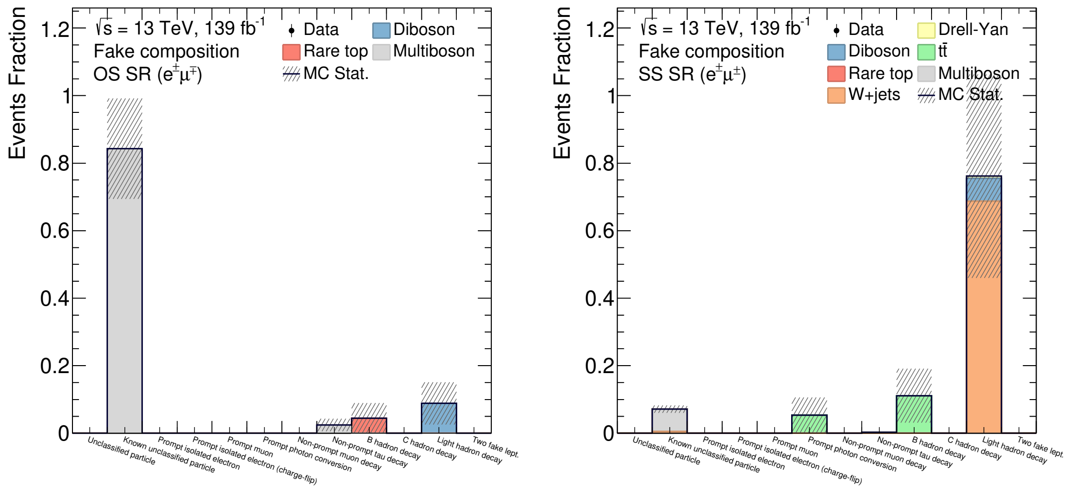

(a) (b)

Figure A.4: Fake lepton composition of the $e\mu$ channel of the cut-based signal region for (a) opposite-sign, and (b) same-sign lepton pairs.

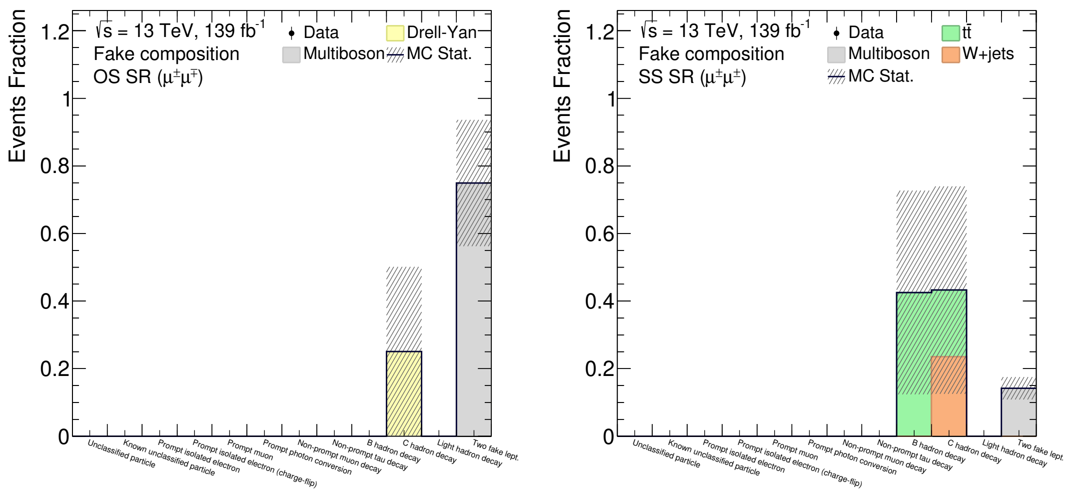

(a) (b)

Figure A.5: Fake lepton composition of the $\mu\mu$ channel of the cut-based signal region for (a) opposite-sign and (b) same-sign lepton pairs.

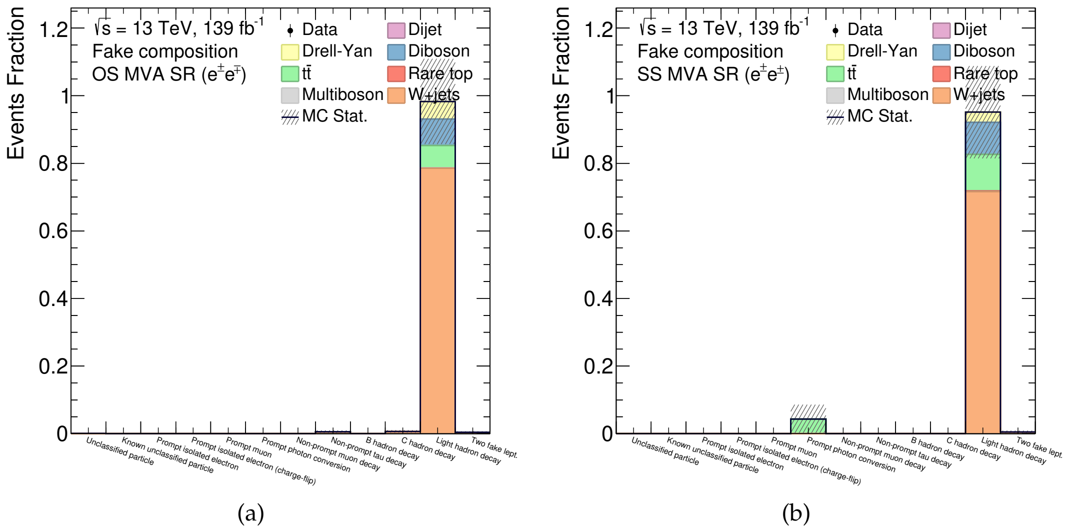

Figure A.6: Fake lepton composition of the ee channel of the multivariate signal region for (a) opposite-sign and (b) same-sign lepton pairs.

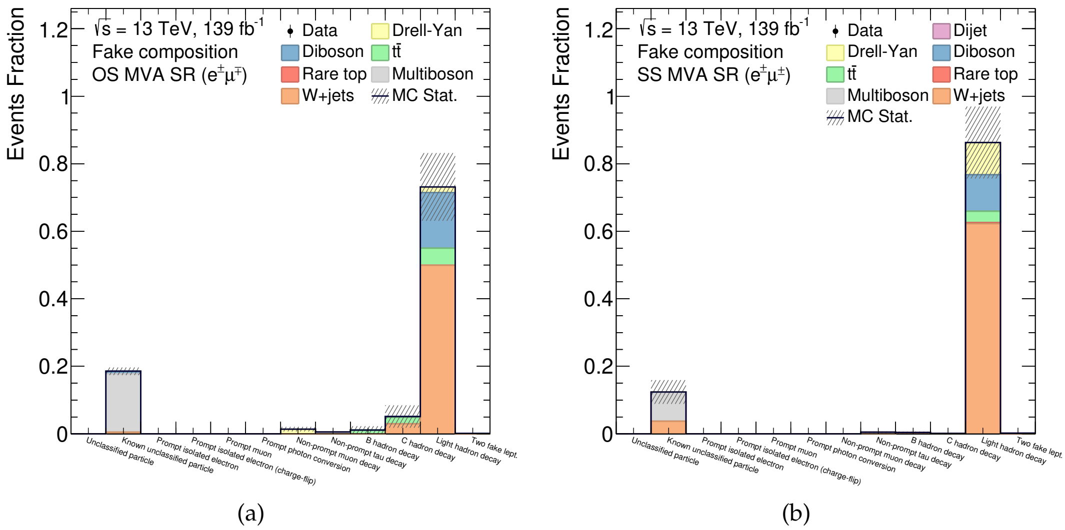

Figure A.7: Fake lepton composition of the $e\mu$ channel of the multivariate signal region for (a) opposite-sign, and (b) same-sign lepton pairs.

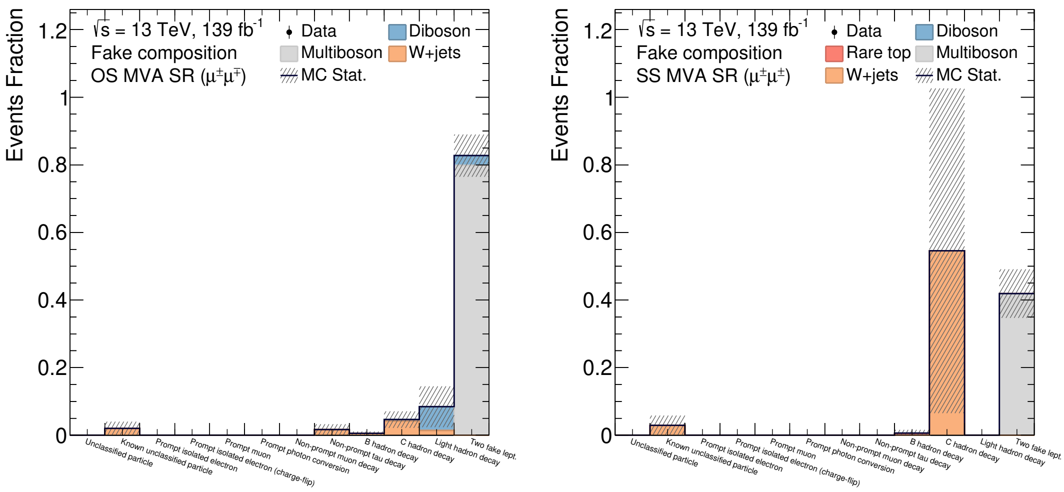

(a) (b)

Figure A.8: Fake lepton composition of the $\mu\mu$ channel of the multivariate signal region for (a) opposite-sign and (b) same-sign lepton pairs.

APPENDIX B

Selected Distributions of the Cut-based Analysis Regions

Selected kinematic distributions are presented to illustrate good agreement between expected and observed events in all cut-based analysis regions. Transverse momenta for leading and sub-leading leptons and jets are shown in following figures:

- Top control regions in Figures B.1 and B.2,
- Diboson control regions in Figures B.3 and B.4,
- opposite-sign validation regions in Figures B.5 and B.6,
- same-sign validation regions in Figures B.7 and B.8,
- opposite-sign signal regions in Figures B.9 and B.10,
- same-sign signal region in Figures B.11 and B.12.

Each of the presented figures has leading lepton or jet p_{T} distribution in the first column and sub-leading lepton or jet p_{T} in the second one. The ee channel is shown in the first row, the $e\mu$ channel in the second row, and the $\mu\mu$ channel in the last row.

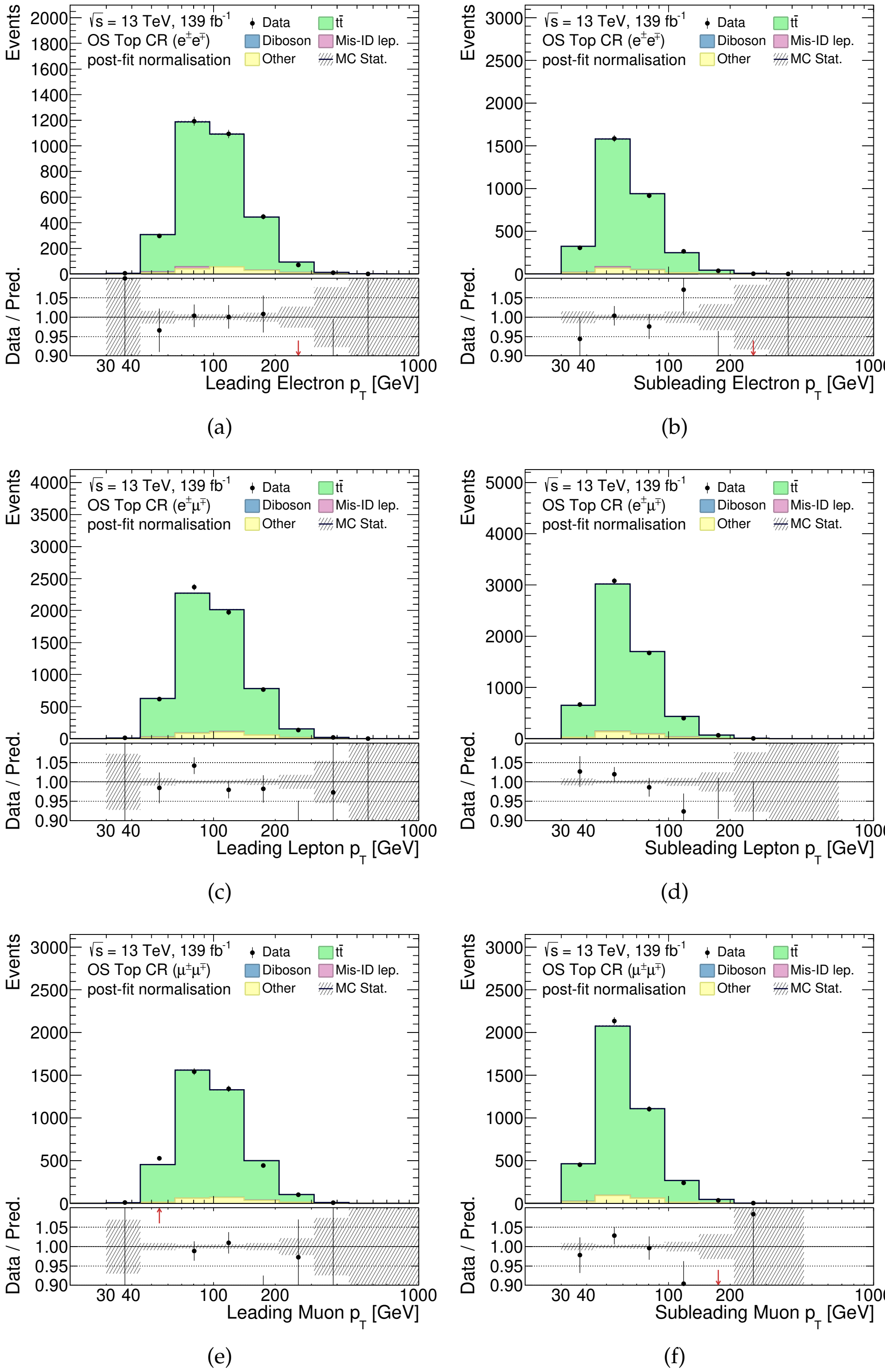

Figure B.1: Leading and sub-leading lepton momentum distributions in cut-based Top control regions for all flavour combinations. Post-fit normalisation scales are applied. Uncertainties are statistical only.

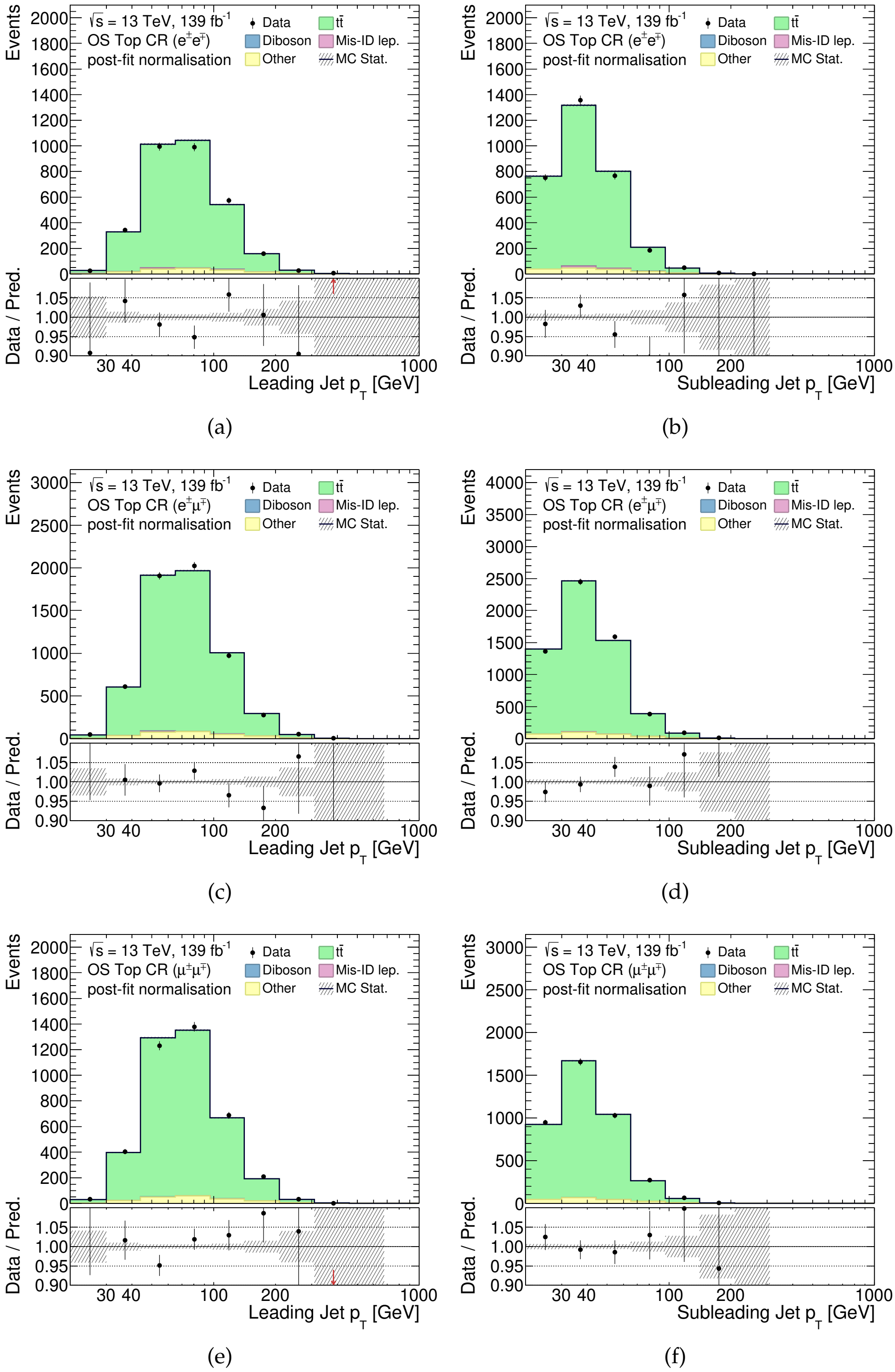

Figure B.2: Leading and sub-leading jet momentum distributions in cut-based Top control regions for all flavour combinations. Post-fit normalisation scales are applied. Uncertainties are statistical only.

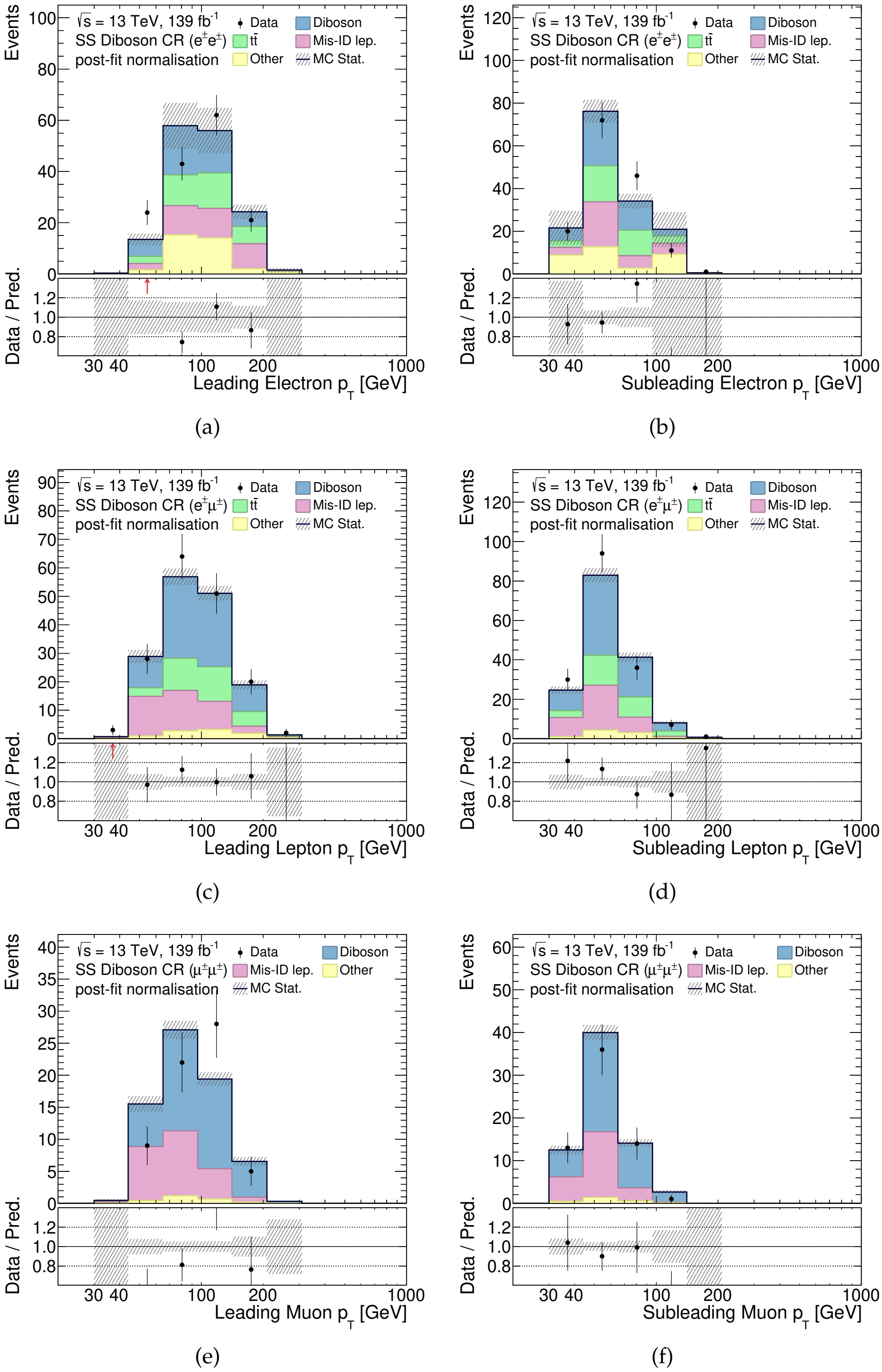

Figure B.3: Leading and sub-leading lepton momentum distributions in cut-based Diboson control regions for all flavour combinations. Post-fit normalisation scales are applied. Uncertainties are statistical only.

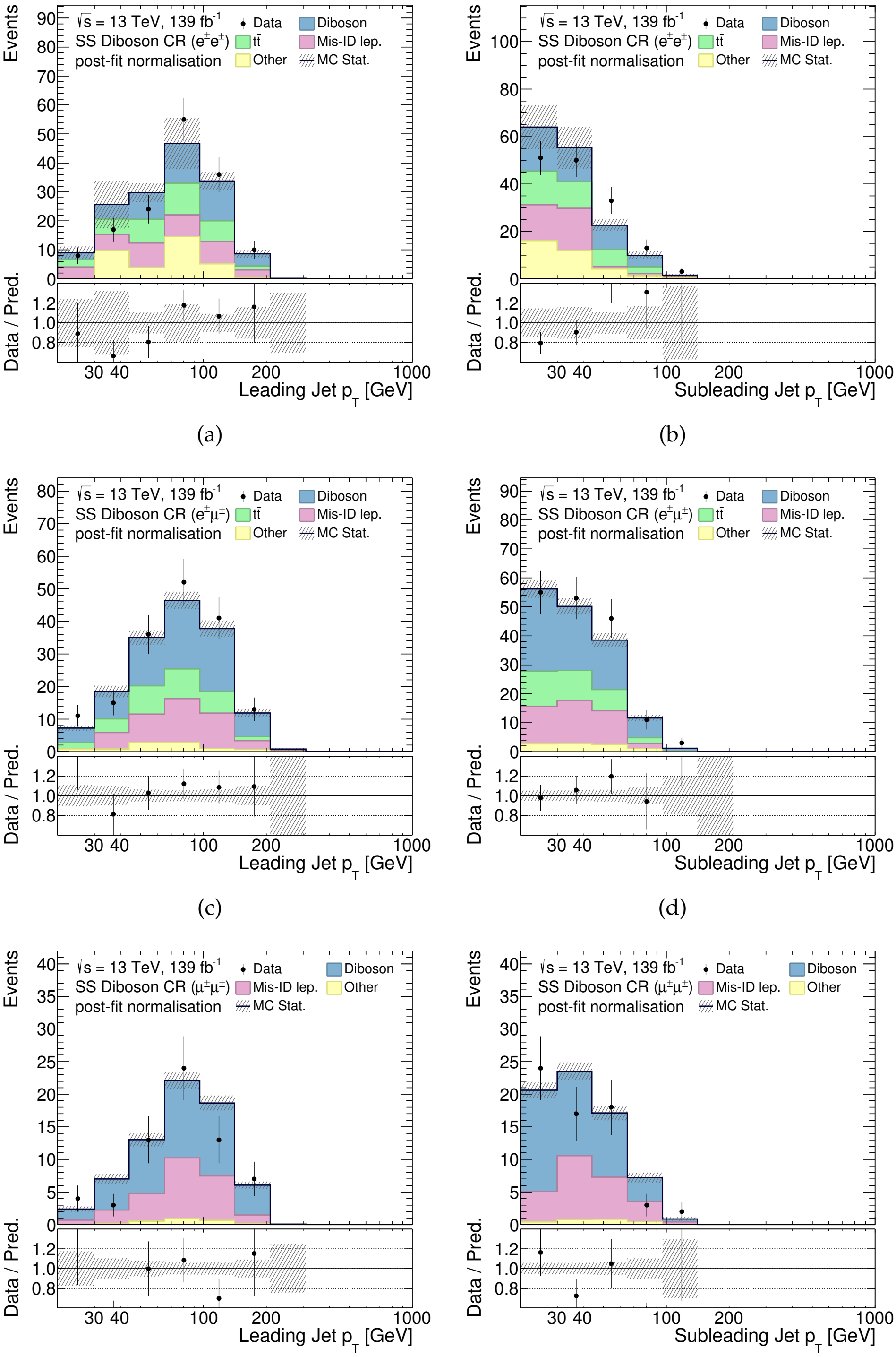

(a) (b) (c) (d) (e) (f)

Figure B.4: Leading and sub-leading jet momentum distributions in cut-based Diboson control regions for all flavour combinations. Post-fit normalisation scales are applied. Uncertainties are statistical only.

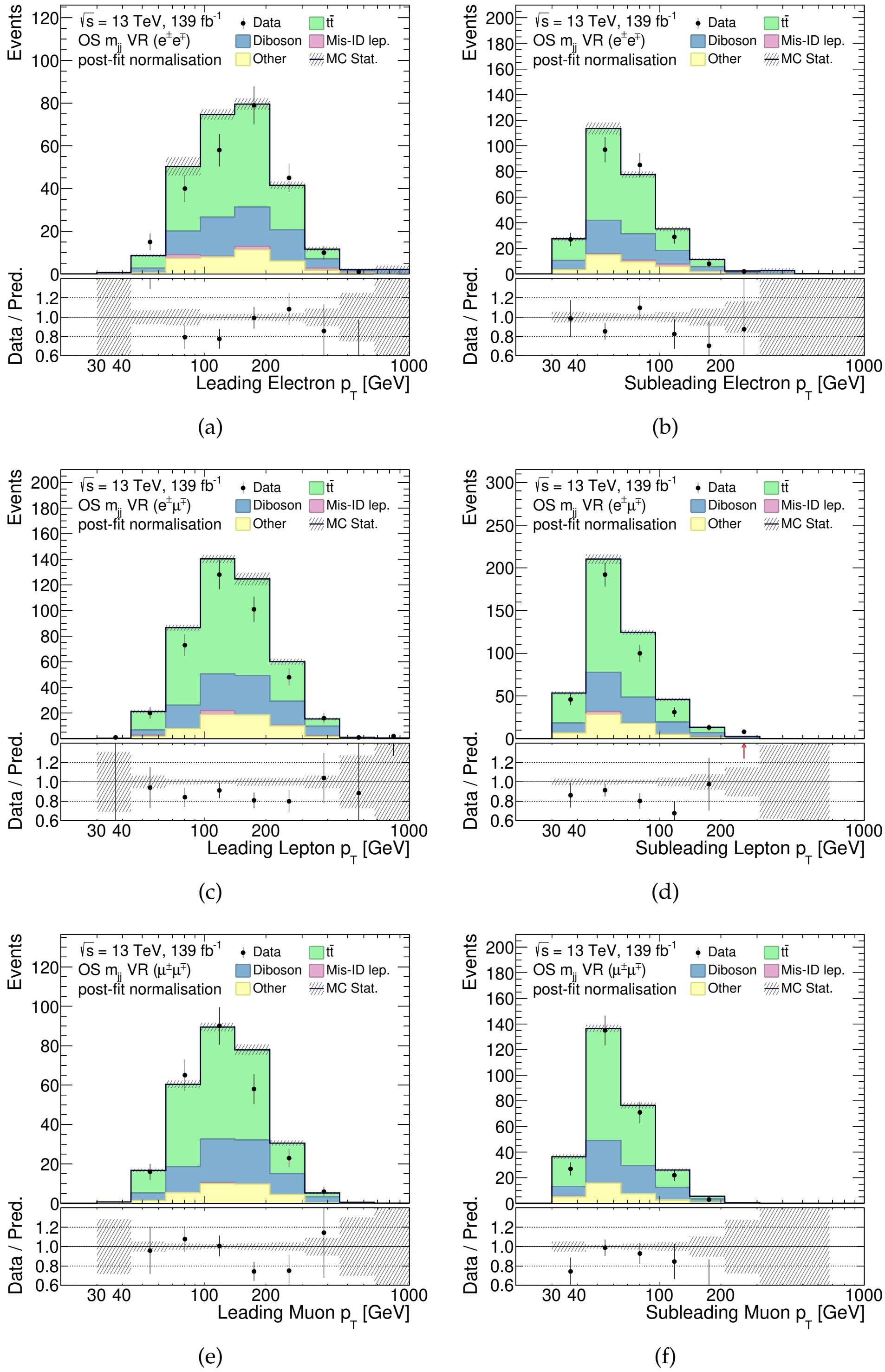

Figure B.5: Leading and sub-leading lepton momentum distributions in cut-based opposite-sign validation regions for all flavour combinations. Post-fit normalisation scales are applied. Uncertainties are statistical only.

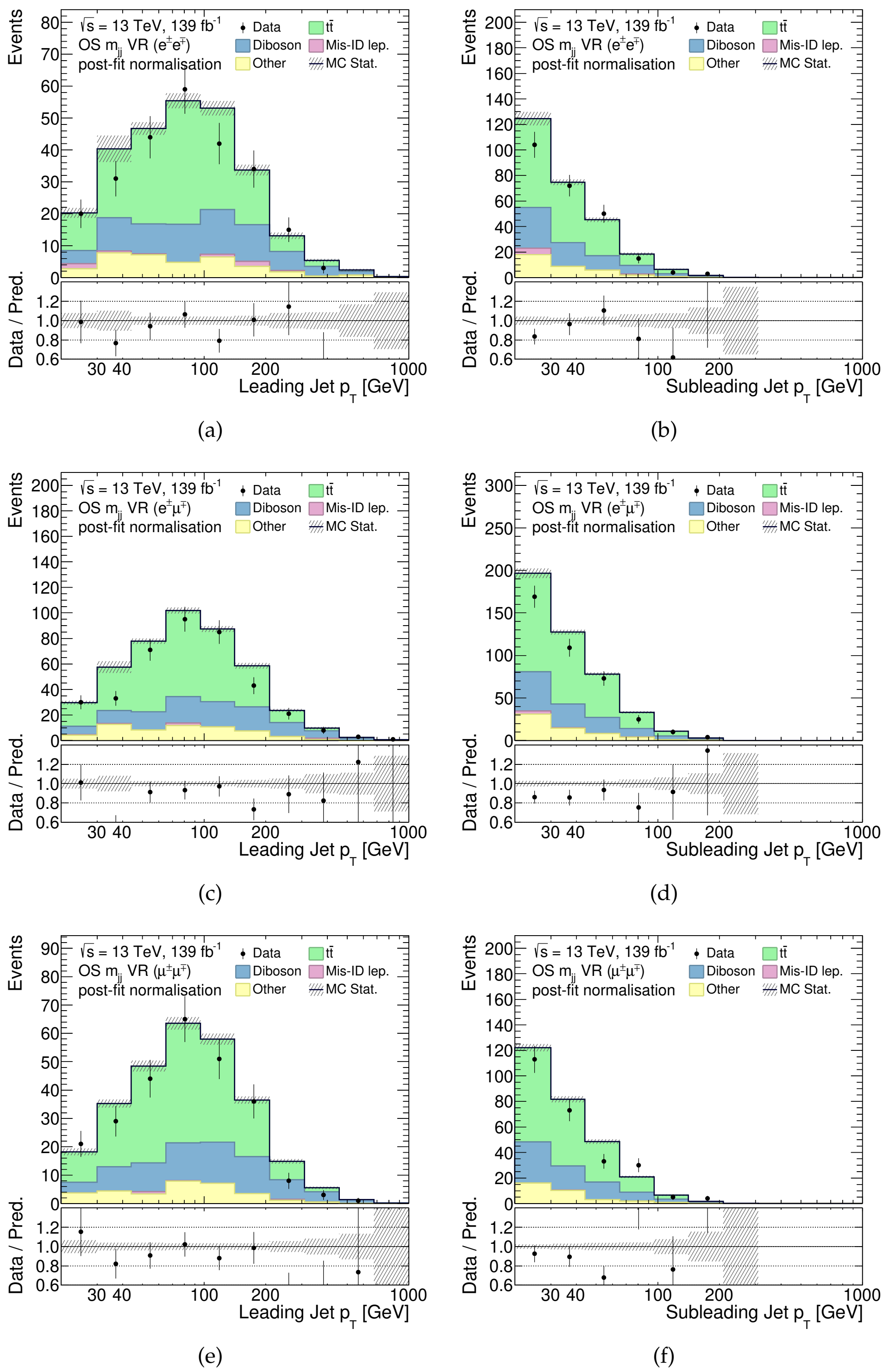

Figure B.6: Leading and sub-leading jet momentum distributions in cut-based opposite-sign validation regions for all flavour combinations. Post-fit normalisation scales are applied. Uncertainties are statistical only.

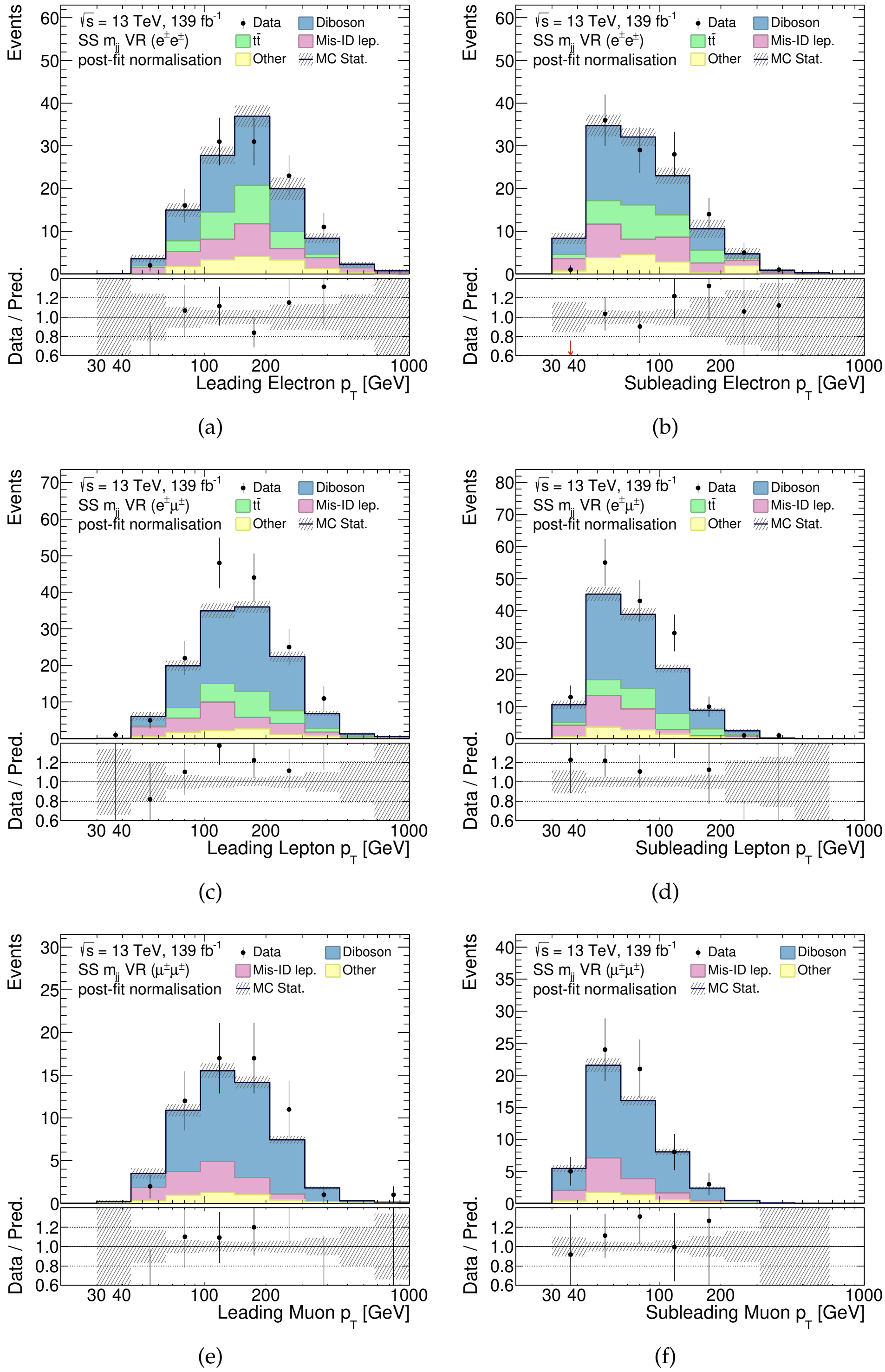

Figure B.7: Leading and sub-leading lepton momentum distributions in cut-based same-sign validation regions for all flavour combinations. Post-fit normalisation scales are applied. Uncertainties are statistical only.

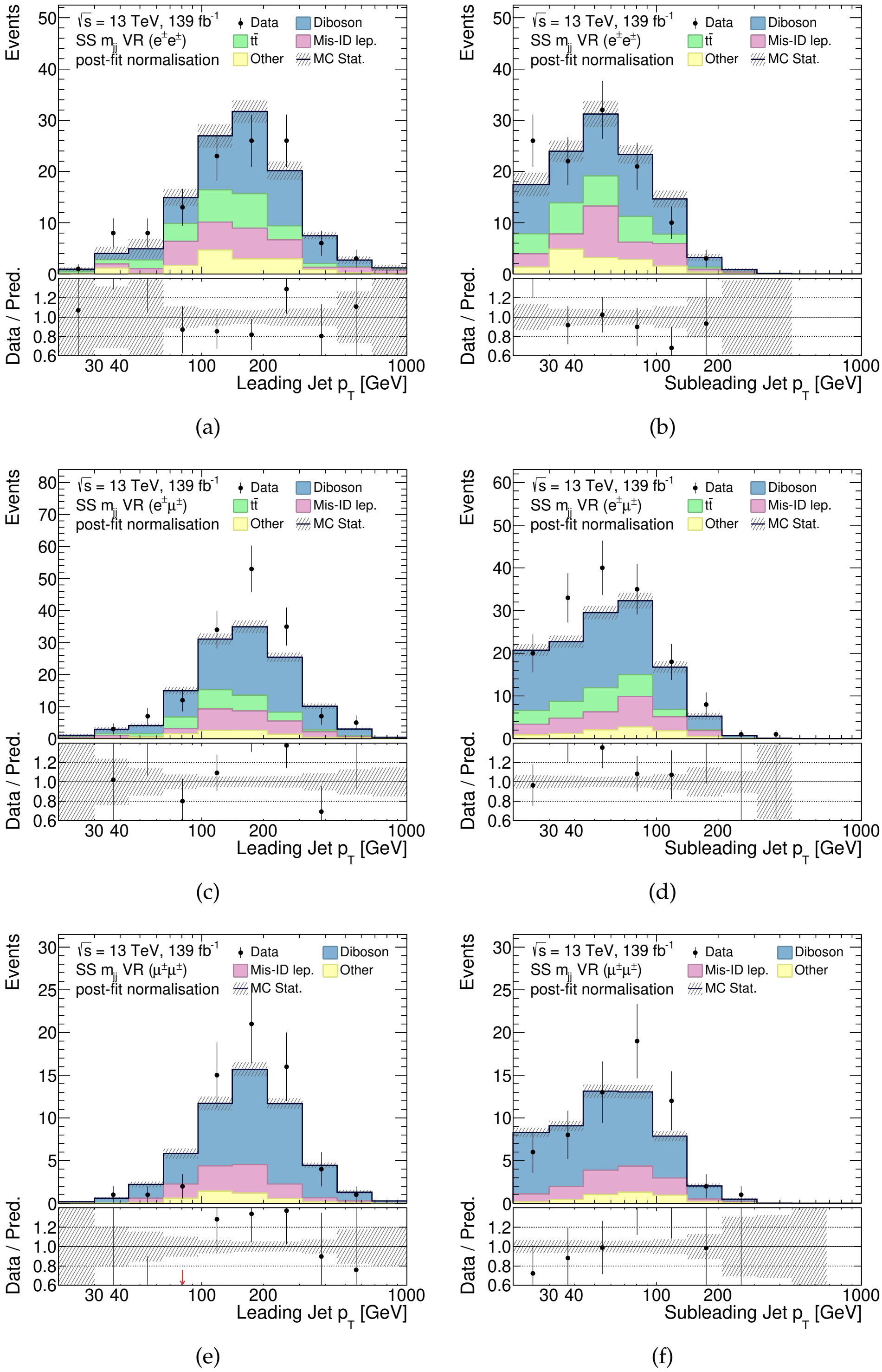

Figure B.8: Leading and sub-leading jet momentum distributions in cut-based same-sign validation regions for all flavour combinations. Post-fit normalisation scales are applied. Uncertainties are statistical only.

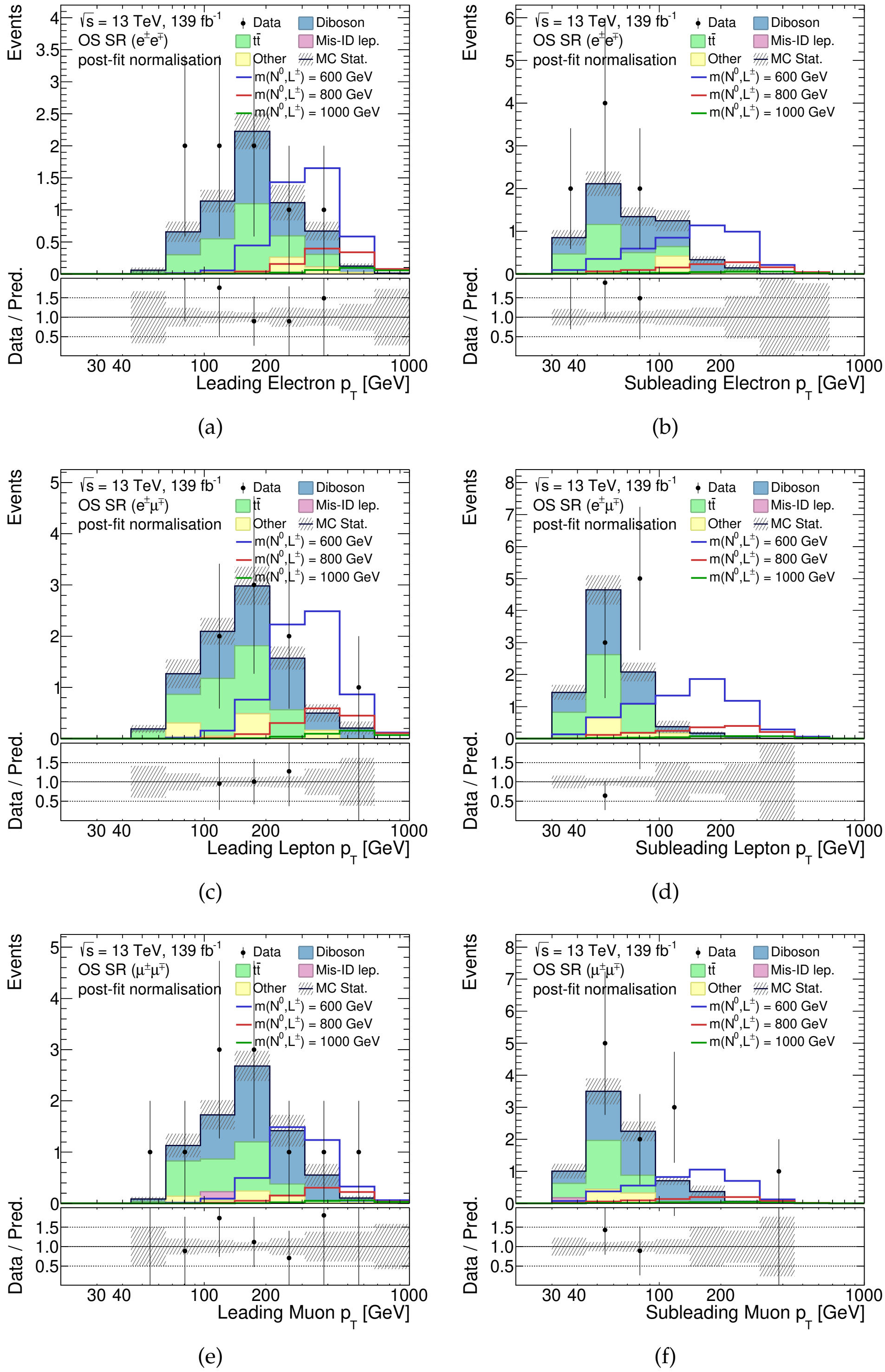

Figure B.9: Leading and sub-leading lepton momentum distributions in cut-based opposite-sign signal regions for all flavour combinations. Post-fit normalisation scales are applied. Uncertainties are statistical only.

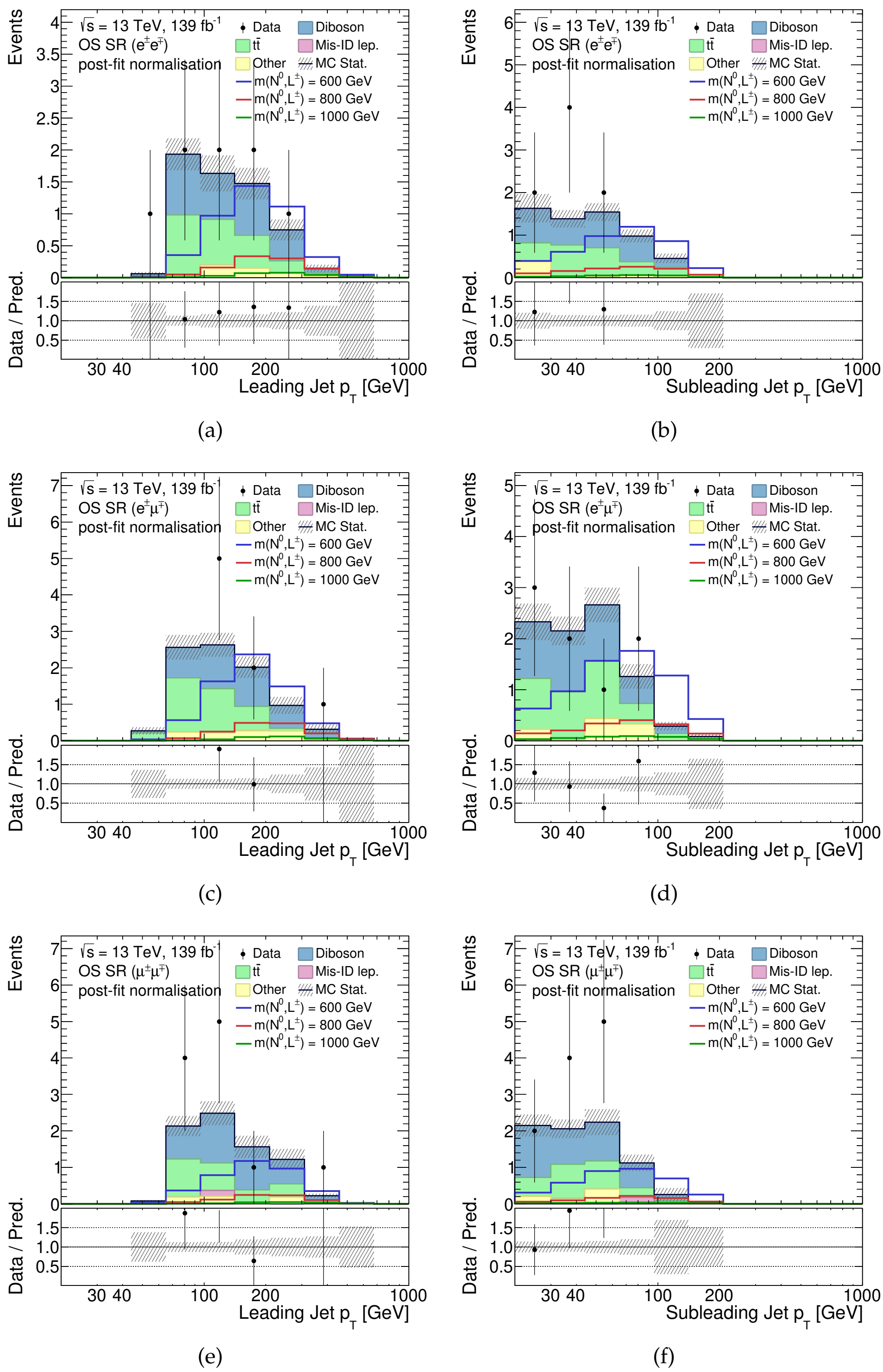

Figure B.10: Leading and sub-leading jet momentum distributions in cut-based opposite-sign signal regions for all flavour combinations. Post-fit normalisation scales are applied. Uncertainties are statistical only.

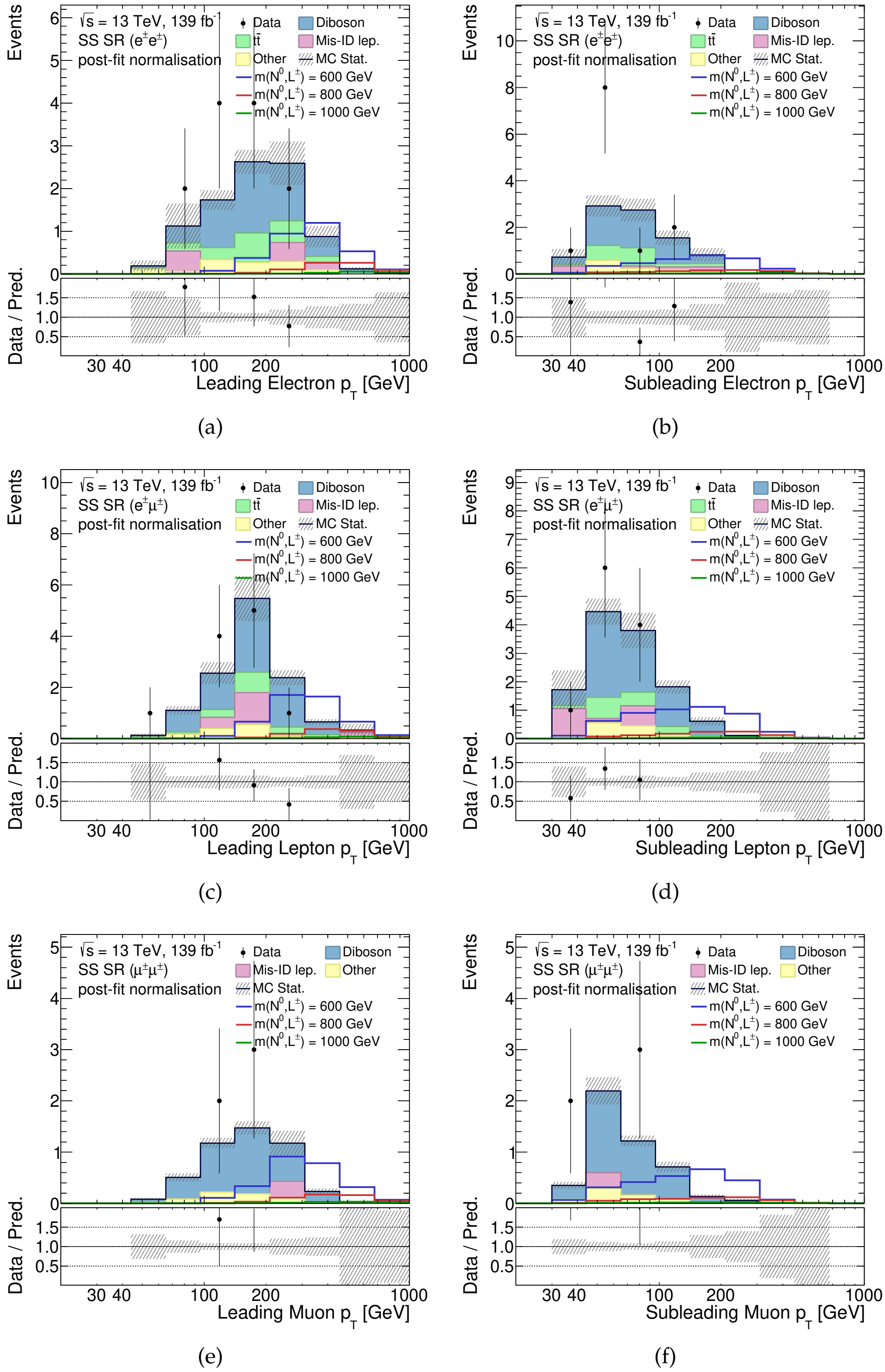

Figure B.11: Leading and sub-leading lepton momentum distributions in cut-based same-sign signal regions for all flavour combinations. Post-fit normalisation scales are applied. Uncertainties are statistical only.

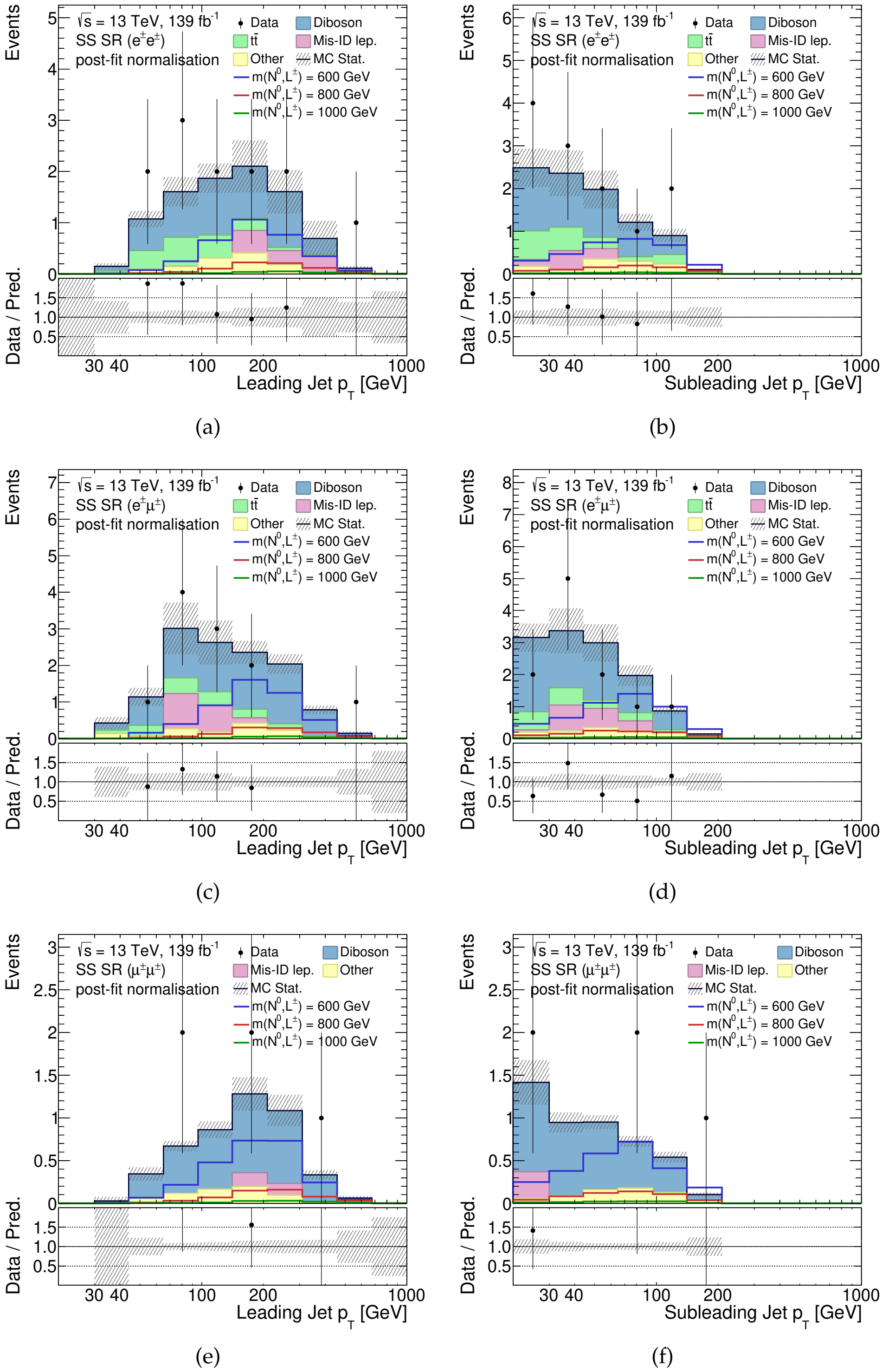

Figure B.12: Leading and sub-leading jet momentum distributions in cut-based same-sign signal regions for all flavour combinations. Post-fit normalisation scales are applied. Uncertainties are statistical only.

APPENDIX C

Selected Distributions of the Multivariate Analysis Regions

Selected kinematic distributions are presented to illustrate good agreement between expected and observed events in all multivariate analysis regions. Transverse momenta for leading and sub-leading leptons and jets are shown in following figures:

- Top control regions in Figures C.1 and C.2,
- opposite-sign control regions in Figures C.3 and C.4,
- same-sign control regions in Figures C.5 and C.6,
- opposite-sign validation regions in Figures C.7 and C.8,
- same-sign validation regions in Figures C.9 and C.10,
- opposite-sign signal regions in Figures C.11 and C.12,
- same-sign signal region in Figures C.13 and C.14.

Each of the presented figures has leading lepton or jet p_{T} distribution in the first column and sub-leading lepton or jet p_{T} in the second one. The ee channel is shown in the first row, the $e\mu$ channel in the second row, and the $\mu\mu$ channel in the last row.

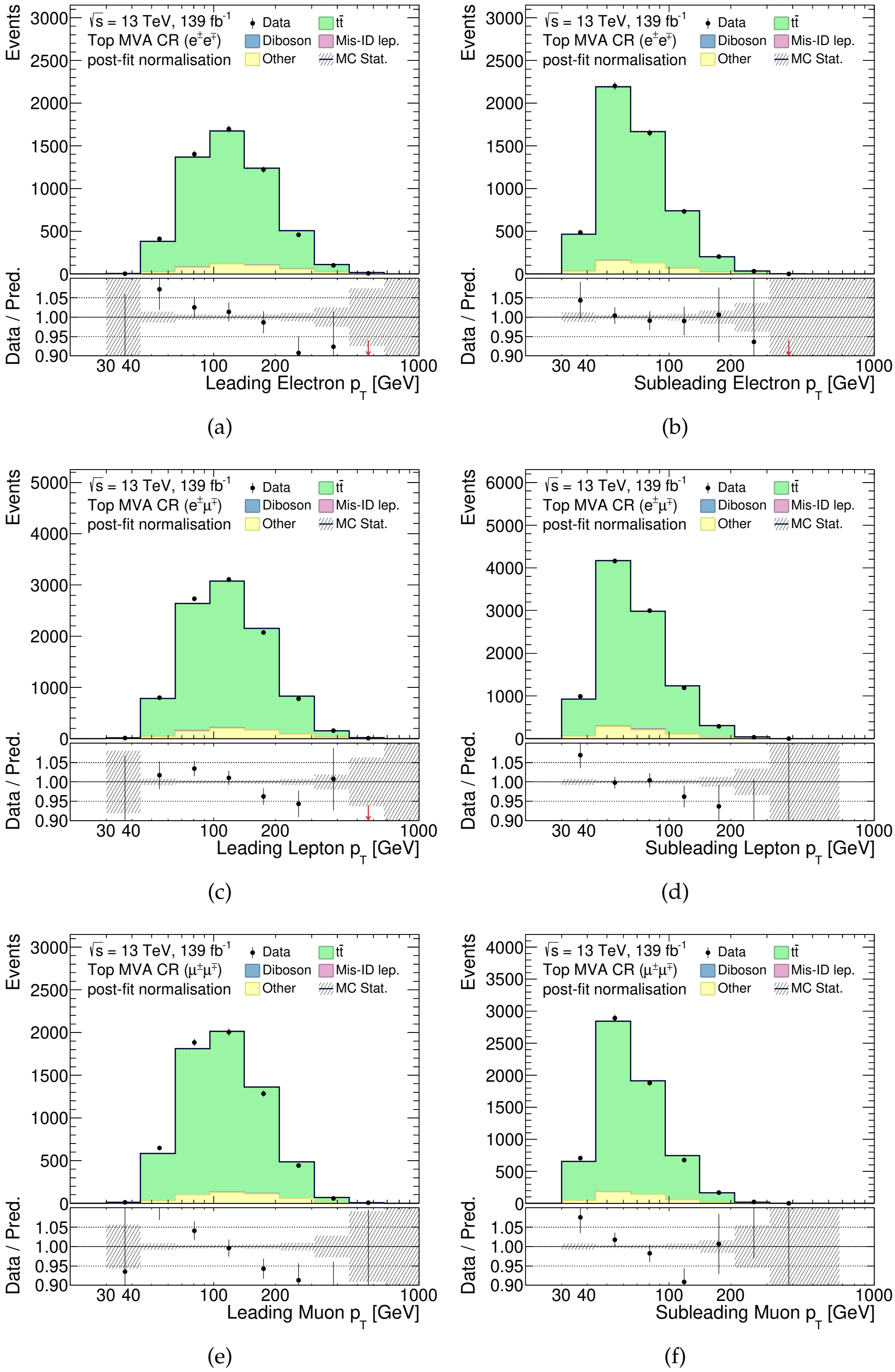

Figure C.1: Leading and sub-leading lepton momentum distributions in multivariate Top control regions for all flavour combinations. Post-fit normalisation scales are applied. Uncertainties are statistical only.

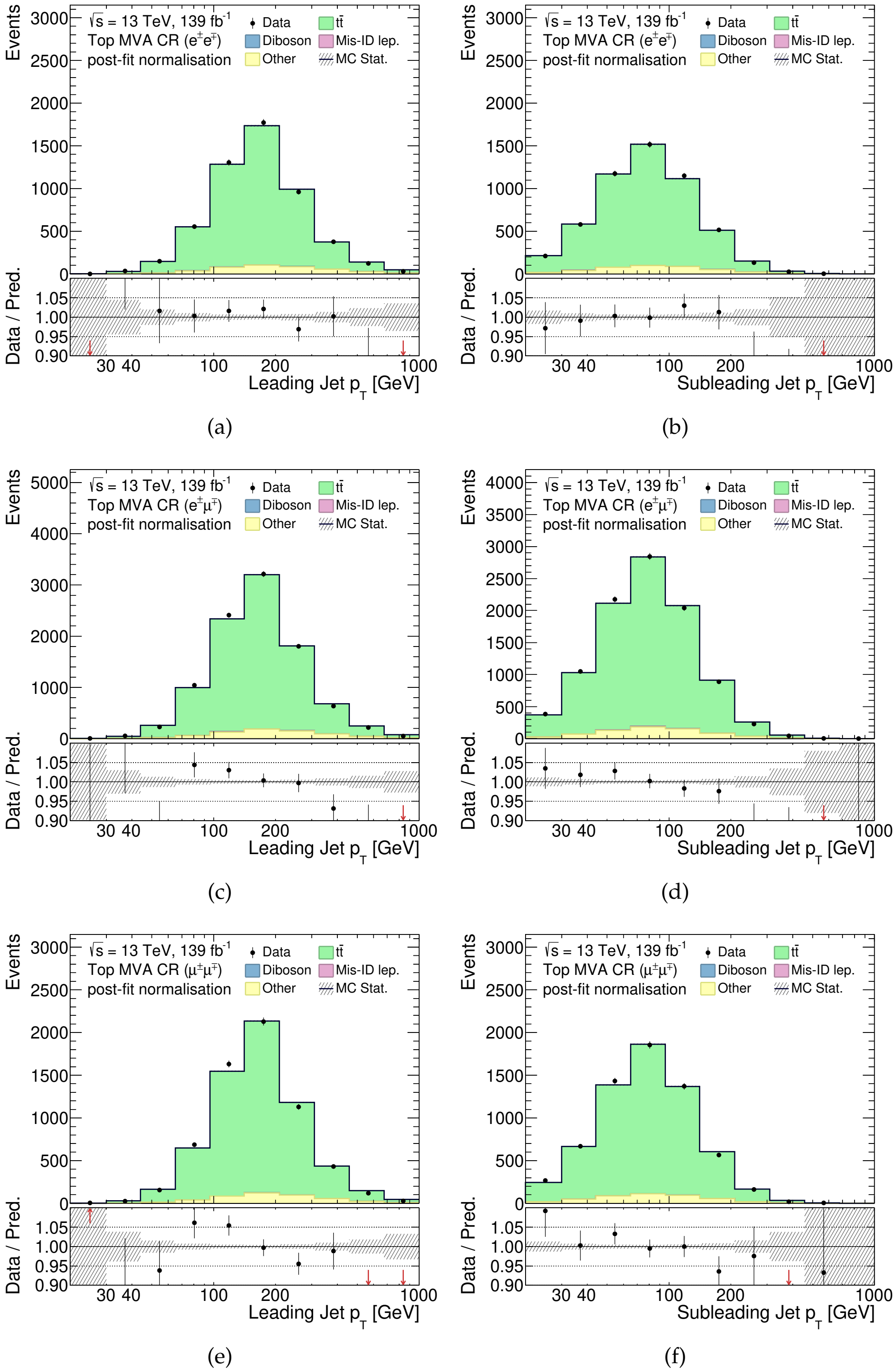

Figure C.2: Leading and sub-leading jet momentum distributions in multivariate Top control regions for all flavour combinations. Post-fit normalisation scales are applied. Uncertainties are statistical only.

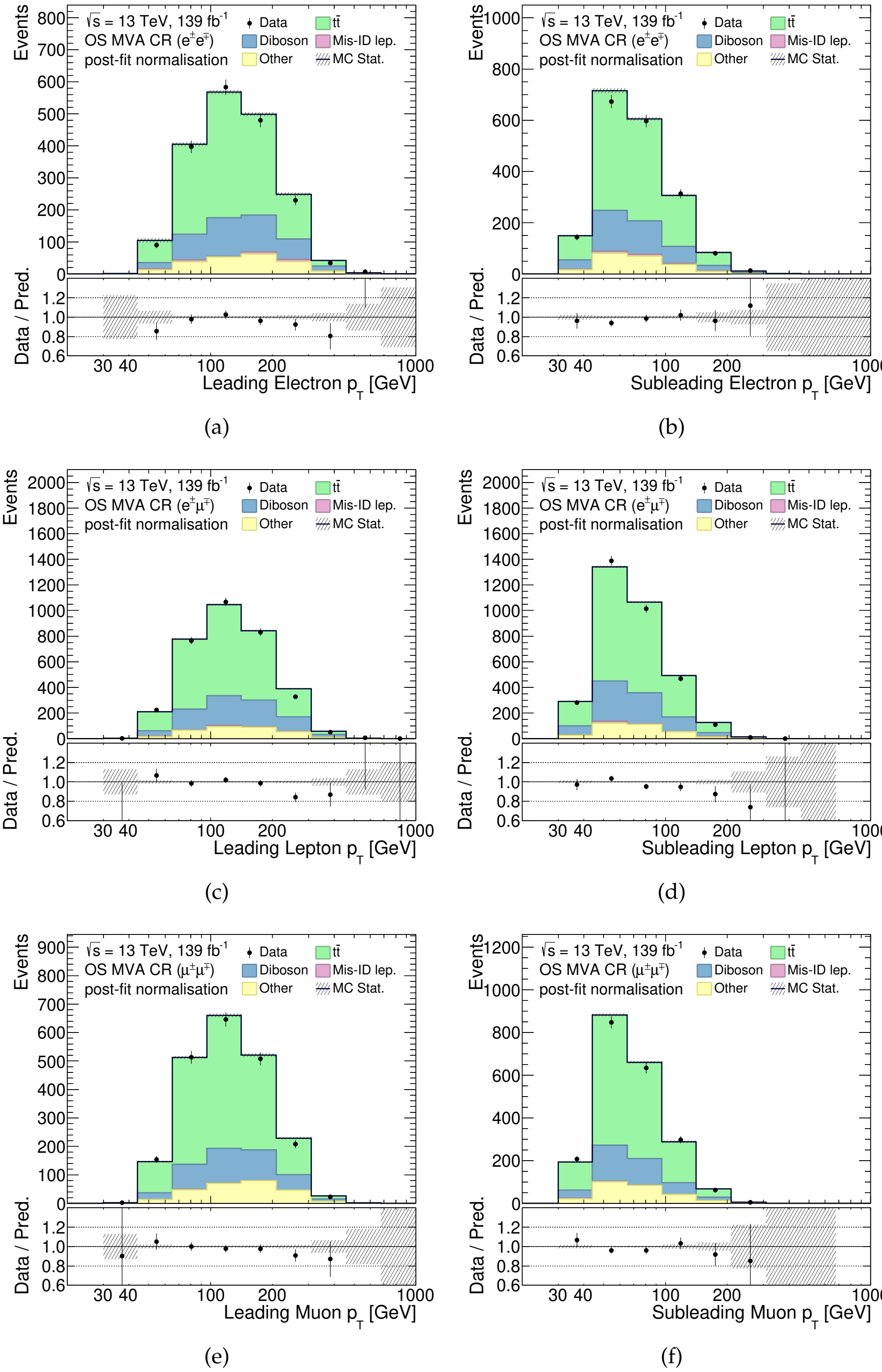

Figure C.3: Leading and sub-leading lepton momentum distributions in multivariate opposite-sign control regions for all flavour combinations. Post-fit normalisation scales are applied. Uncertainties are statistical only.

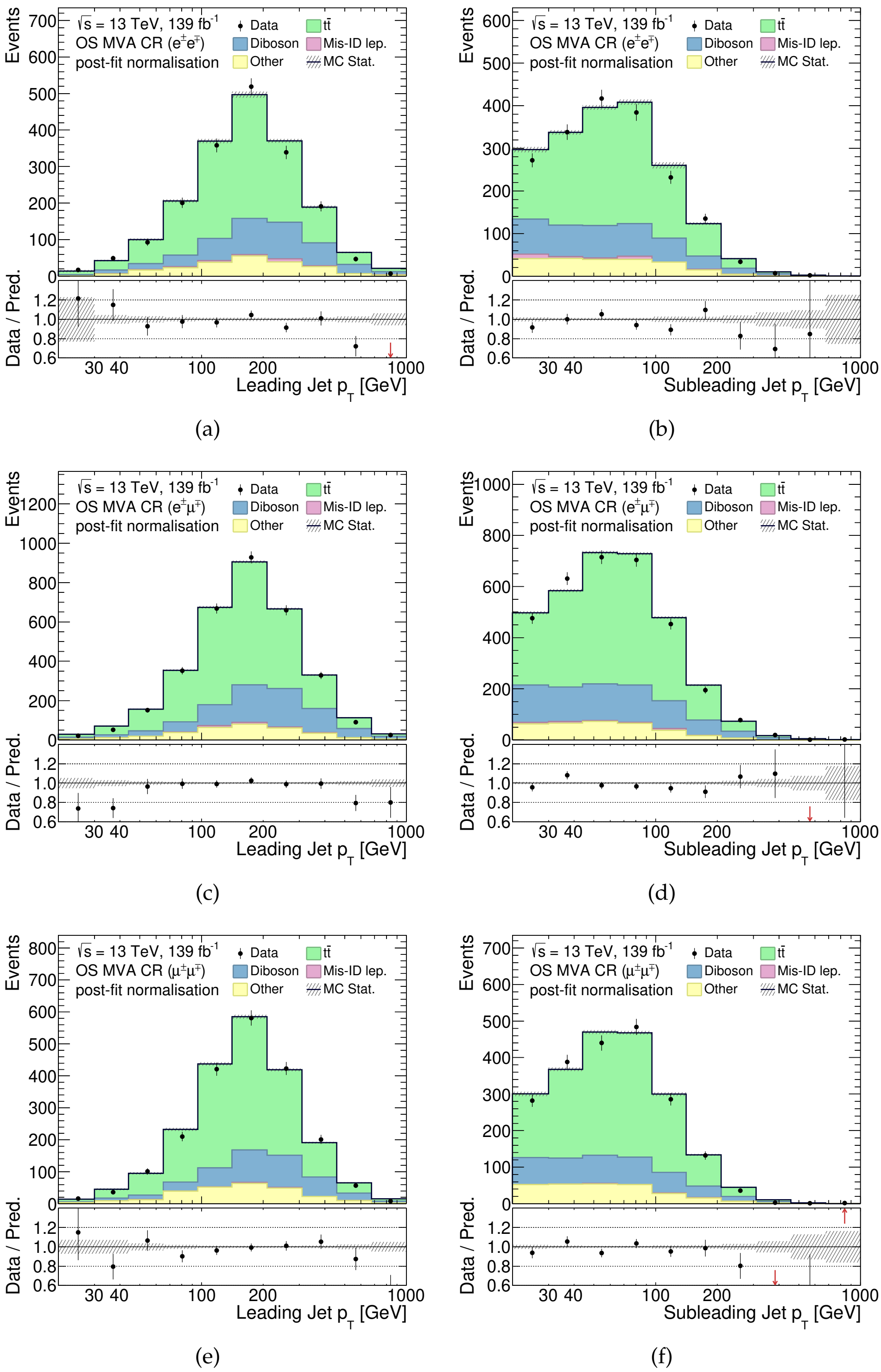

Figure C.4: Leading and sub-leading jet momentum distributions in multivariate opposite-sign control regions for all flavour combinations. Post-fit normalisation scales are applied. Uncertainties are statistical only.

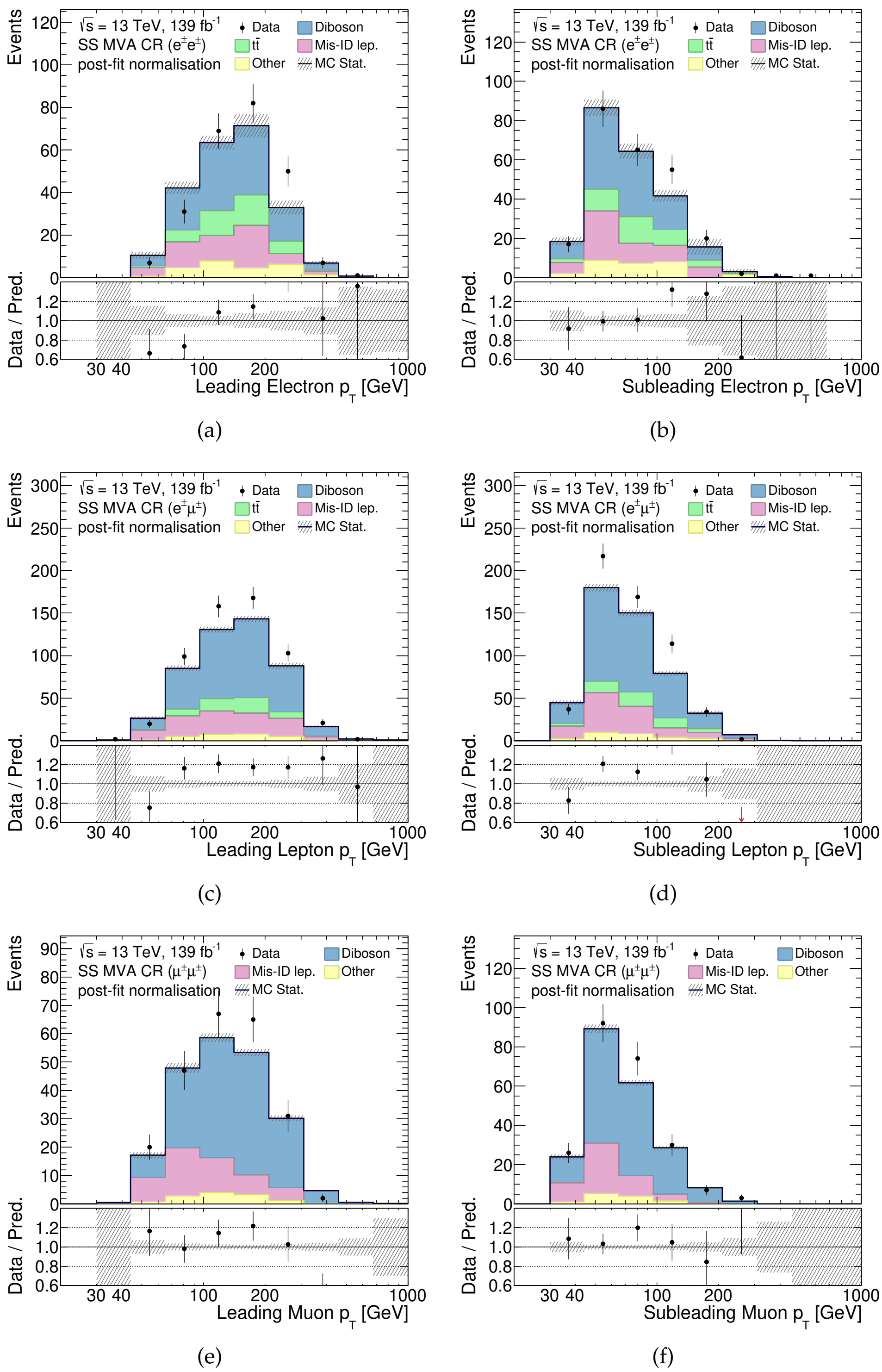

Figure C.5: Leading and sub-leading lepton momentum distributions in multivariate same-sign control regions for all flavour combinations. Post-fit normalisation scales are applied. Uncertainties are statistical only.

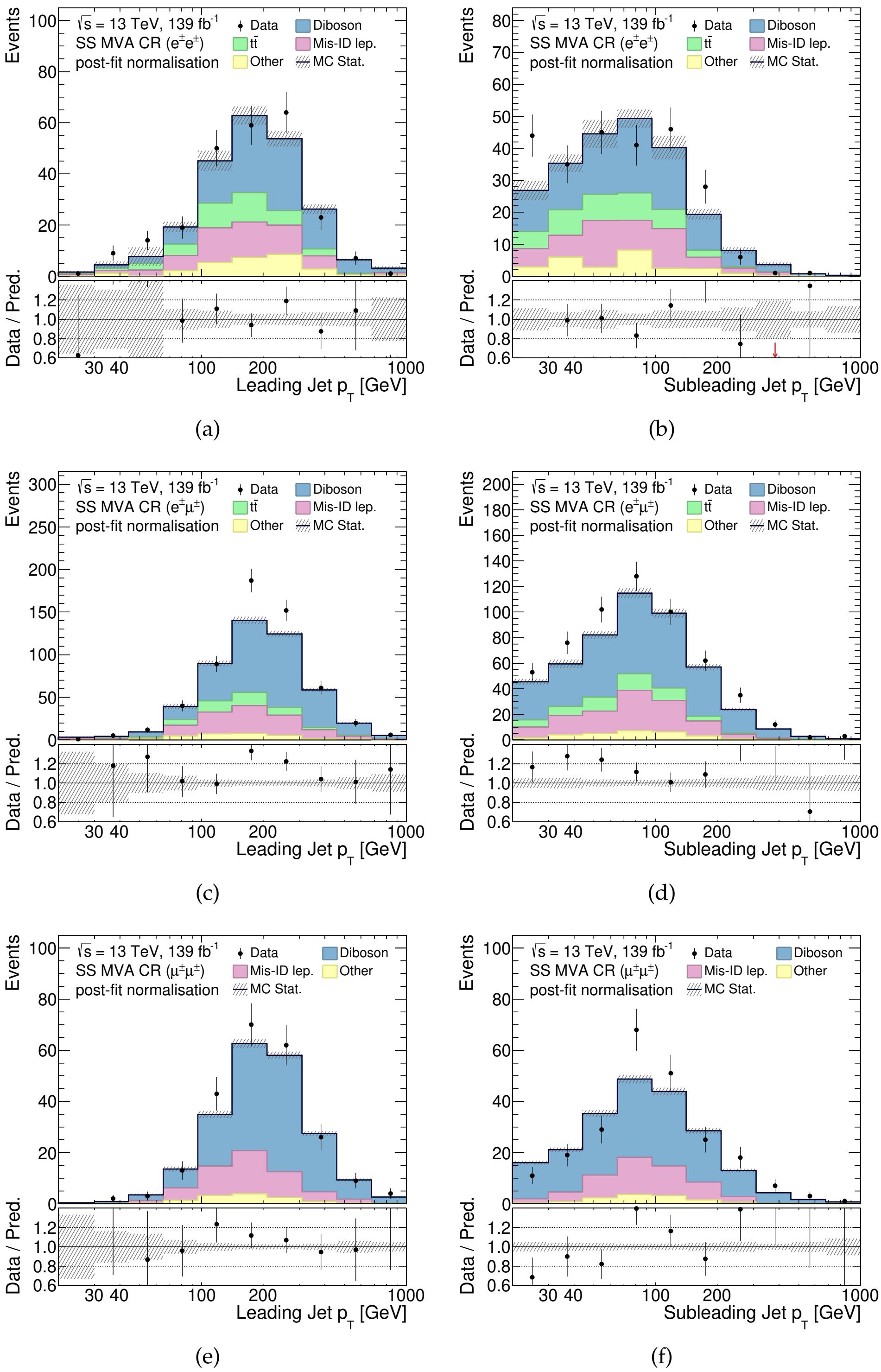

Figure C.6: Leading and sub-leading jet momentum distributions in multivariate same-sign control regions for all flavour combinations. Post-fit normalisation scales are applied. Uncertainties are statistical only.

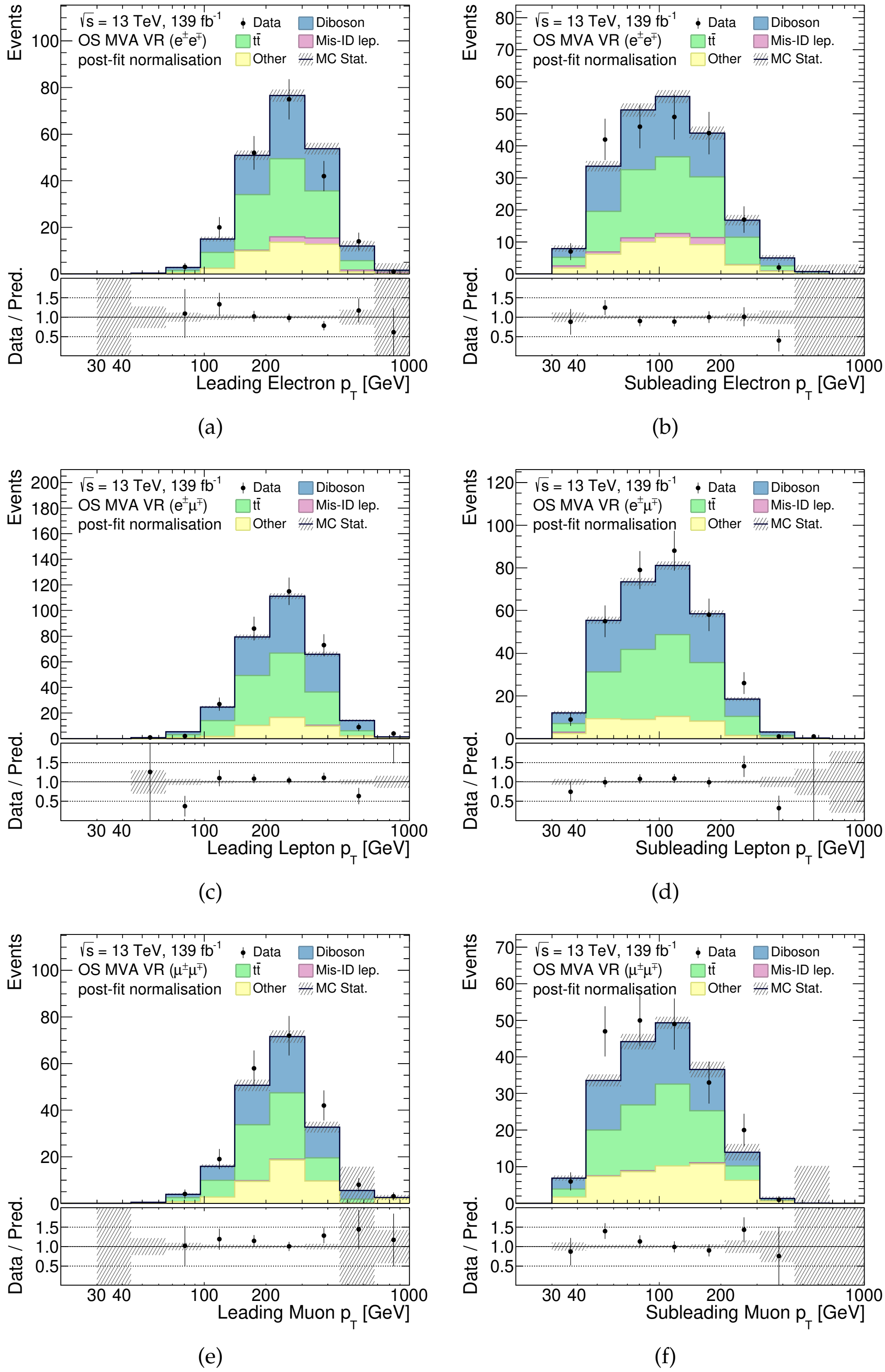

Figure C.7: Leading and sub-leading lepton momentum distributions in multivariate opposite-sign validation regions for all flavour combinations. Post-fit normalisation scales are applied. Uncertainties are statistical only.

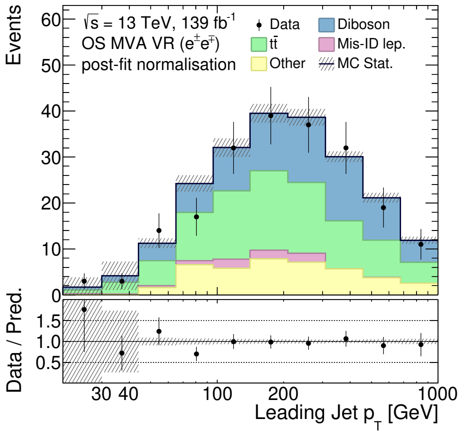

(a)

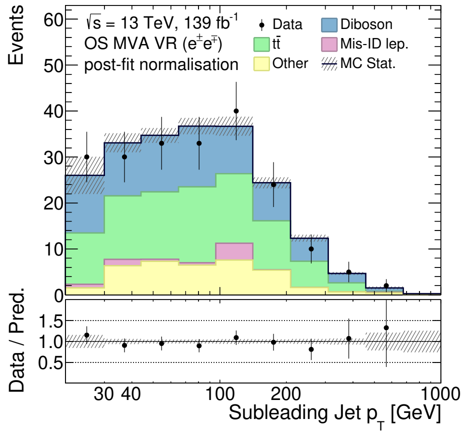

(b)

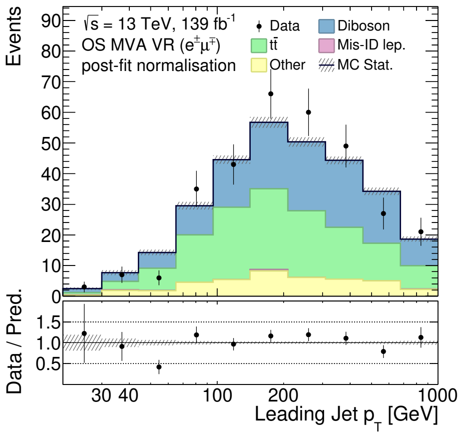

(c)

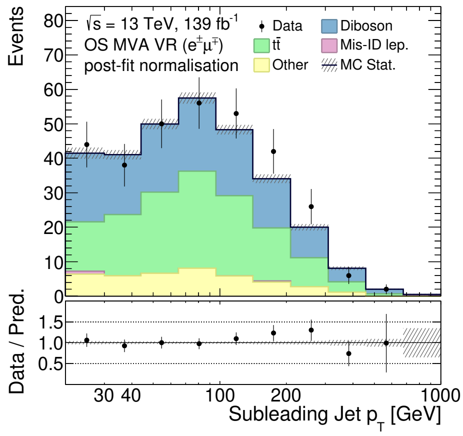

(d)

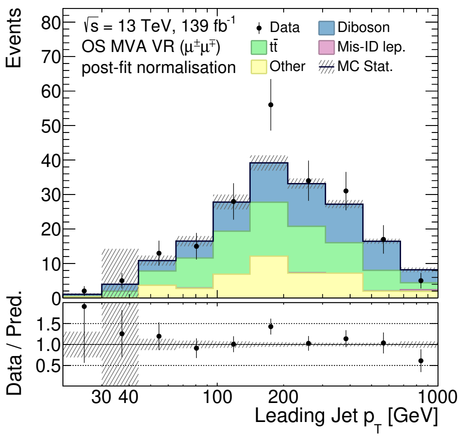

(e)

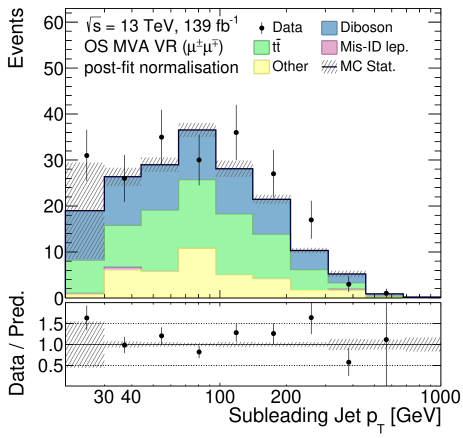

(f)

Figure C.8: Leading and sub-leading jet momentum distributions in multivariate opposite-sign validation regions for all flavour combinations. Post-fit normalisation scales are applied. Uncertainties are statistical only.

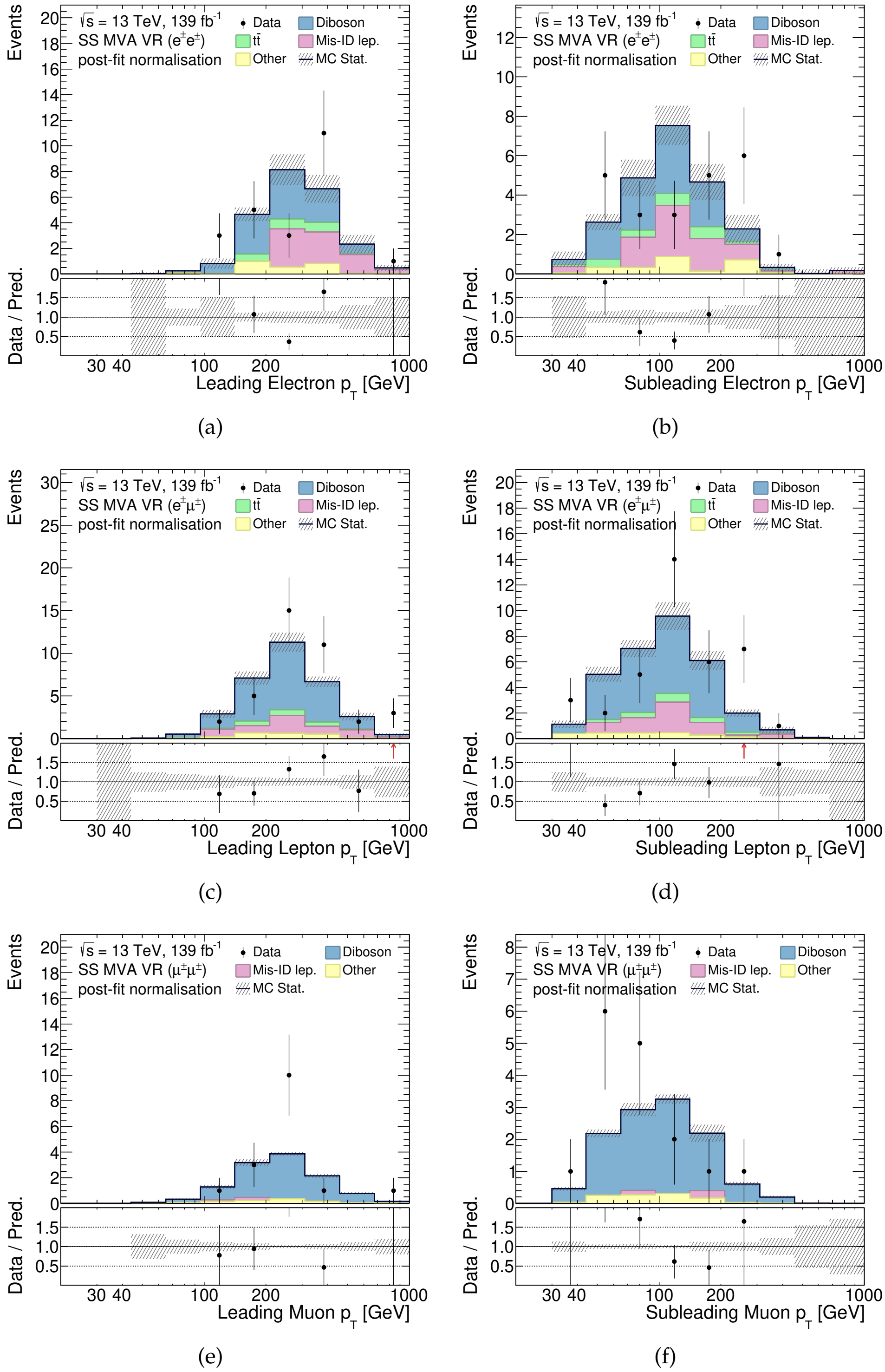

Figure C.9: Leading and sub-leading lepton momentum distributions in multivariate same-sign validation regions for all flavour combinations. Post-fit normalisation scales are applied. Uncertainties are statistical only.

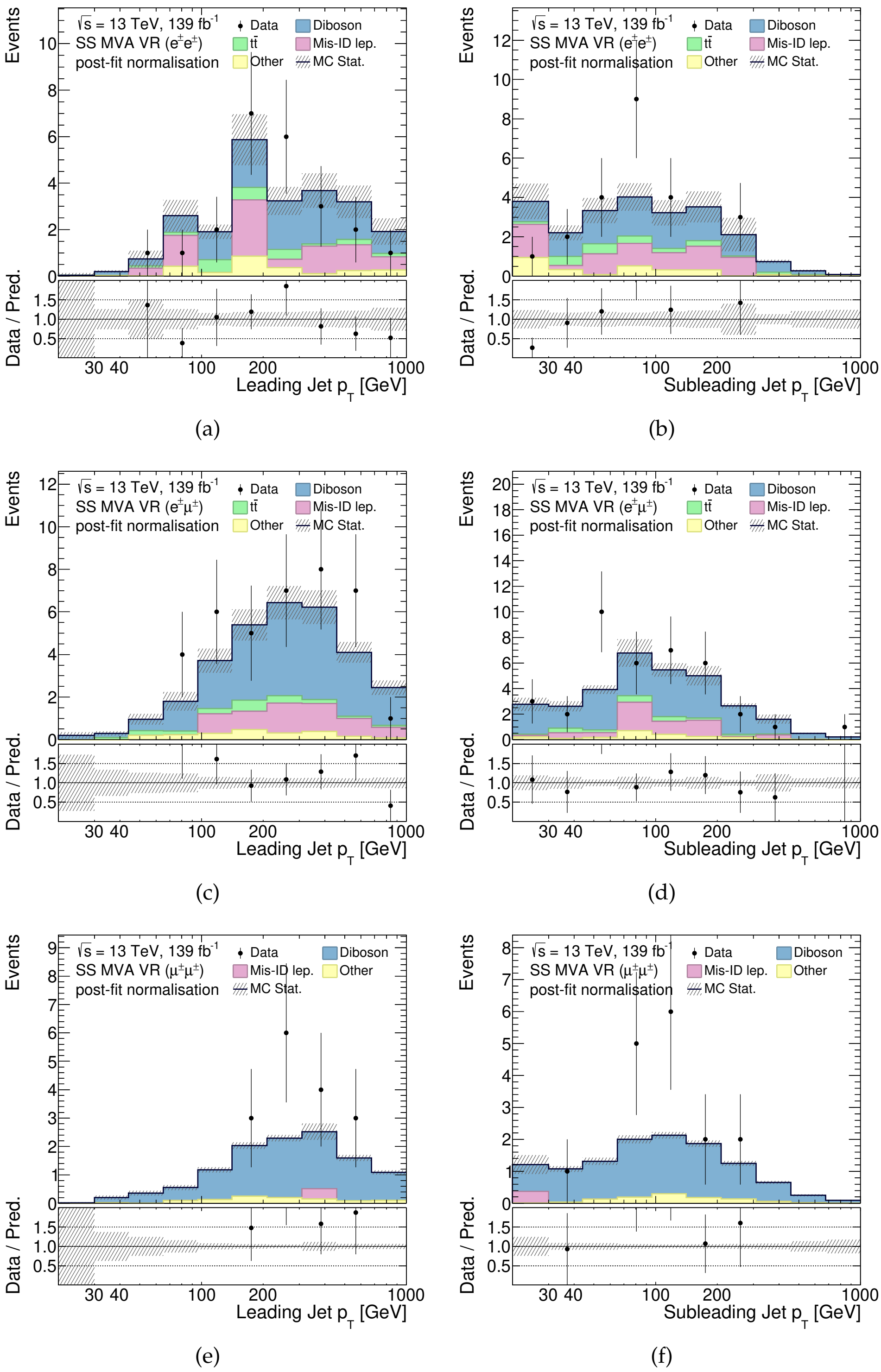

Figure C.10: Leading and sub-leading jet momentum distributions in multivariate same-sign validation regions for all flavour combinations. Post-fit normalisation scales are applied. Uncertainties are statistical only.

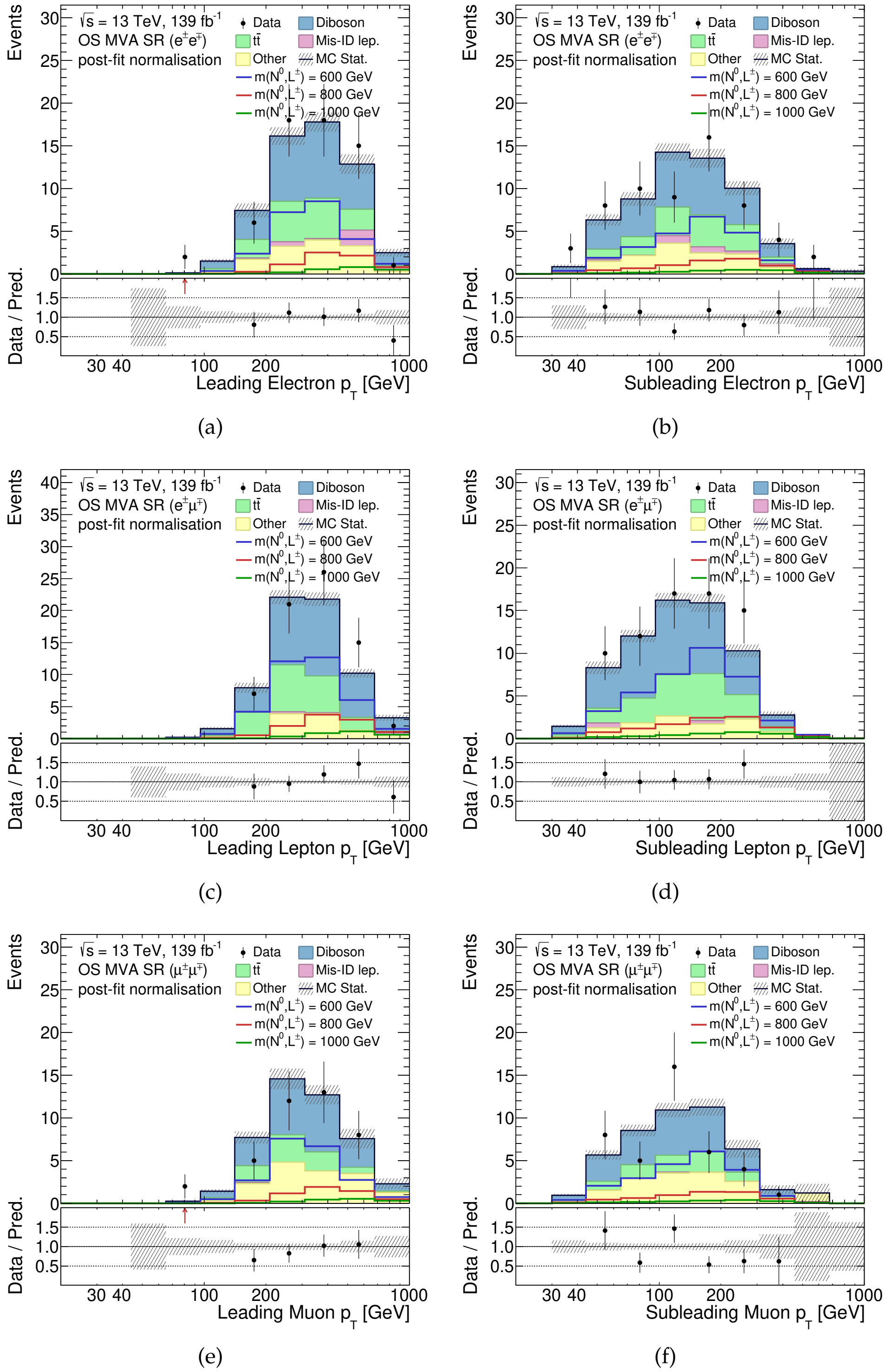

Figure C.11: Leading and sub-leading lepton momentum distributions in multivariate opposite-sign signal regions for all flavour combinations. Post-fit normalisation scales are applied. Uncertainties are statistical only.

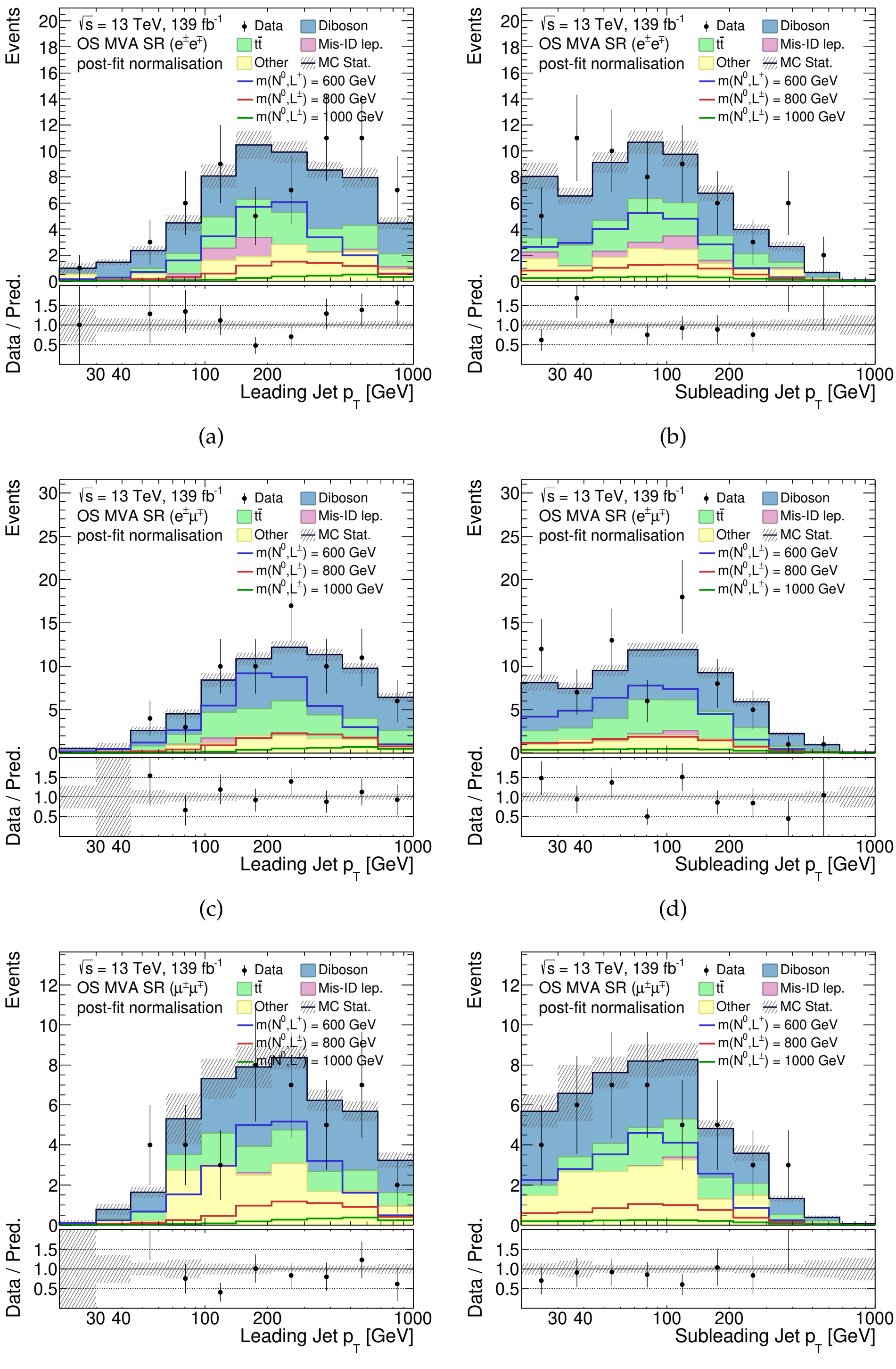

(a) (b)

(c) (d)

(e) (f)

Figure C.12: Leading and sub-leading jet momentum distributions in multivariate opposite-sign signal regions for all flavour combinations. Post-fit normalisation scales are applied. Uncertainties are statistical only.

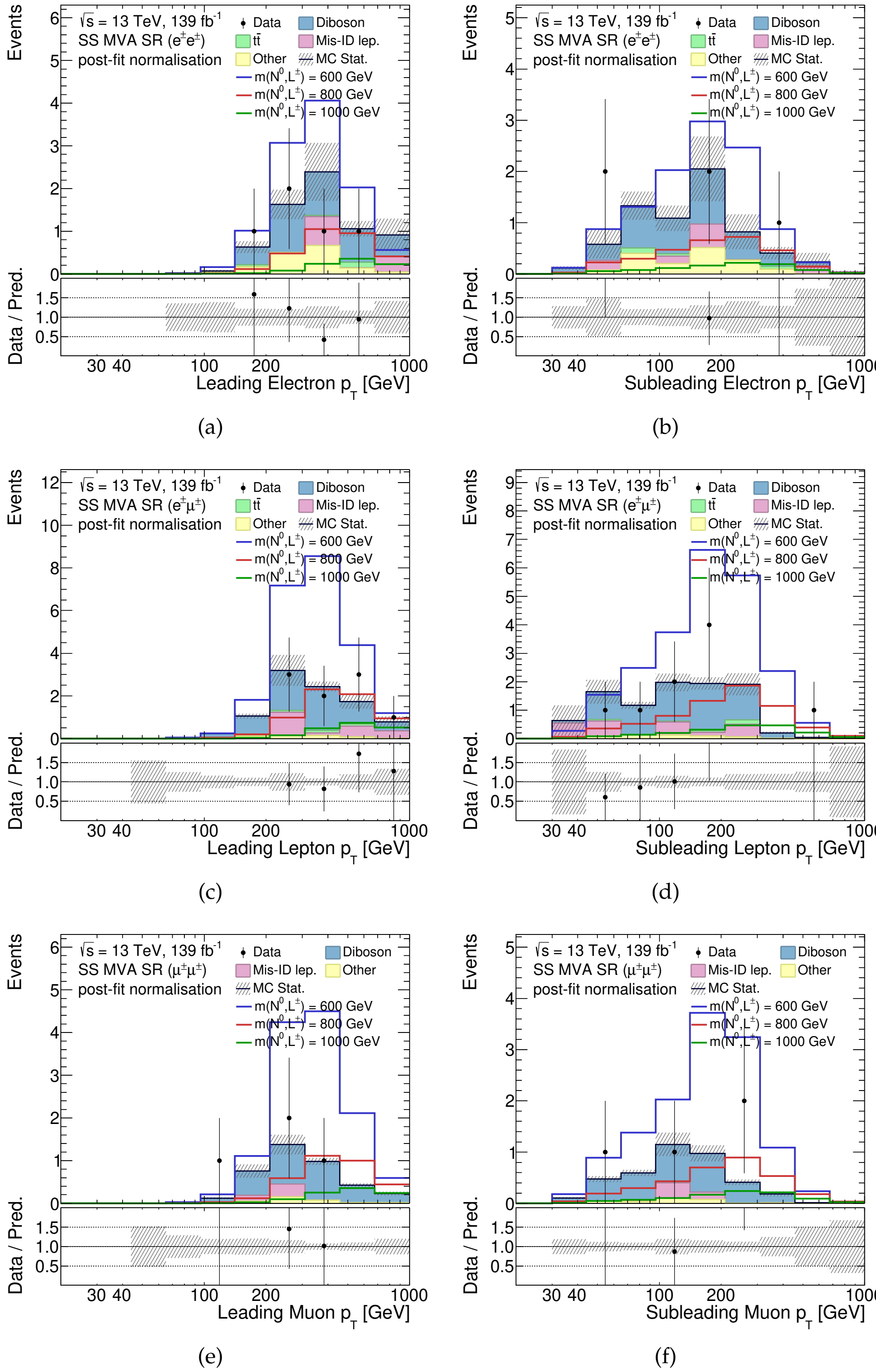

Figure C.13: Leading and sub-leading lepton momentum distributions in multivariate same-sign signal regions for all flavour combinations. Post-fit normalisation scales are applied. Uncertainties are statistical only.

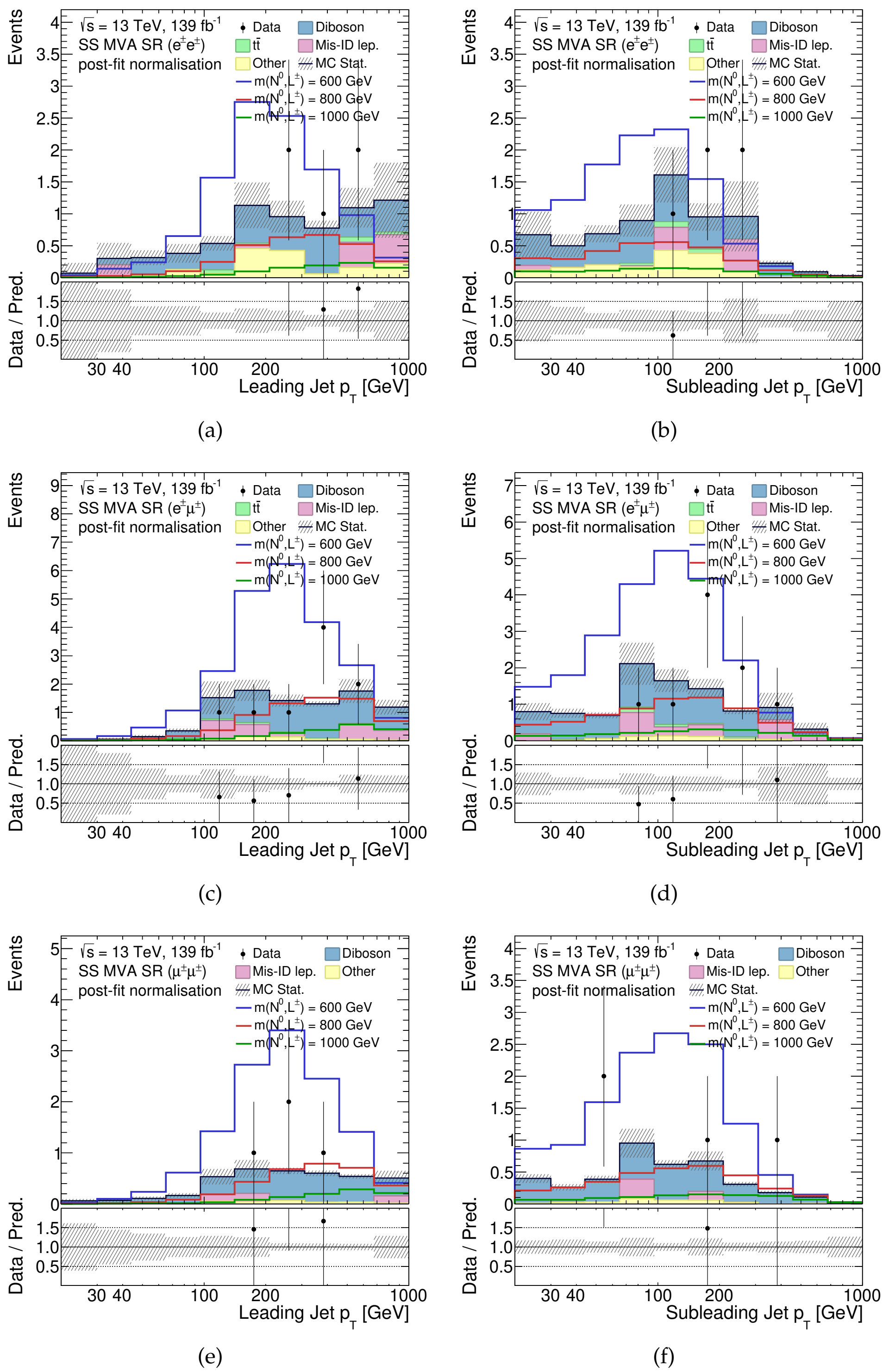

(a) (b)

(c) (d)

(e) (f)

Figure C.14: Leading and sub-leading jet momentum distributions in multivariate same-sign signal regions for all flavour combinations. Post-fit normalisation scales are applied. Uncertainties are statistical only.

BIBLIOGRAPHY

[1] M. Tanabashi et al., *Review of Particle Physics*, Phys. Rev. D **98** (2018) 030001 (cit. on p. 4).

[2] M. Gell-Mann, *A Schematic Model of Baryons and Mesons*, Phys. Lett. **8** (1964) 214 (cit. on pp. 4, 183).

[3] G. Zweig, 'An SU(3) model for strong interaction symmetry and its breaking. Version 2', *Developments in the Quark Theory of Hadrons, Volume 1. 1964 - 1978*, ed. by D. Lichtenberg and S. P. Rosen, 1964 22 (cit. on pp. 4, 183).

[4] D. J. Gross and F. Wilczek, *Ultraviolet Behavior of Nonabelian Gauge Theories*, Phys. Rev. Lett. **30** (1973) 1343, ed. by J. Taylor (cit. on pp. 4, 183).

[5] H. Politzer, *Reliable Perturbative Results for Strong Interactions?*, Phys. Rev. Lett. **30** (1973) 1346, ed. by J. Taylor (cit. on pp. 4, 183).

[6] S. Glashow, *Partial Symmetries of Weak Interactions*, Nucl. Phys. **22** (1961) 579 (cit. on pp. 4, 183).

[7] S. Weinberg, *A Model of Leptons*, Phys. Rev. Lett. **19** (1967) 1264 (cit. on pp. 4, 6, 183).

[8] A. Salam, *Weak and Electromagnetic Interactions*, Conf. Proc. C **680519** (1968) 367 (cit. on pp. 4, 183).

[9] F. Englert and R. Brout, *Broken Symmetry and the Mass of Gauge Vector Mesons*, Phys. Rev. Lett. **13** (1964) 321, ed. by J. Taylor (cit. on pp. 4, 183).

[10] P. W. Higgs, *Broken Symmetries and the Masses of Gauge Bosons*, Phys. Rev. Lett. **13** (1964) 508, ed. by J. Taylor (cit. on pp. 4, 183).

[11] ATLAS Collaboration, *Observation of a new particle in the search for the Standard Model Higgs boson with the ATLAS detector at the LHC*, Phys. Lett. B **716** (2012) 1, arXiv: `1207.7214 [hep-ex]` (cit. on pp. 5, 183).

[12] CMS Collaboration, *Observation of a new boson at a mass of 125 GeV with the CMS experiment at the LHC*, Phys. Lett. B **716** (2012) 30, arXiv: `1207.7235 [hep-ex]` (cit. on pp. 5, 183).

[13] M. Gell-Mann, *The interpretation of the new particles as displaced charge multiplets*, Nuovo Cim. **4** (1956) 848 (cit. on p. 5).

[14] K. Nishijima, *Charge Independence Theory of V Particles*, Prog. Theor. Phys. **13** (1955) 285 (cit. on p. 5).

[15] C. Wu, E. Ambler, R. Hayward, D. Hoppes and R. Hudson, *Experimental Test of Parity Conservation in β Decay*, Phys. Rev. **105** (1957) 1413 (cit. on p. 5).

[16] R. Garwin, L. Lederman and M. Weinrich, *Observations of the Failure of Conservation of Parity and Charge Conjugation in Meson Decays: The Magnetic Moment of the Free Muon*, Phys. Rev. **105** (1957) 1415 (cit. on p. 5).

[17] M. Goldhaber, L. Grodzins and A. Sunyar, *Helicity of Neutrinos*, Phys. Rev. **109** (1958) 1015 (cit. on p. 5).

[18] J. Goldstone, A. Salam and S. Weinberg, *Broken Symmetries*, Phys. Rev. **127** (1962) 965 (cit. on p. 6).

[19] H. Yukawa, *On the Interaction of Elementary Particles I*, Proc. Phys. Math. Soc. Jap. **17** (1935) 48 (cit. on p. 6).

[20] N. Cabibbo, *Unitary Symmetry and Leptonic Decays*, Phys. Rev. Lett. **10** (1963) 531 (cit. on p. 7).

[21] M. Kobayashi and T. Maskawa, *CP Violation in the Renormalizable Theory of Weak Interaction*, Prog. Theor. Phys. **49** (1973) 652 (cit. on p. 7).

[22] B. Pontecorvo, *Mesonium and anti-mesonium*, Sov. Phys. JETP **6** (1957) 429 (cit. on p. 8).

[23] B. Pontecorvo, *Neutrino Experiments and the Problem of Conservation of Leptonic Charge*, Sov. Phys. JETP **26** (1968) 984 (cit. on p. 8).

[24] Z. Maki, M. Nakagawa and S. Sakata, *Remarks on the unified model of elementary particles*, Prog. Theor. Phys. **28** (1962) 870 (cit. on p. 8).

[25] E. Majorana, *Teoria simmetrica dell'elettrone e del positrone*, Nuovo Cim. **14** (1937) 171 (cit. on p. 8).

[26] Y. Fukuda et al., *Evidence for oscillation of atmospheric neutrinos*, Phys. Rev. Lett. **81** (1998) 1562, arXiv: `hep-ex/9807003` (cit. on pp. 8, 183).

[27] Q. Ahmad et al., *Direct evidence for neutrino flavor transformation from neutral current interactions in the Sudbury Neutrino Observatory*, Phys. Rev. Lett. **89** (2002) 011301, arXiv: `nucl-ex/0204008` (cit. on pp. 8, 183).

[28] P. Minkowski, *$\mu \to e\gamma$ at a rate of one out of 10^9 muon decays?*, Phys. Lett. B **67** (1977) 421 (cit. on pp. 9, 184).

[29] T. Yanagida, *Proceedings of the Workshop on Unified Theory and the Baryon Number in the Universe*, KEK Report No. 79-18 **95** (1979), ed. A. Sawada, A. Sugamoto (cit. on pp. 9, 184).

[30] S. Glashow, *Proceedings of the 1979 Cargèse Summer Institute on Quarks and Leptons*, 1980 (cit. on pp. 9, 184).

[31] M. Gell-Mann, P. Ramond and R. Slansky, *Supergravity: Proceedings of the Supergravity Workshop at Stony Brook, New York, 1979*, ed. P. Van Niewenhuizen, D. Freeman, 1980 (cit. on pp. 9, 184).

[32] R. N. Mohapatra and G. Senjanović, *Neutrino Mass and Spontaneous Parity Nonconservation*, Phys. Rev. Lett. **44** (1980) 912, [,231(1979)] (cit. on pp. 9, 184).

[33] M. Magg and C. Wetterich, *Neutrino Mass Problem and Gauge Hierarchy*, Phys. Lett. B **94** (1980) 61 (cit. on pp. 9, 184).

[34] G. Lazarides, Q. Shafi and C. Wetterich, *Proton Lifetime and Fermion Masses in an SO(10) Model*, Nucl. Phys. B **181** (1981) 287 (cit. on pp. 9, 184).

[35] R. N. Mohapatra and G. Senjanović, *Neutrino Masses and Mixings in Gauge Models with Spontaneous Parity Violation*, Phys. Rev. D **23** (1981) 165 (cit. on pp. 9, 184).

[36] R. Foot, H. Lew, X. G. He and G. C. Joshi, *See-saw neutrino masses induced by a triplet of leptons*, Z. Phys. C **44** (1989) 441 (cit. on pp. 9, 184).

[37] B. Bajc and G. Senjanović, *Seesaw at LHC*, JHEP **08** (2007) 014, arXiv: `hep-ph/0612029` (cit. on pp. 9, 184).

[38] B. Bajc, M. Nemevšek and G. Senjanović, *Probing seesaw at LHC*, Phys. Rev. D **76** (2007) 055011, arXiv: `hep-ph/0703080` (cit. on pp. 9, 184).

[39] R. Franceschini, T. Hambye and A. Strumia, *Type-III seesaw mechanism at CERN LHC*, Phys. Rev. D **78** (2008) 033002, arXiv: `0805.1613 [hep-ph]` (cit. on p. 10).

[40] C. Biggio and F. Bonnet, *Implementation of the type III seesaw model in FeynRules / MadGraph and prospects for discovery with early LHC data*, Eur. Phys. J. C **72** (2012) 1899, arXiv: `1107.3463 [hep-ph]` (cit. on pp. 10, 12, 41, 184).

[41] F. del Aguila, J. de Blas and M. Perez-Victoria, *Effects of new leptons in Electroweak Precision Data*, Phys. Rev. D **78** (2008) 013010, arXiv: `0803.4008 [hep-ph]` (cit. on p. 11).

[42] A. Abada, C. Biggio, F. Bonnet, M. B. Gavela and T. Hambye, *mu —> e gamma and tau —> l gamma decays in the fermion triplet seesaw model*, Phys. Rev. D **78** (2008) 033007, arXiv: `0803.0481 [hep-ph]` (cit. on p. 11).

[43] A. Abada, C. Biggio, F. Bonnet, M. B. Gavela and T. Hambye, *Low energy effects of neutrino masses*, JHEP **12** (2007) 061, arXiv: `0707.4058 [hep-ph]` (cit. on p. 11).

[44] ATLAS Collaboration, *Search for type-III seesaw heavy leptons in pp collisions at $\sqrt{s} = 8$ TeV with the ATLAS Detector*, Phys. Rev. D **92** (2015) 032001, arXiv: `1506.01839 [hep-ex]` (cit. on pp. 11, 185).

[45] ATLAS Collaboration, *Search for heavy lepton resonances decaying to a Z boson and a lepton in pp collisions at $\sqrt{s} = 8$ TeV with the ATLAS detector*, JHEP **09** (2015) 108, arXiv: `1506.01291 [hep-ex]` (cit. on p. 12).

[46] CMS Collaboration, *Search for physics beyond the standard model in multilepton final states in proton–proton collisions at* $\sqrt{s} = 13\,TeV$, JHEP **03** (2020) 051, arXiv: 1911.04968 [hep-ex] (cit. on pp. 12, 185).

[47] A. Géron, *Hands-On Machine Learning with Scikit-Learn, Keras, and TensorFlow: Concepts, Tools, and Techniques to Build Intelligent Systems*, O'Reilly Media, 2019 (cit. on pp. 15, 17, 18, 20).

[48] G. Sylvain and J. Howard, *Deep Learning for Coders with fastai and PyTorch*, O'Reilly Media, 2020 (cit. on p. 15).

[49] A. Ustyuzhanin et al., *Fifth Machine Learning in High Energy Physics Summer School*, 2019, URL: https://github.com/yandexdataschool/mlhep2019 (visited on 09/11/2019) (cit. on p. 15).

[50] J. VanderPlas, *Python Data Science Handbook*, O'Reilly Media, 2016 (cit. on p. 19).

[51] M. Messenger, *What exactly is TensorFlow?*, 2020, URL: https://medium.com/datadriveninvestor/what-exactly-is-tensorflow-80a90162d5f1 (visited on 16/06/2020) (cit. on p. 20).

[52] ATLAS Collaboration, *The ATLAS Experiment at the CERN Large Hadron Collider*, JINST **3** (2008) S08003 (cit. on pp. 25, 26, 28–30, 185, 186).

[53] L. Evans and P. Bryant, *LHC Machine*, JINST **3** (2008) S08001 (cit. on pp. 25, 185).

[54] CERN, *The CERN accelerator complex – August 2018*, 2018, URL: https://cds.cern.ch/record/2636343 (visited on 28/08/2018) (cit. on p. 27).

[55] ATLAS Collaboration, *Track Reconstruction Performance of the ATLAS Inner Detector at* $\sqrt{s} = 13$ *TeV*, ATL-PHYS-PUB-2015-018, 2015, URL: https://cds.cern.ch/record/2037683 (cit. on p. 28).

[56] ATLAS Collaboration, *ATLAS Insertable B-Layer Technical Design Report*, ATLAS-TDR-19, 2010, URL: https://cds.cern.ch/record/1291633 (cit. on p. 28), Addendum: ATLAS-TDR-19-ADD-1, 2012, URL: https://cds.cern.ch/record/1451888.

[57] ATLAS Collaboration, *ATLAS Liquid-Argon Calorimeter: Technical Design Report*, ATLAS-TDR-2, 1996, URL: https://cds.cern.ch/record/331061 (cit. on pp. 29, 30).

[58] ATLAS Collaboration, *ATLAS Muon Spectrometer: Technical Design Report*, ATLAS-TDR-10, 1997, URL: https://cds.cern.ch/record/331068 (cit. on pp. 31, 32).

[59] ATLAS Collaboration, *Run 2 Public DAQ plots*, 2019, URL: https://twiki.cern.ch/twiki/bin/view/AtlasPublic/ApprovedPlotsDAQ (visited on 28/10/2019) (cit. on p. 32).

[60] M. Aaboud et al., *Performance of the ATLAS Trigger System in 2015*, Eur. Phys. J. C **77** (2017) 317, arXiv: 1611.09661 [hep-ex] (cit. on pp. 32, 33).

[61] V. Cindro et al., *The ATLAS beam conditions monitor*, JINST **3** (2008) P02004 (cit. on p. 34).

[62] G. Avoni et al., *The new LUCID-2 detector for luminosity measurement and monitoring in ATLAS*, JINST **13** (2018) P07017 (cit. on p. 35).

[63] ATLAS Collaboration, *Luminosity determination in pp collisions at $\sqrt{s} = 13\,TeV$ using the ATLAS detector at the LHC*, ATLAS-CONF-2019-021, 2019, URL: `https://cds.cern.ch/record/2677054` (cit. on p. 35).

[64] S. van der Meer, *Calibration of the Effective Beam Height in the ISR*, (1968) (cit. on p. 35).

[65] ATLAS Collaboration, *The ATLAS Simulation Infrastructure*, Eur. Phys. J. C **70** (2010) 823, arXiv: `1005.4568 [physics.ins-det]` (cit. on pp. 37, 38).

[66] ATLAS Collaboration, *ATLAS computing: Technical design report*, ATLAS-TDR-017, 2005, URL: `http://cds.cern.ch/record/837738` (cit. on p. 37).

[67] S. Agostinelli et al., GEANT4 *– a simulation toolkit*, Nucl. Instrum. Meth. A **506** (2003) 250 (cit. on pp. 38, 187).

[68] E. Ritsch, 'ATLAS Detector Simulation in the Integrated Simulation Framework applied to the W Boson Mass Measurement', Presented 27 Feb 2015, 2014, URL: `https://cds.cern.ch/record/2221649` (cit. on p. 38).

[69] ATLAS Collaboration, *Luminosity Public Results for Run 2*, 2019, URL: `https://twiki.cern.ch/twiki/bin/view/AtlasPublic/LuminosityPublicResultsRun2` (visited on 09/07/2019) (cit. on pp. 38, 39).

[70] ATLAS Collaboration, *Letter of Intent for the Phase-II Upgrade of the ATLAS Experiment*, CERN-LHCC-2012-022, 2012, URL: `https://cds.cern.ch/record/1502664` (cit. on p. 38).

[71] ATLAS Collaboration, *MC+MC Pile-up Overlay Performance Plots*, 2018, URL: `https://atlas.web.cern.ch/Atlas/GROUPS/PHYSICS/PLOTS/SIM-2018-002/` (cit. on pp. 39, 40).

[72] T. Novak, *New techniques for pile-up simulation in ATLAS*, EPJ Web Conf. **214** (2019) 02044, ed. by A. Forti, L. Betev, M. Litmaath, O. Smirnova and P. Hristov (cit. on p. 40).

[73] J. Alwall et al., *The automated computation of tree-level and next-to-leading order differential cross sections, and their matching to parton shower simulations*, JHEP **07** (2014) 079, arXiv: `1405.0301 [hep-ph]` (cit. on p. 41).

[74] A. Alloul, N. D. Christensen, C. Degrande, C. Duhr and B. Fuks, *FeynRules 2.0 - A complete toolbox for tree-level phenomenology*, Comput. Phys. Commun. **185** (2014) 2250, arXiv: `1310.1921 [hep-ph]` (cit. on p. 41).

[75] T. Sjöstrand, S. Mrenna and P. Skands, *A brief introduction to PYTHIA 8.1*, Comput. Phys. Commun. **178** (2008) 852, arXiv: `0710.3820 [hep-ph]` (cit. on p. 41).

[76] ATLAS Collaboration, *ATLAS Pythia 8 tunes to 7 TeV data*, ATL-PHYS-PUB-2014-021, 2014, URL: https://cds.cern.ch/record/1966419 (cit. on pp. 41, 42).

[77] R. D. Ball et al., *Parton distributions for the LHC Run II*, JHEP **04** (2015) 040, arXiv: 1410.8849 [hep-ph] (cit. on p. 41).

[78] R. D. Ball et al., *Parton distributions with LHC data*, Nucl. Phys. B **867** (2013) 244, arXiv: 1207.1303 [hep-ph] (cit. on pp. 41, 42).

[79] B. Fuks, M. Klasen, D. R. Lamprea and M. Rothering, *Gaugino production in proton-proton collisions at a center-of-mass energy of 8 TeV*, JHEP **10** (2012) 081, arXiv: 1207.2159 [hep-ph] (cit. on p. 41).

[80] B. Fuks, M. Klasen, D. R. Lamprea and M. Rothering, *Precision predictions for electroweak superpartner production at hadron colliders with* RESUMMINO, Eur. Phys. J. C **73** (2013) 2480, arXiv: 1304.0790 [hep-ph] (cit. on p. 41).

[81] LHC SUSY Cross Section Working Group, *NLO-NLL wino-like chargino-chargino (C1C1) cross sections*, 2017, URL: https://twiki.cern.ch/twiki/bin/view/LHCPhysics/SUSYCrossSections13TeVx1x1wino (visited on 07/01/2019) (cit. on p. 42).

[82] LHC SUSY Cross Section Working Group, *NLO-NLL wino-like chargino-neutralino (N2C1) cross sections*, 2017, URL: https://twiki.cern.ch/twiki/bin/view/LHCPhysics/SUSYCrossSections13TeVn2x1wino (visited on 07/01/2019) (cit. on p. 42).

[83] S. Frixione, P. Nason and G. Ridolfi, *A positive-weight next-to-leading-order Monte Carlo for heavy flavour hadroproduction*, JHEP **09** (2007) 126, arXiv: 0707.3088 [hep-ph] (cit. on p. 41).

[84] P. Nason, *A new method for combining NLO QCD with shower Monte Carlo algorithms*, JHEP **11** (2004) 040, arXiv: hep-ph/0409146 (cit. on p. 41).

[85] S. Frixione, P. Nason and C. Oleari, *Matching NLO QCD computations with parton shower simulations: the POWHEG method*, JHEP **11** (2007) 070, arXiv: 0709.2092 [hep-ph] (cit. on p. 41).

[86] S. Alioli, P. Nason, C. Oleari and E. Re, *A general framework for implementing NLO calculations in shower Monte Carlo programs: the POWHEG BOX*, JHEP **06** (2010) 043, arXiv: 1002.2581 [hep-ph] (cit. on p. 41).

[87] ATLAS Collaboration, *Studies on top-quark Monte Carlo modelling for Top2016*, ATL-PHYS-PUB-2016-020, 2016, URL: https://cds.cern.ch/record/2216168 (cit. on p. 42).

[88] T. Sjöstrand et al., *An introduction to PYTHIA 8.2*, Comput. Phys. Commun. **191** (2015) 159, arXiv: 1410.3012 [hep-ph] (cit. on p. 42).

[89] D. J. Lange, *The EvtGen particle decay simulation package*, Nucl. Instrum. Meth. A **462** (2001) 152 (cit. on p. 42).

[90] M. Beneke, P. Falgari, S. Klein and C. Schwinn, *Hadronic top-quark pair production with NNLL threshold resummation*, Nucl. Phys. B **855** (2012) 695, arXiv: 1109.1536 [hep-ph] (cit. on p. 42).

[91] M. Cacciari, M. Czakon, M. Mangano, A. Mitov and P. Nason, *Top-pair production at hadron colliders with next-to-next-to-leading logarithmic soft-gluon resummation*, Phys. Lett. B **710** (2012) 612, arXiv: 1111.5869 [hep-ph] (cit. on p. 42).

[92] P. Bärnreuther, M. Czakon and A. Mitov, *Percent-Level-Precision Physics at the Tevatron: Next-to-Next-to-Leading Order QCD Corrections to $q\bar{q} \to t\bar{t} + X$*, Phys. Rev. Lett. **109** (2012) 132001, arXiv: 1204.5201 [hep-ph] (cit. on p. 42).

[93] M. Czakon and A. Mitov, *NNLO corrections to top-pair production at hadron colliders: the all-fermionic scattering channels*, JHEP **12** (2012) 054, arXiv: 1207.0236 [hep-ph] (cit. on p. 42).

[94] M. Czakon and A. Mitov, *NNLO corrections to top pair production at hadron colliders: the quark-gluon reaction*, JHEP **01** (2013) 080, arXiv: 1210.6832 [hep-ph] (cit. on p. 42).

[95] M. Czakon, P. Fiedler and A. Mitov, *Total Top-Quark Pair-Production Cross Section at Hadron Colliders Through $O(\alpha_S^4)$*, Phys. Rev. Lett. **110** (2013) 252004, arXiv: 1303.6254 [hep-ph] (cit. on p. 42).

[96] M. Czakon and A. Mitov, *Top++: A program for the calculation of the top-pair cross-section at hadron colliders*, Comput. Phys. Commun. **185** (2014) 2930, arXiv: 1112.5675 [hep-ph] (cit. on p. 42).

[97] M. Botje et al., *The PDF4LHC Working Group Interim Recommendations*, (2011), arXiv: 1101.0538 [hep-ph] (cit. on p. 42).

[98] A. D. Martin, W. J. Stirling, R. S. Thorne and G. Watt, *Parton distributions for the LHC*, Eur. Phys. J. C **63** (2009) 189, arXiv: 0901.0002 [hep-ph] (cit. on p. 42).

[99] A. D. Martin, W. Stirling, R. Thorne and G. Watt, *Uncertainties on α_S in global PDF analyses and implications for predicted hadronic cross sections*, Eur. Phys. J. C **64** (2009) 653, arXiv: 0905.3531 [hep-ph] (cit. on p. 42).

[100] H.-L. Lai et al., *New parton distributions for collider physics*, Phys. Rev. D **82** (2010) 074024, arXiv: 1007.2241 [hep-ph] (cit. on p. 42).

[101] J. Gao et al., *CT10 next-to-next-to-leading order global analysis of QCD*, Phys. Rev. D **89** (2014) 033009, arXiv: 1302.6246 [hep-ph] (cit. on p. 42).

[102] ATLAS Collaboration, *Studies on top-quark Monte Carlo modelling with Sherpa and MG5_aMC@NLO*, ATL-PHYS-PUB-2017-007, 2017, URL: https://cds.cern.ch/record/2261938 (cit. on p. 42).

[103] S. Dulat et al., *New parton distribution functions from a global analysis of quantum chromodynamics*, Phys. Rev. D **93** (2016) 033006, arXiv: `1506.07443 [hep-ph]` (cit. on p. 43).

[104] L. Harland-Lang, A. Martin, P. Motylinski and R. Thorne, *Parton distributions in the LHC era: MMHT 2014 PDFs*, Eur. Phys. J. C **75** (2015) 204, arXiv: `1412.3989 [hep-ph]` (cit. on p. 43).

[105] M. Bahr et al., *Herwig++ physics and manual*, Eur. Phys. J. C **58** (2008) 639, arXiv: `0803.0883 [hep-ph]` (cit. on p. 43).

[106] J. Bellm et al., *Herwig 7.0/Herwig++ 3.0 release note*, Eur. Phys. J. C **76** (2016) 196, arXiv: `1512.01178 [hep-ph]` (cit. on p. 43).

[107] E. Bothmann et al., *Event Generation with Sherpa 2.2*, SciPost Phys. **7** (2019) 034, arXiv: `1905.09127 [hep-ph]` (cit. on p. 43).

[108] T. Gleisberg and S. Höche, *Comix, a new matrix element generator*, JHEP **12** (2008) 039, arXiv: `0808.3674 [hep-ph]` (cit. on p. 43).

[109] F. Cascioli, P. Maierhöfer and S. Pozzorini, *Scattering Amplitudes with Open Loops*, Phys. Rev. Lett. **108** (2012) 111601, arXiv: `1111.5206 [hep-ph]` (cit. on p. 43).

[110] A. Denner, S. Dittmaier and L. Hofer, COLLIER: *A fortran-based complex one-loop library in extended regularizations*, Comput. Phys. Commun. **212** (2017) 220, arXiv: `1604.06792 [hep-ph]` (cit. on p. 43).

[111] S. Schumann and F. Krauss, *A parton shower algorithm based on Catani–Seymour dipole factorisation*, JHEP **03** (2008) 038, arXiv: `0709.1027 [hep-ph]` (cit. on p. 43).

[112] J.-C. Winter, F. Krauss and G. Soff, *A modified cluster-hadronization model*, Eur. Phys. J. C **36** (2004) 381, arXiv: `hep-ph/0311085` (cit. on p. 43).

[113] S. Höche, F. Krauss, M. Schönherr and F. Siegert, *A critical appraisal of NLO+PS matching methods*, JHEP **09** (2012) 049, arXiv: `1111.1220 [hep-ph]` (cit. on p. 44).

[114] S. Catani, F. Krauss, R. Kuhn and B. R. Webber, *QCD matrix elements + parton showers*, JHEP **11** (2001) 063, arXiv: `hep-ph/0109231` (cit. on p. 44).

[115] S. Höche, F. Krauss, S. Schumann and F. Siegert, *QCD matrix elements and truncated showers*, JHEP **05** (2009) 053, arXiv: `0903.1219 [hep-ph]` (cit. on p. 44).

[116] S. Höche, F. Krauss, M. Schönherr and F. Siegert, *QCD matrix elements + parton showers. The NLO case*, JHEP **04** (2013) 027, arXiv: `1207.5030 [hep-ph]` (cit. on p. 44).

[117] C. Anastasiou, L. J. Dixon, K. Melnikov and F. Petriello, *High precision QCD at hadron colliders: Electroweak gauge boson rapidity distributions at NNLO*, Phys. Rev. D **69** (2004) 094008, arXiv: `hep-ph/0312266` (cit. on p. 44).

[118] E. Bothmann, M. Schönherr and S. Schumann, *Reweighting QCD matrix-element and parton-shower calculations*, Eur. Phys. J. C **76** (2016) 590, arXiv: 1606.08753 [hep-ph] (cit. on p. 44).

[119] ATLAS Collaboration, *The Pythia 8 A3 tune description of ATLAS minimum bias and inelastic measurements incorporating the Donnachie–Landshoff diffractive model*, ATL-PHYS-PUB-2016-017, 2016, URL: https://cds.cern.ch/record/2206965 (cit. on p. 44).

[120] ATLAS Collaboration, *Measurement of the Inelastic Proton–Proton Cross Section at $\sqrt{s} = 13$ TeV with the ATLAS Detector at the LHC*, Phys. Rev. Lett. **117** (2016) 182002, arXiv: 1606.02625 [hep-ex] (cit. on p. 44).

[121] ATLAS Collaboration, *Performance of the ATLAS track reconstruction algorithms in dense environments in LHC Run 2*, Eur. Phys. J. C **77** (2017) 673, arXiv: 1704.07983 [hep-ex] (cit. on pp. 47, 48).

[122] T. Cornelissen et al., *The new ATLAS track reconstruction (NEWT)*, J. Phys. Conf. Ser. **119** (2008) 032014 (cit. on p. 47).

[123] R. Fruhwirth, *Application of Kalman filtering to track and vertex fitting*, Nucl. Instrum. Meth. A **262** (1987) 444 (cit. on p. 47).

[124] ATLAS Collaboration, *Reconstruction of primary vertices at the ATLAS experiment in Run 1 proton–proton collisions at the LHC*, Eur. Phys. J. C **77** (2017) 332, arXiv: 1611.10235 [hep-ex] (cit. on p. 49).

[125] ATLAS Collaboration, *Electron reconstruction and identification in the ATLAS experiment using the 2015 and 2016 LHC proton–proton collision data at $\sqrt{s} = 13$ TeV*, Eur. Phys. J. C **79** (2019) 639, arXiv: 1902.04655 [hep-ex] (cit. on pp. 49, 50).

[126] ATLAS Collaboration, *Electron and photon performance measurements with the ATLAS detector using the 2015–2017 LHC proton–proton collision data*, JINST **14** (2019) P12006, arXiv: 1908.00005 [hep-ex] (cit. on pp. 49, 51, 52, 85).

[127] ATLAS Collaboration, *Topological cell clustering in the ATLAS calorimeters and its performance in LHC Run 1*, Eur. Phys. J. C **77** (2017) 490, arXiv: 1603.02934 [hep-ex] (cit. on p. 49).

[128] ATLAS Collaboration, *Improved electron reconstruction in ATLAS using the Gaussian Sum Filter-based model for bremsstrahlung*, ATLAS-CONF-2012-047, 2012, URL: https://cds.cern.ch/record/1449796 (cit. on p. 50).

[129] ATLAS Collaboration, *Muon reconstruction performance of the ATLAS detector in proton–proton collision data at $\sqrt{s} = 13$ TeV*, Eur. Phys. J. C **76** (2016) 292, arXiv: 1603.05598 [hep-ex] (cit. on pp. 52, 54).

[130] ATLAS Collaboration, *Jet reconstruction and performance using particle flow with the ATLAS Detector*, Eur. Phys. J. C **77** (2017) 466, arXiv: 1703.10485 [hep-ex] (cit. on p. 55).

[131] M. Cacciari, G. P. Salam and G. Soyez, *The anti-k_t jet clustering algorithm*, JHEP **04** (2008) 063, arXiv: 0802.1189 [hep-ph] (cit. on p. 55).

[132] M. Cacciari, 'FastJet: A Code for fast k_t clustering, and more', *Deep inelastic scattering. Proceedings, 14th International Workshop, DIS 2006, Tsukuba, Japan, April 20-24, 2006*, [,125(2006)], 2006 487, arXiv: hep-ph/0607071 [hep-ph] (cit. on p. 55).

[133] ATLAS Collaboration, *Jet energy scale measurements and their systematic uncertainties in proton–proton collisions at $\sqrt{s} = 13$ TeV with the ATLAS detector*, Phys. Rev. D **96** (2017) 072002, arXiv: 1703.09665 [hep-ex] (cit. on p. 55).

[134] ATLAS Collaboration, *Jet energy scale and uncertainties in 2015-2017 data and simulation*, 2018, URL: https://atlas.web.cern.ch/Atlas/GROUPS/PHYSICS/PLOTS/JETM-2018-006/ (cit. on p. 56).

[135] ATLAS Collaboration, *Jet energy resolution in 2017 data and simulation*, 2018, URL: https://atlas.web.cern.ch/Atlas/GROUPS/PHYSICS/PLOTS/JETM-2018-005/ (cit. on p. 56).

[136] ATLAS Collaboration, *Performance of pile-up mitigation techniques for jets in pp collisions at $\sqrt{s} = 8$ TeV using the ATLAS detector*, Eur. Phys. J. C **76** (2016) 581, arXiv: 1510.03823 [hep-ex] (cit. on p. 56).

[137] ATLAS Collaboration, *ATLAS b-jet identification performance and efficiency measurement with $t\bar{t}$ events in pp collisions at $\sqrt{s} = 13$ TeV*, Eur. Phys. J. C **79** (2019) 970, arXiv: 1907.05120 [hep-ex] (cit. on pp. 56, 57).

[138] ATLAS Collaboration, *Optimisation and performance studies of the ATLAS b-tagging algorithms for the 2017-18 LHC run*, ATL-PHYS-PUB-2017-013, 2017, URL: https://cds.cern.ch/record/2273281 (cit. on p. 56).

[139] ATLAS Collaboration, *Performance of missing transverse momentum reconstruction with the ATLAS detector using proton–proton collisions at $\sqrt{s} = 13$ TeV*, Eur. Phys. J. C **78** (2018) 903, arXiv: 1802.08168 [hep-ex] (cit. on p. 57).

[140] ATLAS Collaboration, *E_T^{miss} performance in the ATLAS detector using 2015–2016 LHC pp collisions*, ATLAS-CONF-2018-023, 2018, URL: https://cds.cern.ch/record/2625233 (cit. on p. 57).

[141] ATLAS Collaboration, *Object-based missing transverse momentum significance in the ATLAS Detector*, ATLAS-CONF-2018-038, 2018, URL: https://cds.cern.ch/record/2630948 (cit. on pp. 58, 59, 188).

[142] G. Cowan, K. Cranmer, E. Gross and O. Vitells, *Asymptotic formulae for likelihood-based tests of new physics*, Eur. Phys. J. C **71** (2011) 1554, arXiv: 1007.1727 [physics.data-an] (cit. on pp. 64, 99, 186), Erratum: Eur. Phys. J. C **73** (2013) 2501.

[143] ATLAS Collaboration, *Search for type-III seesaw heavy leptons in dilepton final states in pp collisions at $\sqrt{s} = 13$ TeV with the ATLAS detector*, (2020), Submitted to Eur. Phys. J. C., arXiv: 2008.07949 [hep-ex] (cit. on pp. 64, 101–104, 107–109, 113, 187, 193, 194).

[144] ATLAS Collaboration, *Selection of jets produced in 13 TeV proton–proton collisions with the ATLAS detector*, ATLAS-CONF-2015-029, 2015, URL: https://cds.cern.ch/record/2037702 (cit. on p. 64).

[145] A. V. Dorogush, V. Ershov and A. Gulin, *CatBoost: gradient boosting with categorical features support*, (2018), arXiv: 1810.11363 [cs.LG], URL: https://catboost.ai (cit. on pp. 73, 189).

[146] Martin Abadi et al., *TensorFlow: Large-Scale Machine Learning on Heterogeneous Systems*, 2015, URL: https://tensorflow.org (cit. on pp. 73, 189).

[147] P. Baldi, K. Cranmer, T. Faucett, P. Sadowski and D. Whiteson, *Parameterized neural networks for high-energy physics*, Eur. Phys. J. C **76** (2016) 235, arXiv: 1601.07913 [hep-ex] (cit. on p. 75).

[148] A. Buckley et al., *LHAPDF6: parton density access in the LHC precision era*, Eur. Phys. J. C **75** (2015) 132, arXiv: 1412.7420 [hep-ph] (cit. on p. 79).

[149] ATLAS Collaboration, *Search for type-III seesaw heavy leptons in proton–proton collisions at $\sqrt{s} = 13$ TeV with the ATLAS detector*, ATLAS-CONF-2018-020, 2018, URL: https://cds.cern.ch/record/2621484 (cit. on p. 84).

[150] ATLAS Collaboration, *Search for doubly charged Higgs boson production in multi-lepton final states with the ATLAS detector using proton–proton collisions at $\sqrt{s} = 13$ TeV*, Eur. Phys. J. C **78** (2018) 199, arXiv: 1710.09748 [hep-ex] (cit. on pp. 85, 188).

[151] M. Baak et al., *HistFitter software framework for statistical data analysis*, Eur. Phys. J. C **75** (2015) 153, arXiv: 1410.1280 [hep-ex] (cit. on p. 97).

[152] R. Brun and F. Rademakers, *ROOT – An object oriented data analysis framework*, Nucl. Instrum. Meth. A **389** (1997) 81, ISSN: 0168-9002 (cit. on p. 97).

[153] W. Verkerke and D. Kirkby, *The RooFit toolkit for data modeling*, 2003, arXiv: physics/0306116 [physics.data-an] (cit. on p. 97).

[154] K. Cranmer, G. Lewis, L. Moneta, A. Shibata and W. Verkerke, *HistFactory: A tool for creating statistical models for use with RooFit and RooStats*, tech. rep. CERN-OPEN-2012-016, New York U., 2012, URL: https://cds.cern.ch/record/1456844 (cit. on p. 98).

[155] A. L. Read, *Presentation of search results: the CL_S technique*, J. Phys. G **28** (2002) 2693 (cit. on pp. 99, 192).

[156] G. Apollinari, O. Brüning, T. Nakamoto and L. Rossi, *High Luminosity Large Hadron Collider HL-LHC*, CERN Yellow Rep. (2015) 1, ed. by G. Apollinari, I. Béjar Alonso, O. Brüning, M. Lamont and L. Rossi, arXiv: `1705.08830 [physics.acc-ph]` (cit. on p. 132).

[157] E. Ma, *Pathways to Naturally Small Neutrino Masses*, Phys. Rev. Lett. **81** (1998) 1171, arXiv: `hep-ph/9805219 [hep-ph]` (cit. on p. 183).

Razširjeni povzetek v slovenskem jeziku

Široko področje fizike osnovnih delcev raziskuje osnovne gradnike snovi okoli nas. Standardni model fizike osnovnih delcev [2–10] je osnovna teorija, ki opisuje fundamentalne sile, elektromagnetno, šibko in močno interakcijo, z izjemo gravitacije. Model uspešno klasificira vse trenutno poznane osnovne delce. Odkritje Higgsovega bozona leta 2012 pri eksperimentih ATLAS [11] in CMS [12] je bil še zadnji korak k polni potrditvi teorije, ki pa preko različnih eksperimentalnih rezultatov pušča kar nekaj vprašanj neodgovorjenih.

Osnovne delce lahko razdelimo na fermione in umeritvene bozone. Med slednje spada 8 brezmasnih in električno nevtralnih gluonov, nosilcev močne interakcije, foton, ki je posrednik elektromagnetne interakcije, ter štirje masivni bozoni, $W^{\pm}$, Z^0 in H, kjer prvi trije sodelujejo pri šibki interakciji, zadnji pa je Higgsov bozon. Fermione radelimo na kvarke in leptone. Obstaja šest okusov kvarkov, ločenih v tri generacije. Leptonski okusi so samo trije, vsak pripada svoji generaciji. V vsako generacijo spada nabit lepton, e, μ ali τ, ter njegov nevtralen partner nevrino, ν_e, ν_μ ali ν_τ. Vsakemu fermionu pripada tudi njegov antidelec, ki ima nasproten električni naboj in ostala kvantna števila.

Nevtrini so posebni delci, saj so električno nevtralni in interagirajo samo preko šibke interakcije. Eksperimentalno dostopni nevtrini so vedno polarizirani. Nevtrini so lahko le levo-ročni, anti-nevtrini pa desno-ročni. Standardni model ne predvideva desno-ročnih nevtrinov, če pa taki nevtrini obstajajo, je njihova interakcija lahko samo preko gravitacije ali Higgsovega mehanizma, sj jih v šibkih interakcijah nismo opazili. Higgsov mehanizem razloži izvor mase večine delcev, nevtrini pa so brez vpeljave dodatnih delcev brezmasni.

Opažanje nevtrinskih oscilacij pri eksperimentih Super-Kamiokande [26] na Japonskem in pri Sudbury Neutrino Observatory (SNO) [27] v Kanadi nakazuje, da nevtrini maso imajo ter da so njihove pričakovane mase precej manjše od nabitih leptonov. Slednji maso pridobijo preko sklopitve s Higgsovim bozonom (H), maso nevtrinov pa lahko razloži več razširitev Standardnega modela. Ena izmed elegantnih možnosti je vpeljava t.i. Majorana masnih členov [157] z novimi delci. Novi delci se sklapljajo z nevtrini in Higgsovim poljem in omogočajo majhne a neničelne mase nevtrinov. Mase teh novih težkih delcev se nato sklapljajo z maso lahkih nevtrinov preko t.i. gugalničnega mehanizma (ang. *seesaw*). Tem večja je masa novih delcev, tem manjša je masa nevtrinov. V najpreprostejšem primeru le enega novega tipa delcev lahko vpeljemo tri razširitve Standardnega modela:

1. vsaj dva fermionska singleta, t.i. desnoročna nevtrina — gugalnični mehanizem tipa I [28–32];

2. triplet skalarjev v $SU(2)_L$ — gugalnični mehanizem tipa II [33–35];

3. vsaj dva tripleta fermionov v $SU(2)_L$ — gugalnični mehanizem tipa III [36].

Hkrati lahko nastopajo tudi kombinacije večih tipov gugalničnega mehanizma, npr. mešanica tipa I in tipa III [37, 38].

Gugalnični mehanizem tipa III vpelje triplete fermionov v adjungirani reprezentaciji grupe $SU(2)_L$ brez hiper-naboja, ki se sklapljajo s šibkimi bozoni in preko Higgsovega mehanizma generirajo mase nevtrinov. Posledično bi se novi nabiti in nevtralni leptoni lahko opazili v trkih protonov na Velikem hadronskem trkalniku (LHC). V poenostavljenem modelu obravnavamo le en triplet, ki generira eno maso nevtrinov, a v splošnem lahko dodamo poljubno število novih delcev, tako fermionske singlete kot triplete. Uporabljen model se smatra kot nizkoenergijska limita obsežnejše teorije. Ta poenostavitev nima znatnega vpliva na fiziko, dostopno na LHC, saj trenutno lahko dosegamo le energije velikostnega reda TeV, ki v večini teorij izven Standardnega modela omogočajo le najlažja končna stanja. Vpeljani triplet težkih leptonov označimo z (L^+, L^-, N^0), kjer sta L^+ in L^- antidelca, N^0 pa sam sebi antidelec, torej delec Majorana. Predpostavimo, da imajo vsi trije novi delci enako maso.

Leptoni N^0 in $L^\pm$ v trkih pp nastajajo v parih preko umeritvene sklopitve [40]. Prav tako razpadajo v umeritvene bozone W, Z in H. Največje razvejitveno razmerje imajo v bosone W, na kar sem se osredotočil tudi v tem doktorskem delu. Eden izmed bozonov

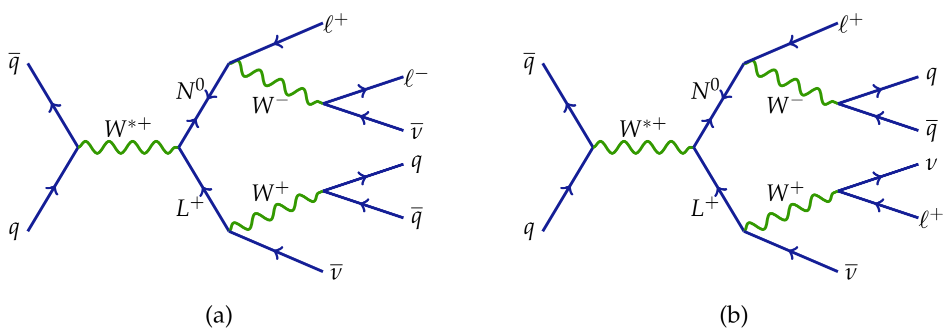

Slika 1: Feynmanovi diagrami dominantnih razpadnih kanalov težkih leptonov gugalničnega mehanizma tipa III z dvema leptonoma v končnem stanju, ki sta (a) nasprotnega ali (b) enakega naboja.

razpade leptonsko, drugi pa hadronsko. Feynmanovi diagrami opazovanih produkcijskih in razpadnih procesov so prikazani na sliki 1. Kot rezultat v končnem stanju pričakujemo dva leptona z visoko transverzalno gibalno količino (p_{T}), dva pljuska hadronov (ang. *jets*), ki izhajata iz hadronskega razpada bozona W, in visoko manjkajočo transverzalno gibalno količino ($E_{\mathrm{T}}^{\mathrm{miss}}$). Leptona sta lahko enakega ($\pm\pm$, SS) ali nasprotnega naboja ($\pm\mp$, OS), prav tako pa tudi enakega (ee ali $\mu\mu$) ali različnega leptonskega okusa ($e\mu$), pri čemer so upoštevani tudi leptonski razpadi leptonov τ.

Analiza, ki je predmet tega doktorskega dela, predstavlja razširitev predhodne analize podatkov, zajetih z eksperimentom ATLAS med prvim obdobjem zajemanja podatkov (Run 1) pri težiščni energiji $\sqrt{s} = 8$ TeV [44], kjer so bili težki leptoni z maso pod 335 GeV izključeni v dogodkih z istim končnim stanjem. Na podatkih iz drugega obdobja (Run 2) pri težišni energiji $\sqrt{s} = 13$ TeV je eksperiment CMS opravil analizo dogodkov [46] z vsaj tremi leptoni v končnem stanju in postavil limito na 880 GeV. V tem delu obravnavana analiza podatkov tako trenutno predstavlja edino iskanje v tem zahtevnem končnem stanju. V primerjavi s prejšnjo analizo pri eksperimentu ATLAS so se izboljšali opis ozadja in izbor predvidenih dogodkov signala ter teoretični opis obravnavanega modela, ki skupaj izboljšajo občutljivost analize na nove delce.

Detektor ATLAS (A Toroidal LHC ApparatuS) [52] v CERN-u (Evropska organizacija za jedrske raziskave) je večnamembni detektor osnovnih delcev, del pospeševalniškega kompleksa LHC [53]. Detektor valjaste oblike se nahaja približno 100 m pod zemljo ter je dolg 44 m in visok 25 m. Svoje ime je dobil po treh velikih toroidnih magnetih, ki ga obdajajo z vseh strani. Na sliki 2 je prikazana shema glavnih detektorskih komponent. Sledi nabitih delcev in njihove izvorne točke se merijo v Notranjem detektorju, ki je sestavljen iz polprevodniških blazinčnih in pasovnih detektorjev na notranji strani ter iz detektorjev prehodnega sevanja na zunanji strani. Energija delcev se meri z ustavljanjem delcev v kalorimetrih, elektromagnetnem kalorimetru s tekočim argonom in hadronskim kalorimetu iz scintilacijskih plošč. Mionski spektrometer obdaja kalorimetre in tako celoten eksperiment. V pospeševalniku protoni trkajo vsakih 25 ns, kar je preprosto prevelika količina podatkov, ki bi jo lahko zapisali. V ta namen ATLAS uporablja poseben sistem strojnega in programskega proženja, ki glede na hitro ocenjene lastnosti trka (npr. število elektronov z izbrano minimalno gibalno količino) povprečno izbere 1000 dogodkov na sekundo. Kriteriji so prilagojeni tipu dogodkov, ki nas zanimajo, a ob tem poskušajo zavreči najbolj pogoste procese v Standardnem modelu. Podroben opis detektorja v angleškem jeziku je v poglavju 3.

Pri analizi podatkov v detektor ATLAS umestimo koordinatni sistem s središčem v interakcijski točki. Os z je vzporedna s smerjo žarka protonov. Po trku nastali delci iz središča letijo v vse smeri, zato za njihov opis uporabljamo krogelne koordinate. Polarni kot θ se meri od žarkovne osi, azimutni kot ϕ pa okoli te osi. Namesto kota θ običajno uporabljamo psevdorapidnost, definirano kot $\eta = -\ln\tan(\theta/2)$. Ob tem lahko definiramo še nekaj osnovnih kinematičnih količin. Transverzalna gibalna količina p_{T},

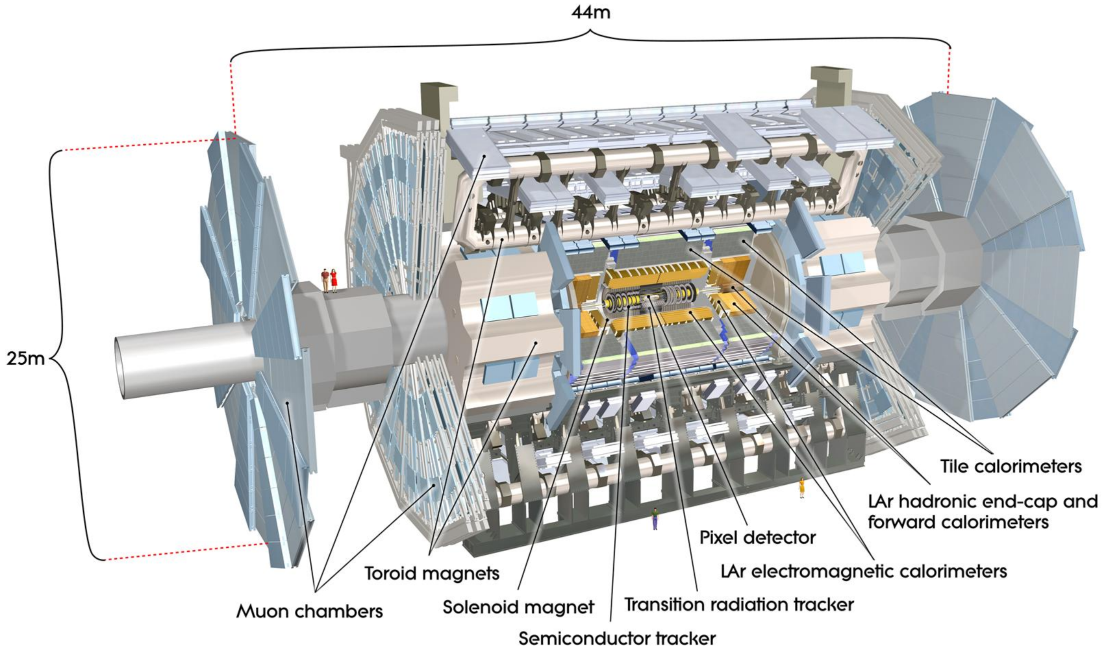

Slika 2: Prerez detektorja ATLAS, ki prikazuje sistem magnetov in glavne štiri komponente: notranji detektor, elektromagnetni kalorimeter, hadronski kalorimeter in mionski spektrometer. Vzeto iz vira [52].

transverzalna energija E_T in manjkajoča transverzalna gibalna količina $E_\mathrm{T}^\mathrm{miss}$ so vse definirane v ravnini x-y. Slednja je definirana kot velikost vektorske vsote vseh delcev brez upoštevanja osi z.

Verjetnost za nastanek kakršnihkoli novih delcev je zelo majhna. Izmed vseh zajetih podatkov moramo izbrati ustrezno rekonstruirane delce v dogodkih, ki se čim bolj razlikujejo od ozadja, ki ga predstavljajo že znani procesi Standardnega modela. Izbrane dogodke glede na njihov namen lahko razdelimo v različna kinematična območja: Signalna območja (SR) so zasnovana z namenom čim boljše občutljivosti glede na obravnavani model. Signifikanca iskanega signala v primerjavi z ozadjem mora biti čim večja in je definirana kot [142]

$$\sqrt{2[(S+B)\ln(1+S/B)-S]}\,,$$

kjer sta S in B števili dogodkov za signal in ozadje, ocenjeni iz simulacije. V tem območju se pri končni statistični obravnavi primerjajo izmerjeni podatki s predpostavljeno hipotezo o količini signala in ozadja (poglavje 8). Kontrolna območja (CR) se uporabljajo za oceno normalizacije nekaterih prispevkov ozadja, ki se nato preveri s preverjalnimi območji (VR). Oba tipa območij sta zasnovana tako, da vsebujeta čim več enega prispevka k ozadju, vendar sta kinematično še vedno blizu signalnim območjem.

Doktorsko delo primerja dva tipa zasnove signalnih območij. V prvem primeru dogodke izberemo z individualnimi rezi glede na izbrane kinematične opazljivke, ki so med seboj funkcijsko neodvisni oz. pravokotni (objavljeno v [143]). Ta postopek se lahko razširi z uporabo strojnega učenja, ki upošteva funkcijsko odvisnost posameznih količin. Pred optimizacijo teh območij je smiselno opraviti simiselen predizbor dogodkov. Med podatki se izberejo le dogodki, ki so bili kvalitetno izmerjeni in rekonstruirani v celotnem detektorju. Dogodke razdelimo v šest ločenih kategorij glede na okus in naboj leptonov. Za vsako izmed kombinacij ee, $e\mu$ in $\mu\mu$ si izberemo kriterij za proženje, ki zahteva dva leptona z minimalno gibalno količino prvega leptona med 12 GeV in 22 GeV ter drugega med 8 GeV in 17 GeV. Pri tem zahtevamo, da dogodek vsebuje rekonstruirane leptone, ki so sprožili zapisovanje. Dodatno zahtevamo, da imata leptona gibalno količino vsaj 40 GeV, obravnavani pljuski hadronov pa vsaj 20 GeV. Vsi delci se nahajajo v centralnem delu detektorja, ki zajema območje z $|\eta| < 2.5$. Uporabil sem vse podatke zajete v drugem obdobju trkov protonov in zajemanja podatkov (Run 2). Skupna integrirana luminoznost znaša 139 fb^{-1}, z nedoločenostjo 1.7%.

Pri iskanju nove fizike v pospeševalniških eksperimentih je zelo pomembna dobra ocena ozadja. Izmerjene podatke primerjamo z napovedjo ozadja in vsako neskladje lahko nakazuje možnost novih osnovnih delcev. Za natančno obravnavo ozadja tako uporabimo vso trenutno znanje fizike osnovnih delcev. Izvor nabitih leptonskih kandidatov lahko klasificiramo v tri glavne skupine: neposredno ozadje, posredno ozadje in lažno ozadje.

Leptone, ki izvirajo iz neposrednega ozadja, napovemo s podrobno simulacijo Monte Carlo, kjer natančno izračunamo procese v Standardnem Modelu. To so predvsem razpadi bozonov Z, W in H ter neposredni leptonski razpadi leptonov τ ali kvarkov t. V moji analizi pričakujemo pretežno leptonske razpade parov $t\bar{t}$ in procese z dvema vektorskima bozonoma v končnem stanju (npr. ZW). Glede na napovedan teoretični model dogodke najprej računalniško generiramo, nato pa njihovo interakcijo z detektorjem simuliramo z orodjem GEANT 4 [67]. Rezultat simulacije so digitalni podatki, kot bi prišli iz dejanskega detektorja, ki se rekonstruirajo na enak način kot zajeti podatki iz trkov protonov.

Leptone v posrednem in lažnem ozadju je še težje napovedati. Posredni leptoni so pravi leptoni, vendar izhajajo iz razpadov hadronov v pljuskih delcev, ki se zgodijo med njihovim letom, ali pa so rezultat pretvorbe fotona v par elektron-pozitron. Lažni leptoni niso pravi leptoni, le rekonstruiramo jih kot le-te. Med njimi najdemo hadrone ali pljuske delcev, ki v detektorju povzročijo podoben signal kot leptoni. Simulacije lahko opišejo ti dve skupini leptonov z omejenimi zmožnostmi, zato za njihovo oceno uporabljamo metode, ki uporabljajo podatke. V simulacijah bi drugače morali izjemno natančno poznati stanje posameznih detektorskih komponent v različnih časovnih obdobjih, kar pa žal ni mogoče.

Za elektrone in mione sem uporabil t.i. *metodo fake-factor* [150]. Število lažnih leptonov se ekstrapolira iz namenskih kontrolnih območij v signalna območja. Vsakemu takemu leptonu se določi utež, t.i. *fake-factor*, ki je sorazmerna verjetnosti, da bi lahko tak lepton rekonstruirali kot neposreden. Kontrolno območje za določitev uteži pripravimo z delitvijo leptonov na dve skupini, ki se med seboj ne prekrivata. Kandidati za signal spadajo v skupino *tight*, v skupini *loose* pa za leptone zahtevamo bolj ohlapne kriterije za identifikacijo in izolacijo. Izolacija se interpretira kot razdalja leptona od ostalih delcev, s tem kriterijem zmanjšamo verjetnost, da tak lepton izhaja sekundarnega razpada znotraj pljuska hadronov. V tej specifični analizi se za lažne leptone izpusti izolacijski kriterij, za elektrone pa se dodatno zmanjša zahtevnost identifikacije. Razmerje števil leptonov iz obeh kategorij je naš fake-factor $F = N_{\text{tight}}/N_{\text{loose}}$ in je odvisen od p_{T} in η leptona ter $E_{\text{T}}^{\text{miss}}$ celotnega dogodka. V signalnem območju z dvema leptonoma tako lahko izračunamo celotno število ozadja lažnih leptonov kot

$$N_{\text{lažni}}^{\text{2lep.}} = \left[\sum_{TL} F_2 + \sum_{LT} F_1 - \sum_{LL} F_1 F_2\right]_{\text{podatki}} - \left[\sum_{TL} F_2 + \sum_{LT} F_1 - \sum_{LL} F_1 F_2\right]_{\substack{\text{simulirani}\\ \text{neposredni razpadi}}}$$

Pri tem je potrebno upoštevati, da naša ocena lahko vsebuje tudi neposredne razpade z neuspešno rekonstrukcijo teh leptonov. Zato od števila lažnih leptonov, ocenjenega iz podatkov, odštejemo število simuliranih neposrednih razpadov, ki ne zadoščajo polnim identifikacijskim in izolacijskim kriterijem.

Še vedno pa tudi vseh vrst neposrednih razpadov protonov ne moremo natančno simulirati zaradi omejitev pri detekciji in rekonstrukciji trkov. Eden izmed pomembnih primerov so leptoni, ki jim napačno dodelimo naboj, kar se lahko zgodi v dveh primerih:

- Za elektrone je značilno zavorno sevanje. Nastali foton zaradi interakcije s snovjo v detektorju lahko pretvori v par elektron-pozitron. Končni trije leptoni so močno poravnani, kar otežuje identifikacijo prvotnega delca. Tako lahko rekonstruiramo napačen naboj elektrona.
- Elektroni imajo lahko zelo visoko energijo. Za meritev naboja uporabljamo ukrivljenost sledi delca v magnetnem polju. Če je p_{T} sledi zelo visoka, jo je dosti težje pravilno rekonstruirati, saj ima majhen krivinski radij.

Območja analize sem določil posebej za obe izmed strategij. Pri pristopu s pravokotnimi rezi je zasnova signalnih območij temeljila na maksimizaciji občutljivosti na signal. Zaradi nevtrinov v končnem stanju je $E_{\text{T}}^{\text{miss}}$ ena izmed najpomembnejših opazljivk. Za izbor dogodkov uporabimo posebno količino $\mathcal{S}(E_{\text{T}}^{\text{miss}})$, ki oceni signifikanco meritve $E_{\text{T}}^{\text{miss}}$ glede na ločljivost meritev posameznih delcev, ki so bili uporabljeni pri njenem izračunu [141]. Za dogodke s pari leptonov različnega naboja je vrednost reza $\mathcal{S}(E_{\text{T}}^{\text{miss}}) > 10$ za pare z enakim nabojem pa $\mathcal{S}(E_{\text{T}}^{\text{miss}}) > 7.5$. V končnem stanju zahtevamo tudi vsaj dva pljuska hadronov. Pri tem s posebnim algoritmom izločimo tiste, ki izhajajo iz razpadov kvarka b. Dva najbolj energetska izmed njih naj bi izhajala iz bozona W, zato za njuno invariantno maso zahtevamo $60\,\text{GeV} < m_{jj} < 100\,\text{GeV}$. V izogib parom leptonov iz razpadov $Z \rightarrow ee$, še posebej tistim, ki imajo mogoče nepravilno določen naboj, zavržemo vse dogodke z invariantno maso para leptonov ($m_{\ell\ell}$) pod 110 GeV za OS in pod 100 GeV za končna stanja SS. Dodatno za dogodke s pari leptonov z nasprotnim nabojem zahtevamo še najmanjši azimutni kot med katerikolim leptonom in smerjo manjkajoče gibalne količine $\Delta\phi(E_{\mathrm{T}}^{\mathrm{miss}}, \ell)_{\mathrm{min}} > 1$. Prav tako določimo spodnje meje gibalne količine parov leptonov $p_{\mathrm{T}}(\ell\ell)$ in pljuskov $p_{\mathrm{T}}(jj)$. Pričakovana energija razpadnih produktov novih težkih leptonov je visoka. Za reprezentativno količino, ki opiše take dogodke, si izberemo skalarno vsoto transverzalnih gibalnih količin parov leptonov in pljuskov ter manjkajoče transverzalne gibalne količine $H_{\mathrm{T}} + E_{\mathrm{T}}^{\mathrm{miss}} > 300\,\text{GeV}$. Porazdelitve po tej količini uporabimo tudi pri končni statistični obdelavi.

Glavna prispevka k ozadju sta razpada para $t\bar{t}$ in para dveh vektorskih bozonov, kjer v obeh primerih lahko dobimo dva leptona v končnem stanju. Za vsako izmed teh ozadij določimo kontrolno območje, kjer bo izmerjen normalizacijski faktor teh dveh procesov. Za določitev teh območij določene reze ali obrnemo ali pa popolnoma odstranimo, da zagotovimo zadostno število dogodkov v posameznem območju. Vsa območja so povzeta v tabeli 1.

Zasnova območij, ki uporabljajo strojno učenje, temelji na že definiranih območjih prvega dela analize. Najprej določimo osnovni izbor dogodkov, na katerem se bo računalnik učil. Na tej stopnji dogodkov še ne razbijemo na šest območij glede na naboj in okus leptonov. Izberemo dogodke z dvema leptonoma z invariantno maso nad 100 GeV ter vsaj dvema pljuskoma hadronov, ki ne izvirata iz kvarka b. Da dodatno ločimo signal od ozadja zahtevamo še $H_{\mathrm{T}} + E_{\mathrm{T}}^{\mathrm{miss}} > 500\,\text{GeV}$, saj pod to vrednostjo signala ne pričakujemo.

Izbrane simulirane dogodke uporabimo za učenje dveh algoritmov: CatBoost [145], ki uporablja odločevalna drevesa, in TensorFlow [146], ki uporablja nevronske mreže. Cilj algoritmov je klasifikacija dogodkov v dve kategoriji, signal ali ozadje. Algoritma bomo med seboj primerjali, zato za učenje obeh uporabimo iste dogodke. Več podrobnosti o posameznih algoritmih je podanih v poglavju 2.

Pri učenju uporabimo vse različne mase težkih leptonov, ki nas zanimajo, naenkrat. Dogodke naključno razdelimo v razmerju $2:1:1$ na tri sete, ki se uporabljajo za učenje, validacijo in test modelov. Pri delitvi se ohranjajo tako razmerja prispevkov posameznih ozadij kot tudi dogodkov, ki pripadajo posamezni masi novih leptonov. Za učenje uporabimo 24 količin, od katerih so najpomembnejše $m_{\ell\ell}$, $m_{\ell\ell} + E_{\mathrm{T}}^{\mathrm{miss}}$ and $\mathcal{S}(E_{\mathrm{T}}^{\mathrm{miss}})$. Odločevalna drevesa sem treniral preko 10000 iteracij. Nevronsko mrežo sestavljajo tri skrite plasti, vsaka z 256 nevroni, ki so med seboj povezane s funkcijo ReLU. Učenje je poteklo v gručah po 128 dogodkov preko 19 epoh. Rezultat obeh tipov algoritmov je verjetnost, da je dogodek signal z vrednostmi med 0 in 1. Bolje so se

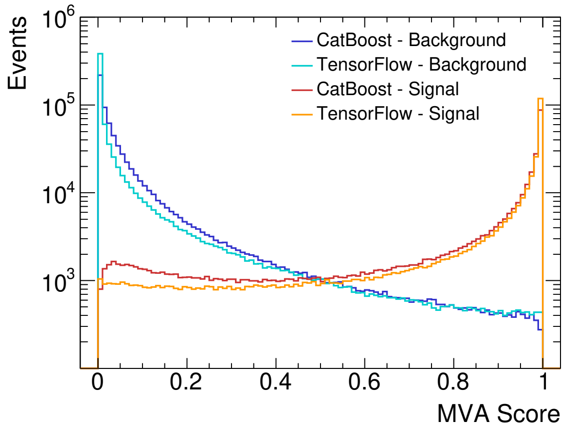

Slika 3: Primerjava delovanja odločevalnih dreves in nevronskih mrež na primeru ločevanja signal od ozadja. Posamezni dogodki niso obteženi glede na sipalni presek in učinkovitost rekonstrukcije.

odrezale nevronske mreže, saj več dogodkov ustrezno razvrstijo v pravilne kategorije, kar vidimo na sliki 3.

Rezultat strojnega učenja je pomembna količina za umestitev dogodkov v posamezna analizna območja. Signal pričakujemo z vrednostmi nad 0.8, kontrolna območja se nahajajo pod vrednostjo 0.4, vmesne vrednosti pa uporabimo za preverjanje ustreznosti opisa ozadja. Izjema so le kontrolna območja s pari leptonov enakega naboja, kjer je zgornja meja znižana na 0.2. Čeprav nevronska mreža dobro opiše naš model so za boljšo občutljivost na signal potrebni dodatni predhodni kriteriji. Z namenom zmanjšanja ozadja iz razpadov $Z \to ee$, se najprej zahteva $\mathcal{S}(E_{\mathrm{T}}^{\mathrm{miss}}) > 5$ v vseh območjih OS ter $\mathcal{S}(E_{\mathrm{T}}^{\mathrm{miss}}) > 4$ v območju SS z dvema elektronoma. Signifikanca signala se sicer rahlo zmanjša, ampak je zato sestava ozadja preprostejša. Tokrat v signalnih območjih prevladujejo predvsem razpadi dveh vektorskih bozonov. Verjetnost za signal je količina, uporabljena v statistični obdelavi. Za izpeljavo normalizacijskega faktorja uporabimo kontrolna območja z nizko verjetnostjo signalnih dogodkov. V ločenem območju izračunamo še normalizacijo razpadov $t\bar{t}$, ki predstavlja drugi glavni prispevek k ozadju. Celoten seznam območij z njihovimi definicijami se nahaja v tabeli 2.

Pomembna je natančna ocena napake tako pri določanju predvidenega ozadja kot tudi števila pričakovanih dogodkov signala. Nedoločenosti vplivajo na število dogodkov in na obliko opazovane porazdelitve. Normalizacija signala ter ozadja iz razpadov $t\bar{t}$ in dveh vektorskih bozonov je določena v kontrolnih območjih, posameznih prispevkov k njeni napaki posebej ne obravnavamo, ampak ocenimo le vpliv na obliko porazdelitve.

Ločimo dva tipa sistematske nedoločenosti oz. napake, eksperimentalno in teoretično napako. K slednji spadajo prispevki zaradi izbranega teoretičnega opisa signala ali

Tabela 1: Povzetek analiznih območij z uporabo pravokotnih rezov za izbiro dogodkov. Izbor je enak za vse kombinacije okusov leptonov.

	OS ($\ell^+\ell^- = e^+e^-, e^\pm\mu^\mp, \mu^+\mu^-$)		
	Top CR	$\boldsymbol{m_{jj}}$ **VR**	**SR**
N(jet)	≥ 2	≥ 2	≥ 2
N(b-jet)	≥ 2	0	0
m_{jj} [GeV]	$(60, 100)$	$(35, 60) \cup (100, 125)$	$(60, 100)$
$m_{\ell\ell}$ [GeV]	≥ 110	≥ 110	≥ 110
$\mathcal{S}(E_{\mathrm{T}}^{\mathrm{miss}})$	≥ 5	≥ 10	≥ 10
$\Delta\phi(E_{\mathrm{T}}^{\mathrm{miss}}, \ell)_{\mathrm{min}}$	—	—	≥ 1
$p_{\mathrm{T}}(jj)$ [GeV]	—	—	≥ 100
$p_{\mathrm{T}}(\ell\ell)$ [GeV]	—	—	≥ 100
$H_{\mathrm{T}} + E_{\mathrm{T}}^{\mathrm{miss}}$ [GeV]	≥ 300	≥ 300	≥ 300
	SS ($\ell^\pm\ell^\pm = e^\pm e^\pm, e^\pm\mu^\pm, \mu^\pm\mu^\pm$)		
	Diboson CR	$\boldsymbol{m_{jj}}$ **VR**	**SR**
N(jet)	≥ 2	≥ 2	≥ 2
N(b-jet)	0	0	0
m_{jj} [GeV]	$(0, 60) \cup (100, 300)$	$(0, 60) \cup (100, 300)$	$(60, 100)$
$m_{\ell\ell}$ [GeV]	≥ 100	≥ 100	≥ 100
$\mathcal{S}(E_{\mathrm{T}}^{\mathrm{miss}})$	≥ 5	≥ 5	≥ 7.5
$\Delta\phi(E_{\mathrm{T}}^{\mathrm{miss}}, \ell)_{\mathrm{min}}$	—	—	—
$p_{\mathrm{T}}(jj)$ [GeV]	—	—	≥ 60
$p_{\mathrm{T}}(\ell\ell)$ [GeV]	—	—	≥ 100
$H_{\mathrm{T}} + E_{\mathrm{T}}^{\mathrm{miss}}$ [GeV]	$(300, 500)$	≥ 500	≥ 300

Tabela 2: Povzetek analiznih območij z uporabo pravokotnih rezov za izbiro dogodkov. Izbor je enak za vse kombinacije okusov leptonov, razen za kanal z dvema elektronoma enakega naboja.

	OS ($\ell^+\ell^- = e^+e^-, e^\pm\mu^\mp, \mu^+\mu^-$)				**SS** ($\ell^\pm\ell^\pm = e^\pm e^\pm, e^\pm\mu^\pm, \mu^\pm\mu^\pm$)		
	Top CR	**CR**	**VR**	**SR**	**CR**	**VR**	**SR**
N(jet)	≥ 2	≥ 2	≥ 2	≥ 2	≥ 2	≥ 2	≥ 2
N(b-jet)	≥ 2	0	0	0	0	0	0
$m_{\ell\ell}$ [GeV]	≥ 100	≥ 100	≥ 100	≥ 100	≥ 100	≥ 100	≥ 100
$H_{\mathrm{T}} + E_{\mathrm{T}}^{\mathrm{miss}}$ [GeV]	≥ 500	≥ 500	≥ 500	≥ 500	≥ 500	≥ 500	≥ 500
$\mathcal{S}(E_{\mathrm{T}}^{\mathrm{miss}})$	≥ 7.5	≥ 7.5	≥ 5	≥ 5	≥ 4 (ee)	≥ 4 (ee)	≥ 4 (ee)
MVA score	—	$(0, 0.4)$	$(0.4, 0.8)$	$(0.8, 1)$	$(0, 0.2)$	$(0.4, 0.8)$	$(0.8, 1)$

ozadja. Druga večja skupina napak so eksperimentalne napake, ki so posledica neujemanja rekonstruiranih dogodkov med podatki in simulacijo. Napako pri kalibraciji delcev se oceni s spremembo gibalne količine delcev glede na nedoločenost posameznega prispevka k napaki. Drug tip eksperimentalnih napak oceni razliko v učinkovitosti posameznih rekonstrukcijskih algoritmov, npr. učinkovitost rekonstrucije naboja in učinkovitost proženja. V tem primeru se dogodki obtežijo glede na ocenjeno napako. Podrobnosti o obravnavanih napakah so podane v razdelku 6.4.

Končno statistično analizo podatkov opravimo z metodo maksimalne zanesljivosti (ang. *maximum-likelihood fit*). Maksimizirana verjetnost je produkt Poissonove verjetnosti, ki primerja število izmerjenih dogodkov s pričakovanimi za primera, ko v podatkih je signal in ko ga ni, in Gaussovih porazdelitev, ki modelirajo proste parametre sistematičnih napak. Njihove širine ustrezajo velikosti teh napak. K verjetnosti dodamo še Poissonove člene, ki modelirajo statistično napako simuliranih procesov, ter proste parametre za normalizacijo izbranih tipov ozadja. Glavni parameter maksimizacije je sipalni presek iskanega procesa nove fizike oz. normalizacijski faktor simuliranih dogodkov. Po maksimizaciji sem primerjal izmerjene podatke s pričakovanimi, kjer nisem opazil statistično signifikantnih odstopanj. V tem primeru lahko izpeljemo zgornje meje za sipalni presek za različne mase težkih leptonov s stopnjo zaupanja 95% z metodo $\mathrm{CL_s}$ [155]. Glede na te rezultate lahko postavimo tudi spodnjo mejo za maso leptonov po gugalničnem mehanizmu tipa III.

Vsakega izmed obeh pristopov analize sem analiziral posebej. V maksimizirani verjetnosti so nastopale celotne porazdelitve in ne samo celotno število dogodkov. Celotni rezultati so predstavljeni v poglavju 8, tukaj pa bom povzel nekaj izmed glavnih zaključkov. Normalizacija razpadov $t\bar{t}$ in parov vektorskih bozonov je prost parameter minimizacije. V analizi s strojnim učenjem so normalizacijski faktorji ločeni glede na kombinacijo okusov leptonov. Na sliki 4 so predstavljena števila izmerjenih in pričakovanih dogodkov v vseh analiznih območij po maksimizaciji. Opazimo dobro ujemanje med trki in simulacijo. Ob tem je pomembno omeniti, da je število dogodkov v signalnih območjih zaradi strojnega učenja lahko ostalo znatno večje, kot pri preprostih pravokotnih rezih. Pričakovane in izmerjene spodnje meje za maso težkih leptonov so prikazane na sliki 5. V primeru pravokotnih rezov pričakovana meja znaša 820^{+40}_{-60} GeV, kjer je napaka razbrana iz pasov $\pm 1\,\sigma$, izmerjena meja pa je 790 GeV. S strojnim učenjem se meje dvignejo na pričakovano 950^{+60}_{-70} GeV in izmerjeno 950 GeV.

Iz rezultatov lahko sklepamo, da funkcijske odvisnosti posameznih merjenih količin pomembno vplivajo na občutljivost analiz na novo fiziko. Z razvojem strojnega učenja in njegove vse preprostejše uporabe bomo v prihodnosti lahko lažje iskali redkejše razpade napovedanih novih delcev, kar nam bo pomagalo k boljšemu razumevanju nepojasnjenih pojavov v fiziki osnovnih delcev.

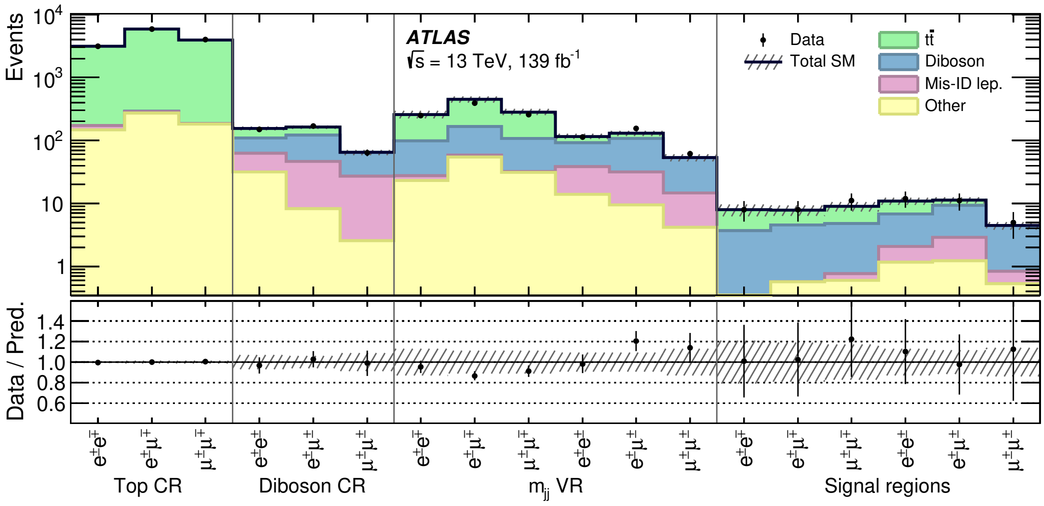

(a)

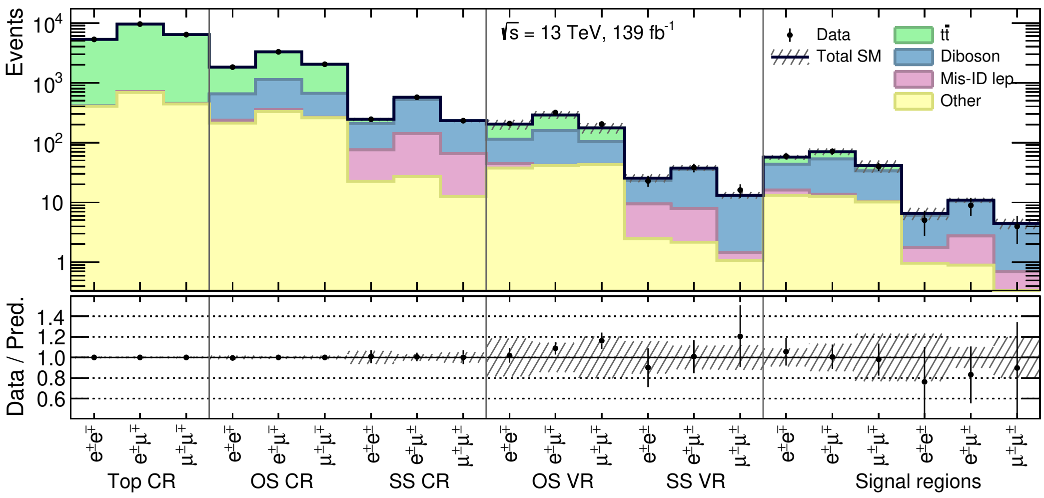

(b)

Slika 4: Število izmerjenih in pričakovanih dogodkov v analiznih območjih za primer (a) pravokotnih rezov [143] in (b) strojnega učenja. Pričakovani dogodki ozadja so rezultat maksimizacije verjetnosti po metodi, opisani v besedilu. Šrafirano območje zajema vse napake z upoštevanimi korelacijami.

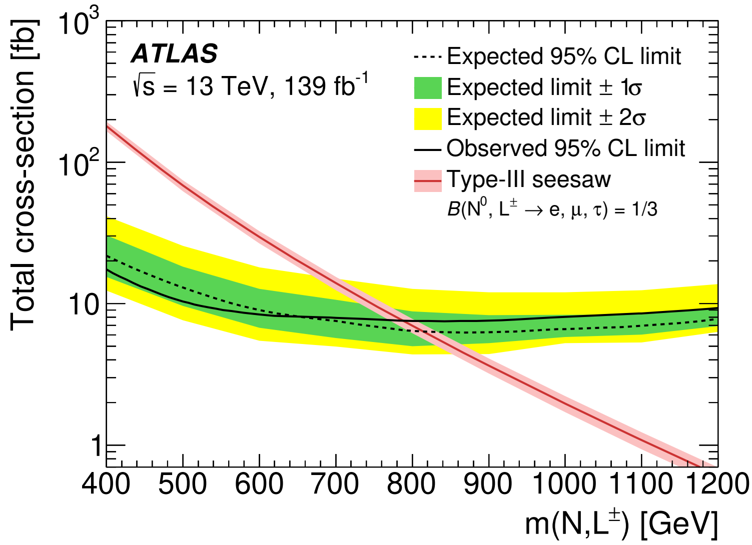

(a)

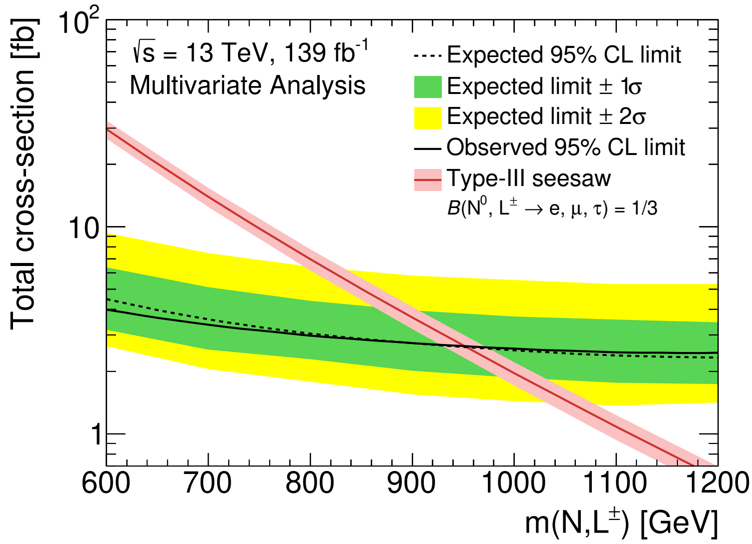

(b)

Slika 5: Spodnja meja s stopnjo zaupanja 95% za maso težkih leptonov po gugalničnem mehanizmu tipa III v primeru (a) pravokotnih rezov [143] in (b) strojnega učenja. Pričakovana teoretična krivulja sipalnega preseka in njena nedoločenost je prikazana z rdečo krivuljo.